CYRIC

ANNUAL REPORT

1997

(January 1997 - December 1997)

CYCLOTRON AND RADIOISOTOPE CENTER
TOHOKU UNIVERSITY

PREFACE

In this eighteenth issue of the CYRIC Annual Report, we summarize the activities for research and development and results of training for radioisotope safe-treatment at Cyclotron and Radioisotope Center, Tohoku University during the calendar year 1997.

In 1997 research programs in various fields such as nuclear physics, nuclear chemistry, solid state physics and element analyses by PIXE and activation were carried out, and radioisotopes were produced for use in biology and medicine. At the same time several facility improvements have been carried out. A total of 2928 hours of the cyclotron beam-time was delivered for the scheduled researches, while 30 hours for research and development for the accelerator and related facilities. In almost 75% of the beam time, protons were accelerated for nuclear physics and short-lived radioisotopes for medical and other studies, in 10% deuteron beams for the same purposes, while in 9% ^{4}He beams for material and solid state physics.

Among the various research programs, studies with PIXE technique have been continuously carried out by using electrostatic accelerator, installed at FNL (Fast Neutron Laboratory) in Graduate School of Technology, Tohoku University, under the scientific tie up between CYRIC and FNL. Indeed, more than six groups are running under this project using a total of its 250 hours beam-time.

During 1997 school year, 553 of staff members and students of Tohoku University were trained at this Center in the beginner's course of safe handling of radiation and radioisotopes, while 213 staff members and students in the "x-ray course". In addition, 87 of staff members and students were trained in the course of safe handling of radiation from a SOR (Synchrotron Orbital Radiation).

It is our great pleasure to inform that the budget in order to replace the present K=50 MeV AVF cyclotron with K=130 MeV AVF cyclotron equipped with high-intensity negative ion-source together with ECR heavy-ion and polarized-ion sources may be authorized by Japanese government in the next school year. Improvements of related experimental facilities such as the beam transport system including the beam swinger, automated synthesis system for short-lived positron emitter labeled compounds, on-line electromagnetic mass separator, and so on should also be scheduled.

On coming March 7, 1998, the ceremony and symposium for the 20th anniversary of the founding of CYRIC are scheduled to be held. In the symposium, four invited talks are presented in a general title of *Expectation for relevant scientific products by the new cyclotron.* Also planed is the memorial publication of a book (in Japanese), where 32 pieces of scientific report from various research fields described, and the list of the dissertations for Master (148) and Doctor (93) degrees, and that of the 545 published papers are compiled.

We are very grateful to Tohoku University and to the Ministry of Education, Science, Sports and Culture for their continuous support.

January 1998

Hikonojo ORIHARA

Director
Cyclotron and Radioisotope Center
Tohoku University

EDITORS:

Hikonojo ORIHARA
Manabu FUJIOKA
Tatsuo IDO
Takashi NAKAMURA
Masatoshi ITOH

WORD PROCESSED BY

Yu-ko YAMASHITA

CONTENTS

I. PHYSICS AND TECHNOLOGY

II. CHEMISTRY

III. MEDICINE AND BIOLOGY (Basic)

IV. MEDICINE AND BIOLOGY (Clinical)

V. RADIATION PROTECTION AND TRAINING OF SAFE HANDLING

I. PHYSICS AND TECHNOLOGY

I. 1. Isovector Part of Optical Potentials Studied by Analog Transitions though (p,n) Reaction at 35 MeV

Jon G. C., Orihara H., Yun C. C.*, Terakawa A.*, Itoh K.*, Yamamoto A.*, Suzuki H.*, Mizuno H.*, Kamurai G*., Ishii K**, and Ohnuma H.****

Institute of Physics, Academia Sinica, Nankang Taipei, Taiwan 11592
*Cyclotron and Radioisotope center, Tohoku University**
*Faculty of Engineering, Tohoku University***
*Department of Physics, Chiba Institute of Technology, Chiba 275-0023, Japan ****

Analog transitions have been studied for $N > Z$ nuclei with the isospin $T_0=(N-Z)/2$, for which the (p,n) reaction excites final states with $T = T_0$ as well as those with $T = T_0 \pm 1$. The $T = T_0$ states, having similar nature to the parent state, are referred to as isobaric analog states. The (p,n) transition to the ground-state analog (IAS) is regarded as elastic scattering with the isospin z-component flipped, and is hence sometimes called quasi-elastic scattering. It corresponds to the Fermi-type β-decay. Quasi-inelastic scattering, those to excited state analog states (EAS) such as 2^+, 3^-, 4^+, have also been observed.

Lane-model optical potential is often used in the macroscopic distorted-wave Born approximation (DWBA) analyses of the quasi-scattering. It is expressed as[1];

$$U(r)= - U_0(r)+(4/A)U_1(r)\,\vec{t}\cdot\vec{T}+U_{so}(r)+(1/2-t_z)V_C(r)\,, \qquad (1)$$

where $\vec{t}$ ($\vec{T}$) is the projectile (target) isospin, U_{so} is the spin-orbit potential, and V_C is the Coulomb potential. The isospin dependent $(t\cdot T)$ term yields t_+T_-, t_-T_+ and t_zT_z, corresponding to (p,n), (n,p) and (p,p) or (n,n) reactions, respectively. Then the (p,n) quasi-scattering takes place through the term

$$U_{pn}(r)=(2/A)\sqrt{N-Z}\cdot U_1(r)\,. \qquad (2)$$

The isovector potential U_1 is usually parametrized in terms of standard Woods-Saxon forms as

$$U_1(r)=V_1 f(x_R) - 4ia_I W_1 \frac{d}{dx_I} f(x_I)\,,$$

$$f(x) = (1 + e^x)^{-1}, \quad x = (r - R_i)/a_i, \quad \text{and} \quad R_i = r_i A^{1/3} \text{ (i = R or I).} \qquad (3)$$

In a macroscopic treatment, V_1 and W_1 in eq. (3) are dependent on energy and mass, and are directly determined by the strength and its q-dependence of the ground-state analog transition. In a microscopic treatment, on the other hand, the analog transition takes place through the isospin dependent part $(\tau \cdot \tau)\, V_\tau f(q)$ of the effective interaction, which is derived from G-matrix elements based on the free nucleon-nucleon interaction.

Knowledge of U_{pn} gives measures of the strengths of quasi-inelastic scattering leading to excited analog states[2-4] as well. Recently particular attention has been paid to the isovector potential strength. It plays a dominant role for coupling between the giant isovector monopole state and the isobaric analog state, yielding a spreading width for the latter[5]. Studies of Fermi-type transitions to the IAS by the (p,n) reaction present a good place to explore this potential. Carlson and his collaborators reported[6] a systematic optical model analysis of quasi elastic (p,n) reactions at 22.8 MeV on 29 nuclei ranging from ^{9}Be to ^{208}Pb. They derived U_1 for each target nucleus, and gave a smooth parametrization of the best-fit parameters in U_1 for all the nuclei investigated. However, their data and analysis were limited by experimental conditions and theoretical treatment of mixed analog transitions.

We have reported[7] observation of analog transition at E_p = 35 MeV in (p,n) reactions on thirteen target nuclei ranging $17 \le A \le 48$, ^{17,18}O, ^{22}Ne, ^{25,26}Mg, ^{30}Si, ^{34}S, ^{38,40}Ar, and ^{42,44,48}Ca. Pure $\Delta J^\pi = 0^+$ Fermi-type transitions were observed for six of them. As for the other seven nuclei, contributions from mixed $\Delta J^\pi \neq 0^+$ components or those from unresolved transitions were evaluated by microscopic DWBA calculations to subtract them from the raw data and extract pure Fermi-type transition strengths. The best-fit parameters for the Lane-type isovector potential (V_1, W_1, r_I, a_I) were obtained for each transition, and then each parameter was expressed as a linear function of $A^{1/3}$. The values of V_1 were determined within $\pm 3 \sim \pm 5\%$ accuracy in the mass region studied. It was found that W_1 was almost independent of $A^{1/3}$.

In this report we extend our previous work and discuss the isovector part of the Lane potential based on experimental data of (p,n) reactions at E_p = 35 MeV on a variety of target nuclei ranging $7 \le A \le 15$ and $50 \le A \le 208$; namely, ^{7}Li, ^{9}Be, ^{13,14}C, ^{15}N, ^{50}Cr, ^{54,56}Fe, ^{58,60,62,64}Ni, ^{70}Zn, ^{71}Ga, ^{92}Zr, ^{110,112,114,116}Cd, ^{116,118,120}Sn, ^{172,174,176}Yb, in addition to the sd-shell and f-shell nuclei discussed in Ref. 7.

The experiment was performed at the Cyclotron and Radioisotope Center, Tohoku University, with a 35-MeV proton beam from an AVF-cyclotron and a beam swinger system. The details of the experimental setup have been described previously[8,9]. Neutron energies were measured by the time-of-flight technique (TOF), where neutrons were detected by a detector array located at 44.3 m from the target. The detectors, 23.2 ℓ in a total sensitive volume, were filled with organic liquid scintillator NE213. The absolute efficiencies of the detectors were obtained from the ^{7}Li(p,n) ^{7}Be activation analyses with an error less than ± 6%. Errors in the absolute magnitude of (p,n) cross sections were estimated to be less than

12%. All the targets were enriched isotopes with enrichments better than 95%. Figures 1 and 2 illustrate the angular distributions of the (p,n) reactions on ^{13}C and ^{70}Zn leading to the ground state and IAS as representative cases.

As discussed in detail in Ref. 7, for the nuclei in $7 \leq A \leq 15$ except for the case of ^{14}C, it was necessary to subtract contributions from $\Delta J^{\pi} \neq 0^{+}$ components. Here, we describe the procedure of microscopic DWBA calculations needed to extract cross sections for the pure $\Delta J^{\pi} = 0^{+}$ Fermi-type transition from the raw data by subtracting other contributions.

The data for the p-shell nuclei were first compared with microscopic DW results calculated by the computer code DWBA-74[10], which includes knock-on exchange effects in an exact manner. Note that fully antisymmetrized calculations were made in the present microscopic DW analysis, in which non-normal parity terms such as $\Delta J(\Delta L, \Delta S) = 1(1, 0)$ for the $0^{+} \rightarrow 1^{+}$ transition also contribute to the cross section. Optical potential parameters of Becchetti and Greenlees[11] were used for the entrance channel. Those for the exit channel were self-consistent potential parameters derived by Carlson et al[6]. The effective nucleon-nucleon interactions used in the present DW analysis were those by Bertsch et al. (M3Y) [12]. Sensitivity of such calculations to the optical-potential parameters is elaborated in Ref. 13.

Spectroscopic amplitudes (OBTD) for the microscopic DWBA analysis for the p-shell nuclei were obtained from full p-shell model calculations[14] using the code OXBASH with the interaction by Millener and Kurath[15]. Single-particle radial wave functions used in DW calculations were generated in a Woods-Saxon potential with $r_0 = 1.25$ fm, $a = 0.6$ fm, $V_{LS} =$ 6 MeV and the depth adjusted to reproduce the binding energy of a valence nucleon.

Assuming the (p,n) reaction leading to the IAS is caused by the isovector potential expressed as Eq. (3), which has a volume-type real part and a surface-type imaginary part, the parameters to be determined are the potential depths V_1 and W_1, geometrical parameters for the real part r_R and a_R, and those for the imaginary part r_I and a_I To reduce the number of parameters to be fitted, the real geometrical parameters r_R and a_R were fixed to those by Becchetti and Greenlees[11], since these are usually taken as fixed in both entrance and exit channels when they are used in distorting potentials. Then we carried out a parameter search with the program IASEARCH[16] to find the best-fit parameter set to reproduce differential cross sections for each IAS transition. Finally, we found global relation for each parameter as a linear function of $A^{1/3}$ by least-squares fit.

Table 1 lists the best-fit parameters obtained for each reaction together with those for sd- and f-shell nuclei in Ref. 7. The radius of the imaginary potential decreases gradually, while the diffuseness parameter increases, as $A^{1/3}$ increases. The real potential depth V_1 increases as well. The imaginary potential depth W_1 seems to be almost constant in the mass region studied. These best-fit parameters are plotted as a function of $A^{1/3}$ in Figs. 3 and 4. It should be noted that the values obtained from the "subtracted data" lie on a smooth line, confirming again the validity of the procedure described before and reliability of microscopic calculations. The solid lines indicate results of least-squares fit assuming that all parameters

are a linear function of $A^{1/3}$. Taking the diagonal and off-diagonal elements of the error matrices, we were able to describe $A^{1/3}$ dependence of the potential parameters as :

$$V_1 = 6.377 + 2.244A^{1/3} \pm \sqrt{0.3864 - 2\times 0.09384A^{1/3} + 0.02423(A^{1/3})^2}$$
$$W_1 = 5.087 + 0.3931A^{1/3} \pm \sqrt{0.2194 - 2\times 0.05834A^{1/3} + 0.01640(A^{1/3})^2} \quad , \qquad (4)$$

and

$$r_1 = 1.978 - 0.1522A^{1/3} \pm \sqrt{0.003669 - 2\times 0.001028A^{1/3} + 0.0003021(A^{1/3})^2}$$
$$a_1 = -0.09018 + 0.2239A^{1/3} \pm \sqrt{0.001983 - 2\times 0.0005315A^{1/3} + 0.0001508(A^{1/3})^2} \quad . \qquad (5)$$

The dotted and dash-dotted lines in Figs. 3 and 4 indicate values one standard deviation above and below the best-fit value, respectively.

One discussion should be given on the feedback of the isovector potential U_1 to the potentials used to construct distorted waves in the entrance and exit channels in the DW analysis. These correction terms are $\pm 2U_1 (N - Z)^{1/2}/A$ for the proton and neutron channels, respectively, and less than a several % of the distorting potential strengths. Their effects on the final results may be therefore ignored. The data were reanalyzed by using the corrected optical potential parameters. It was indeed found that the contributions from the correction terms were negligibly small, and the results in the previous section are hardly changed.

In the present study, the imaginary part of U_1 was taken as free parameters, whereas the strength of this term has so far been thought to be one half of the real part[6]. As seen in Fig. 5, the A-dependence of the imaginary depth is weaker than that derived from $W_1 = 1/2V_1$. It seems almost constant and about 6 MeV over the mass region studied. When we compare the present results with those of earlier work by Carlson et al. at E_p = 22.8 MeV[6], although they do not give error estimates and furthermore they have limited the applicable region as $A \geq 40$ ($A^{1/3} \geq 3.420$), almost same results were obtained for geometrical parameters r_1 and a_1 except that the present values are less $A^{1/3}$ dependent. Due to the difference in the incident proton energies, the magnitudes of the present V_1 are 20% smaller than those of Ref. 6.

To summarize, analog transitions have been observed at E_p = 35 MeV in (p,n) reactions on thirteen target nuclei ranging $7 \leq A \leq 15$ and $50 \leq A \leq 208$. Pure $\Delta J^\pi = 0^+$ Fermi-type transitions were observed for nuclei in $50 \leq A \leq 208$. As for the nuclei in $7 \leq A \leq 15$, contributions from mixed $\Delta J^\pi \neq 0^+$ components were evaluated by microscopic DWBA calculations to subtract them from the raw data and extract pure Fermi-type transition strengths. The best-fit parameters for the Lane-type isovector potential (V_1, W_1, r_1, a_1) were obtained for each transition, and then each parameter was expressed as a linear function of $A^{1/3}$. The values of V_1 were determined by present parametrization within $\pm 3 \sim \pm 5$% accuracy in the mass region studied. It was found that W_1 is almost independent of $A^{1/3}$.

References

1) Lane A. M., Phys. Rev. **8**, 171 (1962).
2) Orihara H. et al., Phys. Lett. **106B**, 171 (1981).
3) Murakami T. et al., Nucl. Phys. **A377**, 163 (1982).
4) Maeda K. et al., Nucl. Phys. **A403**, 1 (1983).
5) Suzuki T. et al., to be published in Phys. Rev.
6) Carlson J. D., Zafiratos C. D. and Lind D. A., Nucl. Phys. **A249**, 29 (1975).
7) Jon G. C. et al., Phys. Rev. C **56** (1997) 900.
8) Orihara H. and Murakami T., Nucl. Instrum. Methods **181**, 15 (1981).
9) Orihara H. et al., Nucl. Instrum. Methods **A257**, 189 (198 7).
10) Schaeffer R. and Raynal J., unpublished.
11) Becchetti F. D. and Greenlees G. W., Phys. Rev. **182**, 1190 (1969).
12) Bertsch G. et al., Nucl. Phys. **A284**, 399 (1977).
13) Ohnuma H. et al., Nucl. Phys. **A467**, 61 (1987).
14) The shell model code OXBASH, Echegoyen A. E. et al., National Superconducting Cyclotron Laboratory Report No. 524 (1984)
15) Millener D. J. and Kurath D. Nucl. Phys. **A255** (1975) 315.
16) A parameter search code for elastic and quasi-elastic scattering. Quasielastic calculations are made using the Lane model and adopted from the code DWUCK4 originally written by Kunz P. D.

Table 1. Best-fit parameters of isovector potential for each nucleus.

Reaction	E_{exc} of IAS (MeV)	V_1 (MeV)	W_1 (MeV)	r_1 (fm)	a_1 (fm)
^{7}Li(p,n)^{7}Be	0.0	11.65±1.56	5.62±1.10	1.923±0.072	0.386±0.072
^{9}Be(p,n)^{9}B	0.0	12.53±1.10	6.36±0.87	1.780±0.064	0.420±0.054
^{13}C(p,n)^{13}N	0.0	12.38±1.05	6.20±0.81	1.697±0.063	0.462±0.052
^{14}C(p,n)^{14}N	2.3129	13.20±1.07	6.64±0.78	1.754±0.052	0.462±0.049
^{15}N(p,n)^{15}O	0.0	11.56±0.98	6.30±0.82	1.730±0.061	0.408±0.051
^{17}Op,n)^{17}F	0.0	12.00±1.25	6.00±0.80	1.750±0.050	0.450±0.050
^{18}O(p,n)^{17}F	1.041	11.26±1.08	5.76±0.60	1.560±0.039	0.451±0.053
^{22}Ne(p,n)^{22}Na	0.657	12.19±0.73	5.59±0.63	1.600±0.054	0.450±0.055
^{25}Mg(p,n)^{25}Al	0.0	12.06±1.56	6.24±0.87	1.584±0.065	0.500±0.065
^{26}Mg(p,n)^{26}Al	0.228	12.66±0.58	6.27±0.40	1.543±0.034	0.533±0.036
^{27}Al(p,n)^{27}Si	0.0	11.00±1.50	5.89±0.98	1.403±0.061	0.500±0.070
^{30}Si(p,n)^{30}P	0.677	11.84±1.22	6.50±0.32	1.493±0.032	0.528±0.034
^{34}S(p,n)^{34}Cl	0.0	12.90±0.78	6.20±0.59	1.425±0.033	0.580±0.047
^{38}Ar(p,n)^{38}K	0.130	13.27±0.87	6.50±0.48	1.404±0.023	0.668±0.032
^{40}Ar(p,n)^{40}K	4.384	13.97±0.55	5.89±0.30	1.373±0.024	0.722±0.029
^{42}Ca(p,n)^{42}Sc	0.0	13.20±0.50	6.69±0.50	1.414±0.029	0.704±0.029
^{44}Ca(p,n)^{44}Sc	2.783	14.80±0.97	6.99±0.87	1.414±0.050	0.699±0.050
^{48}Ca(p,n)^{48}Sc	6.677	13.86±0.93	6.38±0.80	1.400±0.029	0.720±0.028
^{54}Fe(p,n)^{54}Co	0.0	16.61±0.73	7.56±0.70	1.320±0.086	0.906±0.065
^{56}Fe(p,n)^{56}Co	3.5	16.25±0.89	7.31±0.78	1.450±0.079	0.870±0.058
^{58}Ni(p,n)^{58}Cu	0.203	14.96±1.02	7.44±0.85	1.365±0.071	0.880±0.063
^{60}Ni(p,n)^{60}Cu	2.54	14.40±0.89	6.67±0.83	1.407±0.067	0.878±0.049
^{62}Ni(p,n)^{62}Cu	4.63	16.40±0.79	7.40±0.81	1.365±0.069	0.908±0.044
^{64}Ni(p,n)^{64}Cu	6.71	16.51±1.21	7.43±0.76	1.382±0.085	0.886±0.058
^{70}Zn(p,n)^{70}Ga	8.26	15.58±1.20	4.87±1.65	1.370±0.090	0.950±0.170
^{71}Ga(p,n)^{71}Ga	8.96	17.24±1.75	7.04±1.20	1.400±0.130	0.832±0.150
^{92}Zr(p,n)^{92}Nb	8.94	14.85±1.80	5.87±1.03	1.230±0.103	0.914±0.078
^{110}Cd(p,n)^{110}In	8.80	16.70±0.92	5.70±0.66	1.355±0.089	0.968±0.071
^{112}Cd(p,n)^{112}In	10.04	17.10±0.97	7.98±0.93	1.188±0.138	1.053±0.153
^{114}Cd(p,n)^{114}In	11.12	16.30±0.89	6.35±0.81	1.344±0.076	0.950±0.058
^{116}Cd(p,n)^{116}In	12.04	16.80±0.93	6.67±0.87	1.356±0.068	0.982±0.051
^{116}Sn(p,n)^{116}Sb	8.61	18.30±0.94	5.97±1.23	1.275±0.095	1.100±0.120
^{118}Sn(p,n)^{118}Sb	9.36	16.41±0.82	6.58±0.73	1.341±0.092	0.969±0.051
^{120}Sn(p,n)^{120}Sb	10.24	16.86±0.86	7.02±0.95	1.345±0.098	0.980±0.067
^{140}Ce(p,n)^{140}Pr	11.04	18.80±1.29	7.59±0.98	1.178±0.087	1.046±0.053
^{172}Yb(p,n)^{172}Lu	13.7	19.304±0.91	8.11±0.92	1.310±0.082	1.120±0.134
^{174}Yb(p,n)^{174}Lu	14.8	18.90±0.84	7.87±0.97	1.179±0.086	1.190±0.096
^{176}Yb(p,n)^{176}Lu	16.0	18.95±0.98	7.02±0.99	1.270±0.098	1.002±0.102
^{208}Pb(p,n)^{208}Bi	15.17	20.17±1.44	8.00±1.27	1.250±0.112	0.960±0.104

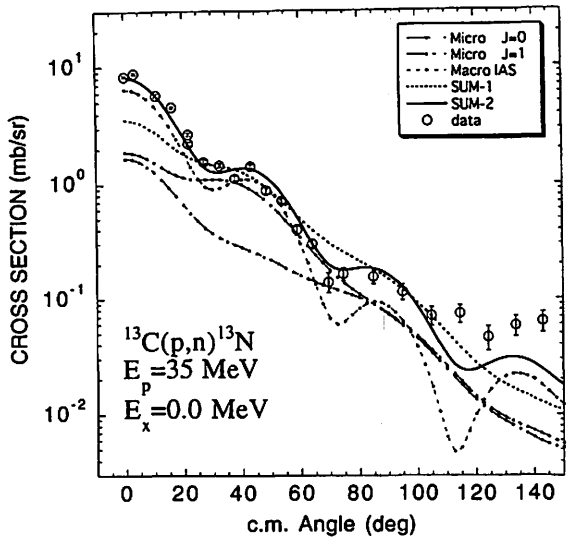

Fig. 1. Differential cross sections for neutrons leading to the ground state of ^{13}C. The curves are DW results for the $1/2^- \rightarrow 1/2^-$ transition for each ΔJ^π. The line denoted by "Macro IAS" is the macroscopic calculation using the isovector potential with the best-fit parameters obtained in the present study. The line denoted by "SUM-1" shows the sum over microscopic predictions for all ΔJ^π including $\Delta J^\pi = 0^+$ Fermi-type transition, while that denoted by "SUM-2" shows the same except that the $\Delta J^\pi = 0^+$ calculation is replaced by "Macro IAS".

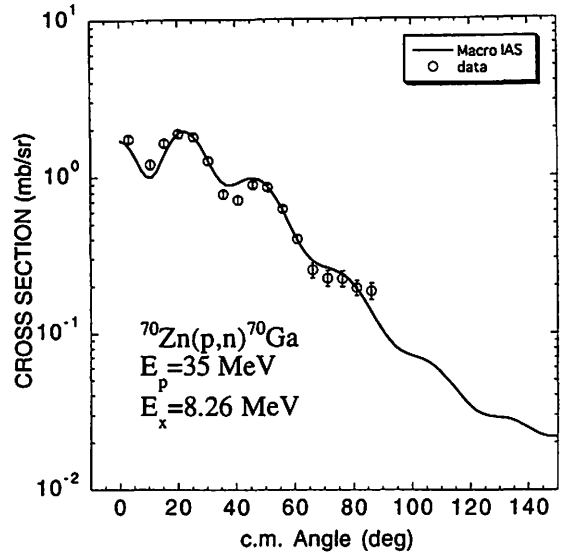

Fig. 2. Differential cross sections for neutrons leading to the 8.26-MeV IAS in ^{70}Zn. This is an example of pure IAS transitions. The solid line shows the macroscopic DW calculation obtained with the best-fit parameters obtained with the best-fit parameters for the isovector potential, and the dotted line shows microscopic DW calculation.

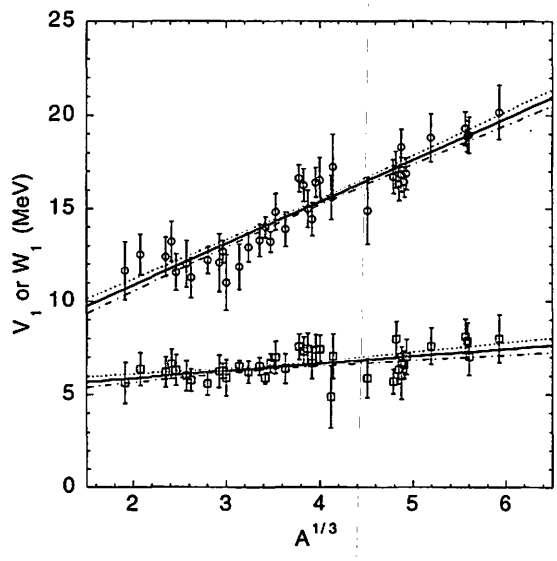

Fig. 3. Best-fit values of V_1 and W_1 plotted as a function of $A^{1/3}$. The solid lines indicate results of least-squares fit with errors shown by the dotted (+σ) and dot-dashed (-σ) lines calculated from error matrices.

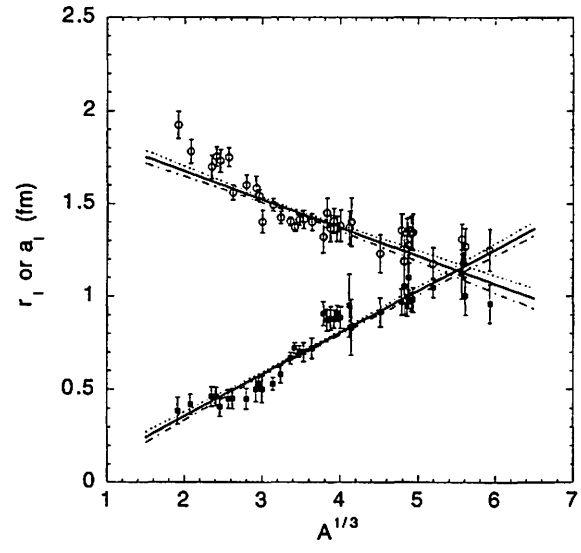

Fig. 4. Same as Fig. 4 but for r_1 and a_1

I. 2. Gamow-Teller Distribution in the $^{27}Al(p,n)^{27}Si$ Reactions at 35 MeV

Orihara H., Yun C. C., Terakawa A., Itoh K., Yamamoto A., Suzuki H., Mizuno H., G. Kamurai, G. C. Jon., Ishii K.**, and Ohnuma H.****

Cyclotron and Radioisotope center, Tohoku University
*Institute of Physics, Academia Sinica, Nankang Taipei, Taiwan 11592**
*Faculty of Engineering, Tohoku University***
*Department of Physics, Chiba Institute of Technology, Chiba 275-0023, Japan ****

Study of the (p,n) reaction at 35 MeV with high-resolution experiments[1-4], together with well-established effective nucleon-nucleon interactions and recently advanced shell-model one-body-transition-densities (OBTD), allows us to evaluate absolutely (p,n) cross sections with microscopic distorted wave Born approximation (DWBA) theory even for the cases where a number of ΔJ^{π} contribute to the transition. In Ref. 4 we have explained successfully the differential cross sections for the $5/2^+ \rightarrow 5/2^+$ transition in the $^{17}O(p,n)^{17}F$(g. s.) reaction where six components of $\Delta J^{\pi} = 0^+$–5^+ pieces contribute. It has been also found that microscopic DWBA analyses successfully reproduce absolute values of the (p,n) cross sections between 20° and 90° for most $\Delta J^{\pi} = 2^+$, 3^+, and 5^+ transitions observed in ^{22}Ne, ^{24}Mg, and ^{34}S[1-3], while a renomalization factor ranging 0.5-0.7 is needed to fit the experimental cross section with the DWBA prediction. Systematic microscopic analyses of the data were reported in these papers using the Brown-Wildenthal (BW) wave functions[5], for which a stringent test with the charge-exchange reaction has been carried.

Since the spin-parity of even-odd nucleus ^{27}Al is $5/2^+$, the transferred ΔJ value is not unique; e.g. for the case of the $3/2^+$ state excitation, $\Delta J^{\pi}=1^+$, 2^+, and 3^+, hence the (p,n) cross section is the incoherent sum over those from $\Delta J^{\pi}=1^+$, 2^+, and 3^+ transitions. As such, $\Delta J^{\pi}=1^+$ ($\Delta L=0$) Gamow-Teller (GT) type transition may be involved in $5/2^+ \rightarrow 3/2^+$, $5/2^+$, and $7/2^+$ transitions. Investigation of the GT strength distribution leading to the individual particle-hole state in sd-shell nuclei is one of the subject of current nuclear physics from view points of a stringent test for the shell-model wave function, and for the relation among β-decay probability, magnetic dipole strength and (p,n) cross section. In this report we discuss briefly how reasonably reproduced the (p,n) cross sections by microscopic DWBA calculations with one-body transition densities (OBTD), by which reduced matrix elements for β -decay and M1 transition are obtained in the same manner.

The experiment was performed at the Cyclotron and Radioisotope Center, Tohoku University, with a 35-MeV proton beam from an AVF-cyclotron and a beam swinger system. The details of the experimental setup have been described previously[6,7]. Neutron energies were measured by the time-of-flight technique (TOF), where neutrons were detected by a detector array located at 44.3 m from the target. The detectors, 23.2ℓ in a total sensitive volume, were filled with organic liquid scintillator NE213. Metallic foil of Al was used for the target. The absolute efficiencies of the detectors were obtained from the ^{7}Li(p,n)^{7}Be activation analyses with an error less than ± 6%. Errors in the absolute magnitude of (p,n) cross sections were estimated to be less than 12%. Overall neutron energy resolution was typically 160 keV. Figure 1 illustrates a typical excitation energy spectrum of neutrons leading to the low-lying states in ^{27}Si following the ^{27}Al(p, n)^{27}Si reaction. In Figs. 2 and 3, the angular distributions of the cross section are presented. The lines in the figures are microscopic DWBA predictions described below.

The data have been compared with microscopic DW results calculated by the computer code DWBA-74[8], which includes knock-on exchange effects in an exact manner. Note that fully antisymmetlized calculations are made in the present microscopic DW analysis, in which non-normal parity terms such as $\Delta J(\Delta L, \Delta S) = 1(1, 0)$ for the $0^+ \rightarrow 1^+$ transition also contribute to the cross section. Optical potential parameters of Becchetti and Greenlees[9] are used for the entrance channel. Those for the exit channel are self-consistent potential parameters derived by Carlson et al[10]. The effective nucleon-nucleon interactions used in the present DW analysis are those by Bertsch et al. (M3Y)[11]. Sensitivity of such calculations to the optical-potential parameters is elaborated in Ref. 12. Spectroscopic amplitudes (OBTD) for the microscopic DWBA analysis were obtained from full-sd shell-model calculations[13] using the code OXBASH with the A-dependent interaction of Wildenthal[5]. Single-particle radial wave functions used in DW calculations were generated in a Woods-Saxon potential with r_0 = 1.25 fm, a = 0.6 fm, V_{LS} = 6 MeV and the depth adjusted to reproduce the binding energy of a valence nucleon.

In Fig. 2, experimental and theoretical cross sections are presented for the (p,n) reactions on ^{27}Al leading to the $5/2^+$ (g.s.), $1/2^+$ (0.781MeV), and $3/2^+$ (0.941MeV) states in mirror nucleus ^{27}Si. The $5/2^+$ (g.s.)$\rightarrow 5/2^+$ (g.s.) transition contains all ΔJ in particle-hole excitation in sd-shell nuclei. As discussed in Ref. 14, the major part of differential cross sections is reproduced absolutely by the incoherent sum over ΔJ=0, 1, 2, 3, 4, and 5 contributions, although a renomalization factor of 0.6 is needed for ΔJ=1 transition. The most prominent component is ΔJ=0 analog transition, while the stretched ΔJ=5 transition plays as well important role to reproduce the cross sections at larger angles. Our interest is focused on the ΔJ=1 GT like transition. The shell-model predicts a value of 0.861 for GT matrix element. This contribution indeed gives a dominant contribution as seen in Fig. 2. The $5/2^+ \rightarrow 1/2^+$ (0.781MeV) transition is only one which dose not contain ΔJ=1, GT

transition, giving us an example to check whether cross sections are absolutely fitted by summation over ΔJ when the ΔJ=1 component dose not exist. Note that fitting is quite reasonable. The $5/2^+ \rightarrow 3/2^+$ (0.941MeV) transition is the first one, its counter part will be seen in Fig. 3 as the second $5/2^+ \rightarrow 3/2^+$ (2.864MeV) with much more intensities. Shell model predictions of GT matrix element for 0.941 and 2.864 MeV states are, respectively, 0.0114 and 0.594, corresponding to the log ft values of 5.75 and 4.03.

Also shown in Fig. 3 are differential cross sections for the $5/2^+ \rightarrow 7/2^+$ (2.164MeV) $5/2^+ \rightarrow 5/2^+$ (2.648MeV), and $5/2^+ \rightarrow 3/2^+$ (2.864MeV) transitions. In the $5/2^+ \rightarrow 7/2^+$ transition, ΔJ=1 GT transition, for which shell-model predicts a B(GT) value of 0.204, carries almost all contribution to this reaction. In the $5/2^+ \rightarrow 5/2^+$ leading to the 2.648 MeV states, ΔJ=0 component is involved, predicted cross section for which is quite small and its angular distribution shows that for knock-on exchange reaction. These all together suggest that this ΔJ=0 transition is anti-analog transition against ΔJ=0 in the ground state. A prominent peak is found at 2.86 MeV in the neutron excitation energy spectrum, for which spin-parity assignment has been given to be $3/2^+$ with some ambiguities. The shell model calculation predict a strong GT transition with a B(GT) value of 0.594 leading to the $3/2^+$ state at 2.78 MeV, thus we may confirm this state to be $3/2^+$.

A result of the present study is listed in Table 1, comparing log *ft* values for each transition with those for β-decay between mirror nuclei. In summary, differential cross sections of the ^{27}Al(p,n) ^{27}Si reaction leading to the six low-lying states in ^{27}Si were measured. Cross sections were fitted with microscopic DWBA predictions by introducing renomarization factor for the $\Delta J^{\pi}=1$, GT like transition. It was found that prominent parts of GT strength distribution were located in the low-lying transition, and a fairly reasonable comparison for the GT matrix elements has been made between those from the (p,n) reaction and β-decay.

References

1) Furukawa K. et al., Phys. Rev. C **36**, 1686 (1987) and Furukawa K., Ph. D. Thesis, Tohoku University, 1986.
2) Orihara H. et al., Phys. Rev. C **41**, 2414 (1990).
3) Kiang G. C. et al., Nucl. Phys. **A499**, 339 (1989).
4) Oura M. et al., Nucl. Phys. **A586**, 20 (1995).
5) Wildenthal B. H., Prog. in Particle and Nuclear Physics, ed. Wilkinson D. H. (Pergamon, London, 1984) vol. 11, p. 5.
6) Orihara H. and Murakami T., Nucl. Instrum. Methods **181**, 15 (1981).
7) Orihara H. et al., Nucl. Instrum. Methods **A257**, 189 (198 7).
8) Schaeffer R. and Raynal J., unpublished.
9) Becchetti F. D. and Greenlees G. W., Phys. Rev. **182**, 1190 (1969).
10) Carlson J. D., Zafiratos C. D. and Lind D. A., Nucl. Phys. **A249**, 29 (1975).
11) Bertsch G., Borysowics J., McManus H. and Love W. G., Nucl. Phys. **A284**, 399 (1977).
12) Ohnuma H. et al., Nucl. Phys. **A467**, 61 (1987).

13) The shell model code OXBASH, Echegoyen A. E. et al., National Superconducting Cyclotron Laboratory Report No. 524 (1984)
14) Jon G. C. et al., Phys. Rev. C **56** (1997) 900.
15) Table of Isotope, Seventh Edition (1978) ed. Lederer C. M. and Shirley V. S.

Table 1. Comparison for log ft values obtained by the ^{27}Al(p,n)^{27}Si reaction with those in β-decay.

Present Result by the ^{27}Al(p,n)^{27}Si Reaction					^{27}Si→^{27}Al [Ref. 15]
Transition	B(GT) shell-model	renormalization factor	B(GT) (p,n) reaction	log *ft**	log ft β-decay
5/2$^+$ (g.s.) → 5/2$^+$ (g.s.)	0.8608	0.6	0.5164	3.61*	3.6
5/2$^+$ → 3/2$^+$ (0.941MeV)	0.0112	0.7	0.0078	-	7.3
5/2$^+$ → 7/2$^+$ (2.164MeV)	0.2040	0.7	0.1428	4.64	4.7
5/2$^+$ → 5/2$^+$ (2.648MeV)	0.1071	0.6	0.0643	4.98	5.0
5/2$^+$ → 3/2$^+$ (2.864MeV)	0.5944	0.5	0.2972	4.32	4.3

* B(F) + B(GT)= 6163.4/*ft*
** B(F)=1

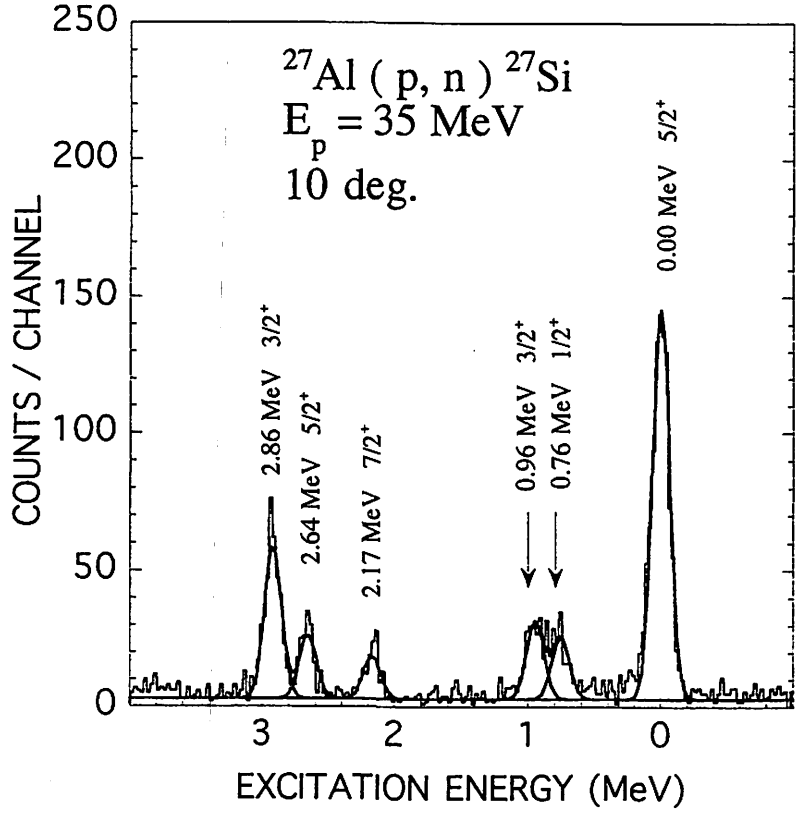

Fig. 1. A sample excitation energy spectrum of neutrons leading to the low-lying states in ^{27}Si following the ^{27}Al(p,n)^{27}Si reaction taken at 3° with a flight path of 44.3 m. Energy per bin is 25 keV.

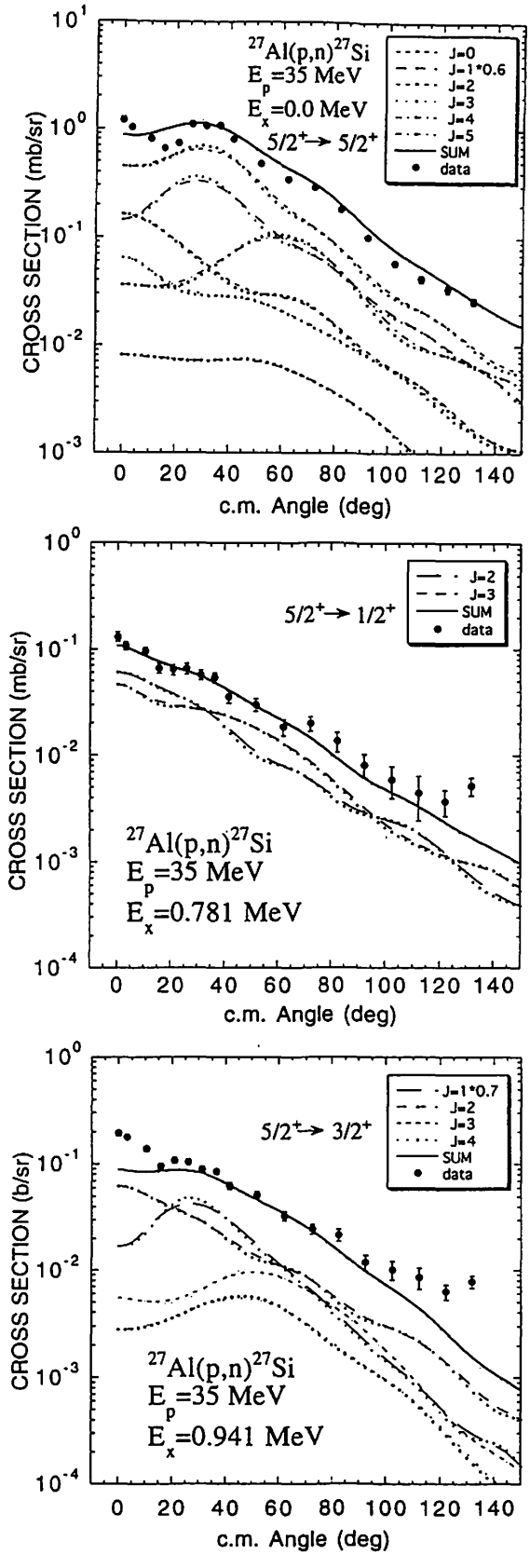

Fig. 2. Differential cross sections for neutrons leading to the ground state and $1/2^+$ and $3/2^+$ states in ^{27}Si. Curves are DW results for the $5/2^+$ (g.s.) → $5/2^+$ (g.s.), $5/2^+$ → $1/2^+$ (0.781MeV) and $5/2^+$ → $3/2^+$ (0.941MeV) transition for each ΔJ^π. The line denoted by "SUM" shows the sum over microscopic predictions for all ΔJ^π.

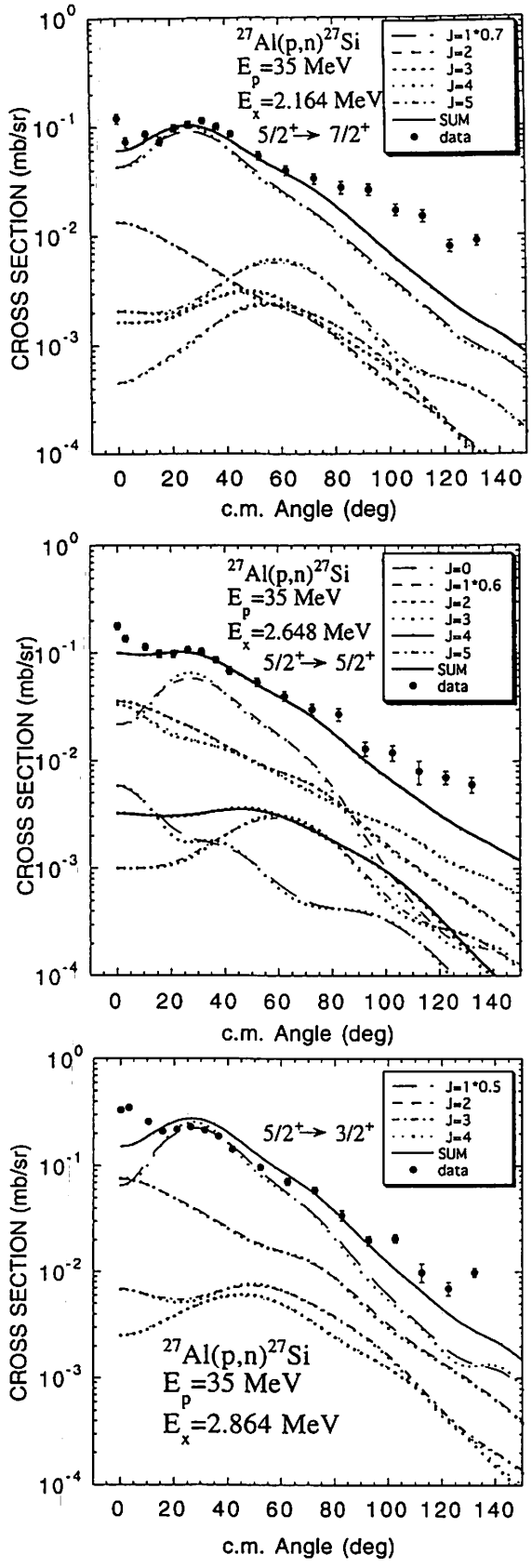

Fig. 3. Same as Fig. 1 but for the $5/2^+ \rightarrow 7/2^+$ (2.164MeV), $5/2^+ \rightarrow 5/2^+$ (2.648MeV) and $5/2^+ \rightarrow 3/2^+$ (2.864MeV) transition for each ΔJ^π.

I. 3. $^{32}S(d,n)^{33}Cl$ Reaction at 25 MeV

Terakawa A., Tohei T., Nakagawa T.**, Takamatsu J.**, Narita A.***, Hosomi K.**, Orihara H., Ishii K.****, Oura M.[‖], Hosaka M.[¶], Jon G. C.[%], Miura K.[†], and Ohnuma H[††].*

Cyclotron and Radioisotope Center, Tohoku University
*Tohoku Institute of Technology**
*Department of Physics, Tohoku University***
*Department of Information Science, Hirosaki University****
*Faculty of Engineering, Tohoku University*****
The Institute of Physical and Chemical Research (RIKEN)[‖]
Institute of Molecular Science[¶]
Institute of Physics, Academia Sinica[%]
Chiba Institute of Technology[††]

Proton single-particle states in 2s1d-shell nuclei have been extensively investigated by means of the high-resolution (d,n) experiments[1,2]. In comparison with the recent shell-model analysis[3] based on the complete 2s1d-shell space, the result of the $^{20,22}Ne(d,n)^{21,23}Na$ reactions have shown that 25-MeV (d,n) reaction deduces reasonable spectroscopic factors[2].

In this report we present the result of the $^{32}S(d,n)^{33}Cl$ reaction at 25 MeV. Although proton single-particle strengths in ^{33}Cl have so far been studied using (d,n)[4] and (^3He,d)[5] reactions, little is known[6] about the high-lying strengths above the one-proton emission threshold.

In this work we aim to study the proton single-particle strength of the 2s1d-shell orbitals as well as 1f2p-shell orbitals. Furthermore, we attempt to deduce the occupation probabilities and the single-particle energies of the proton orbitals near the Fermi surface for ^{33}Cl using the present stripping results in combination with the previous pickup data[7].

The experiment was performed using a 25 MeV deuteron beam from the AVF cyclotron at Cyclotron and Radioisotope Center, Tohoku University. The target used was natural surfer which was sandwiched between two natural platinum foils. The target thickness was 2.2 mg/cm^2. Emitted neutrons were detected with the neutron detector containing NE213 liquid scintillator. Neutron energies were measured by time-of-flight technique. Details of the CYRIC TOF-facility have been described elsewhere[8]. A typical neutron spectrum obtained in the $^{32}S(d,n)^{33}Cl$ reaction is shown in Fig. 1.

In order to extract the spectroscopic strengths in ^{33}Cl, adiabatic deuteron breakup approximation (ADBA) analysis[9] has been made with the code DWUCK4[10]. The adiabatic potential parameters used in the calculations were generated from the global potential of

Becchetti and Greenlees for a proton[11] and that of Martin for a neutron[12]. In the case of unbound transitions, resonant form factors were calculated according to a procedure of Vincent and Fortune[13]. The spectroscopic results from the analysis are listed in Table 1 together with the earlier data[4,5]. The observed strength distributions for the 2s1d-shell orbitals are compared with the shell model estimations[3] in Fig. 2.

Since the $1d_{5/2}$ and $2s_{1/2}$ proton orbitals in Surfer isotopes are filled under the simple shell-model consideration, a small amount of the 2s1d-shell strength will be observed in the stripping reaction. Indeed, the populations of the 2s1d-shell strength in the present measurement are only four transitions leading to the ground, 0.81-MeV, 2.35-MeV and 6.86 MeV states. The 0.81-MeV, l = 0 transition is a important signature of the partial occupancy of the $2s_{1/2}$ proton orbital due to ground state correlations. The strength distribution of the 2s1d-shell strengths have been reproduced by the shell model calculation[3].

All other observed transitions are the proton stripping to the 1f2p-shell orbitals. The location of these strengths has been characterized by low-lying dominant strengths and additional highly fragmented components up to E_x=10MeV.

Occupation probabilities and single-particle energies of proton orbitals near the Fermi surface for ^{32}S have been estimated according to the procedure used in the previous studies[14]. The results are shown in Fig. 3 together with the shell model predictions[3]. The 2s1d shell model calculations reasonably reproduce the observation.

In conclusion, the proton single-particle states in ^{33}Cl have been studied through the $^{32}S(d,n)^{33}Cl$ reaction at 25 MeV. The spectroscopic strengths for both the 2s1d-shell and the 1f2p-shell orbitals have been derived from the ADBA analyses. The observed strength distributions and the occupation probabilities for the 2s1d-shell orbitals are in reasonable agreement with the respective shell-model predictions[3].

References

1) Miura K. et al., Nucl. Phys. **A467**, 79 (1987).
2) Terakawa A. et al., Phys. Rev. C **48**, 2775 (1993).
3) Wildenthal B. H., Prog. Part. Nucl. Phys. **11**, 5 (1984).
4) Egun Paul M. et al., Phys. Rev. C **38**, 2495 (1988).
5) Kozub R. L. and Youngblood D. H., Nucl. Phys. **A140**, 97 (1970).
6) Endt P. M., Nucl. Phys. **A521**, 1 (1990)
7) Mackh H. et al, Z. Phys. **269**, 353 (1974).
8) Orihara H. and Murakami T., Nucl. Instrum Methods 188, 15 (1981).,Orihara H. et al., Nucl. Instrum Methods, **A257**, 189 (1987).
9) Johnson R. C. and Sorper P. J. R., Phys. Rev. C **1**, 976 (1970).
10) Kunz P. D., Computer code DUCK (unpublished).
11) Becchetti F. D. and Greenlees G. W., Phys. Rev. **182**, 1190 (1969).
12) Martin Ph., Nucl. Phys. A466, 119(1987).
13) Vincent C. M. and Fortune H. T., Phys. Rev. C **2**, 782 (1970).
14) Mairle G. et al., Nucl. Phys. **A565**, 543 (1993).

Table 1: Experimental spectroscopic strengths in $^{33}C\ell$.

$E_x^{A)}$	$J^{\pi A)}$	$E_x^{B)}$	$n\ell j^{B)}$	$(2J+1)C^2S$ $B)$	$C)$	$D)$
0	$\frac{3}{2}^+$	0	$1d_{3/2}$	2.86	2.36	2.52
0.81	$\frac{1}{2}^+$	0.82	$2s_{1/2}$	0.74	0.34	0.74
2.35	$\frac{3}{2}^+$	2.36	$1d_{3/2}$	0.26		0.24
2.69	$\frac{7}{2}^-$	2.69	$1f_{7/2}$	3.33	7.36	3.28
2.85	$\frac{3}{2}^-$	2.86	$2p_{3/2}$	2.25	4.80	2.32
4.12	$\frac{3}{2}^-$	4.13	$2p_{3/2}$	0.53		0.30
4.52	$\frac{1}{2}^-$	4.55	$2p_{1/2}$	0.44		
4.78	$\frac{7}{2}^-$	4.79	$1f_{7/2}$	0.41		0.32
5.08	$\frac{1}{2}^-$	5.09	$2p_{1/2}$	0.44		0.14
5.28	$\frac{5}{2}^-$	5.27	$1f_{5/2}$	0.19		
5.65	$\frac{3}{2}^-$	5.66	$2p_{3/2}$	0.33		0.10
5.88	$\frac{5}{2}^-$	5.89	$1f_{5/2}$	0.17		0.16
6.29	$\frac{7}{2}^-$	6.29	$1f_{7/2}$	0.46		0.40
6.39	$\frac{3}{2}^-$	6.44	$2p_{3/2}$	0.15		
6.63	$(\frac{5}{2},\frac{7}{2})^-$	6.66	$1f_{5/2}$, $1f_{7/2}$*)	0.46, 0.36		0.37, 0.27
6.86	$(\frac{3}{2},\frac{5}{2})^+$	6.84	$1d_{3/2}$*), $1d_{5/2}$	0.22, 0.19		
6.92	$\frac{5}{2}^-$	6.97	$1f_{5/2}$	0.28		
6.99	$\frac{5}{2}^-$					
7.30	$\frac{9}{2}^+$	7.33	$1g_{9/2} + 1f_{7/2}$	0.22+0.15		0.33
7.32	$\frac{7}{2}^-$					
7.45	$\frac{3}{2}^-$	7.49	$2p_{3/2}$	0.44		
		7.72	$1f_{5/2}$, $1f_{7/2}$*)	0.14, 0.11		
		7.93	$1f_{5/2}$, $1f_{7/2}$*)	0.20, 0.15		
		8.11	$1f_{5/2}$, $1f_{7/2}$*)	0.11, 0.09		
		8.29	$1f_{5/2}$, $1f_{7/2}$*)	0.30, 0.40		0.25, 0.20
		8.49	$1f_{5/2}$, $1f_{7/2}$*)	0.30, 0.23		(0.18), (0.16)
		8.86	$1f_{5/2}$, $1f_{7/2}$*)	0.42, 0.32		0.30, 0.24
		9.56	$1f_{5/2}$, $1f_{7/2}$*)	0.27, 0.20		
		9.78	$1f_{5/2}$, $1f_{7/2}$*)	0.27, 0.20		

A) Ref. [6].
B) (d,n) at 25 MeV. Present work.
C) (d,n) at 8.0-8.6 MeV. Ref. [4].
D) (^{3}He,d) at 34.5 MeV. Ref. [5].
*) Assumed $n\ell j$ in the summation of the spectroscopic strength.

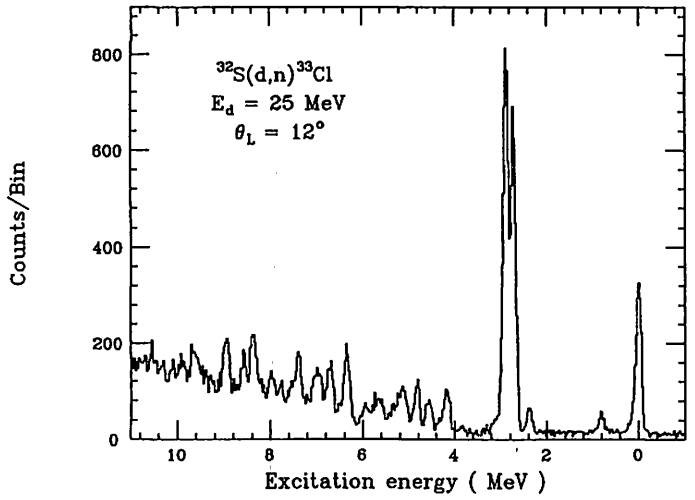

Fig. 1. A neutron spectrum obtained from the ^{32}S(d,n)^{33}Cl reaction at 25 MeV. Energy per channel is 25 keV.

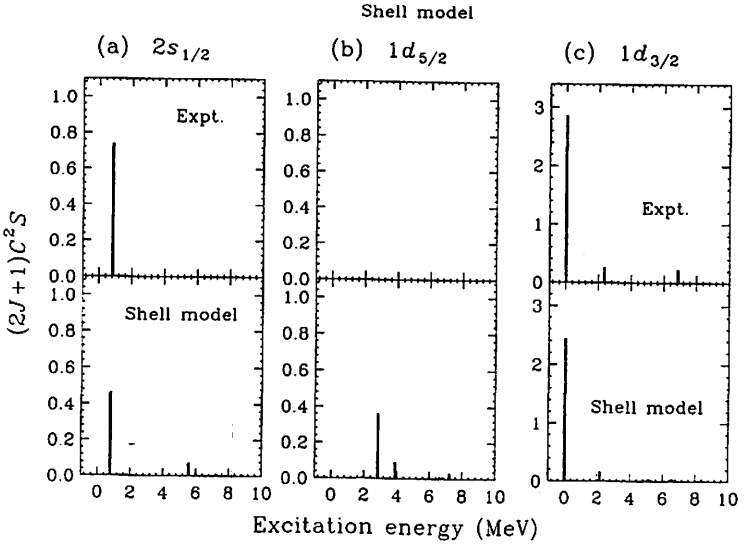

Fig. 2. Experimental and theoretical strength distributions for the 2s1d orbitals.

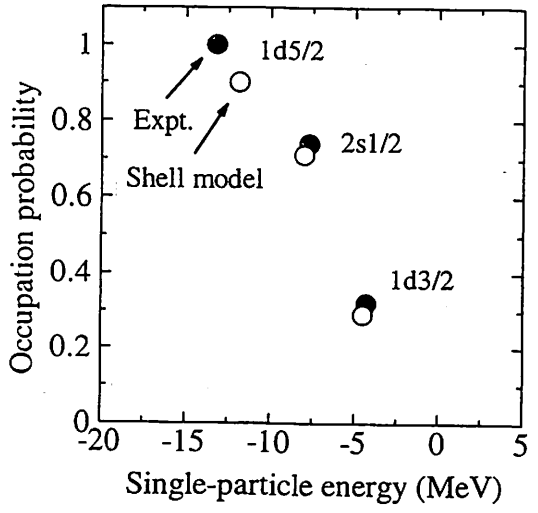

Fig. 3. Experimental and theoretical occupation probabilities of the 2s1d orbitals.

I. 4. Single-particle States in the ^{59}Co Nuclei

Matsunaga M., Nakagawa T., Fujii Y., Aizawa T., Yamazaki A., Kumagai K., Hirai M., Orihara H., Terakawa A.*, Itoh S. K.*, Yun C. C.*, Yamamoto A.*, Matsumura N.*, Kawami K.*, Suzuki H.*, Kamurai G.*, Mizuno H.*, Abe K.**, Ishii K.**, Tohei T.***, Suehiro T.***, and Ohnuma H.*****

Department of Physics, Tohoku University
*Cyclotron and Radioisotope Center, Tohoku University**
*Department of Nuclear Engineering, Tohoku University***
*Tohoku Institute of Technology Sendai Japan****
*Chiba Institute of Technology Chiba Japan*****

A deuteron stripping reaction at higher incident energy, is a very useful tool to study a one-proton state as a target nucleus plus one proton. From spectroscopic factors derived as a ratio of experimental differential cross section to one calculated with distorted wave Born approximation (DWBA), we can get some information for the ground state of a target nucleus, such as proton occupation probabilities and single-particle energies of shell-model orbits. Therefore, the (d,n) reaction plays an important role in the nuclear spectroscopic study.

In nuclear shell-model, Z or N = 20-28 nuclei are expected to have simpler configurations in the ground state wave function, because of large energy gaps between orbits above and below $1f_{7/2}$ and itself. From this point of view, the spectroscopic studies for Sc , Co and Cu isotopes have been done through the (d,n) reactions in the Ca (Z = 20) , Fe (Z = 26) and Ni (Z = 28) isotopes at E_d=25MeV, so far[1-4].

It becomes clear from these studies that the ground state wave function for a nucleus cannot be described by a simple shell model, because of change of proton single-particle energies with neutron number, even if the nucleus has the same proton number. Therefore, it is a very interesting problem how much the proton occupation probabilities and energy gaps between each shell-model orbit in $1f_{7/2}$ shell nuclei are. This time, basing on above systematic results, a spectroscopic study has been done by the (d,n) reaction for the ^{58}Fe (Z = 26) target at E_d=25MeV.

The experiment was accomplished at CYRIC using the AVF cyclotron and 44 m time of flight facility[5,6]. The ^{58}Fe target consisted of a self-supporting foil with 5.4 mg/cm^2 thickness, and an it's isotopical enrichment 74±9 % determined with another experiment. Angular distributions of the differential cross section were measured between 0° and 65° at laboratory angles. An excitation energy spectrum at θ=19° is shown in Fig. 1. Energy

resolution for the ground state was about 280 keV. The angular distributions were measured for states up to about 11 MeV in excitation energy range.

DWBA calculations were done using the code DWUCK4[7,8]. Finite range and nonlocality corrections were applied to these calculations and the method of Vincent & Fortune[9] was used for DWBA calculations of unbound states. Taking into account of deuteron break-up effect, the adiabatic approximation by Jonson & Soper[10] was used for the optical model potential parameters of the incident channel. In this treatment, the potential parameters for a proton and neutron were taken from the systematics of Becchetti & Greenlees[11] and Carlson et al[12], respectively. The potential parameters of Carlson et al. were also used for the outgoing neutron. Typical differential cross sections for the ^{58}Fe(d,n)^{59}Co reaction are shown in Fig. 2.

For ^{59}Co, the information for the transfer momentum ℓ and spectroscopic factor were restricted the result of (^{3}He, d)[13] in 1965, up to about 2 MeV. In the present work, we have observed many proton-single-particle states in the excitation energy region over 2 MeV. And we could assign the transfer momentum ℓ and get the spectroscopic factors for many states, which have never been assigned by one proton transfer reactions up to this time.

Obtained spectroscopic factors for ^{59}Co are shown in Table 1, and excitation energy distributions of the spectroscopic factors for each transfer momentum ℓ are shown in Fig .3. In this figure, entirely, fragmentations have been seen from a comparison between^{55,57}Co and ^{59}Co. Particularly in ℓ =1 states, the fragmentations occur, so the spectroscopic factors disperse into a lot of weak states in the wide exicitaion energy region. In ℓ =3 states, the tendency that $1f_{7/2}$ states almost concentrate in the ground states, has been observed in ^{55,57,59}Co in common.

The sums of the spectroscopic factors for each orbit are shown in Fig. 4. In the figure, the dotted lines show the simple shell-model limits and the solid lines show the derived values in the present work. That for the $1f_{7/2}$ orbit reaches the sum rule limit, so almost all strengths for this orbit are considered to be observed. The strengths for the 2p and $1f_{5/2}$ orbits are smaller than the shell-model limits. This may imply that there exist weak peaks, because of a fragmentation, which has not been observed in the present measurement, or strengths distribute also in the excitation energy region above 11 MeV.

In conclusion, we have observed many proton-single-particle states for the ^{59}Co nucleus by the (d,n) reaction at E_d=25MeV in the excitation energy region up to about 11 MeV and assigned the transfer momentum ℓ for each state, which had been never assigned. In the obtained spectroscopic factors, the fragmentations have been observed from a comparison between ^{55,57}Co and ^{59}Co. The sums of those for each orbit are lower than the sum-rule limits from simple shell-model, but for $1f_{7/2}$, almost all strengths are observed.

References

1) Mori S., Phys. M. thesis, Tohoku University 1988.
2) Hino T., Phys. M. thesis, Tohoku University 1995.
3) Aizawa T., Phys. M. thesis, Tohoku University 1996.
4) Inomata T., Phys. M. thesis, Tohoku University 1992.
5) Orihara H. and Murakami T., Nucl. Instrum. and Meth. **188** (1981) 15.
6) Orihara H. et al., Nucl. Instrum. and Meth. **A257** (1987) 189.
7) Kunz P. D., a DWBA code. Univ. Colorado, unpublished.
8) Comfort J. R., Extended version for the program DWUCK4. unpublished.
9) Vincent C. M. and Fortune H. T., Phys. Rev. **C2** (1970) 782.
10) Johnson R. C. and Soper P. J. R., Phys. Rev. **C1** (1970) 976.
11) Becchetti F. D. and Greenlees G. W., Phys. Rev. **182** (1969) 1190.
12) Carlson J. D. et al., Nucl. Phys. **A249** (1979) 15.
13) Blair A. G. et al., Phys. Rev. **140** (1965) 1567.
14) Banks S. M. et al., Nucl. Phys. **A437** (1985) 381.
15) Puttaswamy N. G. et al., Nucl. Phys. **A401** (1983) 269.
16) Reiner K., Nucl. Phys. **A472** (1987) 1.
17) Mairle G., Nucl. Phys. **A543** (1992) 558.

Table. 1. Experimental spectroscopic factors for ^{59}Co.

	Present work E_d=25MeV				^{58}Fe(^{3}He,d)^{59}Co [13] E=22MeV			
No.	Ex	ℓ	j^π	$(2j+1)C^2S$	Ex	ℓ	j^π	$(2j+1)C^2S$
1	g.s	3	7/2⁻	1.67	g.s	3	7/2⁻	1.36
2	1.10	1	(3/2⁻)	0.31	1.10	1	3/2⁻	0.44
			(1/2⁻)	0.32				
3	1.34	1	(3/2⁻)	1.33	1.29	1	3/2⁻	1.36
			(1/2⁻)	1.38				
					1.43	1	1/2⁻	0.74
4	1.74	1+3	(3/2⁻)+5/2⁻	0.04+0.07				
			(1/2⁻)+5/2⁻	0.04+0.08				
5	2.12	3	(5/2⁻)	1.64	2.08	3		unresolved multiplet
			(7/2⁻)	1.09				
6	2.80	1	(3/2⁻)	0.22				
			(1/2⁻)	0.23				
7	3.15	1+3	(3/2⁻)+5/2⁻	0.07+0.65				
			(1/2⁻)+5/2⁻	0.07+0.66				
8	3.47	1	(3/2⁻)	0.18				
			(1/2⁻)	0.19				
9	3.78	1+4	(3/2⁻)+9/2⁺	0.10+0.23				
			(1/2⁻)+9/2⁺	0.10+0.27				
10	4.30	1+4	(3/2⁻)+9/2⁺	0.33+1.50				
			(1/2⁻)+9/2⁺	0.33+1.61				
11	4.92	1	(3/2⁻)	0.14				
			(1/2⁻)	0.15				
12	6.43	1+3	(3/2⁻)+5/2⁻	0.13+0.21				
			(1/2⁻)+5/2⁻	0.12+0.16				
13	6.75	1+3	(3/2⁻)+5/2⁻	0.31+0.20				
			(1/2⁻)+5/2⁻	0.29+0.26				
14	7.06	1+4	(3/2⁻)+9/2⁺	0.06+0.10				
			(1/2⁻)+9/2⁺	0.05+0.11				
15	7.36	1+3	(3/2⁻)+5/2⁻	0.07+0.03				
			(1/2⁻)+5/2⁻	0.07+0.05				
16	7.59	1	(3/2⁻)	0.06				
			(1/2⁻)	0.08				
17	7.93	1+4	(3/2⁻)+9/2⁺	0.09+0.11				
			(1/2⁻)+9/2⁺	0.09+0.12				
18	8.34	1+4	(3/2⁻)+9/2⁺	0.05+0.09				
			(1/2⁻)+9/2⁺	0.05+0.10				
19	8.66	1	(3/2⁻)	0.12				
			(1/2⁻)	0.12				
20	8.91	1	(3/2⁻)	0.10				
			(1/2⁻)	0.10				
21	9.27							
22	9.55	2	(5/2⁻)	0.20				
			(3/2⁻)	0.22				
23	9.81	1	(3/2⁻)	0.10				
			(1/2⁻)	0.10				
24	10.06	1+3	(3/2⁻)+5/2⁻	0.09+0.38				
			(1/2⁻)+5/2⁻	0.08+0.41				
25	10.35	2	(5/2⁺)	0.09				
			(3/2⁺)	0.10				
26	10.69	1+4	(3/2⁻)+9/2⁺	0.12+0.13				
			(1/2⁻)+9/2⁺	0.07+0.33				
27	11.10	1+4	(3/2⁻)+9/2⁺	0.19+0.33				
			(1/2⁻)+9/2⁺	0.19+0.38				

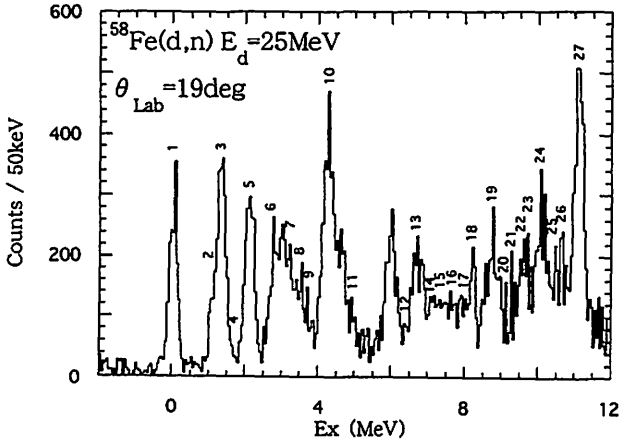

Fig. 1. A typical neutron energy spectrum in the ^{58}Fe(d,n)^{59}Co reaction at E_d = 25MeV.

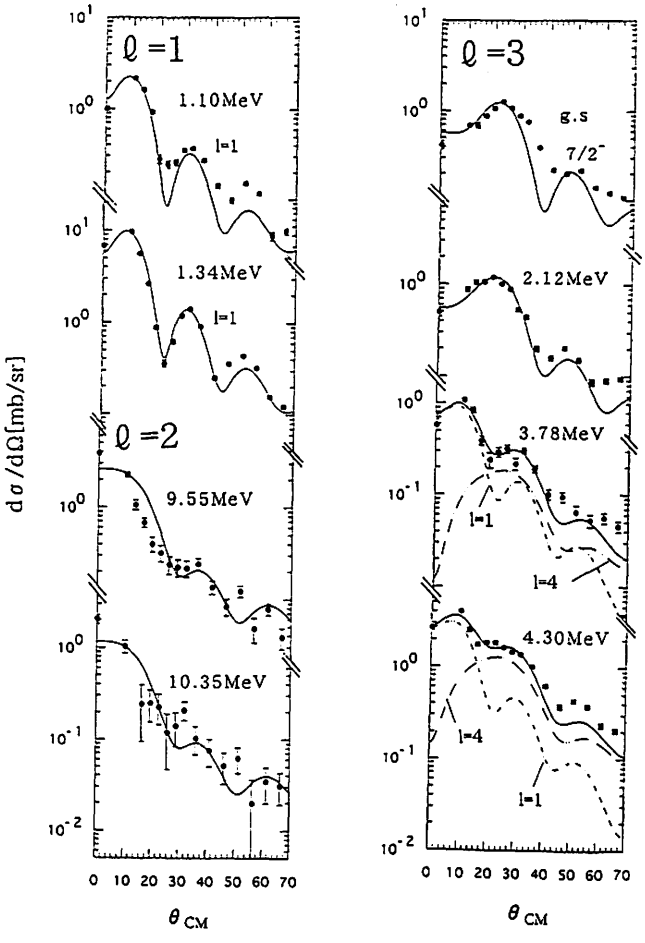

Fig. 2. Typical differential cross sections for the ℓ=1-4 transitions in the ^{58}Fe(d,n)^{59}Co reaction.

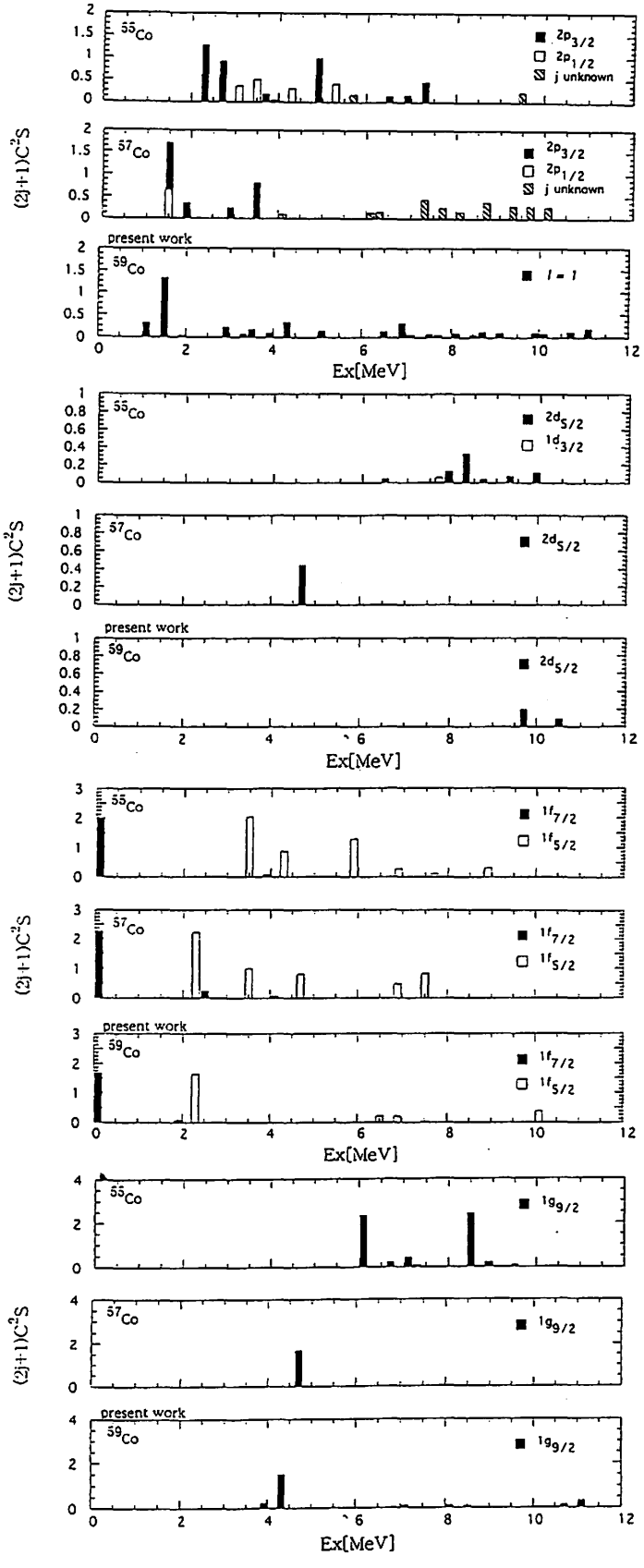

Fig. 3. Excitation energy distributions of single particle strengths for each orbit in ^{55,57,59}Co.

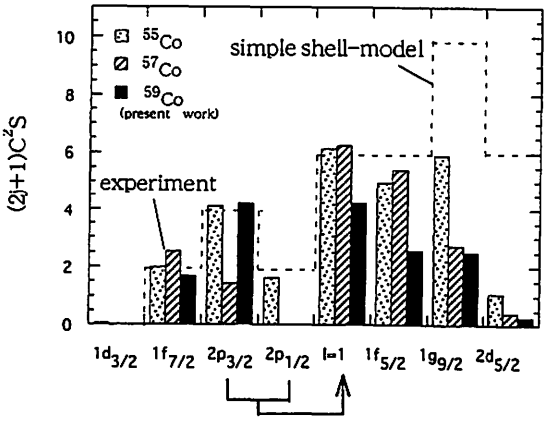

Fig. 4. Summed spectroscopic factors of ^{59}Co for each ℓ, together with those of ^{55,57}Co.

I. 5. Measurement of the Life Time of the First Excited State of $^{64}_{31}Ga_{33}$

Sekiguchi K., Tanigaki M., Shinozuka T.*, Fujita M.*, Hoshino T., Baba T., Kawamura N.**, and Fujioka M.**

Department of Physics, Tohoku University
*CYRIC, Tohoku University**
*Department of Engineering, Aomori University***

It was said that isospin was well preserved in nuclei because of Pauli-blocking in spite of the presence of electric force. But near the N=Z line the blocking effect is decreased and we can see the effects of isospin mixing in some parameters of the nucleus. In a recent experiment of ^{64}Ge strong nuclear deformation and isospin forbidden E1-gamma transition was observed[2] ; therefore ^{64}Ge and nuclei around it are attracting attention. So we decided to measure the life time of the first excited state of ^{64}Ga. ^{64}Ga is the isotone of ^{64}Ge and life time of its first excite state was only known to be longer than 1μs. (see Fig. 1.) The life of an isomer strongly depends on the wave-function of two states (initial and final states), so it is a very important quantity for the study of nuclear structure.

We used the 34-course of Cyclotron and Radioisotope Center (CYRIC) in this experiment. In this course there is a Pulse-type beam chopper (P-chopper)[3] and it can change beam burst and interval freely; we can measure life times of 1μs~1s.

Since the life time was considered to be several tens of μs, we selected the beam burst and interval of 15μs and 150μs respectively (15μs beam on and 150μs beam off). ^{64}Ga was produced via the ^{63}Cu(^{3}He, 2n) ^{64}Ga reaction at 16 MeV of ^{3}He energy. The first excited state^{2+} of ^{64}Ga decays to ground state 0^{+} by E2-transition emitting gamma-ray of energy 42.89 keV. Therefore we detected this gamma-ray by a HP-Ge gamma-ray detector. We measured energy of gamma ray emitted from ^{64}Ga first excited state and its incidence time to the HP-Ge detector at the same time and made 2 dimension experimental data. The life time was obtained by analyzing the data and making the decay curve .

The analysis was done by the next procedure.

1) making gamma-ray energy spectrum every 3μs,
2) fitting by gaussian- curve to the photo peak of 42.89 keV and deriving its areas,
3) making the decay curve by plotting the peak areas versus the decay time, and
4) fitting by an exponential curve to the decay curve and obtaining the life time.

In this way we obtained the life time to be

$31.9 \pm .4 \mu s$.

Here we compare the experimental value and a calculated one (Weisskopf unit) in terms of reduced transition probability $B(E2)$. Correcting the internal conversion coefficient $(\alpha=13)^4$, we obtained

$B(E2)= 10.2\ e^2\ fm^4$;(experimental).

On the other hand calculated Weisskopf unit is

$B(E2)=15.2\ e^2\ fm^4$;(Weisskopf unit).

The two values are in good agreement if we consider that the Weisskopf unit is a very coarse approximation. But Weisskopf unit is based on the simplest single-particle (proton) model, and that ^{64}Ga is a rather complicated odd-odd(31-33) nucleus ; this agreement is rather surprising and suggests the nuclear structure of ^{64}Ga to be interesting. Further elucidation of the nuclear structure of ^{64}Ga by measuring g-factor etc. is desired.

We conclude;

1) the low-lying states of odd-odd nucleus ^{64}Ga may be well described by the many-particle shell model. A detailed calculation is under progress[5], and
2) we can take off the bracket from the J^{π}Œassignment of the first-excited state (2^+), i.e. , we can safely assign J^{π}Œ$=2^+$ to this state.

References

1) Hansen L. F. ,et al., Levels of ^{64}Ga via the ^{64}Zn(p, n) and ^{64}Zn(p, nγ) reaction, Physical Review **C10** (1974) 1111.
2) Robertson R. F. H. and Austin S. M., Neutron-deficient isotopes ^{64}Ge and ^{65}Ge, Physical Review C9 1801.
3) Kawamura N. et al., CYRIC annual report (1980) 263.
4) Way K. ed., Atomic And Nuclear Data Reprints, Academic Press Inc., London (1973).
5) Ogawa K., private communications.

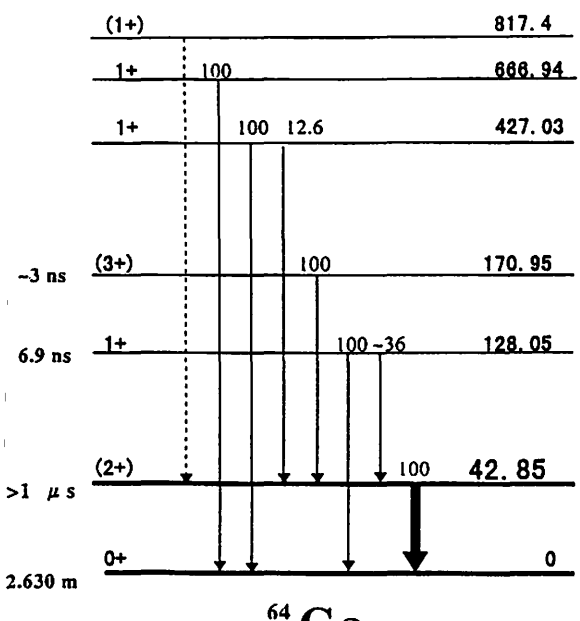

Fig. 1. Level scheme of ^{64}Ca.

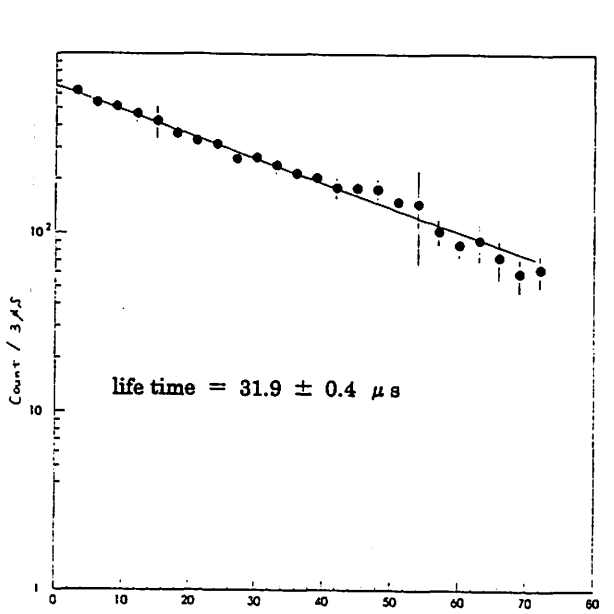

Fig. 2. Decay curve of the first excited state of ^{64}Ca.

I. 6. Measurement of the Nuclear g-factor of the First-excited 3^- State of ^{146}Gd

Fujita M., Tanigaki T., Sekiguchi K., Hoshino T.*, Baba T.*, Kawamura N.**, Shinozuka T. and Fujioka M.*

Cyclotron and Radioisotope Center, Tohoku University
*Department of Physics, Tohoku University**
*Faculty of Technology, Aomori University***

In N = 83 nuclei with even Z from Ba to Gd, low-lying $13/2^+$ states are observed systematically in the range of excitation from 1540 keV in ^{139}Ba to 997 keV in ^{147}Gd. These energies are quite consistent with an interpretation of these states as the $i_{13/2}$ single particle excitation, but the measured half-lives indicate the B(E3) enhancement in comparison with the s.p. estimation. It has been therefore attributed to an admixture of collective 3^- excitation built on the $f_{7/2}$ ground state into the $i_{13/2}$ state[1], because the 3^- octupole states in N = 82 nuclei have been systematically found in even isotones from ^{136}Xe to ^{146}Gd. To obtain which component is dominant in these $13/2^+$ states, the measurement of the g-factor is quite effective.

In the previous works, the g-factors of 1229 keV $13/2^+$ state of ^{143}Nd[2] and 1579 keV 3^- state of ^{146}Gd[3] were measured at CYRIC. But the precise mixture ratio of the two components could not be derived because of the large ambiguity of the paramagnetic correction factor (β) for the Gd ions in Sm_2O_3, which must be known to obtain the g-factor as below.

In the case of paramagnetic materials, such as rare earth elements, the effective magnetic field at the nucleus (B_{eff}) are obtained from the relation

$$B_{eff} = \beta B_{ext},$$

where β is called the paramagnetic correction factor, and must be measured independently to obtain the g-factor.

Since the temperature dependence of β is given by

$$(\beta - 1) \propto 1/T$$

for the rare earth atoms[4], a plot of $g \cdot \beta$ versus $1/T$ should give a straight line cutting the ordinate axis at the value of g. This means that the external magnetic field should not be disturbed by the surrounding electrons at the high temperature limit.

In order to achieve a β-free measurement, a target heating system, which consists of an infrared lamp and a quartz lod, has been constructed. Infrared rays are transported to the target position by means of the total reflection in a quartz lod. The advantages to use infrared rays are that there is no distortion of the magnetic field and the heating system can be located out of the vacuum chamber.

The nuclear g-factor of the 1579 keV 3^- state of ^{146}Gd was remeasured by the TIPAD method. The excited states were populated by the reaction ^{144}Sm (α ,2n)^{146}Gd at E_α = 23.5 MeV from the 680-Cyclotron at CYRIC in Tohoku University. An enriched ^{144}Sm metal target of ~ 10 mg/cm^2 was placed in an external magnetic field ($\boldsymbol{B}_{ext}$) of 13.6 kG applied perpendicularly to the beam - detector plane.

The angular distributions of the γ - rays were measured by a HPGe detector at seven angles between 64° and 130° with respect to the beam direction. The X-rays of Sm were measured by another HPGe detector in order to normalize the beam intensity.

The perturbed angular distribution of γ-rays at different temperatures between 300 and 750 K has been measured. The typical angular distributions are shown in Fig. 1. The contribution of the spin relaxation effect, which may disturb the angular distribution, has also been confirmed (see Fig. 2). As a result, this effect was negrected because the measured spin relaxation time was much longer than the half-life of the 3^- state.

The temperature dependence of the product $g\cdot\beta$, extrapolated to $T \rightarrow \infty$, yields the result

$$g(3^-) = +1.14\ (22)\ .$$

If only the ($\nu f_{7/2} \otimes 3^-$) and $\nu i_{2/13}$ components are considered for the 1229 keV state of ^{143}Nd, the g-factor of the $13/2^+$ state can be written by the additivity relation as

$$g(13/2^+) = 1/13\ [\ 7g(f_{7/2}) + 6g(3^-)\ ]\ a^2 + g(i_{13/2})\ (1 - a^2)\ ,$$

where a is the amplitude of the ($\nu f_{7/2} \otimes 3^-$) admixture. The value of a^2 is evaluated to be a^2 = 0.40(9) from the present work by using the effective g-factors for each component listed in Table 1. This large admixture of the ($\nu f_{7/2} \otimes 3^-$) component in the 1229 keV level should cause the enhancement of B(E3) and is similar to the case of the 997 keV $13/2^+$ level in ^{147}Gd[5,6].

References

1) Kleinheintz P. et al. , Phys. Lett. **B53** (1975) 442.
2) Kawamura K. et al., Z.Phys. **A348** (1994) 173.
3) Kimura Y. et al., CYRIC Annual Report-1994 (1995) P22.
4) Gunther C., and Lindgren I., in Pertubed angular correlations, ed. Karlsson E., (North Holland, Amsterdam, 1964) 357.

5) Hässer O. et al., Rev. **42** (1979) 1451.
6) Dafni E. et al., Phys. Lett. **B199** (1987) 26.
7) Smith K. F., Proc. Phys. Soc. **86** (1965) 1249. 8).
8) Rafailovich M. H. et al., Phys. Rev. C **41** (1990) 1268.

Table 1. Effective g-factors for components.

Component	g – factor	Reference
3^- State	+1.14 (22)	present work
$13/2^+$ State	+0.058 (2)	^{143}Nd [2]
$\nu\, f_{7/2}$	- 0.304 (2)	^{143}Nd [7]
$\nu\, i_{13/2}$	- 0.15 (2)	Isotopes of lead and mercury [8]

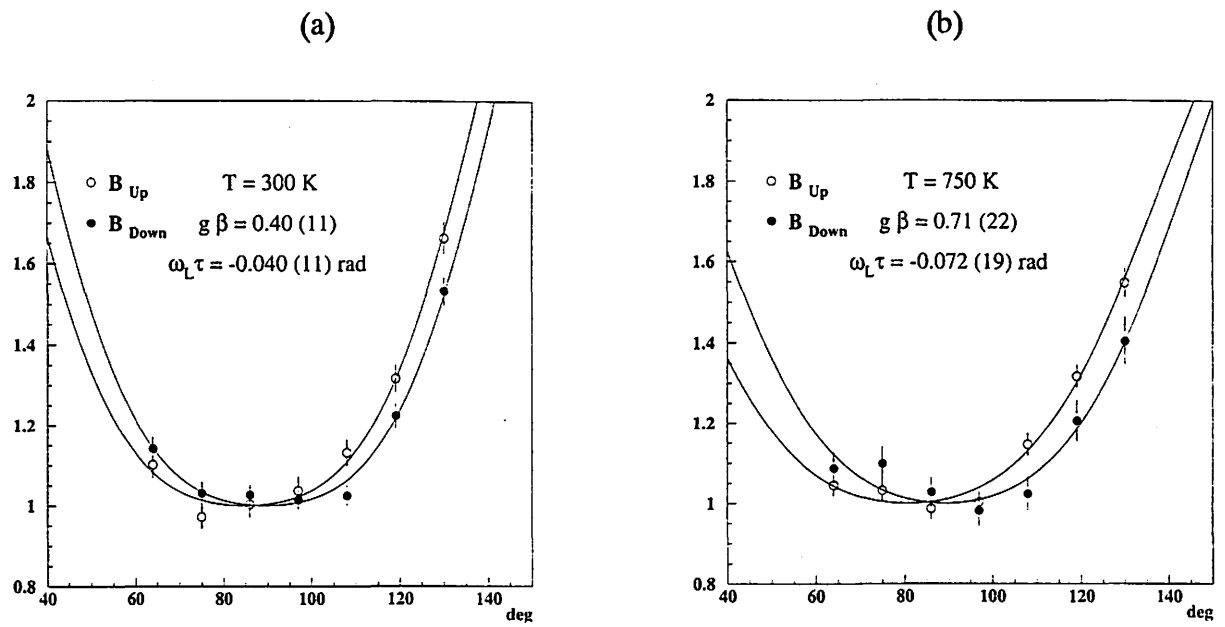

Fig. 1. The angular distribution for the 1579 keV γ-ray at the room temperature (a), and at 750 K (b).

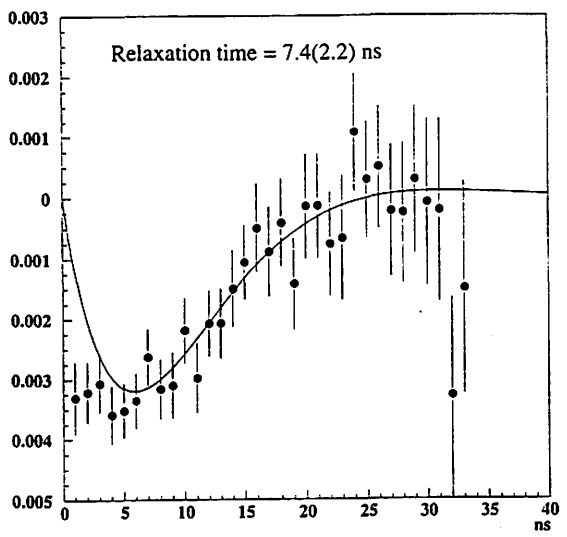

Fig. 2. The spin relaxation time at 650 K.

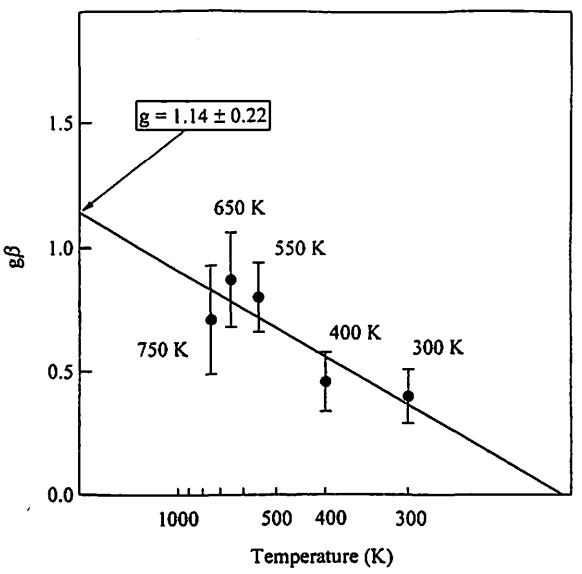

Fig. 3. The temperature dependence of the product g $\cdot \beta$.

I. 7. Nuclear Charge Distribution of Fission Products in the System of Proton-Induced Fission of ^{232}Th

Kaji D., Goto S., Kudo H., Fujita M., Shinozuka T.*, and Fujioka M.**

Department of Chemistry, Faculty of Science, Niigata University Niigata 950-2102
*Cyclotron and Radioisotope Center, Tohoku University**

The process of a nuclear charge division of a nucleus fissioning into two fragments is of great interest in connection with a mass splitting in nuclear fission. Accordingly, the charge distribution of fission products provides an important information about nuclear fission mechanism.

In the present work, nuclear charge distributions of fission products in the proton-induced fission of ^{232}Th have been studied by the use of an ion-guide isotope separator on-line, IGISOL. The incident proton energies were 13, 16, 20, 24, and 26 MeV. The determination of fission products was made by a gamma-ray spectrometry. The obtained radioactivities were converted to either independent yields or partial cumulative yields by correcting the amount of the feeding from precursors, if any. The analysis was performed by assuming a Gaussian charge distribution with representative parameters Z_p and C, where Z_p is the most probable charge of a given mass chain and C is the width of the distribution[1]. In the present work, an energy dependence of the parameter Z_p was discussed.

The difference of the Z_p of a given mass chain for the different energies was discussed with eliminating transport efficiencies in IGISOL. If two different elements Z_1 and Z_2 for different bombarding energies E_1 and E_2 are observed, the difference of the Z_p is expressed as follows[2]

$$dZ_p = Z_{p,E_1} - Z_{p,E_2} = \frac{C}{2(Z_2 - Z_1)} \ln\left(\frac{P_{Z_1 E_1} P_{Z_2 E_2}}{P_{Z_2 E_1} P_{Z_1 E_2}}\right),$$

where $P_{Zi,Ei}$ is an independent yield and the width parameter C was assumed to be the same for different energies[3]. The obtained dZ_p for A=90, 121, 135, and 142 are plotted versus the incident energy in Fig. 1. It is found that the Z_p of A=121 slowly increases in the investigated energy range, and that the Z_p's of A=90, 135, and 142 rapidly increase in the energy range of 16-24 MeV and slowly increase in 24-26 MeV.

A mass chain A=121 belongs to a typical symmetric mass division and those of A=90, 135, and 142 belong to a typical asymmetric mass division. According to the calculated

contribution of multiple chance fission, in the symmetric fission only the 1st chance fission (*p, f*) mainly contributes in present incident energy region, while in the asymmetric fission the 3rd chance fission (*p, 2nf*) becomes predominant at higher energies[4]. Therefore, the influence of the multiple chance fission on dZ_p should be taken into account. As a first approximation, it was assumed that in asymmetric fission only the 1st chance fission contributes in the low energy region, while only 3rd chance fission contributes at high energies (24-26 MeV). Therefore, it may be concluded that the Z_p for A=90, 135, 142 increases rapidly at the range of 16-24 MeV by the influence of a multiple chance fissions and increases slowly at the range of 24-26 MeV without the influence of chance fission. That is to say, the presence of multiple chance fissions is indicated for asymmetric mass division.

The slope for dZ_p of A=135 is larger than that of A=90, 142 at the range of 13-20 MeV. Mass chain A=135 includes nuclei of N=80 neutron shell. This is probable because the Z_p of A=135 increases rapidly at the range of 16-24 MeV. The detailed analysis is now in progress.

References

1) Whal A., Atomic Data and Nucl. Data Tables **39**, (1988) 1.
2) Kudo H., et al., Phys. Rev. **C57**, (1998) 178.
3) McHugh and M. C. Michel, Phys. Rev. **172**, (1968) 1160.
4) Kudo H., et al., Phys. Rev. **C25**, (1982) 3011.

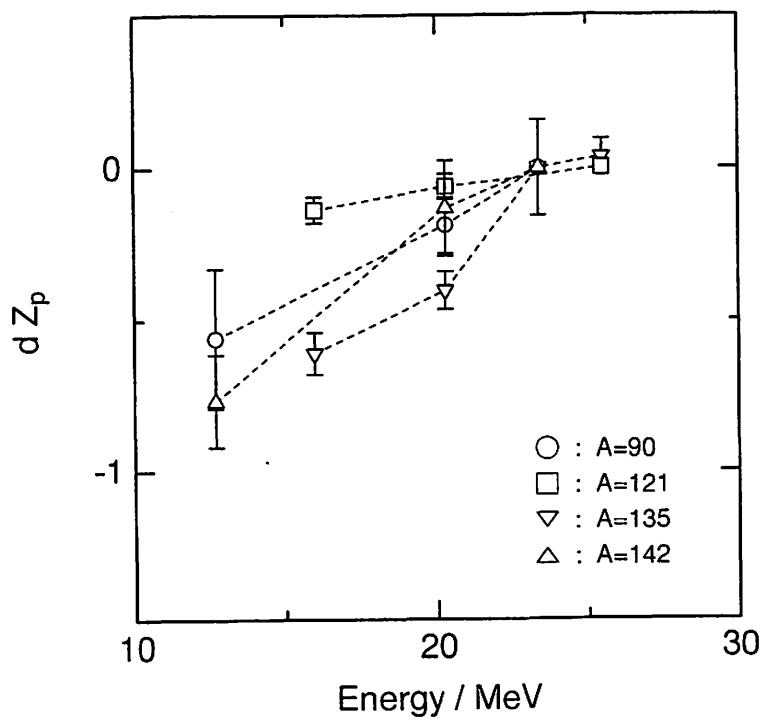

Fig. 1 Energy dependence of the most probable charge in proton-induced fission of ^{232}Th.

I. 8. PAC Spectroscopy of Fe Oxidized in 1 Atm Air

Hanada R.

Institute for Materials Research, Tohoku University

Introduction

In a previous report by the present author, a huge PAC signal was observed in Fe oxidized in a poor vacuum (10^{-2}-10^{-1} Torr, a vacuum by a mechanical pump[1]). A magnetite phase (Fe_3O_4) is formed at the surface layer where the implanted ^{111}In probe resides thus giving rise to a large precession signal, of which origin is a magnetic interaction. The work has been extended further to a specimen oxidized in 1 atm air in the present.

Purposes of the present experiment are (1) to examine the reproducibility of the reported experimental results and (2) to give interpretations for the results. For instance, the site of ^{111}In in the magnetite, the sign of the hyperfine field, the temperature dependence of the signal etc. Also the present results will be compared with those of the past researches performed as ferrite researches[2-4].

Experimental

A Johnson Matthey Fe specimen was implanted with ^{111}In at the energy of 50 keV to several 10 μ Ci at RT. The specimen was annealed at 300 C in 1 atm air for 45 min. With measuring PAC spectrum at RT, the specimen was annealed in a high or low vacuum for the total of 7 hrs.

Result

Fig. 1 shows PAC spectra for the specimens treated as described above. As reported in a previous report, the precession signal is not large and almost featureless in the as oxidized state (i). After 1 hr annealing in a high vacuum at 400-500 C, the signal remains featureless as shown (ii) or (iii). This is a different result from the one oxidized in 10^{-2}-10^{-1}Torr in ref. 1, where the PAC signal grows to a huge ones in only 1 hr annealing in a high vacuum. This trend remains up to the prolonged annealing for 2.5 hrs in the present.(iii)-(vi). After the annealig for 7 hrs in a high or low vacuum, a largr precession signal corresponding to a magnetite takes place as shown (vii)-(viii). The effect of the vertical magnetic field is a lso the same as reported in ref. 1. The only difference of the present result from the ones reported in ref. 1 is the longer annealing time of 7 hrs in a vacuum to obtain a large PAC signal. In the

present treatment, the oxidation treatment in 1 atm air seems to form a thick layer of mag-hematite (Fe_2O_3) in which the signal remains featureless as reported in ref. 1. The longer annealing time is necessary for the mag-hematite to transform into the magnetite. At present, how this transformation takes place is not known. Possibilities are (1) the mag-hematite phase front proceeds to a metallic Fe phase producing the magnetite phase or (2) part of oxygen difuses out to the vacuum thus reducing Fe_2O_3 into Fe_3O_4.

Discussion

Extensive works have already be done on physical properties of ferrites of which part will be summarized in the followings[5,6]. For magnetite, 36 oxygen ions form a fcc structure, of which tetrahedral sites (surrounded by 4 oxygen ions) are ocuupied by 8 Fe^{+++} ions and octahedral sites (6 oxygen ions) by 8 Fe^{+++} and 8 Fe^{++} ions. This configuration is energetically infavorable (Coulomb energetically the other way has lower energy) but the nature works in this way and many ferrites system takes this configuration. So this group is called "inverse" spinels. Sometimes, the tetrahedral site is called A site and the octahedral as B site. The magnetite is a ferrimagnetic material that Fe ions at A sites have opposite spin against those in B sites. The macroscopic magnetization is carried by 8 Fe^{++} ions in B site since A and B sites Fe^{+++} spins cancel out each other[5].

First, we discuss the site which In ion occupies in the magnetite. The substitution of non-magnetic In ions with Fe ions causes a net increase of the macroscopic magnetization, which means that In ions substitute for Fe ions in A site[2]. In a previous report by the present author, a CEMS result was reported where ^{57}Fe ions occupy two different site in the magnetite designated as I and II[1]. This naming shuld be changed as A and B site. The one (I) with a higher hyperfine field should be called as A site and with the lower one (II) as B. So the ^{111}In in the present PAC spectroscopy occupies the A site in the magnetite since stable In or radioactive In behaves in the same way chemically.

Next, we discuss the sign of the hyperfine field at ^{111}In nucleus at A site. A close inspection of the period of the precession signal (a Fourier analysis shows the trend better but not shown here) reveals that the period of the precession is slightly shorter for the spectrum with an external magnetic field than that without the field. This means that the hyperfine field at ^{111}In nulceus is increased with the application of the external field. Namely the external field is additive to the hyperfine field or the sign of the hyperfine field is positive. Since the macroscopic magnetization is caused by the Fe^{++} ions in B site, the Fe^{+++} ions in A site should have an opposite spin direction. So one can conclude that the hyperfine field direction at A site ^{111}In nucleus is parallel to the B site ions magnetization and anti-parallel to that of A site ions. The opposite field direction for ion againt that of the nucleus as observed for A site is quite common for magnetic materials, the best known example is that for metallic Fe.

Next, we discuss the temperature dependnce of the spectrum. Fig. 2 shows a spectrum measured at 77K which shows a strong dumping that have never been observed at

RT measurement on the same specimen. The dumping is a result of the hyperfine field broadening as shown by the Fourier component's broadening. (Not shown here)

The magnetite has been known to be a good conductor at RT but the conductivity drops by 2 order of magnitude below the Verley transition at 125K[6]. This is interpreted as the electron hopping among Fe^{++} and Fe^{+++} ions in B site is frozen below the transition. If this model is applied to the present, the hyperfine fluctuation at A site by B site electron hopping is smoothed out at RT because of the high hopping rate (A motional narrowing). Below the Verley transition, the hopping ceases giving rises to the fluctuation which results in the broadening.

The ferrites Fe_2O_3 and Fe_3O_4 have been studied by Asai et al in details by PAC spectroscopy[3,4]. Although their specimens preparation method or the geometry of the PAC spectroscopy are different from the present, the results on the hyperfine parameters , the sign and the magnitude, the temperature dependence show an excellent agreement with the present.

References

1) Hanada R : CYRIC Annual report 96,31 (1997).
2) Miyahara. Y., and Iida S: J. Phys Soc. Japan 37, 1248 (1974).
3) Asai K.,.Okada T., and. Sekizawa H: J .Phys. Soc. Japan, 54, 4325 (1985).
4) Asai K., Ambe F., Ambe S., and Sekizawa H: J. Phys. Soc. Japan, 53, 4109 (1984).
5) Kittel C:Introduction to Solid State Physics 2nd edition (1956) p443, pub by John Wiley.
6) V. A. M. Brabers: "Progrss in Spinel Ferrite Research" in Handbook of Magnetic Materials,vol 8 Elsevier Science (1995).

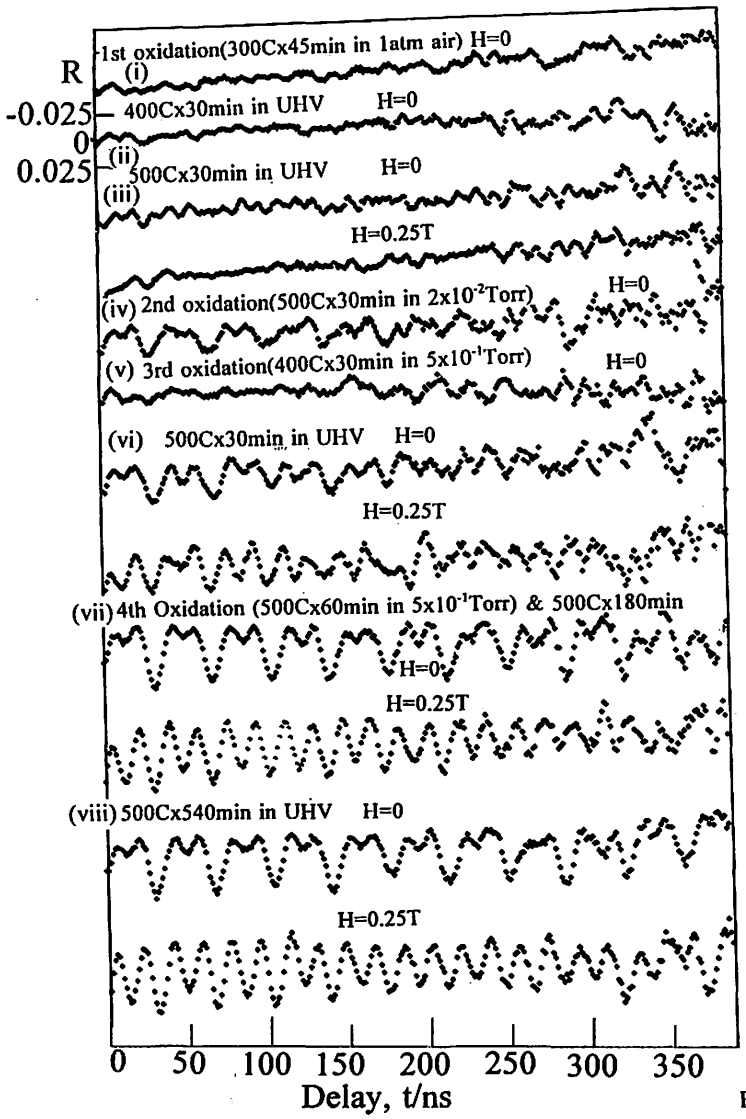

Fig.1

Fig. 1. PAC spectra for Fe oxidized in 1 atm air and during subsequent annealing.

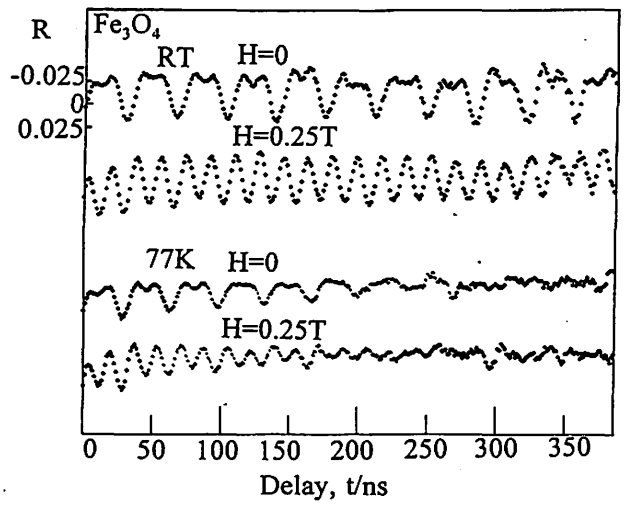

Fig. 2. PAC spectra for Fe_3O_4 measured at 77K.

I. 9. Fe Oxides Phase Transformation by CEMS and TMS

Hanada R.

Institute for Materials Research, Tohoku University

Introduction

In several reports by the present author[1], a huge PAC signal by ^{111}In in magnetite (Fe_3O_4) has been found for Fe oxidized in a low vacuum (10^{-2} Torr). CEMS for an enriched foil given the same treatment as PAC has proved that PAC signal is large in magnetite (Fe_3O_4) but not in mag-hematite (Fe_2O_3). A result of similar PAC spectroscopy on Fe oxidized in 1 atm air is reported in a separate paper in this volume where a detailed interpretations and comparison with others are described.

In this report CEMS as well as well as transmission Mossbauer spectroscopy (TMS) have been applied to identify several kind of Fe oxides formed after oxidation or reduction treatments. These results will be useful to examine species of oxides formed or how they transform to each other at certain temperature range. Also it is expected that combined measurements of CEMS and TMS on a specimen should show how deeply these oxides are formed on Fe surface.

Experimental

An ^{57}Fe enriched foil ($10\times10mm^2\times1.3\mu m$) oxidized at 500C in 10^{-1} Torr air for 30 min. After the initial oxidation treatment, the specimen was annealed in a high vacuum (10^{-7}Torr) between 500 and 1000 C. During the annealing CEMS and TMS have been applied. CEMS probes the surface layer of 0.1μm thickness and TMS covers the whole thickness of 1.3μm.

Results and Discussion

Fig. 1 shows the CEMS results. Right after the oxidation treatment (i), we can see only Fe and Fe_2O_3 components in CEMS. So only Fe_2O_3 is formed on the surface region of thickness 0.1 μm mixed with not yet oxidized Fe. The Fe_2O_3 visible in CEMS is almost completely missing in TMS showing the layer thickness is too small for TMS. Qualitative analysis for this result is now in progress.

Annealing in a vacuum, however, transforms this Fe_2O_3 into Fe_3O_4 phase as shown by Fig. 1-(ii) and (iii). This reproduces the previous result for PAC and CEMS on oxidized

Fe reported[1]. Fig. 1-(iv) is a CXMS (conversion x-ray spectroscopy) result on the specimen for (iii) to compare the range of CXMS with those of CEMS and TMS but the results will not be discussed here.

After these measurements the specimen was warmed up to 1000 C and then the spectrum was measured at RT.(Fig. 1-(v)). Here a new oxide component takes place between -2 and 0mm/s, which is identified as FeO (wüstite phase) by a measurement on FeO powder obtained as a chemical. This wüstite phase grows with the expense of Fe and Fe_3O_4 phases by further annealing at 900 C in the vacuum. (Fig. 1-(vi) ,(vii)). This result shows that FeO phase is the stable phase in these temperatures.

These results may be summarized as follows. Once oxygen is introduced to Fe host by equilibration with oxygen atmosphere, Fe_2O_3 phase is formed first on the surface. When this oxidized Fe is annealed in a high vacuum, the oxide transforms into other oxide phases with less O/Fe ratio.(Fe_2O_3=1.5, Fe_3O_4=1.33, FeO=1.0). TMS spectra in these temperature range also show the FeO phase but only partly and metallic Fe phase still remains. So the oxides formation is still limited to the surface region.

After all the measurement the specimen was annealed in 1 atm hydrogen atmosphere at 600C for 3 hrs (Fig. 1-(viii)). With this treatment, the spectrum recovers into that of metallic Fe. So this hydrogen annealing is sufficient enough to remove the oxide phases from the specimen.

Fig. 2 summarizes the results described above, where the amount of each phase is plotted against the annealing temperature together with the same values obtained by TMS. The measurement have been done successively as arrows in Fig. 2 indicate.

These results will be useful to prepare an oxide phase which one wishes to study by a nuclear method as PAC. Direct ^{111}In implantation to the oxides seems not to work probably because of the damage introduced at the same time[2]. Unfortunately ^{111}In diffuses out of the Fe or oxides specimen below 600C and so the technique will not be applicable to FeO phase, for which formation an annealing above this temperature necessary as shown in Fig. 2.

As far as Fe_2O_3 or Fe_3O_4 concerned, the present method of oxides preparation is more simple and convenient than the chemical synthesis method, where a sophisticated radio chemical technique is required for the probe introduction.

References

1) Hanada R.: CYRIC Annual Report-96 p 31.
2) Wichert Th. : private communication.

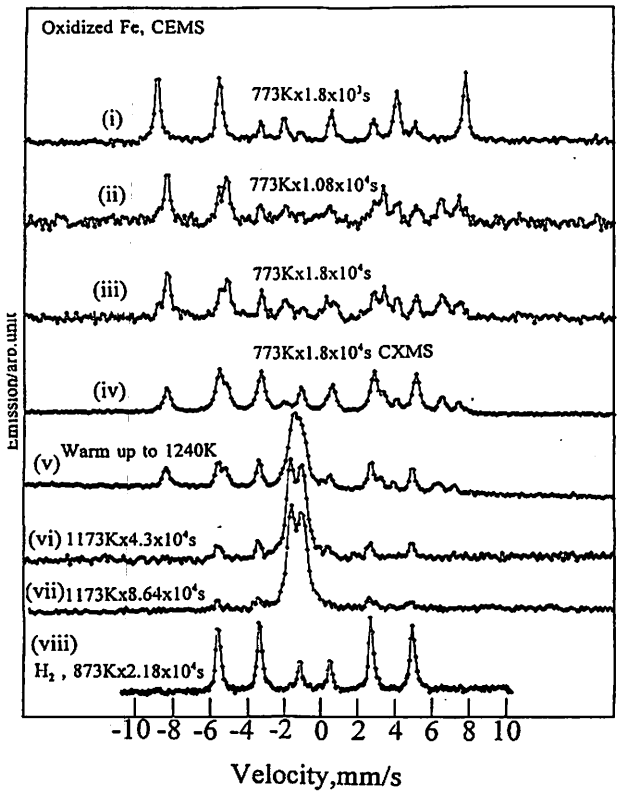

Fig. 1. CEMS spectra for ^{57}Fe foil oxidized in 10^{-1} Torr air or reduced in a vacuum or in H_2.

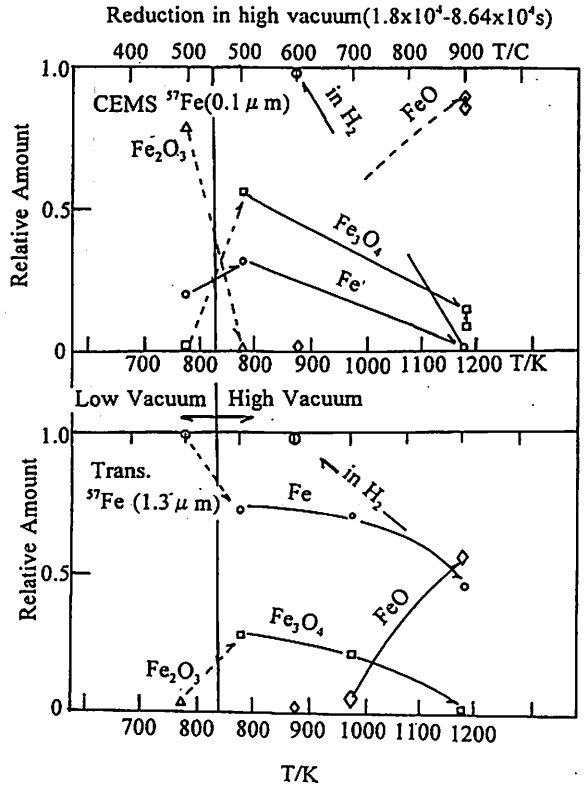

Fig. 2. Fe oxides phase transformation during the annealing in a high vacuum(10^{-7}Torr) Top: CEMS, Bottom: Transmission Mössbauer Spectroscopy.

I. 10. PAC Spectroscopy Fe Heavily Damaged at 77 K

Hanada R.

Institute for Materials Research, Tohoku University

Introduction

Recovery of point defects introduced at low temperature irradiation has been one of the major subject in solid state research. Different from other metals, stage I of Fe is present exceptionally at high temperature, say between 77 K and 120 K, and so a damage study is possible even after the irradiation at 77 K. To apply the PAC technique for the study of point defects recovery in Fe and extend the temperature range of investigation, a radiation damage at 77 K and subsequent annealing between 77 K and RT for PAC spectroscopy have been attempted in the present, of which results will be reported in the following. The results remain preliminary and further study will be necessary.

Experimental

One of the simplest way to introduce a radiation damage in hyperfine techniques is the probe implantation at low temperature, say at 77 K or 4.2 K. Namely, if the PAC probe ^{111}In is implanted at 50 keV, about 500 pairs of Frenkel defects (pair of a vacancy and an interstitial) are produced per one incident ion, of which distribution almost overlaps with that of implanted ions. So one can perform the damage and the probe introduction at the same time in this method. This method was applied first and found not to work. All ^{111}In activity attached to a specimen by the 77 K implantation was found to be washed out by dipping the specimen in acetone bath after the annealing study between 77 K and RT. Gases (water and hydrocarbon) in the implantation chamber seems to have condensed on the specimen surface during the implantation and ^{111}In seems to be stopped in the condensed gases layer. This is confirmed by the fact that no precession signal with the 11 ns, the well known one for ^{111}In in Fe substitutional site, has been found in the annealing experiment between 77 K and RT. Better vacuum (10^{-6} Torr in the present) and/or introduction of a cold spot in the chamber will be necessary for the successful implantation at a low temperature.

So this method was discarded in the present and another approach has been applied. Here, ^{111}In implantation has been done at RT followed by the annealing at 400C, and then the specimen was cooled to 77 K for a radiation damage by ions implantation or rather to say, by

ion irradiation. The annealing at 400C is to eliminate the damage by the ^{111}In implantation and the ion irradiation for the production of damage.

The temperature of 400C may not be high enough to anneal out the all the damage introduced by the implantation but must be limited to it since part of ^{111}In diffuse out of the specimen if annealed above that.(See separate report in this volume for ^{111}In TDS).

For the ion irradiation at 77 K, Ar ions at 40 keV was applied to doses between 0.5,1.0 and 5×10^{16}/cm^2. A high purity Johnson Matthey Fe was used for the specimens. Three runs were performed among which the result for the one with the dose 10^{16}/cm^2 will be reported.

Results and discussion

Fig. 1 shows a calculated damage and ion distribution (TRIM) for Ar ions at 40keV in Fe. The maximum of the damage is at 100 A, almost the same with that of the 50 keV ^{111}In ion distribution, and the Ar ion maximum concentration is at 200 A. The damage is so high that it is plotted in the unit of dpa (displacement per atom). The dpa 20 means an Fe atom at one lattice site is displaced 20 times by the irradiation. This number, however, should not be taken too latterly, since TRIM neglects all the dynamical recovery or the effect of thermal spike, by which part of Frenkel pairs recombine to lower the real damage concentration. Nevertheless, Fig. 1 shows the low energy ion irradiation is quite efficient as a mean of damage production. This is reasonable since all the ion energy is dissipated just in a thin layer of several 100 A thickness near the surface. Also Ar concentration is quite high as 4.5×10^{-2}(4.5at%or 4.5×10^4 atppm) if compared with ^{111}In concentration of 10^{-6}(1 atppm) for 10μCi, typical for PAC spectroscopy.

Fig. 2 shows the PAC spectra for JM Fe before and after the Ar irradiation as well as during the isochronal annealing (10 min) between 77 K and 200 C measured at 77 K. As shown in Fig. 2, the precession signal of the period 11 ns, well known as for the ^{111}In in the substitutional (S) site without trapping defects or impurities, is the main one in the present. Despite of these high Ar concentration as well as the damage concentration, most of the implanted ^{111}In are at the substitutional sites in the Fe lattice without trapping defects or Ar impurity. A Fourier analysis (not shown here) of the result also supports the view that the main component is at about 40 T (the angular frequency is converted to the hyperfine field by the relation $\omega=g\mu H/\hbar$) corresponding to ^{111}In at the S site. The first harmonic (2ω) is present though the amplitude is much smaller than that expected for the case of no external magnetic field as in the present.

Except for these, several additional components with smaller amplitudes were noticed at 34 T between 170K and 300K, 26 T between 130 K and 260 K and at 14 T for all temperatures. If one applies a naive picture of the effect of a defect on the hyperfine field of Fe, namely non magnetic defect (a lattice vacancy) substitution for one Fe atom among the 8 nearest neighbors reduces the hyperfine field by 1/8, these components should correspond to

1V, 3V and 5V, respectively. The 5V component is probably formed by the ^{111}In implantation and during the annealing at 400C.

The present method of damage production by ions irradiation is considered to be better than the simultaneous production during the probe implantation. This is because that one can control the damage and ion distribution, the amount of damage etc by selecting the species of ions. Also one can avoid the effect of correlated damage, which is inevitable in the simultaneous damage introduction during the probe introduction.

Further experiments with varying the species of irradiating ions and energy are now in progress.

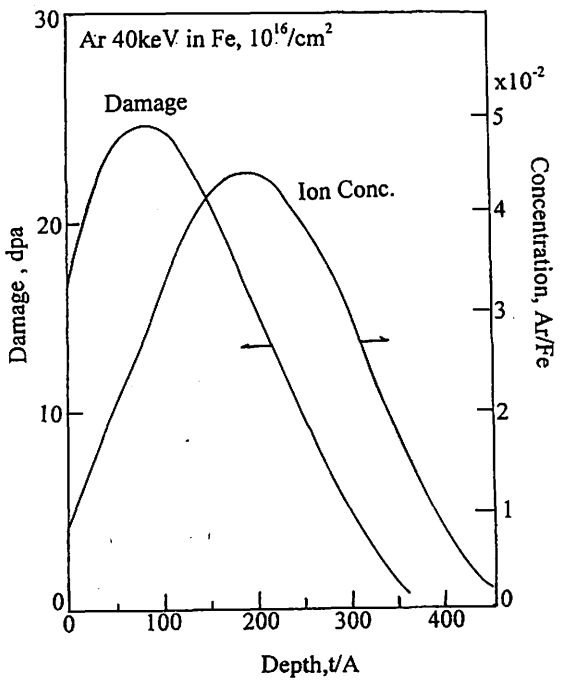

Fig. 1. TRIM calculation of ion and damage distributions in Fe. 40keV Ar ions to a dose of $10^{16}/cm^2$

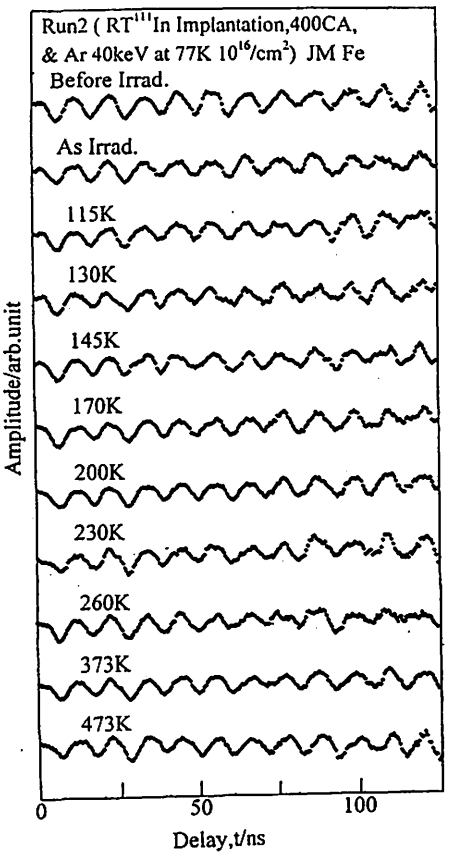

Fig. 2. PAC spectra by ^{111}In in Fe damaged 77K by Ar ions. The damage introduction at 77K were done separately from the probe introduction.

I. 11. TDS of ^{111}In Implanted to Fe by A Radioactivity Measurement

Hanada R.

Institute for materials Research, Tohoku University

Introduction

As shown in several reports, TDS (Thermal Desorption Spectroscopy) is an useful method to study the state of impurities or to determine the diffusion coefficients of them in solids. Usually gas impurities as He or other rare gases are implanted to specimens (metals ,semiconductors etc) and their desorption upon heating is monitored by a proper gas analyzer as a mass filter. In this report, an experimental result will be shown to demonstrate that such a TDS is possible for non gaseous impurities by measuring the radioactivity loss from a specimen upon heating.

Here TDS of a PAC probe ^{111}In implanted to metallic Fe or to an amorphous alloy has been performed of which result will be described in the followings.

Experimental

^{111}In was implanted to Fe or an amorphous alloy at the energies between 30 and 50keV. The radioactivity was several micro Ci which is high enough for a G-M counter to detect it. The specimens ($5\times20\times0.2mm^3$) were placed in a quartz tube evacuated to 10^{-7} Torr and annealed isochronally (20K/10min). After each annealing at a temperature, the radioactivity of the specimen was measured at a constant distance between the specimen and the detector with a proper correction for the background. This procedure was repeated for each annealing temperature between 100 and 800C.

Result

Fig. 1 shows the results of the measurement for 3 different specimens (2 Fe and 1 amorphous alloy (2605S2)). The heating rates were obtained by deviding the temperature interval by the duration of the isochronal annealing. The upper three curves are the normalized radioactivity left in the specimens after each annealing. The lower one is the temperature derivative for one of the upper curves for Fe to show the desorption process more clearly. Fig. 1 reveals that ^{111}In is diffusing out of the specmens between 500 and 600C of which center is at about 520C for Fe and slightly higher for the amorphous alloy. The part of

^{111}In that diifuse out of the specimen deposits at the inner wall of the quartz tube. Fig. 2 shows the radioactivity distribution of the quartz tube after the completion of the experiment. Fig. 2 reveals that ^{111}In activity deposits at the part that is the outside of the furnace. The furnace part is too warm for ^{111}In to deposit. If one places specimens at this part with a high activity, one can possibly prepare a PAC specimen for a surface state study. Such a method has indeed been employed by a Konstanz group[1)]

Discussion

The result in Fig. 1 can be used to determine the activation energy (Q) for In diffusion in α Fe . Fig. 3 shows a calculated diffusion distance $\sqrt{Dt}$ as a function of the reciprocal temperature with Q as a parameter. For the pre-exponential factor D_0, a typical experimental value for impurities diffusion in α Fe is used. For the duration t, the experimental value of 10 min is used.

TRIM calculation shows that the In ions at the energy of 30-40KeV are implanted at the depth of 100 A (10 nm) from the surface in the case of Fe. Also Fig. 1 shows that the rate of In desorption is maximum at 520 C. Looking for the diffusion distance of 100 A at 520 C in Fig. 3, the curve with Q=2.4eV shows a reasonable agreement. So one may conclude that this value is a good estimate for the activation energy for In diffusion in Fe. Unfortunately, no tracer diffusion measurement is available for In in Fe. However, a compilation of impurities diffusion data in Fe reveals that the activation energies of impurities diffusion in Fe systematically decrease with increasing family number in the periodic table[2)]. For instance, in the 4th period, the activation energy is the highest for Fe self diffusion and decreases with the increasing family number as Co, Ni and so on. This trend is also true for the 5th period and the measured values for Sn (z=50) or Sb (z=51) are smaller than that of the self diffusion by 0.2-0.4 eV. The absolute value for Fe self diffusion in ferromagnetic region reported as to depend on the ferromagnetic ordering parameter (s) as 2.596 (1+0.156 s^2) eV[3)]. Using the value of s=0.8 at 520 C, the activation energy for Fe self diffusion at 520C is estimated as 2.84 eV. The value for In, Q=2.4eV, obtained in the present also shows the trend of the activation energy decrease with the increasing family number and the magnitude of the decrease is comparable with those of Sn or Sb. So the value is considered to be reasonable. For more precise determination of the activation energy by the present method, an analysis with taking into the initial impurity distribution by ion implantation will be necessary. Also technically, the continuous activity measurement with a proper shielding only to measure the specimen activity will be useful to obtain more precise TDS spectrum with less labor.

References

1) Schatz G. et al: Hyperfine Interactions, **34** (1987) 555.
2) Oikawa H.: Technology Reports, Tohoku University, **47** (1982) 215.

3) Iijima Y. et al : Acta metall: 36 (1988) 2811.

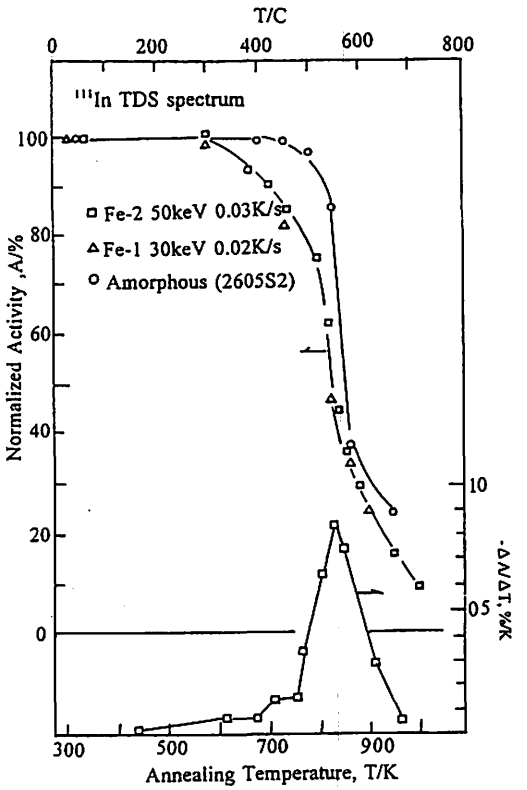

Fig. 1. TDS spectra by the radioactivity measurement of ^{111}In implanted to Fe and an amorphous alloy. Lower: the derivative for one of Fe TDS spectrum.

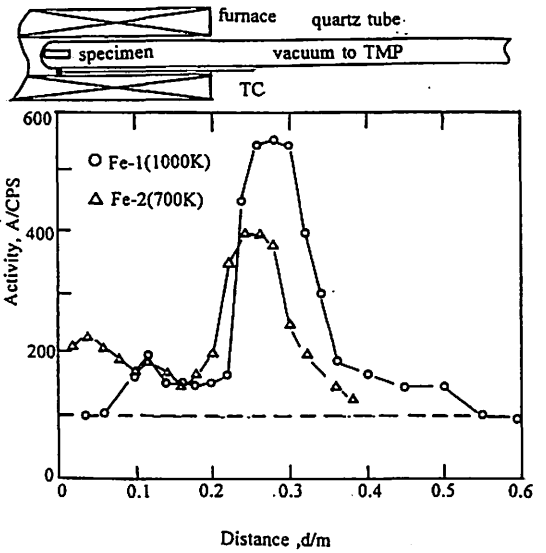

Fig. 2. The radioactivity deposited on the inner surface of the quartz tube used for TDS. The furnace position during the annealing is shown.

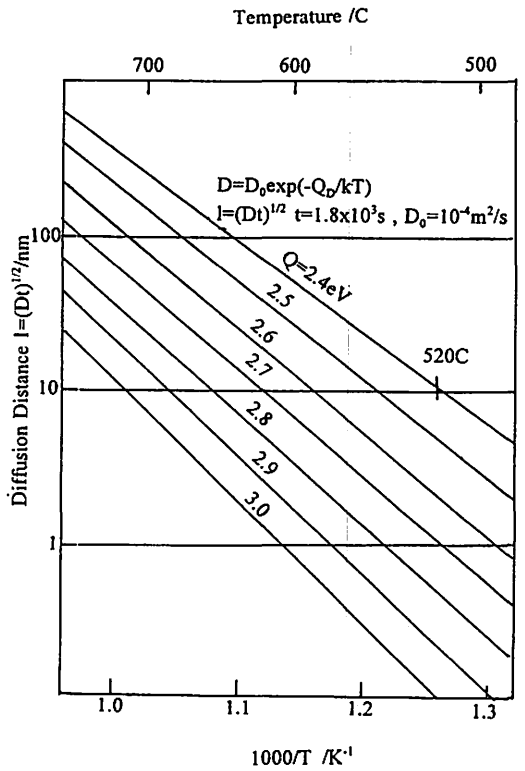

Fig. 3. Calculated diffusion distance as the In-diffusion activation energy as a parameter.

I. 12. Preparation of Si Specimens for ^{57}Fe Mössbauer Spectroscopy

Hanada R.

Institute for Materials Research, Tohoku University

Introduction

Transition metals impurity in Si have been a subject for basic research as well as for industrial application. Especially Fe impurity in Si has been studied extensively by both macroscopic as well as by microscopic methods. This is because that Fe ions form a deep trapping center for carriers and so Fe contamination, which easily takes place during the fabrication, gives rise to a serious problem in the devices manufacturing.

Fe ion in Si is characterized by it's large diffusion coefficient and by the low solid solubility. The activation energy for diffusion is reportedly 0.44eV-0.9eV and the maximum solid solubility of 10^{14}-4×10^{16}/cm^3 (Fe/Si=0.2×10^{-8}-10^{-6})[1]. Moreover the site of Fe ions in Si lattice seems to be not well established, namely whether they sit at substitutional and/or interstitial site.

In a previous report by the present author on PAC spectroscopy on Fe implanted Si[2], a small precession signal was observed near RT, which was ascribed to a pair of Fe ion and the probe ^{111}In. However the local Fe concentration is rather high at that experiment and so Fe may have been precipitated with incorporating ^{111}In. So the signal may have been caused not by the pair but by the EFG of Fe precipitates. So it is desirable to study the state of Fe in Si in detail by other method, for instance, by Mössbauer spectroscopy. Here, in the present, a small amount of metallic ^{57}Fe was thermally dissolved in Si and Mössbauer spectroscopy was performed, of which result will be reported in the followings.

Experimental

Si single crystals ($10\times10\times0.05$mm^3) with (111) and (100) orientations were warmed up to 1200-1300C with a small amount of metallic ^{57}Fe (2-3 mg) in a vacuum. After 10 min at 1250 C, the furnace was moved out to cool the specimen rather fast (100C/s). After the treatment the metallic ^{57}Fe was found melted and diffused into Si bulk. In the case of 1300C annealing, a small hole was found at the point where ^{57}Fe was placed. These observations are reasonable since a Fe-Si phase diagram shows that an eutectic point is present at 1220C[3].

To study the state of ^{57}Fe in Si, Mössbauer spectroscopy was performed in a transmission mode. With a lead shield with a 5mm diameter slit, Mössbauer spectroscopy was performed at several points of the Si specimen.

Results and discussion

Fig. 1 (a) shows the spectrum measured at the point where ^{57}Fe is melted. The spectrum is a superposition of a single paramagnetic line and a doublet, of which origin is quadrupole splitting. This shows that ^{57}Fe is not in the form of metal any more (if so a magnetic sextet should be present) but in a form of a compound with Si. Fig. 1(b) shows the spectrum measured at a point 5 mm from the melted part. Although this part looks as a normal Si crystal and no effect of ^{57}Fe melting is noticed, we see an absorption spectrum by ^{57}Fe. Namely ^{57}Fe diffuses to this part during the short annealing time at 1250C. The spectrum consists of a single paramagnetic line and no doublet splitting is present with the width comparable with that in Fig. 1(a).

The average concentration of ^{57}Fe in Si is estimated as about 2.5 at % or $8\times10^{20}/cm^3$ from the measured weights of ^{57}Fe and Si. This concentration is far above the maximum solid solubility limit of Fe in Si. So one can conclude that ^{57}Fe in the present are in a form of precipitates (compounds) but not in the form solid solution of isolated Fe atoms. The phase diagram suggests ζ compounds (α and β) are the most likely ones to give rise to the absorption spectrum. Although the spectra look simple, the line widths are rather broad suggesting there are many components in them that corresponds to different kind and/or size of the precipitates.

Further measurements at high temperatures are now in progress for further identification of these precipitates. Also more detailed analysis for the present is now in progress.

References

1) Schulz: M. Impurities and Defects in IV Elements and III-V Compounds. Landolt-Börnstein New Series vol 22. Ed by Madelung O. Pub by Springer Verlag (1987).
2) Hanada R. et al: Mat. Sci. Forum. vol. 196-201 (1985) 1369.
3) Massalski T. B.: Binary Phase Diagram: pub by ASM (1986).

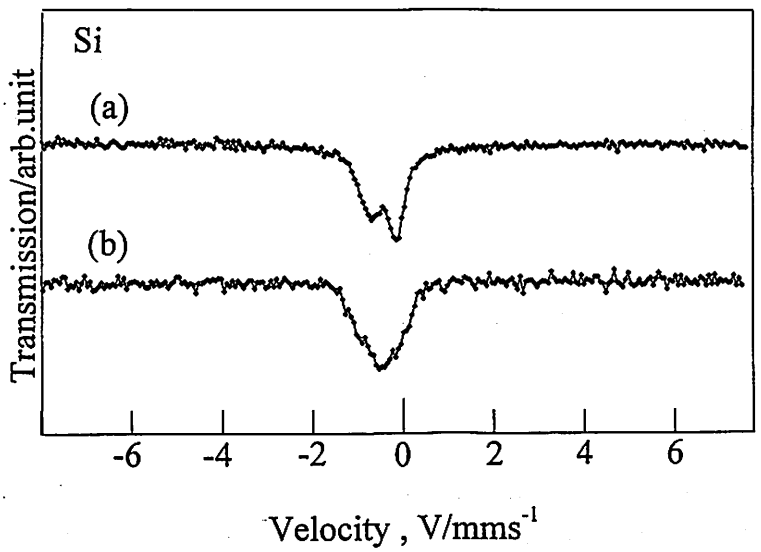

Fig. 1. (a) ^{57}Fe Mössbuer spectrum thermally dissolved in Si(100). Melted part.
(b) The same as Fig.1(a) but 5mm from the melted part.

I. 13. High Temperature Mössbauer Spectroscopy in Ni

Hanada R.

Institute for Materials Research, Tohoku University

Introduction

Mössbauer spectroscopy is an useful tool to investigate physical properties of solid. Among them, study of diffusion process has been one of the subject from the earliest days of the spectroscopy[1,2]. For the diffusion study, a high temperature measurement is inevitable for the case of metals, since the jump rate must be high for the diffusion process to affect the spectrum. Also study of magnetic properties has been one of the main subject of the spectroscopy. Aiming to investigate these properties at high temperature, Mössbauer spectroscopy above RT has been started. Among them, a result on Ni, where the temperature dependence of the magnetic properties are investigated, will be reported.

Experimental

A thin foil of Ni ($10\times10\times0.01mm^3$) was annealed in a vacuum with several mg of metallic ^{57}Fe at 1300-1350 C for 2 hrs. Although Fe and Ni form a complete solid solution if Fe concentration is below 6 at.% as in the present, they stay in a solid form at these temperatures and so a long annealing was necessary for ^{57}Fe to diffuse into Ni bulk. Whether ^{57}Fe diffuses into Ni bulk or not will be judged by the measurement of the hyperfine field as will be shown later.

The Ni specimen was placed in a chamber evacuated by a TMP and Mössbauer spectroscopy was performed in a transmission mode with $^{57}Co/Rh$ as the source. Temperatures during the measurement were measured and controlled by an alumel-chromel thermocouple with ±3 C accuracy.

Result and discussion

Fig. 1 shows the Mössbauer spectra by ^{57}Fe dissolved in Ni at the measuring temperatures between RT and 350 C.

The result at RT shows that the spectrum is a sextet, typical for the probe in a ferromagnetic environment. The separation between the line 1 and 6 measures the magnitude of the hyperfine field and 28.5 T was obtained for ^{57}Fe in Ni lattice, which shows a good

agreement with the reported one[3]. From this result one can conclude that ^{57}Fe has diffused in to Ni substitutional site in the diffusion treatment described above.

Inspection of the results at higher temperature reveals three effects of the temperature. These are,

(1) The reduction of the magnitude of the hyperfine field with the increasing temperature. Namely, the separation 1-6 gets smaller with the increasing temperature.

(2) The decrease in the recoilless fraction (f) with the increasing temperature. Namely the area of the absorption dip gets smaller with the increasing temperature. This means that one must wait for longer time until one can get a good quality spectrum as RT. Even with this precaution, the absorption dips get smaller with the increasing temperature and so the results are plotted in a doubled scale above 473K.

(3) Appearance of a paramagnetic line near 0mm/s above 373 K. This shows that Ni lattice is divided in two phases, a ferromagnetic phase and a paramagnetic phase above 100 C. At the highest temperature of 623 K, the ferromagnetic phase almost disappears and the paramagnetic phase grows to dominate the spectrum.

These results are summarized in Fig. 2, where the populations of each phase and the magnitude of the hyperfine field are plotted as a function of the measuring temperature.

The result (1) is quite common in hyperfine interaction studies in magnetic materials. Namely, that the magnitude of the hyperfine field (at the nucleus) shows almost the same temperature dependence as the macroscopic magnetization.

The result (2) is also quite common in Mössbauer spectroscopy that the recoilless fraction (f) is given as $f=\exp(-6E_R T/k\Theta_D^2)$ where E_R is the recoil energy, 1.94 meV for the present, Θ_D is Debye temperature. So the absorption should get smaller exponentially with the temperature as qualitatively observed in the present.

The results(3) clearly reveals that the Ni magnetic phase consists of two phases, a paramagnetic and a ferromagnetic phase, even below the Curie temperature of 643 K. This means that Weiss's mean field theory for a ferromagnetic phase can not be applied for the experimental results based on the hyperfine interactions technique as in the present, which are in principle microscopic in nature. Namely, the theory based on a short range magnetic ordering will be necessary to explain the present result.

Further investigations are in progress together with Fe which shows almost the same trend as in the present Ni result.

References

1) Singwi K. S. and Sjolander A.:Phys.Rev., **250** (1960) 1093.
2) Boyle A. J. F. et al: Proc.Phys.Soc.(London) **77** (1961).129.
3) Wertheim G. K. and Buchanan D. N. E. : J. Phys. Chem.Solids **28** (1967) 225.

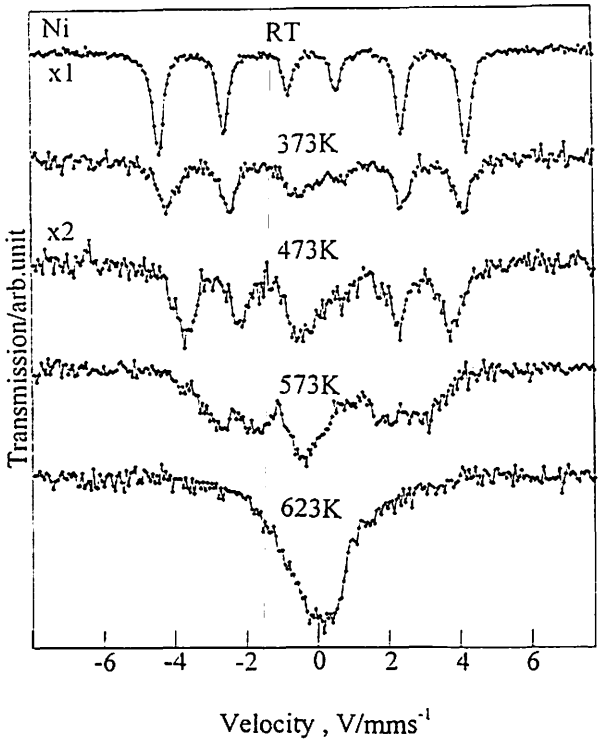

Fig. 1. Mössbauer spectrum by ^{57}Fe dissolved in Ni as a function of measuring temperature.

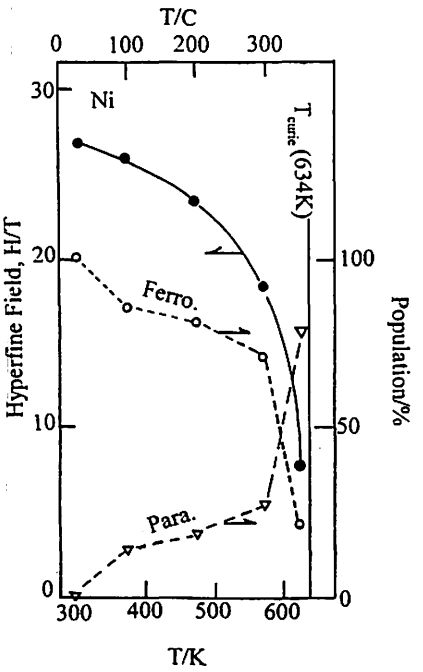

Fig. 2. Summary of the hyperfine field and the population of each phase as a function of the measuring temperature.

I. 14. Evaluation of Ductile-Brittle Transition Behavior of Helium-Implanted Reduced Activation 9Cr-2W Martensitic Steel by Small Punch Tests

Kimura A., Morimura T., Kasada R., Matsui H.*, Hasegawa A.**, and Abe K.*

IAE, Kyoto University,
*IMR, Tohoku University**
*Dept. of Quantum Science and Energy Engineering, Tohoku University***

Introduction

He induced embrittlement is one of the critical issues of fusion structural materials in which several thousands at.ppm of He is estimated to be generated during reactor operation. It is well known that a small amount of He enhances irradiation embrittlement of austenitic steels[1-3] and some vanadium alloys[4,5] in the tests at relatively high temperatures accompanied by the change in the fracture mode from transgranular to intergarnular cracking. In contrast, it was reported that the martensitic steels were highly resistant to He bubble-induced grain boundary embrittlement[6-8] at high temperatures. High resistance to the babble formation in the martensitic steels is considered to be attributed to trapping of He atoms and point defects in the martensitic structure which prevent He atoms segregating to form He bubbles at grain boundaries.

Ductile-brittle transition behavior is characteristic to body centered cubic metals such as martensitic steels, and irradiation hardening usually results in an increase in the transition temperature. He implantation technique is more effective to evaluate He effects directly. In this study, the effects of He implantation on the ductile-brittle transition behavior of martensitic steel has been investigated by means of small punch test technique.

Experimental

The material used is the JLM-1 reduced activation 9%Cr martensitic steel. The specimen was Normalized at 1323K for 30min and then tempered at 1033K for 30min, followed by air cooling. Specimens were punched out into disks, which measure 3mm diameter and 0.22mm thickness. All the specimens were fixed by molten indium on the specimen holder shown in Fig.1 and simultaneously implanted with 36MeV-α particles whose range was estimated to be 0.23mm by cyclotron in Tohoku University. An energy degrader was used to implant He into the specimens homogeneously, and the total He

concentration and displacement damage was estimated to be 120at.ppm and 0.048dpa, respectively. The average specimen temperature is estimated to be 393K.

Following the implantation, small punch (SP) tests were carried out at temperatures between 77K and 293K. The SP-DBTT was obtained by measuring the SP-fracture energy, which was defined as the total area below the SP load-deflection curve, at various test temperatures. Micro-Vickers hardness tests were performed on a specimen as-irradiated condition.

Results

Micro-Vickers hardness measurement

The results of micro-Vickers hardness measurements of both the surfaces of He implanted specimen are shown in Fig.1. As clearly shown in the Hv-distance relationship diagram, the He implantation resulted in an increase in the hardness of the martensitic steel and the irradiation hardening appears to be maximum at the center of the specimen. The average implantation-induced hardening (ΔHv) at the irradiation surface and the reverse side of specimen is 45 and 35, respectively, indicating that almost homogeneous irradiation and/or He implantation was performed on the specimens.

Small Punch Tests

The results of load-deflection curves of unimplanted and implanted specimens at various test temperatures showed that no significant effects of implantation was recognized in the load-deflection curves at temperatures between RT and around 110K. This indicates that the implanted 120at.ppm He has no influence on the ductile shear rupture of the steel. Below 100K, however, the load-deflection curves are markedly influenced by the implantation. In He implanted specimens, the maximum loads at temperatures below 110K are almost the same, suggesting that the load corresponds to the fracture load in the lower shelf energy temperature region. In unimplanted specimens, however, the maximum load still decreases with decreasing temperature, which is because the transition from ductile to brittle does not complete yet even at 77K.

Generally, a transition is observed in the temperature dependence of SP properties in the He implanted specimen, while the transition seems to be still incomplete in unimplanted specimens. The dependence of SP fracture energy on test temperature is shown in Fig. 2 with the fracture surfaces of implanted specimens. The diagram of SA fracture energy-test temperature indicates that the ductile to brittle transition occurs at a low temperature in both the specimens with and without implantation, although again the transition in unimplanted specimens is still incompleted. The brittle fracture mode of He implanted specimen is cleavage fracture mode which is the same to that of the specimen unimplanted. There is no indication of grain boundary embrittlement even at low temperatures after the He implantation to 120 at.ppm. The SP-DBTT, which is defined to be the temperature where the fracture

to 120 at.ppm. The SP-DBTT, which is defined to be the temperature where the fracture energy is the average value (0.18J) of the maximum and lower shelf energy, is evaluated to be 81K and 107K for unimplanted and implanted JLM-1 steel, respectively; the implantation increases the SP-DBTT by 26K.

Since the intergranular fracture was never observed in the He implanted specimen even in the lower shelf energy temperature region, the reduction of intergranular fracture stress caused by formation of He bubbles at grain boundaries can be rejected. The martensitic structure contains a lot of trapping sites for He and point defects, and resultantly prevent He cavities from being formed at grain boundaries. There is the possibility that the trapped He induces the reduction of cleavage fracture stress.

Summary

The effect of He implantation up to 120at.ppm on the ductile-brittle transition behavior of reduced activation 9Cr-2W martensitic steel (JLM-1 steel) was investigated. The He implantation resulted in a shift in SP-DBTT to higher temperature and an increase in the micro-Vickers hardness. These implantation effects were interpreted in terms of irradiation hardening caused by displacement damages without any enhancement by He. The martensitic structure, which consists of a number of dislocations, lath boundaries and carbides, contains a high density of trapping sites for He atoms and prevent He atoms from segregating at any crack nucleation sites. It is expected that the He embrittlement, whichever it is transgranular or intergranular, will not occur until the He generation overcomes the capacity of trapping sites for He.

References

1) Schroeder H. and Batfalsky P. J., Nucl. Mater. **117** (1983) 287.
2) Trinkaus H. J., Nucl. Mater. **133&134** (1985) 105.
3) Schroeder H. J., Nucl. Mater. **155-157** (1988) 1032.
4) Braski D. N. and Ramey D. W., Effects Radiation on Materials, ASTM STP **870** (1985) 1211.
5) Satou M. et al., J. Nucl. Mater. **233-237** (1996) 447.
6) Stamm U. et al., J. Nucl. Mater. **155-157** (1988) 1059.
7) Moslang A. and Preininger D. J., Nucl. Mater. **155-157** (1988) 1064.
8) Hasegawa A. et al., J. Nucl. Mater. **191-194** (1992) 910.

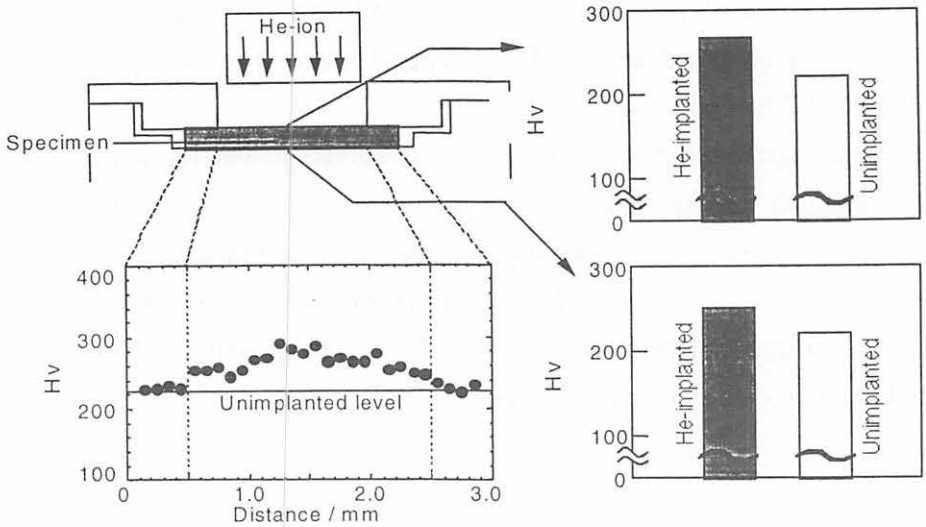

Fig. 1. Micro-Vickers hardness of both the specimen surfaces before and after He implantation.

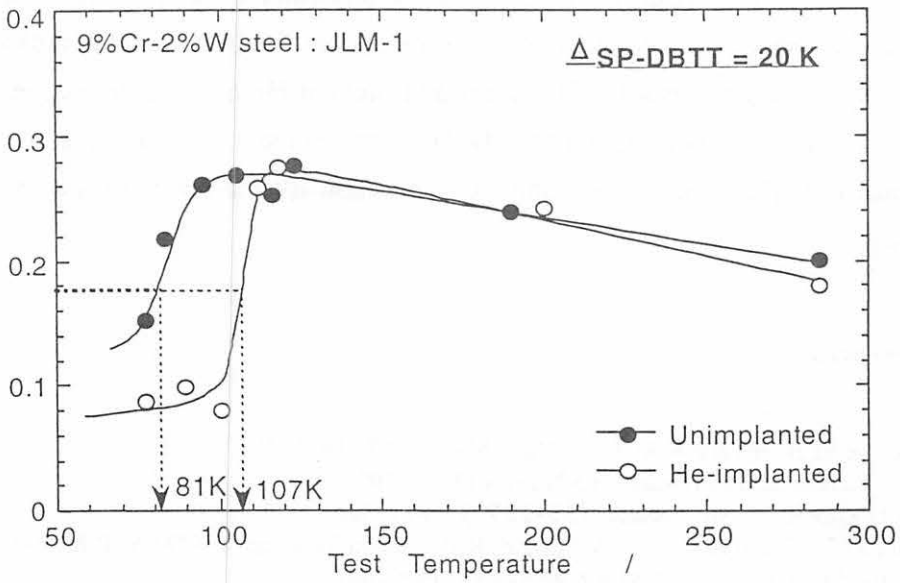

Fig. 2. Dependence of SP-fracture energy (J) on test temperature(K) and fracture surfaces of He implanted JLM-1; Ductile brittle transition is observed at around 110K below which the fracture mode is brittle cleavage, while it is ductile shear rupture above it. No intergranular fracture is observed even in the specimen fractured at 77K.

I. 15. Development of CYRIC TOF-facilities for (p,nγ) Measurement

Orihara H., Kawami K., Yun C. C., Terakawa A., Itoh K., Yamamoto A., Suzuki H., Mizuno H., Kamurai G.

Cyclotron and Radioisotope center, Tohoku University

In the course of development of the CYRIC TOF-Facilities[1,2], we have constructed a fast neutron polarimeter with a liquid-helium scintillator[3], equipment for neutron induced experiments[2], those for high-energy γ -ray detection[4], and neutron-proton coincidence measurement system for the (p,np) experiments[5]. In this report, we describe briefly the recently developed neutron-γ coincidence unit for (p,n γ) measurements.

One of the recent interest of nuclear physics is the quantitative relationship between the allowed β -decay probability and Gamow-Teller type ($\Delta J^{\pi}=1^{+}$, $\Delta L=0$, and $\Delta T=1$) (p,n) cross section, since these two processes are based on spin-isospin excitation, though the latter is form-factor dependent. Proportionality between GT type β-decay and M1 transition is much more straight forward, the driving term for them being similarly $<\sigma\tau>$.

Figure 1 shows a diagram for the relation among β-decay, M1 γ-decay and (p,n) reaction. Bold lines denote the analog states. The life time of the state Ψ_2 and the *ft*-value for the β^{+} transition $\Psi'_1 \rightarrow \Psi_2$ is considered to be related, where Ψ_1's and Ψ_2 belong to the same Wigner supermultiplet. Alternatively, the GT-like (p,n) cross section may be related to the γ-decay matrix elements, which is calculated quite accurately. Thus, (p,nγ) measurements may provide more comprehensive information for quantitative analyses for e.g. quenching effect for the (p,n) reaction.

Protons for this development are obtained by Tohoku K=50 MeV, AVF cyclotron, and neutrons were analyzed by the TOF technique with a flight path of 4.5 m, where a disk type (233ϕ, and 5 cm-thick) of neutron detector filled with NE213 liquid scintillator is located. Figure 2 shows a block diagram for n-γ coincidence measurement including detectors, electronics and data taking devices. Figure 3 shows a single neutron TOF spectrum taken for the ^{90}Zr(p,n)^{90}Nb reaction at a laboratory angle of 45 degree. One of the point of the present experiment is to measure successfully the neutrons with sufficiently low backgrounds in such a short flight-path. Gamma rays are detected by the high-energy detection system[4] which consists of seven BaF_2 crystals. The solid angle for g-ray detection is 8.75 msr.

Figure 4 illustrates a time spectrum for coincidence events, showing that S/N ratio is in the order of 2/1. A prompt peak ROI spectrum is shown in Fig. 5. Note that a peak of

neutrons leading to the isobaric analog state is seen. In Figs. 6(a), (b) and (c) illustrated are those of prompt, random, and true spectra respectively. A peak corresponding to the M1 transition 0^+(IAS) $\rightarrow$ 1^+ (2.3MeV) is resolved, though event rate is poor.

We have accumulated enough data for further improvements: for better statistics of coincidence events, the detection angle of neutrons should be 0 degree, where the (p,n) cross section is maximum, and the solid angle for γ ray detection should be larger as well. An arrangement of detector array with smaller size NaI crystal is favorable.

References

1) Orihara H. and Murakami T., Nucl. Instrum. Methods **181** (1981) 15.
2) Orihara H. et al., Nucl. Instrum. Methods **A257**(1987) 189.
3) Ieki K. et al., Nucl. Instrum. Methods **A262** (1987) 323.
4) Hosaka M. et al., Phys. Rev. C **54** (1996) 2429.
5) Orihara H. et al., Proc. of RIKEN Symposium on *Giant Resonance* Wako (1998).

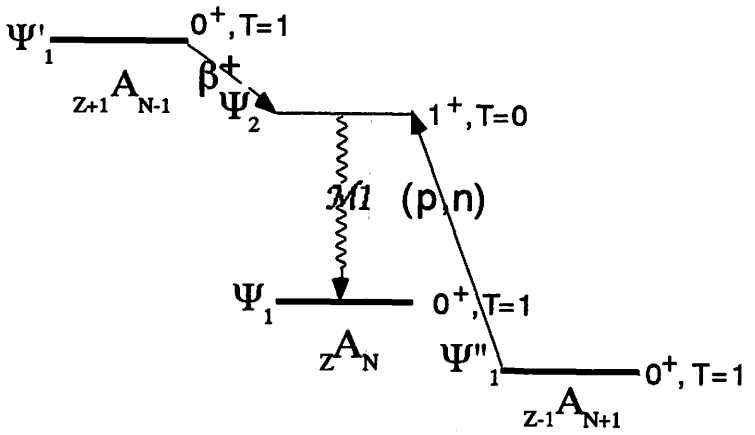

Fig. 1. Diagram of related β-decay, M1 transition and (p,n) reaction.

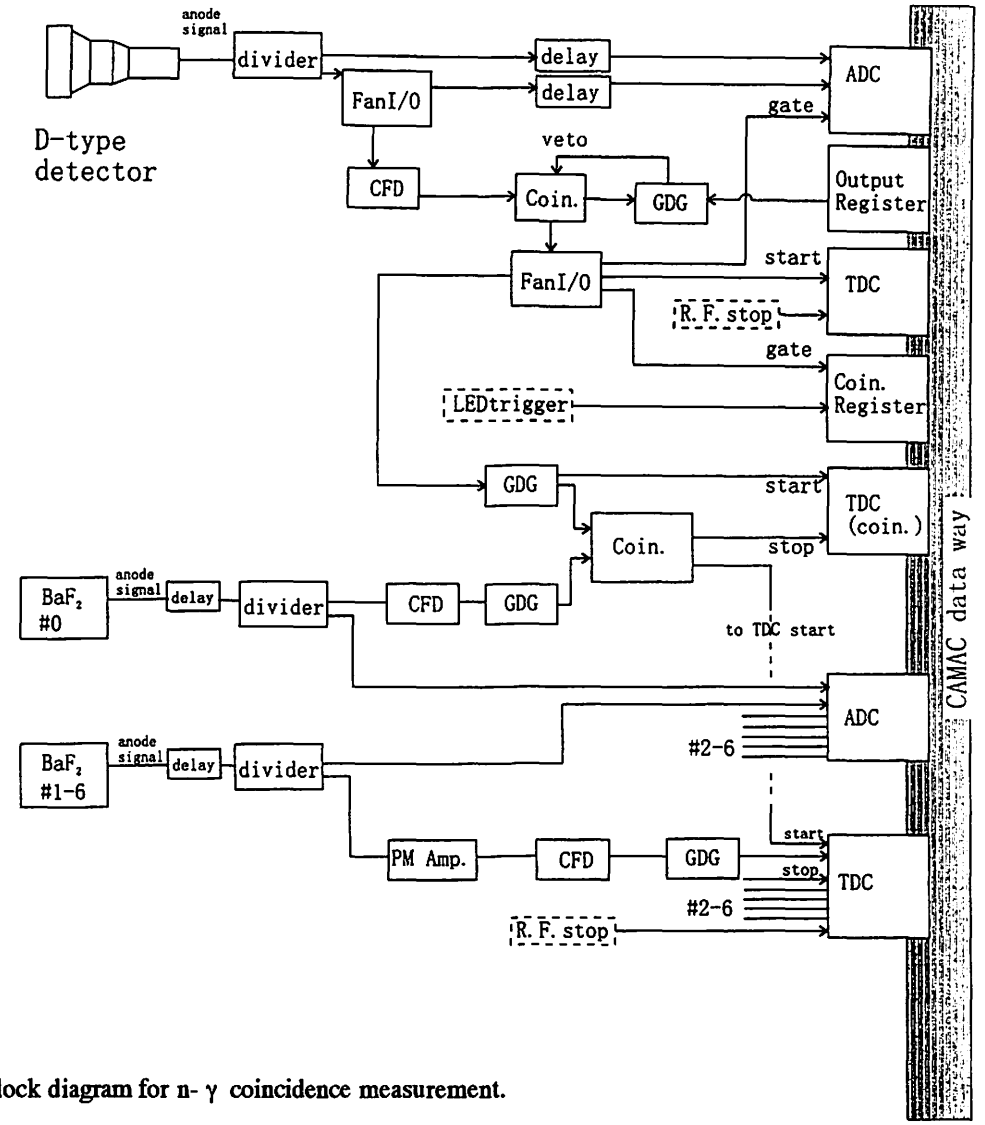

Fig. 2. Block diagram for n- γ coincidence measurement.

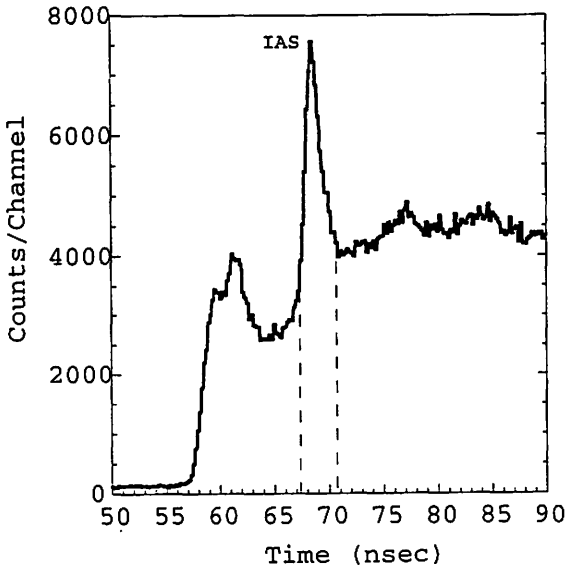

Fig. 3. Single neutron TOF spectrum taken for the $^{90}Zr(p,n)^{90}Nb$ reaction at a laboratory angle of 45 degree.

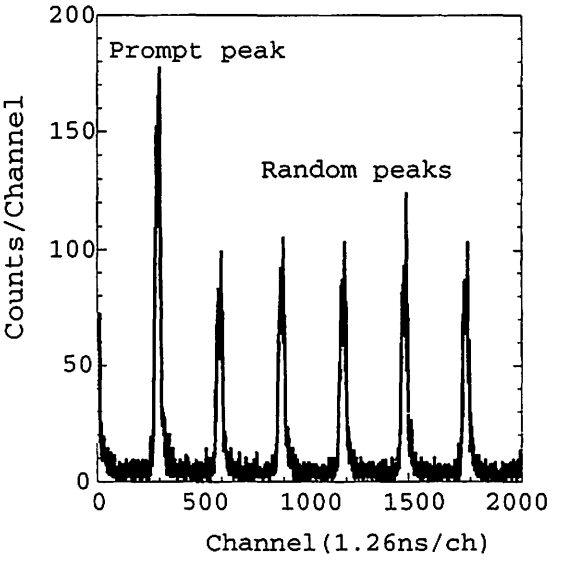

Fig. 4. Time spectrum for coincidence events.

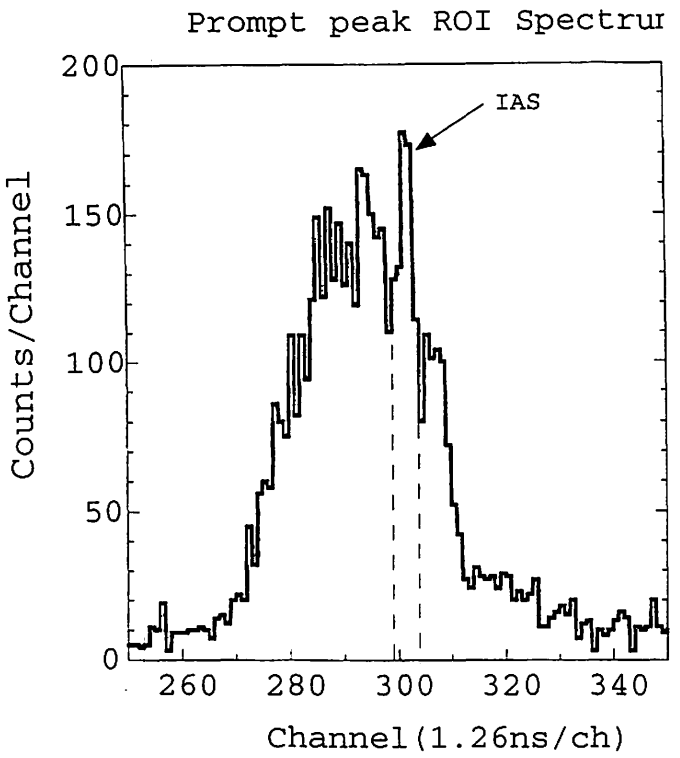

Fig. 5. A prompt peak ROI spectrum.

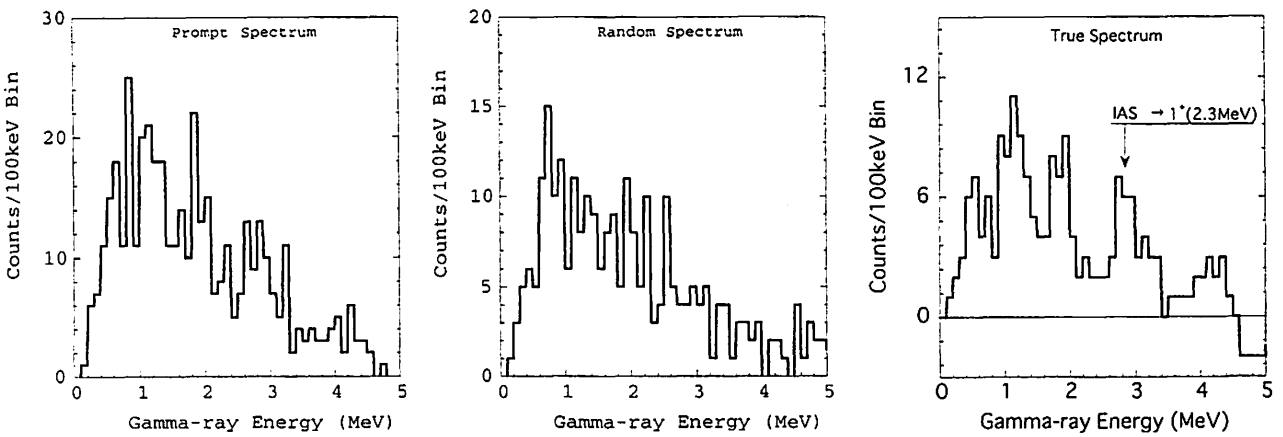

Fig. 6. Prompt(a), random(b), and true(c) γ - ray spectra.

I. 16. A Simple Technique for a Simultaneous Least-squares Fitting of Plural Groups of Data in Terms of the Same Parameter Set

Fujioka M. and Kouda T.

Cyclotron and Radioisotope Center, Tohoku University

For the sake of concreteness we take for example the problem of data analysis of TIPAD (Time-Integral Perturbed Angular Distribution of γ-rays in an in-beam nuclear spectroscopy)[1]:

$$\left.\begin{aligned} W(\theta, \pm B) &= \sum_{\lambda=\text{even}} b_\lambda^{\pm} \cos[\theta \mp (\Delta\theta_\lambda)^{\pm}] \text{ with} \\ (\Delta\theta_\lambda)^{\pm} &= (1/\lambda)\tan^{-1}[\lambda(\omega_L \tau)^{\pm}], \end{aligned}\right\} \quad (1)$$

where ω_L is the wanted Larmor angular velocity and τ the mean life of the isomer emitting the perturbed γ-ray. When fitting experimental data in terms of eq.(1), we are inclined to perform two independent LSF's (Least-Squares Fittings), respectively, for ± B and finally obtain ,e.g.,

$$\omega_L\tau = \frac{1}{2}[(\omega_L\tau)^{+} + (\omega_L\tau)^{-}] \quad (2)$$

; see Fig.1.a).

Another way of analysis, however, is to take advantage of the symmetry properties of electromagnetism and experimental conditions, $b_\lambda^{+} = b_\lambda^{-} \equiv b_\lambda$ and $(\Delta\theta_\lambda)^{+} = (\Delta\theta_\lambda)^{-} \equiv \Delta\theta_\lambda$, which may result in a reduction of estimated error of $\omega_L\tau$:

$$\left.\begin{aligned} W(\theta, \pm B) &= \sum_{\lambda=\text{even}} b_\lambda \cos[\theta \mp (\Delta\theta_\lambda)] \text{ with} \\ \Delta\theta_\lambda &= (1/\lambda)\tan^{-1}(\lambda(\omega_L\tau). \end{aligned}\right\} \quad (3)$$

In this case we have two groups of measurement for the same fitting points of θ and the same parameter set; Fig.1.b). It is not difficult to write a code of LSF according to eq.(3), but in stead we adopted a simple technique[2] for an easy use of the minimization routine MINUIT in PAW[3], i.e., by displacing along the θ-axis the data of -B relative to those of +B, reducing the problem to an ordinary "single-valued" LSF having twice points of meaurement (fitting); see Fig. 2.

Extension to more than two groups of data is straightforward. Other extensions are also possible, but we do not detail further; comparison of Fig. 1. b) and Fig. 2. would suffice. Here it is interesting to note that the present technique reminds us of the Riemann surface for reducing a multi-valued function to a single-valued one.

The authors acknowledge Drs. Shinozuka T. and Tanigaki M. for discussions.

References

1) Steffen R. M. et al. in, Alpha-, beta- and gamma-ray spectroscopy, ed. Siegbahn K. (North-Holland Publ. Comp., Amsterdam, 1966) vol.2, p.1151.
2) Kouda T., Master's thesis, Measurement of the g-factors of low-lying states of ^{66}Ga, 1997, Tohoku University, unpublished.
3) Brun R., Couet O., Vandoni C. and Zanarini P., PAW--Physics Analysis Workstation, Ver.1.07 (1989, CERN, Geneva).

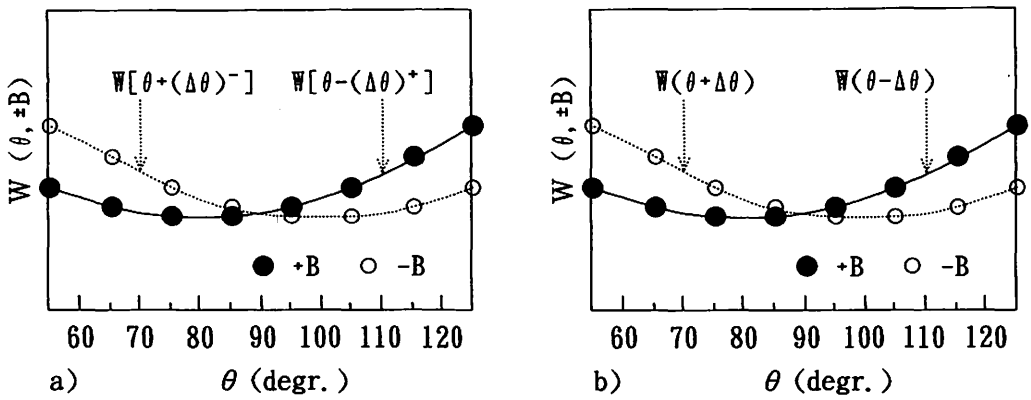

Fig. 1. a) Two independent LSF's of two TIPAD's for ± B. Suffix λ is abbreviated. The $\Delta\theta$ ' s are taken to be negative corresponding to a positive g-factor. b) A simultaneous LSF of two TIPAD's for ± B, the number of fitting parameters being one-half that of a) by taking advantage of the symmetries of the problem.

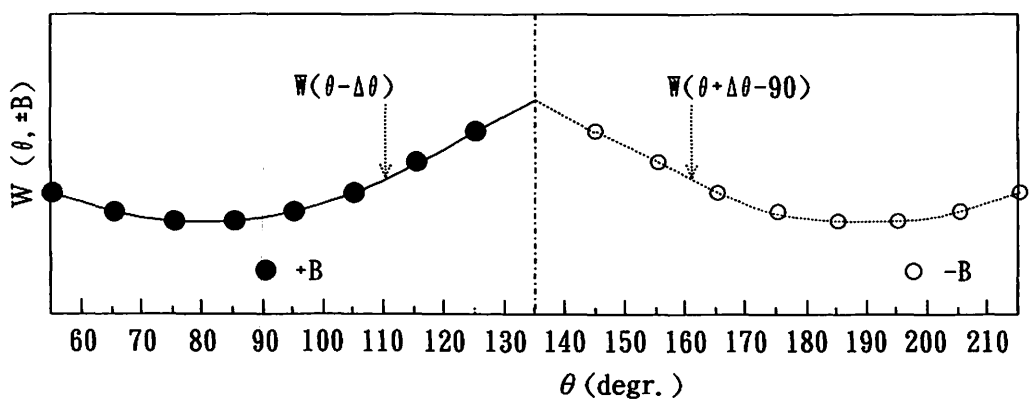

Fig. 2. A simultaneous LSF of two TIPAD's for ± B as one LSF by using an ordinary ready-made routine, which is equivalent to Fig. 1. b). The magnitude of displacement is irrelevant as long as it is larger than 70°; e.g., if one would prefer equi-interval of θ throughout, 80° be used in stead of 90°

I. 17. Weldability of Helium-containing Stainless Steels Using YAG Laser

Kawano S., Nakahigashi S., Uesugi K.*, Nakamura H.*, Kono W.*, Fukuya K., Kano F., Hasegawa A.**, and Abe K.***

Toshiba Corporation
*Japan Power Engineering and Inspection Corporation**
*Department of Quantum Science and Energy Engineering, Tohoku University***

Introduction

The replacement and repair technique for degraded structural components is one on the important technical issues for fission reactor maintenance. Such procedures are likely to require various welding techniques for joining irradiated materials. The reactor components exposed to high-energy neutrons contain large amounts of helium produced by nuclear transmutation reactions. Helium is known to have a large effects on weldability and properties of welded joints[1-6]. Weld metal cracking, heat-affected zone(HAZ) cracking and underbead cracking have been reported in helium-containing stainless steels. Although the full process of weld cracking has not been well understood, helium is considered to affect weldability through rapid growth of bubbles formed at grain boundary under the influence of high temperature and thermal stresses to a sufficient size for grain boundary separation.

The objective of the present study is to investigate the effect of helium concentration and heat input on weldability using YAG laser and demonstrate the applicability of the YAG laser welding technique to stainless steels containing high amount of helium.

Experimental

The material used was SUS304 stainless steels solution annealed at 1323K for 0.5hr. The material was cut into the platelet specimens of 40mm in diameter and 10mm in thickness and surface-finished by #600 paper. The specimens were implanted with 36MeV helium ions from a cyclotron at Tohoku University. A beam energy degrader was applied to obtain uniform implanted helium distribution from the surface to a depth of 0.25mm. The calculated helium concentration was 0.5, 5, and 50appm. The specimen surface temperature was monitored during implantation and kept below 423K.

After implantation, bead-on-plate welding experiments were conducted with 400W continues wave laser beam from a 600W YAG laser oscillator. The laser beam diameter on the specimen surface was 1.6mm. On each specimen, three weld beads were formed across

the helium-implanted area at welding speeds of 0.2, 1 and 4mm/s. The welding at 0.2, 1 and 4mm/s corresponds to nominal heat input of 20kJ/cm, 4kJ/cm and 1kJ/cm, which is typical of high heat input GTA welding, respectively. After welding, liquid penetrant test and SEM observation of surface and transverse cross section of weld bead were preformed.

Results

Figure 1 shows an example of the specimen appearance after welding. The bead width increased slightly from 1.3mm at 1kJ/cm to 1.5mm at 20kJ/cm. Fig. 2 shows shallow surface crack observed HAZ in the specimen containing 50 appm He after welding at 20kJ/cm. The crack was intergranular in nature and was at 0.01mm from the fusion line. No crack in HAZ was detected in the other specimens. No crack was observed on the weld metal in any specimens.

In the cross section around weld joints, small pits along grain boundary in HAZ and isolated pits in the weld metal were observed in the welded specimen with 5 and 50 appmHe. Small pits on grain boundary were formed only within helium-implanted depth and within 0.1mm distance from the fusion lines. These indicate that the grain boundary pits are closely related to the existence of helium and the welding condition and that they are formed on helium bubbles.

Figure 3 shows the effects of helium concentration and heat input on the total length of grain boundary with pits. The bubble growth is clearly dependent on both helium concentraion and heat input. For laser welding with heat input of less than 1kJ/cm, bubble growth was much less than for welding with 4 and 20kJ/cm, which are typical GTA welding method.

Summary

YAG laser welding experiments with heat input up to 20kJ/cm on SUS 304 stainless steel containing helium clearly showed the effect of helium and heat input on weldability. A low heat input YAG laser welding is a promising welding technique for stainless steel with a high amount of helium.

References

1) Lin H. T. et al., Metal. Trans. **21A** (1990) 2585.
2) Kanner W. R. Jr., et al., August (1988) 33.
3) Good S. H. et al., Metal. Trans. **23A** (1992) 1021.
4) Wang C. A. et al., J. Nucle. Mater. **225** (1995) 59.
5) Watanabe K. et al., Fusion Eng. And Des. **31** (1996) 9.
6) Kanner W. R. Jr. et al., J. Nucl. Mater. **225** (1995) 69.

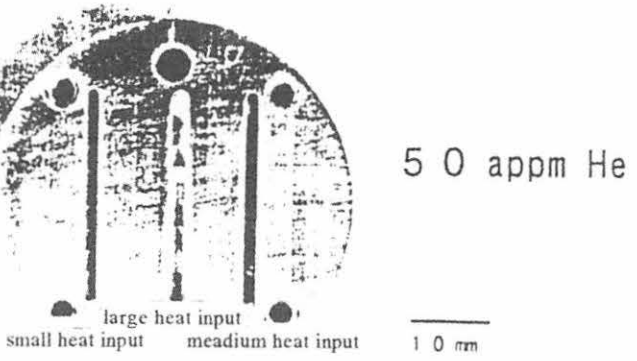

Fig. 1. Surface appearance of 50 appm He specimen after welding.

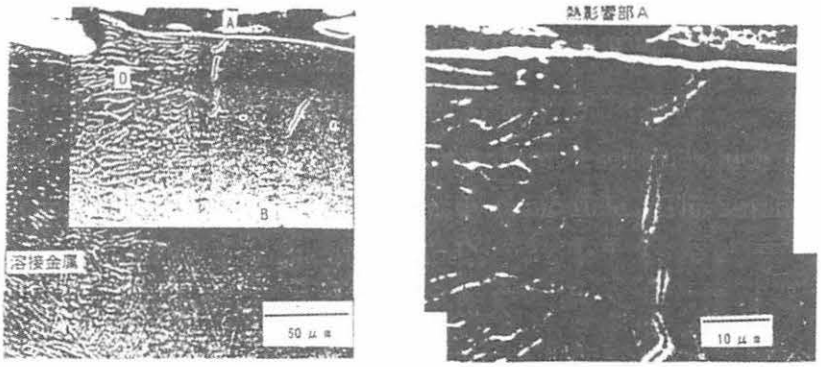

Fig. 2. Surface crack in HAZ in the specimen containing 50appm He welded at 20kJ/cm. (a) Weld bead, (b)crack in HAZ at higher magnification.

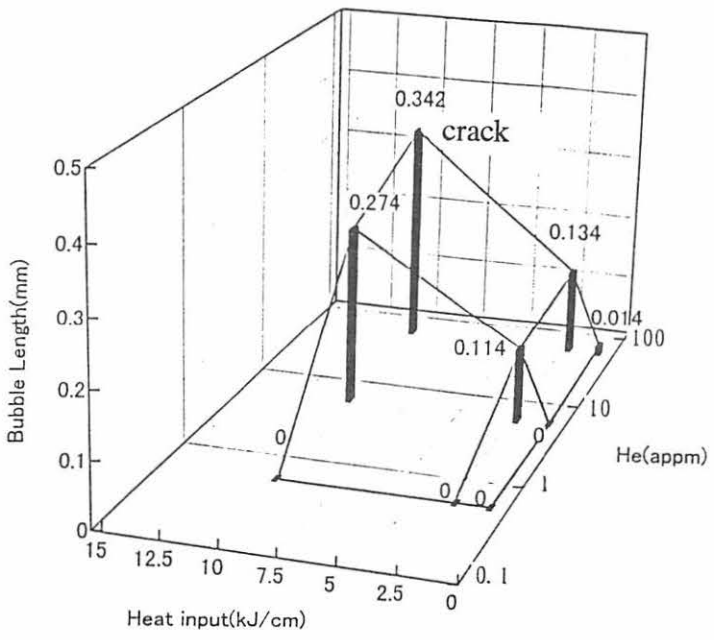

Fig. 3. Length of grain boundary with pits as functions of helium concentration and heat input.

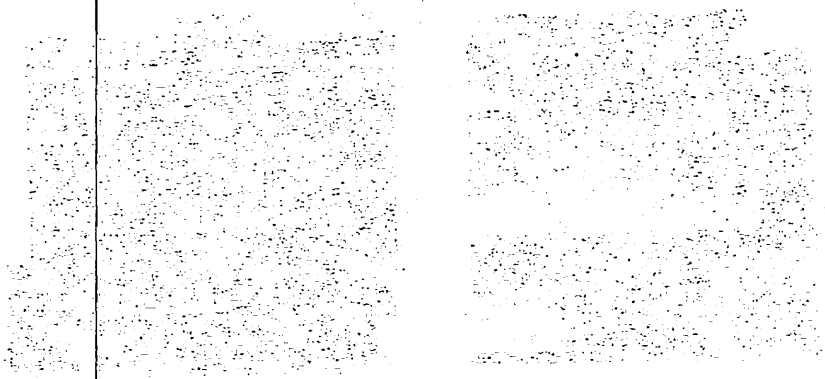

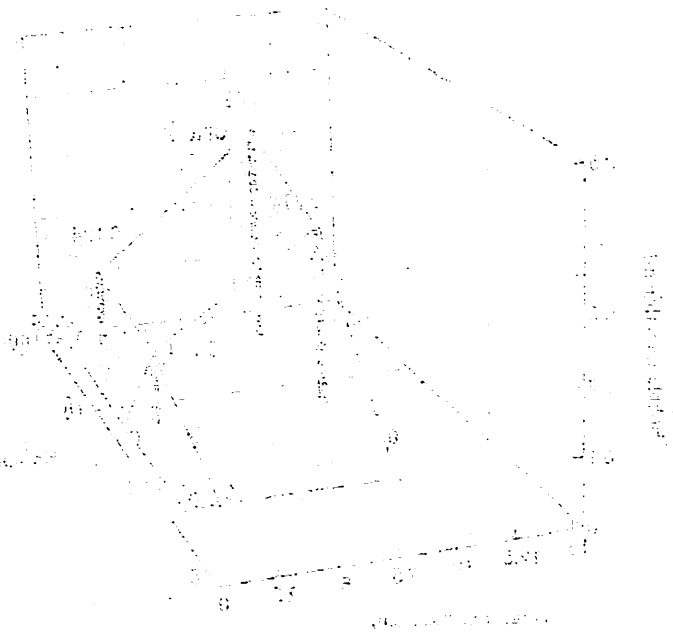

I. 18. Eddy Field Measurement Using a Peaking-Strip

Kanai Y., Adachi T., Fujioka M.**, and Mori Y.**

Department of Physics, Tohoku University,
KEK High energy accelerator research organization
*accelerator division 1-1 Oho,Tsukuba-shi Ibaraki-ken, 305-0801**
*Cyclotron and Radioisotope Center, Tohoku University***

An eddy field in a bending magnet was measured along the longitudinal direction, when the magnet was excited by a sinusoidal current with a repetition of 49.73Hz. The measurement was performed by using a peaking-strip[1]. It was found that eddy field generated in the edge plate made by stainless steel became larger as the position became closer to the magnet edge.

Introduction

In Japan, the JHF(JAPAN HADRON FACILITY) plan is being progressed. The JHF accelerator complex comprises the 200MeV linac, the 3GeV booster synchrotron and the 50GeV synchrotron.

The 3 GeV booster synchrotron is a rapid-cycling synchrotron with a repetition of 25 Hz. In the future, the repetition will be increased up to 50Hz, in order to obtain a beam power over 1MW. Although, in such a rapid-cycling synchrotron, the vacuum chamber used in the magnet is made of ceramics to avoid the field disturbance due to an eddy current, the eddy current is also induced in the magnet, which may disturb the magnet field. Especially, in a dipole magnet, a sextu-pole component of the eddy field must be considered in order to accelerate a high-intensity beam without beam loss.

Field measurement in a dipole magnet has been performed for the purpose of estimations of the field disturbance due to an eddy field. In this paper, the results obtained so far are described.

Field Measurement

A test magnet[2] for the B-factory was excited with the repetition of 49.73Hz using an LC resonant circuit. Fig.1 shows a coordinate of the test magnet. The field measurement was performed on the median plane.

Since the magnet is excited by a sinusoidal current, magnetic flux density(B) is given by

$$B = B_0 \sin \omega t . \tag{1}$$

Since an eddy current depends on $\dot{B}$, the eddy field is given by

$$B_{eddy} = B_{in} \sin \omega t + B_{out} \cos \omega t. \tag{2}$$

B_{in} and B_{out} are caused by diamgnetism and resistance of end part of magnet material respectivily. Then, total magnetic field (B_{tot}) is obtaind as

$$B_{tot} = \sqrt{(B_0 - B_{in})^2 + B_{out}^2} \sin(\omega t + \delta)$$
$$\tan \delta = \frac{B_{out}}{B_0 - B_{in}} , \tag{3}$$

where δ is the phase difference between the main dipole field (B_0-B_{in}) and the eddy field. Therefore, the amplitude of the eddy field can be obtained by measuring the phase difference (δ) and amplitude of the main dipole field (B_0-B_{in}).

Phase difference was measured by two peaking strips, each of which generates a voltage pulse by detecting a zero-crossing timing of a dynamic field. The amplitude of the main field (B_0-B_{in}) was measured by a seach-coil method[3].

Experimental Results

Fig.2 shows a block diagram of the measuring system. Here, peaking strip 1 was fixed at the center of the magnet. Peaking strip 2 and the seach-coil were moved along the longitudinal direction. Signals of two peaking-strips were sent to an osilloscope, and phase difference was measured. A signal of the seach-coil was integrated for the interval between instants givinig the minimum and maximum field, so that the amplitude of the main field was obtained. The time interval for integration was determined by a signal of the back-leg winding.

The eddy field was measured along the longitudinal direction on the median plane. At first, two peaking-strips were set at the center of the magnet, in order to confirm the coincidence of two peaking timings.

The amplitude of the main dipole field at this point was measured by the seach-coil. Therefore, the normalized amplitude of the eddy field (B_{eddy}) is obtained in terms of the following formula:

$$B_{eddy} \equiv \frac{B_{out}(x,y)}{B_0(x=0,y=0)} = \frac{B_0 - B_{in}}{B_0(x=0,y=0)} \tan \delta. \tag{4}$$

Fig.3 shows the position dependence of the normalized amplitude of the eddy field, together

with the magnet cross-section cut by the y-z plane at x=0.

As shown, the eddy field becomes larger as the position becomes closer to the end plate of stainless steel. This result implies that the eddy current induced by the main field can not be ignored around the end plate made by stainless steel.

Conclusion

An eddy field in a bending magnet was measured along the longitudinal direction on the median plane, when the magnet was excited by a sinusoidal current with a repetition of 49.73Hz. The field disturbance due to the eddy field was found to be large around the magnet end part, and amounts to 0.4% of the main dipole field at the magnet center.

The transverse distribution of the eddy field is necessary in order to estimate an effect of the eddy field to a circulating beam in a synchrotron. In addition, a 3-dimensional simulation code for a dynamic field is also being prepared in order to compare the experimental result with the simulation. When the simulation code is confirmed, it gives a guiding principle in design of a magnet for a rapid-cycling synchrotron.

Acknowledgment

The authors would like to say thanks to Mr. H. Someya, Dr. M. Yoshii, Dr. A. Takagi and Dr. F. Q. Zhang for their advice during this work. We must also acknowledge Prof. K. Endo for lending their test magnet and power supply.

References

1) Yamaguchi S., et al, INS REPORT, INS TH **18** (1957).
2) Zhou W., and Endo K., KEK REPORT **93-3** (1993).
3) Kumada, M. et al., KEK REPORT, KEK-**77-30** (1978).

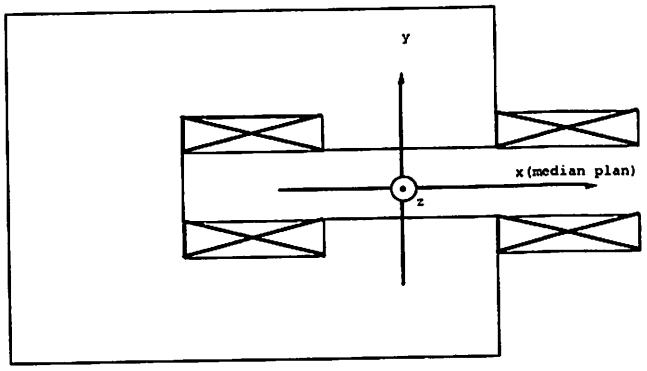

Fig. 1. Coordinate of the test magnet.

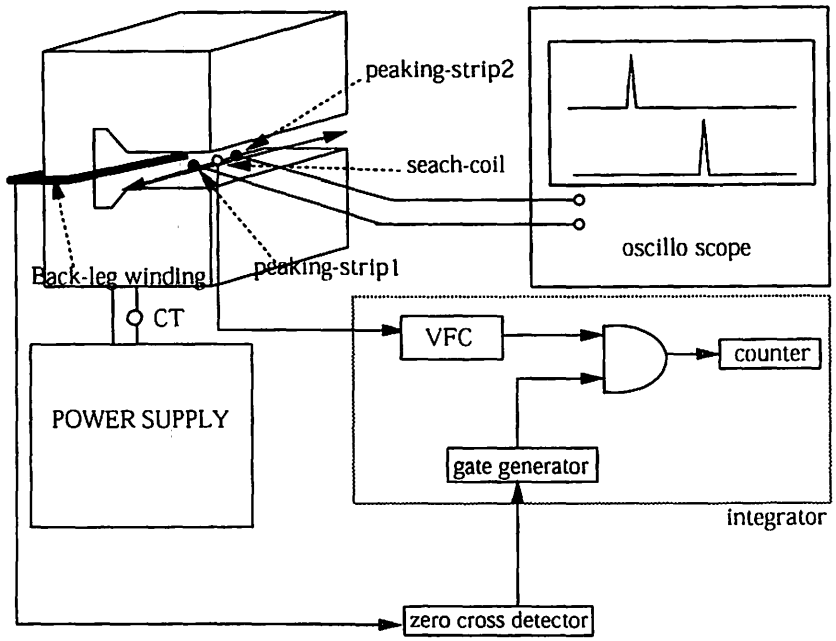

Fig. 2. Block diagram of the measuring system.

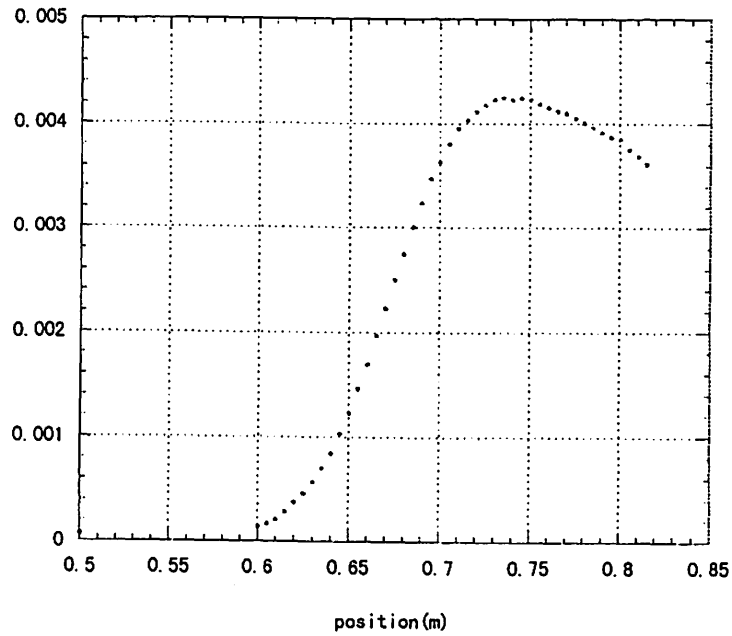

Fig. 3. Position dependence of the eddy field.

I. 19. Basic Studies on CdTe Detectors

Tanigaki M., Baba T., Fujita M., Hoshino T.*, Shinozuka T., and Fujioka M.*

Cyclotron and Radioisotope Center, Tohoku University
*Department of Physics, Tohoku University**

Ge detectors are widely used for the γ-ray spectrometry because of their high energy resolution and detection efficiency, but the requirement for cooling the crystal down to ~77K and the bad price performance make it difficult to build a complicated system such as γ-sphere. As previously reported, we are proposing a γ-ray detection system called "mini crystal ring"[1] for the spectroscopic studies of nuclei in low excited states and looking for a suitable detector.

CdTe, known as one of the II-VI compound semiconductor, is a good candidate for our purposed system, since this device is characterized as;

1) High stopping power due to large Z number atoms (Cd =48, Te=52; e.g. Ge=32),
2) High density; three times higher than Si,
3) Wide band gap around ~ 3 eV; good performance at room temperature,
4) Low price; less than 1/10 of Ge detectors.

Recent developments on the crystal growth technique enables to obtain the single crystal as thick as 2 mm, which is enough for the γ-ray detection up to ~ 1 MeV. Also the technique for forming the Shottokey barrier between electrodes and CdTe enables to apply high bias voltage up to ~1 kV, which results in improved charge collection efficiency. Taking into account such improvements, we have made basic studies on CdTe for the application to the γ -ray spectroscopy.

The detector used in the present study was produced by Japan Energy Co., Ltd. A single crystal of CdTe was synthesized by THM (Traveling Heater Method) and cut to the size of 2 mm × 2 mm × 0.5 mm. In and Pt were attached as the positive and negative electrodes, respectively. In each measurement, the source was placed at 13 mm away from the detector. The source and the detector were placed in the shield box made of Al to avoid the electric noises. The output signal from CdTe was sent to the high gain preamplifier Clear Pulse 5102 and analyzed by a conventional PHA system. All measurements were performed in atmosphere and at room temperature.

From the bias voltage dependence of the energy resolution of γ -ray from ^{137}Cs, the bias voltage was set to 800 V for further measurements. To examine the energy dependence of the spectrum, the γ-rays from ^{241}Am, ^{133}Ba, ^{57}Co, ^{137}Cs and ^{60}Co were measured. Typical spectra and the energy dependence of the energy resolution are shown in Fig. 1 and Fig. 2., respectively. The resolution was achieved up to 2~3 % for γ -ray energy more than 100 keV. On the contrary to the Ge detector, which requires the cooling down to the liquid nitrogen temperature, the present resolution is easily achieved just applying an appropriate bias voltage to the crystal at room temperature. The intrinsic efficiency of CdTe detector was estimated to be 0.05% for the 661 keV γ -ray from the ^{137}Cs, which was 1/5 of that from a theoretical calculation assuming that all of the crystal was active region, or 1/2 of the results from the simulation using the GEANT code.

One of the disadvantage of CdTe detectors is the so called "polarization effect", i.e., the resolution of the energy spectrum becomes worse in several hours. Although this effect can be easily canceled by the removal of the bias voltage for a short while (typically less than 1 minute), this effect must be fatal problem when the CdTe detectors are used for the long time measurements. Therefore, the time dependence of this effect must be studied for setting the appropriate interval of this refreshing process and for investigating the reason of this effect. In the present study, we also measured the time dependence of the energy resolution. The 661 keV γ -ray from ^{137}Cs was measured for 1 hour in every 2 hours interval. The increase of the peak width was clearly seen after ~6 hours (see Fig. 3). From the present result, the refreshing process is required at least every 5 hours to keep the initial resolution.

From the present study, the CdTe detector is found to be useful for the low energy γ ray spectroscopy up to several hundreds keV and a good candidate for the detector for our proposed system. Further studies, such as on the discrepancy of the efficiency between the experiment and the simulation, are now in progress.

The authors are grateful to the courtesy of Japan Energy Co., Ltd. to lent the preamplifier for the present study.

Reference

1) Fujioka M. et al., CYRIC Annual Report - 1996 (1997) 29.

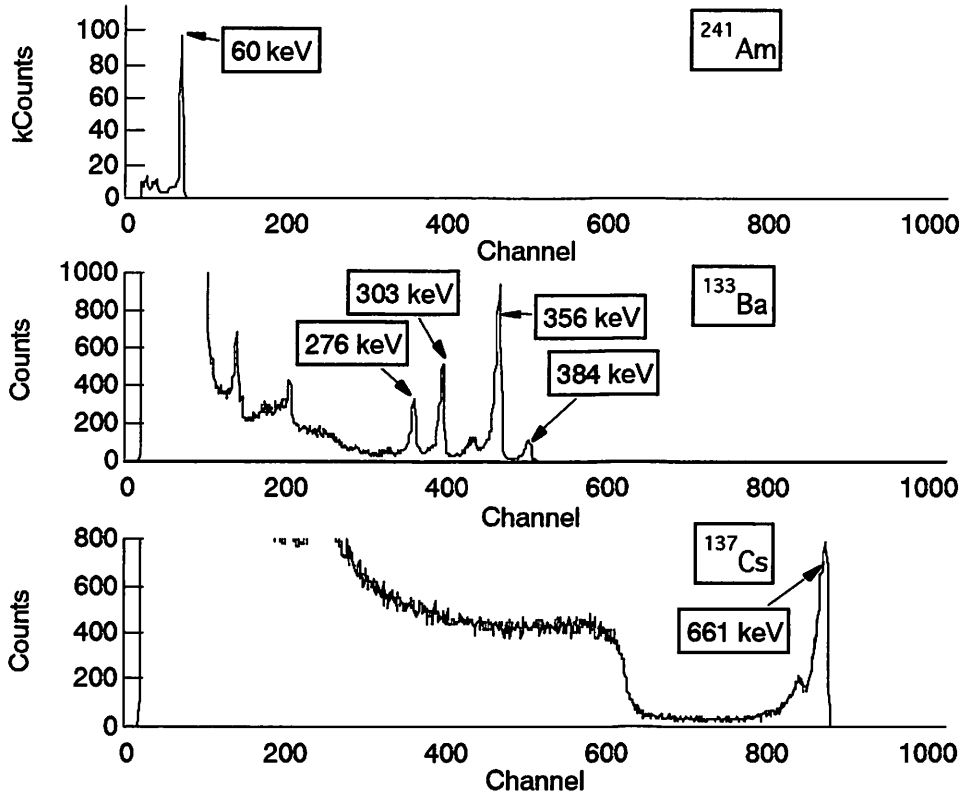

Fig. 1. Typical energy spectra obtained by the CdTe detector.

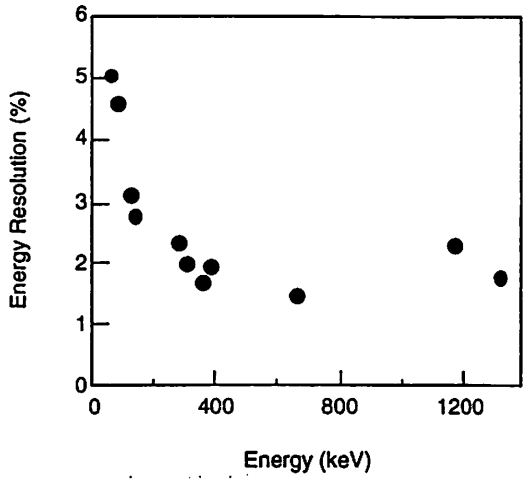

Fig. 2. Energy dependence of the energy resolution of the CdTe detector.

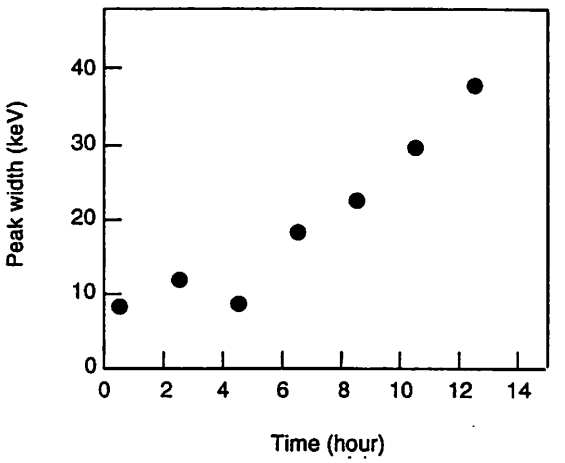

Fig. 3. Time dependence of the energy resolution at Eγ = 661 keV.

I. 20. Measurement and Calculation of Response Functions of Multi-moderator Neutron Spectrometer with ^{6}Li-^{7}Li Glass Scintillators

Taniguchi S. and Nakamura T.

Cyclotron and Radioisotope center, Tohoku University

Introduction

The exposure of space radiation to air crews and astronauts becomes an important problem. The neutron dosimetry is especially important due to its high quality factor, but the neutron measurements in high altitude and space have scarcely been done because of its difficulty in a charged-particle mixed field in space. For use in space, we developed two types of neutron spectrometers to be able to measure neutrons in a charged-particle mixed field; 1) phoswich-type plastic and organic-liquid scintillators for neutrons of energy of several MeV to 100 MeV, 2) multi-moderator-type ^{6}Li-^{7}Li glass scintillators, so called Bonner sphere, for neutrons below 20 MeV.

In this study, we measured the response functions of multi-moderator-type ^{6}Li-^{7}Li glass scintillators to neutrons of 8 keV to 22 MeV and compared with the calculated results.

Detector

A pair of 2.54 cm diam by 2.54 cm long NE912 and NE913 lithium glass scintillators are mounted on 2.54 cm diam by 10 cm long acrylic light guides, which are coupled with two photomultipliers of R1924(Hamamatsu Photonics). The scintillators are covered with spherical polyethylene moderators of 1.5, 3.0, 5.0 and 9.0 cm thicknesses. The cross sectional view of the Bonner sphere is shown in Fig. 1. The NE912 scintillator has a sensitivity to thermal neutrons due to ^{6}Li(n,α)T reaction, while the NE913 has no sensitivity to neutrons. Both scintillators have almost the same sensitivities to other radiations such as photons and charged particles. By subtracting the pulse height spectrum of NE913 from that of NE912, thermal neutrons can be measured, even under the intense charged particle mixed field.

Experiment

The response functions to 8 keV to 22 MeV neutrons were measured in this study by using two mono-energetic neutron calibration fields at Tohoku University, the Fast Neutron

Laboratory(FNL)[1] and the Cyclotron and Radioisotope Center(CYRIC)[2]. At FNL, the response functions to 8 keV, 0.25, 0.55, 1.0, 2.0, 5.0 and 15.0 MeV neutrons were measured and at CYRIC those to 22 MeV neutrons.

In the experiments at FNL the Bonner sphere was about 120 cm away in the forward direction from the neutron production target. The absolute value of neutron fluence was determined with the ^{235}U fission chamber set on a neutron beam line. The neutron fluence during irradiation was monitored with a hydrogen proportional counter off a beam line whose counts were calibrated to the fission chamber counts, because the fission chamber counts were influenced by the neutrons backscattered from the Bonner sphere. The light guide axis of the Bonner sphere (see Fig. 1) was set perpendicularly to the neutron beam line. Only in 0.25, 1.0 and 22 MeV neutron irradiation experiments, with the light guide axis of the Bonner sphere parallel to the beam line, the experiments were repeated to investigate the angular dependence of the response functions.

The experiment at CYRIC was done in the Time-of-Flight(TOF) Extension room. The quasi-monoenergetic neutrons were produced from a thin ^{7}Li target bombarded by 25 MeV protons. The neutrons emitted at 10 degree were transported to the TOF room through a collimator of 20 × 30 cm aperture. The neutron fluence during irradiation was monitored with a ^{232}Th fission chamber set just before the collimator, which was calibrated to the absolute neutron fluence value which was determined from the ^{7}Be activity in the ^{7}Li target.

Calculation

The calculations were made by the NCNP4A[3] Monte Carlo computer code coupled with the ENDF-B/VI cross section data library[4]. The geometry for the calculation is shown in Fig. 2. In these calculations, uniformly-distributed parallel mono-energetic neutron beams were generated and injected to the Bonner sphere perpendicularly to the detector axis. The response functions to 1.0×10^{-6} to 5.0 MeV neutrons were calculated with 5×10^{5} histories.

The counts in the ^{6}Li were estimated as the reaction number of $^{6}Li(n,\alpha)T$ which was obtained from the calculated neutron track length and $^{6}Li(n,\alpha)T$ reaction cross section.

Results and Discussion

The comparison of measured and calculated response functions is shown in Fig. 3. In Fig. 3 the experimental data are shown by symbols and the calculated results are shown in lines. The shapes of response functions are quite similar between experiment and calculation for all polyethylene moderator thicknesses, but the MCNP calculation gives about a half of the experimental results for all cases in absolute values. We are now investigating this discrepancy.

Acknowledgments

The authors wish to thank Dr. Baba, Dr. Terakawa and other stuffs of CYRIC and FNL for their cooperation with these experiments.

References

1) Baba M., et al., Nucl. Instr. and Meth. **A376** (1996) 115-123.
2) Takada M. et al., Nucl. Instr. and Meth. **A372** (1996) 253-261.
3) Briesmeister, J. F.(Ed.); MCNP - A General Monte Carlo N-Particle Transport Code, Version 4A; LA-12625-M (Los Alamos National Laboratory) (1993).
4) Evaluated Nuclear Data File; ENDF-B/VI, National Nuclear Data Center, Brookhaven National Laboratory (1990).

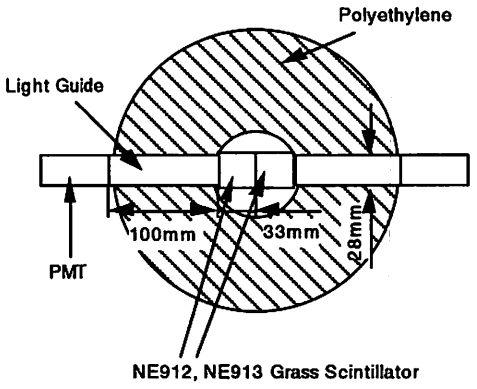

Fig. 1. A cross-sectional view of multi-moderator spectrometer.

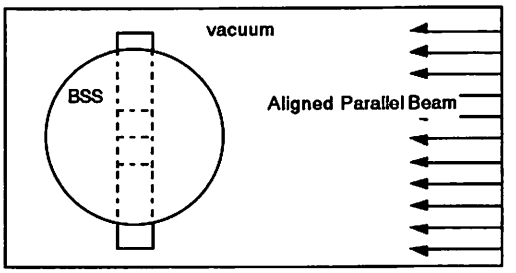

Fig. 2. Calculational geometry of response function.

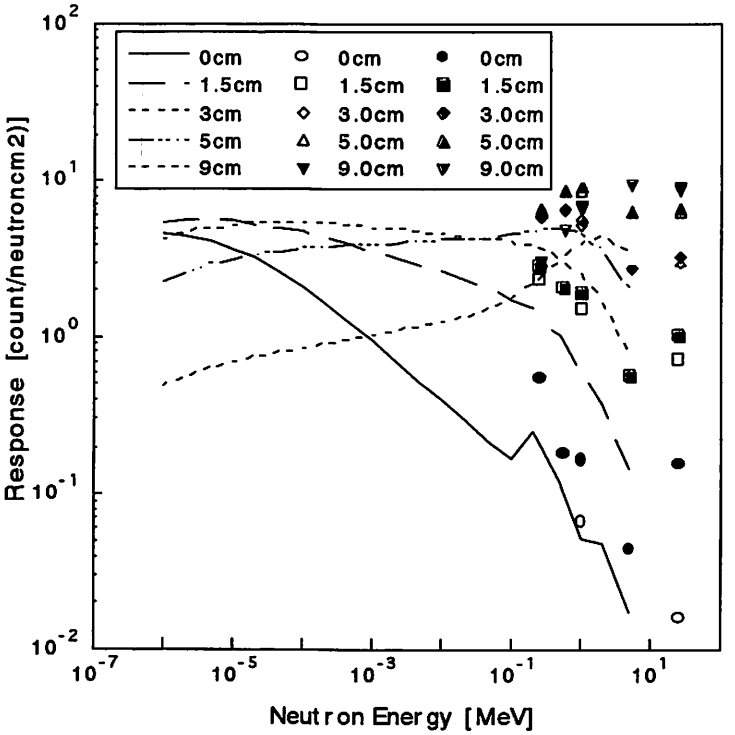

Fig. 3. Comparison of measured and calculated response functions.

I. 21. Radiation Damage Effect by 25MeV Protons on Thallium Bromide Nuclear Radiation Detectors

Hitomi K., Shoji T., Suehiro T., Ohba K., Tohei T., and Hiratate Y.

Department of Electronics, Tohoku Institute of Technology, Sendai 982-8588

Thallium bromide (TlBr) is a compound semiconductor which can be used as a material for radiation detectors. When these detectors are applied in space or in nuclear reaction experiments, radiation damage of the detector is a serious problem. In this study, we irradiated the TlBr detectors with 25MeV protons from Tohoku University cyclotron. In order to characterize the irradiation effects on the TlBr detectors, we measured voltage-current, mobility lifetime ($\mu\tau$) product and spectrometric response. The $\mu\tau$ measurement suggests that electron trap centers which shorten lifetime of the electrons may have been induced by 25MeV protons in the TlBr crystal. As a result spectrometric response for ^{241}Am γ-rays with electrons mainly traversing the detector showed degraded energy resolution after irradiation by 25MeV protons.

Introduction

Thallium bromide (TlBr) is a compound semiconductor characterized by the higher γ-ray stopping power due to its high atomic number (Tl:81, Br:35) and density (7.56g/cm^3). We have investigated TlBr as a material for a radiation detector which works at a room temperature. Recently, we have succeeded in fabricating TlBr radiation detectors which exhibit satisfactory γ-ray spectrometric response. When one uses these detectors in space or nuclear reaction experiments, radiation damage of the detectors is a serious problem because the detectors are exposed to strong ambient radiation. In the present study, we irradiated the TlBr detectors with 25MeV protons to elucidate irradiation effects of the detectors. Degradation of the detectors were characterized by voltage-current, $\mu\tau$ product and spectrometric response measurements.

Experimental

The commercially available TlBr powder with nominal purity of 99.99% was used for the crystal growth. The starting material was purified by the conventional many pass zone refining. Then, TlBr crystals were grown by the TMZ (travelling molten zone) method[1]. The TlBr detectors used in the present experimental were fabricated from these crystals and

were $16mm^2$ in area with $0.8mm^2$ gold electrodes on both sides of wafers. Details of the detector fabrication were reported earlier[2] and are not reviewed here.

The detectors were irradiated with 25MeV protons from the Tohoku University cyclotron. The irradiation was carried out in a vacuum chamber at a room temperature. The irradiation dose was $25nC/cm^2$ and the irradiation time was about 40s.

We have estimated a value of $\mu\tau$ products of electrons and holes by applying the Hecht equation to the voltage dependence of the peak position for 5.48 MeV α particles from a ^{241}Am source for the TlBr detector.

Results and Discussion

The voltage-current characteristic after irradiation is shown in Fig. 1. The leakage current was reduced due probably to radiation induced centers. These centers act as a carrier removal that diminishes the carrier concentration responsible for the electric conduction. Thus the resistivity of the detector was increased by the irradiation.

The estimated $\mu\tau$ products were listed in table 1. In case of the electron, the $\mu\tau$ product was deteriorated after irradiation. On the other hand, no difference was observed between $\mu\tau$ products for holes before and after irradiation in marked contrast to the case of electrons. The above mentioned result suggests that the electron trap centers which shortened lifetime of the electrons should have been induced by 25MeV protons in the TlBr crystal.

The spectrometric responses for ^{241}Am γ-rays of the TlBr detector biased at 100V are shown in fig. 2 obtained with the γ-rays incident on the cathode and with the γ-rays incident on the anode in fig. 3. Since many electron-hole pairs are produced by the γ-rays near the detector surface of incidence at the γ-ray energies under consideration (<60keV), the electrons (holes) mainly traverse the detector in almost full length in case of cathode incidence (anode incidence). As shown in Fig. 2, the full width at half maximum (FWHM) of the 59.5keV photo peak before irradiation is 8keV, while the FWHM of the peak after irradiation by 25MeV protons is 18keV. In Fig. 3, FWHM of the 59.5keV peak before irradiation is 6keV, while the FWHM of the peak after irradiation is 13keV. It becomes thus evident that the detector has been damaged seriously by 25MeV proton irradiation. It can be clearly observed in fig. 2 that both of the 59.5keV peak and the low energy X-ray peak were deteriorated by irradiation by 25MeV protons because the values of the $\mu\tau$ products of electrons were largely changed by the irradiation, as shown in Table 1. In fig. 3, only the 59.5keV peak was deteriorated by irradiation of 25MeV protons, and the low energy X-ray peak was almost unchanged before and after irradiation. Since the energies of photo electrons induced by the low energy X-rays are completely absorbed in the near-surface region of the detector, displacement of holes mainly affects the shape of the low energy X-ray peak in fig. 3. Therefor, so far as the values of $\mu\tau$ product for holes were almost unchanged by the irradiation, it is natural that the low energy X-ray peak in Fig. 3 was kept unchanged. On the contrary photo electron energies accompanying the 59.5keV γ-rays are absorbed in the entire

region of the detector, and displacement of both electrons and holes contribute to the shape of the 59.5keV peak. Therefor, the 59.5keV peak in Fig. 3 was deteriorated by irradiating 25MeV protons due to the largely changed $\mu\tau$ values of electrons.

Acknowledgement

We would like to express our gratitude to the staffs of CYRIC in Tohoku Univ.

References

1) Deich V. and Roth M., Instrum Nucl., Methods, A380, p. 169, (1996).
2) Saito F., Hitomi K., Murayama T., Shoji T., Suehiro T. and Hiratate Y., Extended Abstracts (The 45th Spring Meeting, 1998); The Japan Society of Applied Physics and Related Societies, p. 123, (1998).

Table 1. Results of $\mu\tau$ measurement before and after irradiation.

	$\mu\ \tau$ products (cm^2/V)	
	electron	hole
Before Irradiation	3.2×10^{-6}	9.3×10^{-6}
After Irradiation	1.0×10^{-6}	7.4×10^{-6}

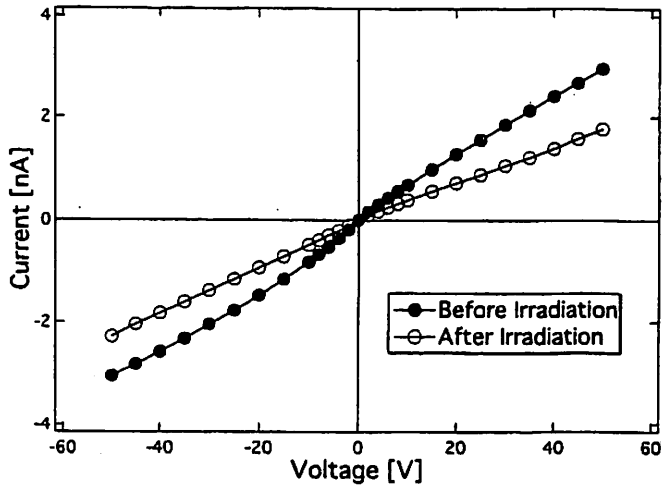

Figure 1. Voltage-current characteristics of the TlBr detector before and after irradiation.

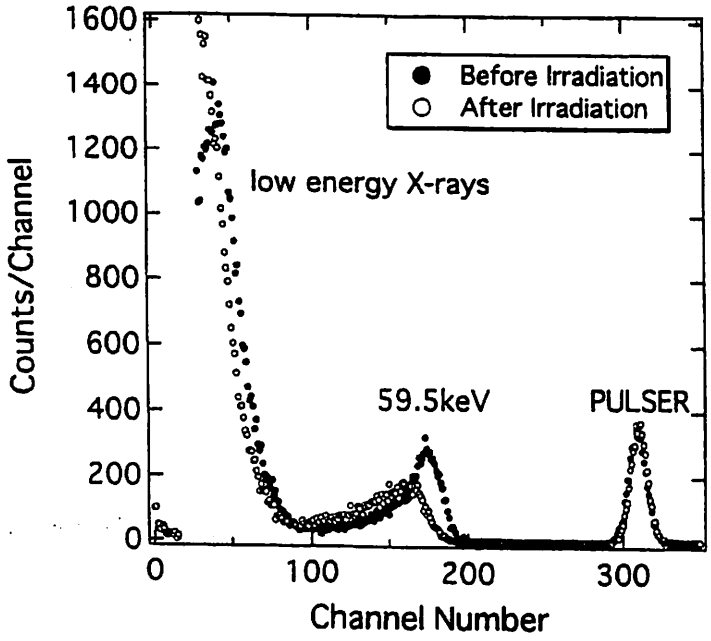

Figure 2. The spectrometric responses for ^{241}Am γ-rays of the TlBr detector with the γ-rays incident on the cathode.

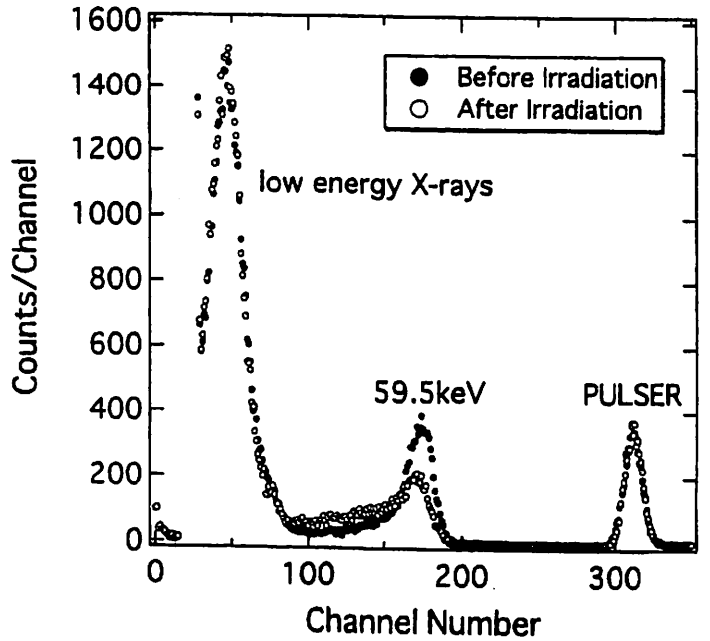

Figure 3. The spectrometric responses for ^{241}Am γ-rays of the TlBr detector with the γ-rays incident on the anode.

II. CHEMISTRY

II. 1. Analysis of Coagulation Processes of Tc(IV) Colloids in Aqueous Solutions

Sekine, T., Kino, S., Kino, Y. and Kudo, H.

Department of Chemistry, Graduate School of Science, Tohoku University

Introduction

Migration of ^{99}Tc ($t_{1/2}$ = 2.1 × 10^5 y) from a nuclear waste repository in deep underground is an important subject to environmental research[1]. In deep groundwater under reducing conditions, pertechnetate is reduced to Tc(IV) in the chemical form of $TcO(OH)_2$ (aq) at neutral pH. It has been suggested that if the concentration of technetium exceeds the solubility of $TcO_2 \cdot nH_2O$ (solid), real-colloids of Tc(IV) is formed[2]. In addition to the formation of real-colloids, aqueous Tc(IV) is adsorbed on naturally occurring colloid particles in groundwater, giving pseudo-colloids owing to the strong adsorption properties of aqueous Tc(IV)[3,4]. However, little attention has been paid to the colloidal technetium species and knowledge on the formation as well as the stability of its real-colloids or pseudo-colloids in aqueous solutions is limited.

We have reported the formation of Tc(IV) colloids by reduction of pertechnetate with stannous ions[5]. The growth of the particle size of Tc(IV) colloids with time was observed in aqueous solutions by means of laser induced photoacoustic spectroscopy (LPAS). In this report, we describe details of the growth of Tc(IV) colloids formed from pertechnetate, with emphasis on the coagulation process. The feature of colloid particle growth is explained by a particle collision model based on the DLVO (Derjaguin-Landau-Verwey-Overbeek) theory.

Experimental

Ammonium pertechnetate ($NH_4{}^{99}TcO_4$) from the Radiochemical Center, Amersham, was used after labeling with ^{95m}Tc ($t_{1/2}$=61 d) which was produced by the $^{93}Nb(\alpha, 2n)\ ^{95m}Tc$ reaction at the Cyclotron Radioisotope Center, Tohoku University[6].

The concentration of the pertechnetate ion was chosen as $6 \cdot 10^{-5}$ mol·L^{-1}. To a pertechnetate solution, an aliquot of stannous chloride solution freshly prepared was added under stirring. The amount of the stannous ion was kept slightly smaller than that needed for the complete reduction of pertechnetate in the solution, to confirm the stoichiometrical reduction of pertechnetate. The pH was kept at 4.4 with a acetate buffer and the ionic strength was adjusted from 10^{-4} to 10^{-1} by changing the buffer concentration. The total amount of

Tc(IV) colloids formed in the solution was determined by ultrafiltration (Ultra Filter UK-10, Toyo Roshi Kaisha, Ltd.).

Figure 1 shows a sketch of the experimental equipment. The test tube containing the Tc(IV) colloid solution was set in front of an NaI(Tl) scintillation detector that was covered with lead blocks with slit width of 5 mm. The ^{95m}Tc γ-rays through the slit was continuously monitored. If the particle size is large enough, the sedimentation of Tc(IV) colloids started and the counting rate decreased with increasing time, as shown in Fig. 2. When the counting rate decreased to the background level, the test tube was gently shaken to redisperse the Tc(IV) colloids, and the counting was started again. This procedure was repeated, and the sedimentation velocity was obtained by the differential analysis of the decrease in counting rate with time (Fig.2).

A relationship between the average size of colloid particles and their sedimentation velocity in solutions is given by the Stokes' law as,

$$V_t = \frac{(\rho_p - \rho_f)\, g\, d^2}{18\,\eta}, \qquad (1)$$

where V_t is the sedimentation velocity ($m \cdot s^{-1}$), g the gravitational acceleration (9.8 $N \cdot kg^{-1}$), d the particle size (diameter, m), η the coefficient of medium viscosity (0.01 $N \cdot s \cdot m^{-2}$), and ρ_p and ρ_f (1.0 $kg \cdot m^{-3}$) are the density of particles and medium, respectively. Thus, the average size of the Tc(IV) colloids was evaluated as a function of the standing time at the prescribed ionic strength of the solution. However, the density of Tc(IV) colloids (ρ_p) was difficult to estimate exactly from two reasons; contamination of technetium hydroxide with tin(IV) oxide and a change of its structure after the preparation. In this calculation, we made an assumption that the density of colloids did not change throughout the observation period. It may cause an ambiguity on the calculation of particle size by using Eq.(1) because the density change of Tc(IV) colloids was unknown. We adopted the value of ρ_p as 3.02 of TcO_2 (crystal)[7] as rough approximation, which gave an error within 60% in the calculation of diameter.

Results and Discussion

Formation and Stability of Tc(IV) colloids

The particle size evaluated by Eq.(1) is plotted against the standing time in Fig. 3 for the solutions with different ionic strength. When the ionic strength of the solution was larger than 10^{-4}, the size was comparatively large (larger than 1 μm) even just after the formation by reduction. Under such high ionic strength conditions, the size was rapidly enlarged and the Tc(IV) became precipitate within 2 days. The gradual increase of particle sizes within the size of 1 μm was observed only at ionic strength 10^{-4}. Further analysis of the Tc(IV) colloids in this case by TEM is in progress, and will be reported as well as information of their composition.

Important information on the particle growing processes of Tc(IV) colloids was given from the determination of amount of Tc(IV) colloids by ultrafiltration. Figure 4 shows the results for the solution of 10^{-4} of ionic strength. We note at first that the amount of pertechnetate reduced was stoichiometrically consistent with the amount of stannous ions added, and second, that the amount of Tc(IV) formed was constant independent of the standing time. The fact indicates that Tc(IV) colloids are formed at the moment of addition of stannous ions, and further reduction to feed Tc(IV), which may cause the particle growth, does not occur. Namely, the main process of particle growth of Tc(IV) colloids should be attributed to coagulation of particles which are originally formed by reduction of pertechnetate in solution.

Analysis of coagulation of Tc(IV) colloid particles

A particle collision model or the DLVO (Derjaguin-Landau-Verwey-Overbeek) theory[8] is used to explain coagulation of colloids. The theory is based on the short range attraction inside the repulsive Coulomb barrier, ΔE. We applied the following model to explain the growth of Tc(IV) colloids as an example.

To solve the problem practically, we assume the Maxwell-Boltzmann distribution

$$P(v) = \sqrt{\frac{2}{\pi}}\left(\frac{m}{kT}\right)^{\frac{3}{2}} v^2 \exp\left(-\frac{mv^2}{2kT}\right), \tag{2}$$

for the number of colloid particles with kinetic energy $E = m\,v^2 / 2$, where m, v are particle weight and velocity, respectively, and k the Boltzmann constant, T the temperature. It is reasonable to consider that the particles with kinetic energy high enough to exceed the barrier can coagulate each other in collision from the DLVO theory.

The number of particles, N, in the unit volume of solution is given by

$$N = \frac{CM}{m} = \frac{3CM}{4\pi a^3 \rho_p}, \tag{3}$$

where C is the mole concentration, M the molecular weight, a the particle radius and ρ_p the density of colloid particles. From Eq.(3) the differential change in the number of particles dN/dt is given by

$$\frac{dN}{dt} = -\frac{9CM}{4\pi a^4 \rho_p}\frac{da}{dt}. \tag{4}$$

On the other hand, since a decrease of the number of particles is due to coagulation of the colloid particles, dN/dt is also given by

$$\frac{dN}{dt} = -\int_{v_x}^{\infty} v_c N \sigma(v) P(v) dv, \tag{5}$$

where, $v_x = \sqrt{\frac{2\Delta E}{m}}$ is the minimum velocity which exceeds the barrier, $\sigma(v)$ the coagulation cross section described below and v_c the relative velocity between the two particles. For the value of v_c, we actually use $\sqrt{2}\,v$, which is averaged over the collision angle.

Because the strong attractive potential in DLVO potential exists near the surface of the particles, we have to take the centrifugal barrier into account in addition to the DLVO interaction. The centrifugal potential $V_{cen}(r)$ is given by

$$V_{cen}(r) = \frac{(\mu b v_c)^2}{2\mu}\frac{1}{r^2} = E\frac{b^2}{r^2}, \tag{6}$$

where $\mu = m/2$ is the reduced mass of two particles, b the impact parameter, r the distance between two particles. Note here, $E = mv^2/2 = \mu v_c^2/2$. Setting $r = 2a$ in Eq.(6), the total barrier between the two particles is estimated at $\Delta E + E\cdot b^2/(4a^2)$. The following condition needs to be satisfied in order that coagulation takes place.

$$\Delta E + E\frac{b^2}{4a^2} \le E, \tag{7}$$

and then

$$\pi b^2 \le 4\pi a^2\left(1 - \frac{\Delta E}{E}\right). \tag{8}$$

Here, $4\pi a^2$ corresponds to the geometrical cross section. If the kinetic energy is the same as ΔE, only a head-on reaction takes place. Otherwise, if the kinetic energy is high enough, a peripheral reaction is also possible. Therefore, it is appropriate to assume the coagulation cross section as

$$\sigma(v) = 4\pi a^2\left(1 - \frac{\Delta E}{E}\right). \tag{9}$$

From above Eqs. we have

$$-\frac{9CM}{4\pi a^4 \rho_p}\frac{da}{dt} = -\int_{v_x}^{\infty} \sqrt{2}v\frac{3CM}{4\pi a^3\rho_p}\sigma(v)\sqrt{\frac{2}{\pi}}\left(\frac{m}{kT}\right)^{\frac{3}{2}}v^2\exp\left(-\frac{mv^2}{2kT}\right)dv. \tag{10}$$

With analytical integration for the integral term in Eq.(10), we reach the following differential equation for the particle radius

$$\frac{da}{dt} = \frac{2\sqrt{3}}{\pi}\frac{CM\sqrt{kT}}{\rho_p^{3/2}}\exp\left(-\frac{\Delta E}{kT}\right)a^{-3/2}. \tag{11}$$

We can solve the Eq.(11) numerically to simulate the growth of colloid particles.

The fitting was performed on the experimental results for the gradual coagulation at 10^{-4} of ionic strength, because the size of particles at higher ionic strength was too large; so-

called precipitate would give ambiguities to fitting with the above mentioned model. In the fitting, we have set the density of Tc(IV) colloids as a constant irrespective to the particle growth. The χ-square fit was made using the Hamaker coefficient and the surface potential involved in the DLVO interaction as the fitting parameters. In practical calculations, a choice of these parameters was strongly limited, because of the non-linearity of the equation and the singularity at $a = 0$. The results of fitting are shown as a solid line in Fig. 5, together with the experimental data. The Hamaker coefficient was obtained as $1.8 \cdot 10^{-19}$ J and the surface potential was 24 mV. These values seem reasonable compared with generally accepted for other kind of colloids[9]. Although density and surface potential were assumed to be constant irrespective of the particle sizes in the calculation, the solid line in Fig. 5 shows it reliable to explain the growth of Tc(IV) colloid particles through coagulation.

Conclusion

By applying the DLVO theory to analysis of experimental data, the growth of Tc(IV) colloid particles was found to proceed through coagulation of small particles. Namely, the coagulation took place between two small particles whose kinetic energy was larger than the potential barrier.

Acknowledgment

The authors acknowledge to the crew of Cyclotron Radioisotope Center, Tohoku University, for their assistance in irradiation.

References

1) In : *Technetium in the Environment.* eds. Desmet, G. and Myttenaere, C., Elsevier, London/New York, 1986.
2) Rard, J. A. : In : Lawrence Livermore Nat. Lab. Report UCRL-53440, 1983.
3) Lieser, K. H., Gleistsmann, B., Steinkopff, Th. : *Radiochim. Acta*, **40**, 33 (1986).
4) Lieser K. H., Bauscher Ch. : *ibid.*, **42**, 205 (1987).
5) Naito, S., Sekine, T., Kino, Y., Kudo, H :" 6th International Conference on the Chemistry and Migration Behavior of Actinides and Fission Products in the Geosphere (Migration '97)", Oct.26 - 31, 1997, Sendai, Japan, Abs. No. A5-01.
6) Sekine, T., Konishi, M., Kudo, H., Tagami, K. and Uchida, S. : *J. Radioanal. Nucl. Chem., Articles*, in press.
7) Rogers, D. B., Shannon, R. D., Sleight, A. W., Gillson, J.L. : *Inorg. Chem.*, **8**, 841 (1969).
8) Hunter, R.J.: In : *Foundations of Colloid Science.* Vol. 1., Oxford Univ. Press, (Clarendon), London/New York, 1986.
9) Visser, J. : *Adv. Colloid Interface Sci.*, 3, 331 (1972).

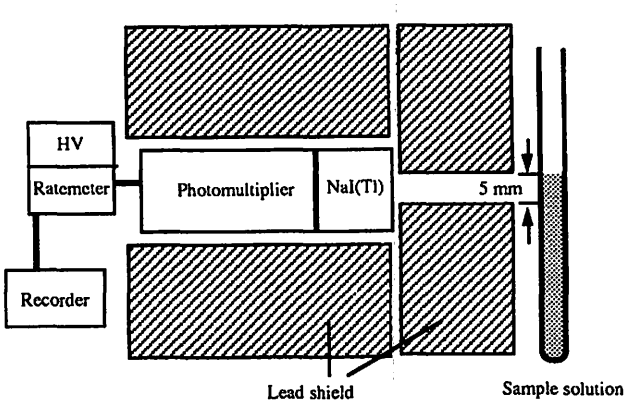

Fig. 1 A schematic illustration of experimental setup to observe the sedimentation velocity of the Tc(IV) colloids labeled with ^{95m}Tc.

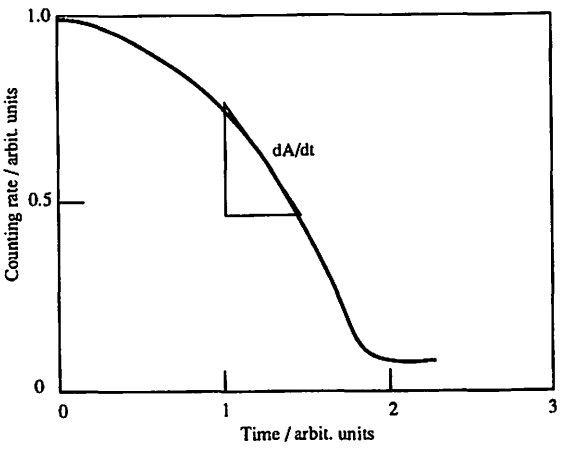

Fig. 2 The shape of the decrease of the counting rate by sedimentation of the Tc(IV) colloids against standing time.

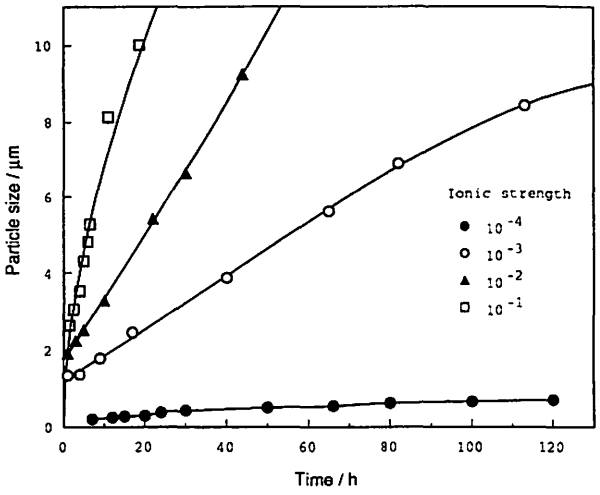

Fig. 3 Change of Tc(IV) colloid particle size given by Eq.(1) for the Tc(IV) colloids solutions (pH 4.4) with different ionic strengths. The initial concentration of pertechnetate was $6 \cdot 10^{-5}$ mol·L^{-1}. Ionic strength ; ● 10^{-4}, ○ 10^{-3}, ▲ 10^{-2}, □ 10^{-1}.

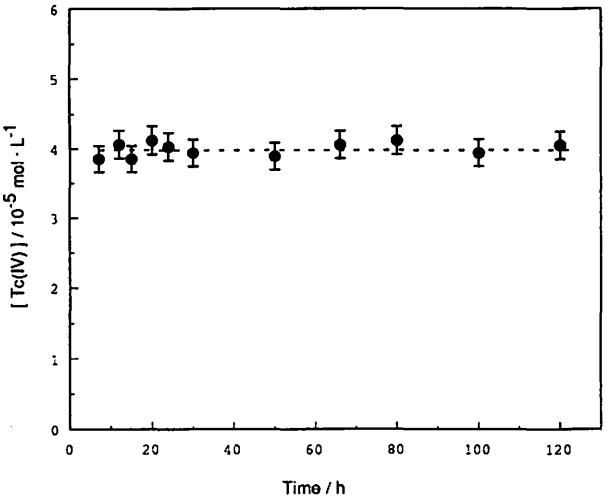

Fig. 4 Amount of Tc(IV) colloids formed in the aqueous solution (pH 4.4, Ionic strength 10^{-4}).

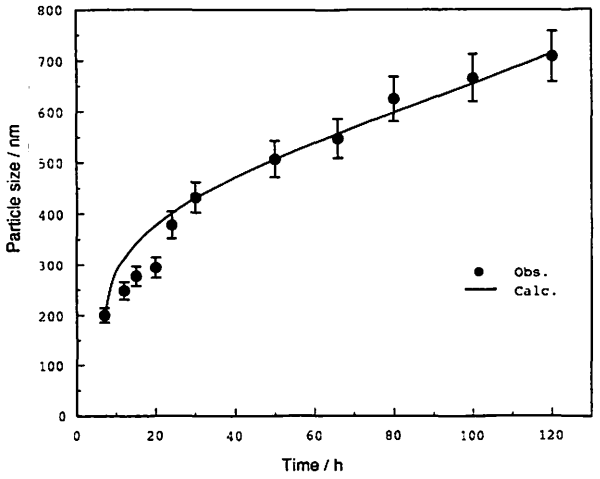

Fig. 5 Size of Tc(IV) colloid particles in aqueous solution (pH 4.4, ionic strength 10^{-4}) against standing time. Data in the figure are the averaged values for 5 times experiments. The solid line is the result calculated based on the coagulation model described in the text (the Hamaker coefficient $1.8 \cdot 10^{-19}$ J, the surface potential 24 mV).

II. 2. Preparation of Thin Polycarbonate Film and Its Application to PIXE Analysis of Anionic Elements in Water Samples

Yamazaki H., Tsutsumi K., Ishii K., Matsuyama S., Murozono K., Inoue J., Iwasaki S., and Orihara H.*

Department of Quantum Science and Energy Engineering, Tohoku University
*Cyclotron and Radioisotope Center, Tohoku University **

Introduction

Owing to great awareness of a pollution problem in natural environment, composition of rain and surface water has been studied for many years. In our previous papers[1,2], a combination of chelation by dibenzyldithiocarbamate (DBDTC) ions with subsequent condensation into dibenzylidene-*D*-sorbitol (DBS) gels has been developed for preconcentration of heavy metals in water samples, in conjunction with rapid preparation of thin uniform targets containing zirconium as an internal standard for PIXE analysis. The methodology was applied to monitor time variation of heavy-metal concentrations in drinking water. Chromium(VI) and arsenic(V) are anionic species of great interest in quality of water to drink. Due to high sensitivity of PIXE analysis, it looks a promising target preparation to deposit a small volume of water sample containing anionic species of interest on a thin backing film, which should be as free as possible of trace elements and as thin as possible, commensurate with retaining sufficient strength for sample deposition and subsequent irradiation. Moreover, an acid-resistant film is preferable because an acidic solution of metal rare in environment can be used as an internal standard in targets for the PIXE analysis.

Carbon foils, which are very thin material among commercially-available backings, are little used now partly because of expense and variability in their impurity elements. Some commercially available polymer films, *e.g.*, polyimides Kapton and polyesters Mylar, are widely used as support films. These films produce a strong continuum X-ray background due to their thickness of more than 1mg/cm^2. User-made polymer films such as polystyrene and polyvinyl formal are used widely and offer the lowest continuum background[3,4]. On the other hand, preparation of these films requires much skill and is time-consuming, resulting in a general decline of use of the user-made films in PIXE. Iwata et al. developed a simple preparation technique for thin Formvar film[5]. As expected from chemical property of Formvar, however, it is not allowed to deposit acidic sample solutions on its surface.

In this study, we have developed a simple preparation method for acid-resistant polycarbonate film referring to procedure reported by Iwata *et al*[5].; the thin film was created

by dropping a polycarbonate solution on a sucrose solution. The films with thickness of around 0.1- 0.3 mg/cm^2 offer a good combination of mechanical strength and low continuum backgrounds, and are used as a target backing in the PIXE analysis of anions (sulfate, chromic salt and arsenate) in a wide concentraion range (10-2000 ppb).

Experimental

Reagents

Poly(Bisphenol A carbonate) of an extra pure reagent of molecular weight of around 64000 (Aldrich, No.18162-5) was used. Sucrose used was a reagent for the density gradient centrifugation method (Wako Pure Chemical Industries). Chloroform and benzene are specially prepared reagents for spectrophotometry (Dojindo). All the other chemicals used are the highest purity grade with low metal content obtained from Wako Pure Chemical Industries, Ltd. A doubly distilled Milli-Q water was used in all chemical procedures.

Preparation of the polycarbonate film

25 cm^3 of 50 wt% sucrose aqueous solution were placed in a Teflon dish (80 mm diameter) and a Mylar target frame (30mm width × 40mm length × 0.5 mm thick) with a round opening of 20-mm diameter was floated on the solution. For preparation of a casting solution, 0.5 wt% solution of polycarbonate in chloroform was diluted by a factor of two to three with benzene just before use; benzene was added for controlling volatility of the chloroform solvent. As chloroform and benzene are hazardous for human health, an equipment for ventilation is quite necessary. A thin film was created by slowly dropping 0.20-0.32 cm^3 of the polycarbonate solution on a surface of 3.14-cm^2 aperture of target frames floating on the sucrose solution. Films mounted on the aperture of target frames were picked up from the sucrose solution and after washing, were dried over silica gel. Thickness of the prepared polycarbonate film was calculated to be 0.14 to 0.37 mg/cm^2 by assuming uniform spread of the casting solution on the surface of sucrose solution within the round opening of target frame floating on the solution.

PIXE analysis of standard targets of anions

Standard targets were prepared by micropipetting onto the polycarbonate films 100 μl of test solution containing known amounts of each of SO_4^{2-}, $Cr_2O_7^{2-}$, and AsO_4^{3-} in addition to 1 ppm of Ga^{3+} as an internal standard; 20 μl of the solution were deposited on the film five times after dried in an oven at 60 °C using a micropipett that was calibrated to a precision of ± 0.7 %, and consequently, the amount of elements was totally added with a precision of ±1.6 %. The specimen formed had a spot of around 3-mm diameter. The test solutions were made up from standard solutions of the certified concentrations (1.00 mg/ml) for either atomic absorption spectrophotometry or ion chromatography. Gallium can serve as a suitable

internal standard, because it is a rare element in natural water and its characteristic X-rays rarely interfere with these of elements of interest.

The target was bombarded in vacuum by 3 MeV protons (apparent current, 5nA; beam diameter, 2mm) fom the 4.5-MV Dynamitron of Tohoku University[6]. In this system, X-rays from targets pass through a 120 μm polyethylene sheet and are measured with a Si(Li) detector (4-mm diam. crystal with 25 μm Be window) which viewed the target position at 90 deg with respect to the beam axis. A least-squares fitting computer program, named SAPIX,[7] was used for the X-ray spectrometry.

Results and Discussion

Preparation of the polycarbonate film and its properties

Poly(bisphenol A carbonate) is insoluble in water, so it must be dissolved in an organic solvent. Chloroform is known to be the only solvent which can dissolve poly(bisphenol A carbonate) pellets. Iwata *et al.* reported that the best formation of polyvinylformal (PVF) film is achieved at 0.5-1.0 % PVF in tetrahydrofuran spreaded on 50 % sucrose solution (density = 1.23 g/cm^3)[5]. A solution of polycarbonate (0.5 wt%) in chloroform was chosen because of the same density of poly(bisphenol A carbonate) (1.20 g/cm^3) as that of PVF (1.23 g/cm^3); 50 mg of poly(bisphenol A carbonate) pellets were dissolved into 10 g of chloroform solvent keeping in dark overnight. An attempt was made to creat a uniform film in a 20-mm round opening of Mylar target frame floating on sucrose aqueous solution (50 wt%) in a Teflon dish. Although density, viscosity and surface tension of chloroform are small, this solvent can not spread out polycarbonate uniformly on the water surface. This might be due to extremely high volatility of the solvent. Benzene is freely miscible with chloroform and has lower volatility. Then the polycarbonate solution was diluted by a factor of two to four with benzene. No sedimentation of polycarbonate was observed in the mixed solvent, and this mixture was used as a casting solution for the film-preparation. As stability of polycarbonate in the mixed solvent is not completely confirmed, however, the polycarbonate in chloroform was diluted with benzene just before use. Except for the polycarbonate solution diluted to four times in volume, a uniform film was created in the aperture of Mylar target frame by slowly dropping more than 0.2 cm^3 of the casting solution on the water surface. After picking up the target frame with a thin polycarbonate film from aqueous sucrose solution, water washing easily removed the sucrose solution adhering to the film. The film obtained is mechanically strong enough to use as a backing for targets in PIXE analysis. As shown in Fig.1, a continuum X-ray background is observed upto around 7 keV, but there is no peak indicating existence of impurities. Traces of Fe and Br impurities are detected in a commercial polycarbonate film.

Figure 2 shows the results of 6-μC irradiation of prepared polycarbonate films of different thickness, which is calculated by assuming uniform spread of the casting solution on the surface of sucrose aqueous solution within the aperture of target frames floating on the

solution. Intensity of the bremsstrahlungs integrated over an energy interval of 1-6 keV is plotted as the ordinate. A linear relationship is obtained between the calculated thickness and the bremsstrahlung intensity, and holds on a nuclepore filter of nominal thickness of 1.0 mg/cm^2. Two films, which are made independently under the same condition, give an approximately equal bremsstrahlung background; this was examined at two different thicknesses (0.14 and 0.27 mg/cm^2). Although not shown in Fig. 2, the bremsstrahlung intensity does not change beyond ± 12 % at three different points of an identical film. These findings indicate that the prepared films have good uniformity and the thickness is not so different from the calculated values. In a test of durability of the prepared polycarbonate films, a small amount (0.1 cm^3) of strong acid (1M HCl and HNO_3) and 1M Na_2CO_3 solution was dropped on the films and evaporated in an oven at 60 ° C. No deterioration of the films was observed irrespective of the thickness, indicating good chemical stability of the prepared polycarbonate films.

Calibration curves using matrices of known compositions

In order to evaluate reliability of the quantitative PIXE analysis for samples deposited on polycarbonate films, calibration curves were measured for 3-μC accumulated charges using 0.1 cm^3 of the test solutions (pH 1) containing 1ppm Ga^{3+} as an internal standard. The measurement covered the concentration range from 10 to1000 ppb for $Cr_2O_7^{2-}$ and AsO_4^{3-}, and from 20 to 2000 ppb for SO_4^{2-}.

Figure 3 shows the results for the calibration measurements; the experimental concentration (C_{exp}) is plotted against the nominal one (C_{th}). The straight line corresponds to the relation of $C_{ex} = C_{th}$. The experimental concentration is determined from the formula

$$C_E = \frac{N_E}{N_{Ga}} \times \frac{(\sigma\gamma\varepsilon\eta)_{Ga}}{(\sigma\gamma\varepsilon\eta)_E} \times \frac{A_E}{A_{Ga}} \times C_{Ga} \ ,$$

where C represents the elemental concentration in sample solutions [ppb], N is the number of photons in characteristic peaks for 3μC of accumulated charges, A is atomic weights, σ is total K-shell X-ray production cross-sections for 3 MeV protons, ε is correction factors for the relative intensities of multiplets in the characteristic X-ray spectrum, ε is the detection efficiency of 5 mm-thick Si(Li) detector with 25 μm-thick beryllium window, which has been determined in the X-ray energy range of 2-60 keV, η is linear attenuation coefficient of 120 μm polyethylene absorber, and the subscripts of Ga and E are used to designate Ga^{3+}-internal standard and the elements of interest, respectively. The σ- and γ-values for each characteristic X-ray were obtained from the text book by S. A. E. Johansson and J. L. Campbell[8], and the

attenuation coefficients were quoted from the text book by K. Debertin and R. G. Helmer[9]. The differences between the nominal and the analyzed concentrations seldom exceed ± 15 % in the wide concentration range, although around 40% deviation is observed in the case of 10 ppb AsO_4^{3-} probably due to inhomogeneity of the target caused by multiple deposition of the test solution on the film. A relatively good accuracy in the PIXE analysis reveals reliability of the X-ray production cross-sections cited in the literature[8]. Moreover, the PIXE measurement of samples containing an internal standard enables the quantitative analysis of anionic elements in water without exact knowledge of the analytical arrangement of PIXE setup used. The limit of quality of water to drink is < 50 ppb for Cr(VI) and < 10 ppb for As(V). It is clear from this figure that these low concentrations can be determined without any preconcentration by means of the PIXE measrement for targets which are prepared by depositing a small amount of water sample directly onto thin polycarbonate films of low continuum X-ray backgrounds.

Table 1 shows the reproducibility of the PIXE analysis for $Cr_2O_7^{2-}$. These samples were individually prepared under the same condition. The counts in Ga K_α-peak varied two times among the samples, even though all samples contained an equal amount of Ga^{3+}-internal standard. This probably is ascribed to the fact that a different portion of the deposit on a film was irradiated by proton beams of 3 mm-diameter spot due to shift of the deposit from the center of the film mounted on the aperture (20 mm diameter) of Mylar target frame. As cited in this table, however, counts in the Cr K_α-peak which are normalized by ones in the Ga K_α-peak give the results in agreement with the nominal concentrations; the deviation is smaller than ± 13 %. This fact indicates reliability of the PIXE analysis for the deposited targets containing an internal standard.

In conclusion, thin polycarbonate films, which were prepared by dropping the casting solution on the surface of an aqueous sucrose solution, offer a good combination of mechanical strength, chemical stability and low continuum backgrounds. The concentrations of SO_4^{2-}, $Cr_2O_7^{2-}$ and AsO_4^{3-} were determined in the range from 10 to 2000 ppb by the PIXE measurement of the targets which were prepared by means of depositing 100 μl of the test solutions containing Ga^{3+}-internal standard onto the films.

References

1) Yamazaki H. et al., *Int. J. PIXE,* **6** (No. 3 & 4), 471 (1996).
2) Yamazaki H. et al., submitted for publication in *Int. J. PIXE.*
3) Campbell J. L., *Nucl. Instr. and Meth.*, **142**, 263 (1977).
4) Russell S. B., Schulte C. W., Faig S. and Campbell J. L., *Anal. Chem,* **53**, 571 (1981).
5) Iwata Y. et al., *Int. J. PIXE,* **2** (No.3), 381 (1992). 0
6) Iwasaki S. et al., *Int. J. PIXE,* **6** (no.1&2), 117 (1996).
7) Private communication from Dr. Sera K., (Cyclotron Research Center, Iwate Medical University, Takizawa 020-01, Jpn.).

8) Johansson S. A. E. and Campbell J. L., "*P I X E. A Novel Technique for Elemental Analysis,*" John Wiley & Sons, New York (1988), 313-329.
9) Debertin K. and Helmer R. G., "*GAMMA- AND X-RAY SPECTROMETRY WITH SEMICONDUCTOR DETECTORS,*" Elsevier Science Publishers B. V., (1988), 339-344.

Table 1. Reproducibility of the PIXE analysis for targets ($Cr_2O_7^{2-}$) deposited on films

Nominal concentration [ppb][1)]	Measured concentration [ppb]			
1000	962 ± 32[2)]	1074 ± 89	1003 ± 45	-
400	407 ± 10	392 ± 19	421 ± 20	396 ± 12
40	38 ± 3	45 ± 2	42 ± 3	-

1): ±1.6 % error due to dilution of stocked solutions of the metals. 2): the statistical deviations of the characteristic X-ray yields.

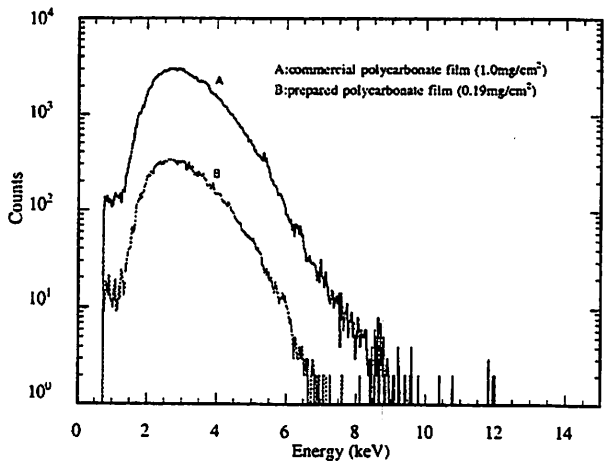

Fig. 1. PIXE spectra of the prepared and the commercial polycarbonate films irradiated by 6μC of 3 MeV protons.

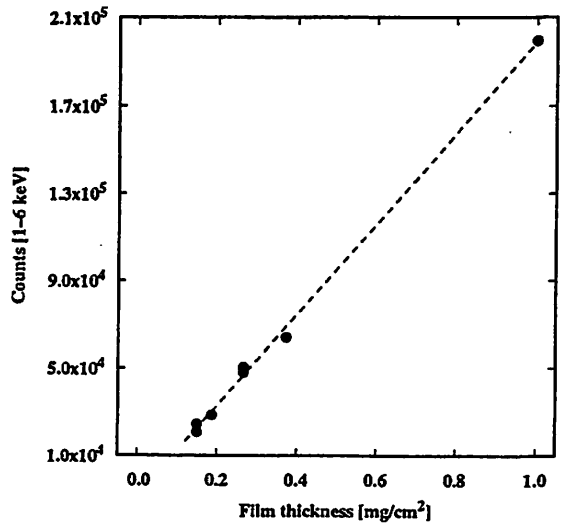

Fig. 2. Bremsstrahlung intensity of various film thickness for 6-μC irradiation.

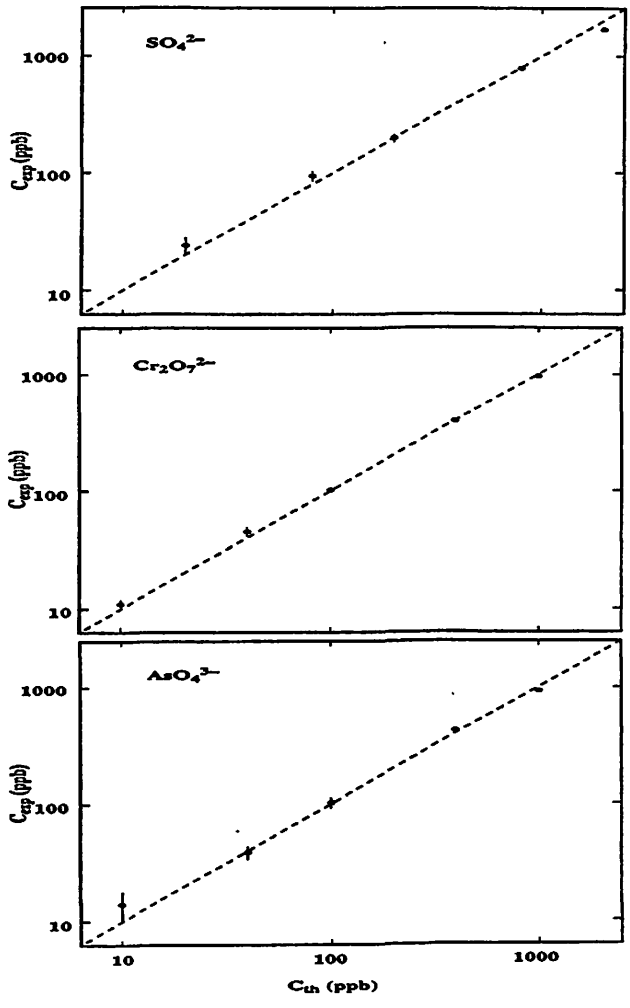

Fig. 3. Experimental results (C_{exp}, ppb) versus nominal concentrations (C_{th}, ppb) for calibration measurements of anionic species.

II. 3. Determination of Heavy-Metal Concentrations in Water by PIXE Analysis Using Zirconium as an Internal Standard

*Yamazaki H., Tanaka M., Tsutsumi K., Ishii K., Matsuyama S., Inoue J., Murozono K., Iwasaki S., and Orihara H.**

Department of Quantum Science and Energy Engineering, Tohoku University
*Cyclotron and Radioisotope Center, Tohoku University**

Introduction

Owing to great awareness of a pollution problem in natural environment, composition of rain and surface water has been often analyzed for many years by atomic absorption spectrophotometry (AAS). Particle-induced X-ray emission (PIXE) has been used extensively for analyzing aerosol samples and offered higher sensitivity (nano-gram level) than AAS measurements[1-5]. However, little work has been reported on the PIXE analysis of water samples due to problems of sample preparation[6-7]. Since PIXE is conveniently used for analysis of thin uniform samples, metals in aqueous samples should be concentrated into a thin solid-target of uniform composition, *i.e.,* some chemical treatment is required for the target preparation in PIXE measurements.

In a preceding paper[8], a combination of chelation by dibenzyldithiocarbamate (DBDTC) ions with subsequent condensation into dibenzylidene-*D*-sorbitol (DBS) gels has been developed for preconcentration of heavy metals (Fe^{3+},Co^{2+},Hg^{2+}) in conjunction with rapid preparation of thin uniform targets for PIXE analysis. The DBS gels containing the metals in solutions are then collected on a nuclepore filter for direct irradiation by 3 MeV protons in a system of vertical beam type in-air PIXE at 4.5-MV Dynamitron laboratory of Tohoku University. Details of the system was described in Reference 9. At present, proportionality of the beam current *vs.* X-ray yields was confirmed to be good, but the absolute value of the impinging beam current has remained uncertain. In order to maintain high quality of the PIXE analysis, it is necessary not only to procure the accurate value of impinging beam current but also to calibrate the detection efficiency of the analytical system at regular intervals. Use of an internal standard in the PIXE analysis enables determination of the absolute concentrations of metals from the elemental X-ray yields without exact knowledge both of the surface density of incident protons and of the measuring arrangement. However, we can find few reports on a metal-preconcentration procedure using an internal standard for the PIXE analysis. This is probably ascribed to the difficulty in preparing thin target specimens containing homogeneously an internal standard element.

In this study, elemental reactions in the preconcentration step (the metal-DBDTC complex formation and condensation into DBS gels) are optimized to contain the internal standard of zirconium in target specimens. The modified preconcentration procedure is applied to preparation of targets obtained from solutions containing seven heavy metals (Fe, Co, Ni, Cu, Cd, Hg, Pb) in different amounts, and the accuracy in determination of the metal-concentraions in the 5-100 ppb range is examined on the present in-air PIXE setup of our laboratory.

Preparation of targets with Zr internal standard

In the preceding paper[8], the following procedure was recommended for preconcentration of metals in the ppb-ppm range: Into 25 ml of a solution containing a heavy metal (4<pH<5), 3.5 moles of DBDTC (1.25 ml of 0.1% (w/v) DBDTC in methanol) were pipetted, and the solution was kept stirred for 4 minutes. After pH of the solution was adjusted to around 5.2 with 1M acetate buffer solution, 0.4 mg of DBS (10μl of 4%(w/v) DBS in dimethylsulfoxide) was added and immediately set to gelation. The metal-DBDTC complexes condensed into the DBS gels were collected under a reduced pressure (~250 mm Hg) on a nuclepore filter (0.2 μm pore) for direct irradiation by proton beams. On the other hand, the filtration was carried out under a reduced pressure of ~400 mm Hg through a nuclepore filter of 0.4 μm pores (10 μm thick and 1×108 pore density) in the present study; the filtration time was shortened to < 3 minutes, and no loss of metals was detected in the filtrates. A thin layer of the gels on the filter (13 mm diameter) was washed with 10 ml of deionized and distilled water and then dried over silica-gel. The filter was mounted on a Mylar holder, which was screwed on a steel slide frame for the direct irradiation.

Zirconium can serve as a suitable internal standard, because it is a rare element in natural water and its characteristic X-rays do not interfere with determination of elements of interest to measure water pollution by PIXE. However, the PIXE analysis shows low sensitivity to zirconium due to the small inner-shell ionization by protons of 2-3 MeV. As compared with the reported concentrations of heavy metals in surface water samples, a large amount of Zr (25 μg) must be used from the standpoint of statistical errors of the Zr-peaks in the PIXE spectrum; under the present condition of the PIXE analysis (3 MeV proton beams of 3-mm diameter and 2 nA of apparent currents), the X-ray yield of Zr atoms in target specimens is around 2000 counts in its K_α peak for 2 μC of accumulated charges. On the other hand, Zr ions are easily hydrolyzed even in strongly acidic solutions[10]. The principal species, which is formed by reversible hydrolysis at concentrations of acid greater than several tenths molar, is a polynuclear $Zr_4(OH)_8^{8+}$. At lower acidity, a slow irreversible hydrolysis occurs, accompanied by an increase in polymerization. Therefore, a standard solution containing 1000 ppm zirconium in 1 M HNO_3 is used, and it is assumed that Zr ions might act as the "yl" ion, ZrO^{2+}, in the chemical reaction with DBDTC ions.

Zr-recovery in the preconcentration step was investigated as a function of the amounts of DBDTC ions; a desired amount of DBDTC ions was added into 25 ml of 1 ppm Co^{2+} solution of pH around 4 and then 25 μl of the standard solution of zirconium in 1000 ppm was pipetted while stirring. The concentrations of Zr and Co ions in the filtrates were determined by spectropho-tometry using arsenazoIII as coloring reagent[11] and by atomic absorption spectrophotometry, respectively. The Co-concentrations in filtrates were lower than the detection limit (0.01 ppm), indicating the quantitative recovery. On the other hand, Table 1 reveals constant but incomplete recoveries of Zr ions (94~96 %), even though a large excess amount of DBDTC ions exists in terms of the stoichiometric DBDTC-complexation of ZrO^{2+} and Co^{2+} ions totally in 0.7 μmole. The Zr-recovery also was examined in sample solutions free from Co ions, but there appeared no improvement of the recovery. These facts suggest a decrease in chemical reactivity of polymerized zirconium species such as $Zr_4(OH)_8^{8+}$.

Figure 1 shows the effect of pH on the recovery of 25μg Zr in preconcentration step of 1 ppm Co solution (25 ml) at 1 pH 5 by the use of 8.5 μmole of DBDTC and 0.4 mg of DBS. The recovery obviously depends on the pH values in sample solutions; the largest recovery (95 ± 1 %) can be obtained only when DBDTC ions are initially added to samples at pH=4 and then Zr-DBDTC complexes are formed at pH around 3. The succeeding changes of pH value to both lower and higher sides ($2 \leq pH \leq 5$) have no effect on the Zr-recovery. There appeared milky turbidity when the DBDTC-solution was added to samples at pH 3, indicating precipitation of carbamic acid due to the small dissociation constants ($2.95 \leq pK_a \leq 5.19$)[12], *i.e.,* an undesirable side reaction of DBDTC ions added to sample solutions. The Zr-recovery slightly decreases in a solution buffered at pH 5. This might be ascribed to slow irreversible hydrolysis of Zr ions accompanied by increase in polymerization to less reactive species.

Based on the results shown in Table 1 and Fig. 1, the following procedure was derived for target preparation: 2.5 ml of 0.1% (w/v) DBDTC solution was added into 25 ml of a sample solution, which is initially neutralized (4 pH 5)and then 25 μl of 1000 ppm Zr in 1M HNO_3 was pipetted as the internal standard. This solution was processed by the same manner as before. The thin layer of DBS gels containing metals and Zr-standard on a nuclepore filter was mounted on a sample holder and ready to be exposed to proton beams.

Table 2 shows the results of the PIXE analysis of four targets independently prepared under the same condition. The counts in Co- and Zr-K_α peaks were normalized to 2μC of accumulated charges. A little bit larger fluctuation appears in the counts of the K_α photons (3.3~4% of standard variation) than in the ratios of Co- to Zr-counts (2.4 % of standard variation). The ratio remains unchanged within the statistical errors of the peak counts for different location of impinging beam spots on the identical target. These facts indicate the

reliability of the PIXE analysis using an internal standard and the reproducibility of preparing the target specimens of uniform composition.

Calibration with using matrices of known compositions

In order to evaluate reliability of the quantitative PIXE analysis through the present system, calibration curves were measured for a multielemental sample of 25 ml containing 25 μg of Zr as an internal standard, which was prepared by adding known and different amounts of seven metals (obtained from atomic absorption spectrophotometry standard solutions) to deionized and distilled water. The seven heavy metals, *viz*, Fe^{3+}, Co^{2+}, Ni^{2+}, Cu^{2+}, Cd^{2+}, Hg^{2+} and Pb^{2+}, were used from the standpoint of an analysis of water quality. The measurement covered the concentration range from 5 to100 ppb of the seven metals.

Typical PIXE spectra of the targets with and without the metals are shown in Fig. 2. The X-rays emitted from excited heavy atoms are superimposed onto a continuum of bremsstrahlungs and γ-ray Compton tails. The continuous components come from the air gap over the targets (0.6 cm), the sample sediments (<10 μm thick) and the nuclepore filter (10 μm thick). The spectrum of the blank, which does not contain the seven metals, reveals no detectable impurities under the experimental condition; no other X-ray peak except K X-rays of S in DBDTC, Ar in air and Zr standard was observed in the blank spectrum. The computer program, named SAPIX,[13] was used in order to separate peaks in the PIXE spectra. In this program, a combination of a polynominal curve and two exponential ones is fitted to the continuous components in the spectrum by the least-squares method. The polynominal curve describes the lower energy side of the bremsstrahlungs, while the two exponential curves express the higher energy side of the bremsstrahlungs and the γ-ray Compton tails. Succeedingly, the peak area of X-rays characteristic to each element is determined by the Gaussian-peak fitting. When the K_β peak of an element Z overlaps with the K_α peak of element Z+1, the counts in K_α peak of the element Z+1 are obtained by substructing the product of the K_α peak counts and the intensity ratio (K_β/K_α) of the element Z[14] from the total counts in the overlapping peak. In this way, the yield of K_α X-ray characteristic to each element can be determined for the irradiated target specimens.

Figure 3 shows calibration curves for the PIXE analyses of the seven heavy metals. The ratio of peak counts of the metals to those of Zr-standard is plotted against the nominal metal concentration in ppb; the counts in K_α X-ray peak are used except for Hg and Pb, where the L_α X-ray yields are used for the analysis. A good linear relationship is obtained between the concentrations and the X-ray yields for all the metals, indicating a good quantitative analysis of these metals in the concentration range of 5-100 ppb by means of the PIXE setup of our laboratory. The use of Zr internal standard can eliminate systematic errors in charge integration of impinging beams and in determination of the geometrical parameters of the analytical arrangement (the distance between target and detector, the solid angle subtended by a beam spot on target at the detector, etc.).

The absolute concentrations of the metals in sample solutions were calcurated from the experimental results in order to evaluate the accuracy of the PIXE analyzing system in our laboratory. Since chelation of DBDTC can be exerted in the same way to almost all of monomeric transition metals[12], the recovery of the seven metals in target preparetion is taken as 100 % except for Zr-standard, for which the constant recovery (95 ± 1 %) is obtained as shown in Table 1 and Fig. 1. Based on the mass attenuation coefficients of X-rays in the energy range from 5 to 20 keV[15], the authors can estimate almost flat efficiency curve for a 5 mm-thick Si(Li) detector of 25 μm-thick beryllium window, along with attenuation less than 4 % due to 0.85 cm of the air gap between the targets and the detector and a 12 μm-thick Kapton film on the beam exit assembly with a built-in detector. Detection efficiency of the analytical system can clearly be assumed to be constant over the X-ray energy region from 5 to 20 keV. Under these conditions, we use the formula

$$C_M = \frac{N_M}{N_{Zr} \cdot \alpha} \times \frac{\sigma_{Zr} \cdot \gamma_{Zr}}{\sigma_M \cdot \gamma_M} \times \frac{A_M}{A_{Zr}} \times C_{Zr} \ , \qquad (1)$$

where C represents the metal concentration in sample solutions [ppb], N is the number of photons in K - or L -peak per 2 μC of accumulated charges, A is the atomic weight of metal, α is total K- or L-shell X-ray production cross-sections for 3 MeV protons [10^{-24} cm^2], α is the correction for the Zr-recovery in preconcentration [1.05 ± 0.01], γ is the correction for the relative intensities of multiplets in PIXE spectrum, and the subscripts of Zr and M are used to designate the zirconium internal standard and the metal of interest, respectively. The values of the physical parameters used in quantification (Table 3) were obtained from the text book by Johansson and Campbell[14].

Table 4 shows the metal concentrations along with the precision from counting statistics under the present arrangement of in-air PIXE system; the impinging beam spot (2 nA of 3 MeV protons) on targets has around 3 mm diameter, and the 5 mm-thick Si(Li) detector of 30 mm^2 area is placed at 135° position and a distance of 30 mm from the target surface. Although there appears rather poor precision in determination of Cd-concentrations due to the low X-ray yield, the concentrations of other metals can be determined with a small statistical deviation (less than ± 7 %). The differences between the nominal and the analyzed concentrations seldom exceed ± 14 % in the concentration range from 5 to 100 ppb. Good accuracy in the PIXE analysis reveals applicability of the X-ray production cross-sections cited in the literature[14]. Moreover, it is clear that the PIXE measurement of targets containing Zr-internal standard enables the quantitative analysis of elements producing X-rays of 5-20

keV without exact knowledge of the beam current and the analytical arrangement of the PIXE setup used.

PIXE analysis of drinking water

As just described, many kinds of heavy metals together with Zr internal standard can be simultaneously concentrated into thin uniform target specimens, and the peak areas in PIXE spectra can be correctly translated into the absolute concentrations in terms of the reported data pertinent to inner shell ionization and subsequent X-ray emission[14]. Hence, the methodology is applied to monitor time variation of heavy metal-concentrations in drinking water.

A sample of drinking water (30 ml) was collected from a faucet in our laboratory at four hour intervals and was chemically treated in the same manner as before. The targets were irradiated by 2 nA of 3 MeV proton beams in the PIXE system, and the spectrum was analyzed by the SAPIX program. The absolute concentrations of detected elements in drinking water were determined in accordance with the equation (1); the values of parameters relevant to the X-ray productions of detected elements were also obtained from the reference (14).

Figure 4 shows the time variation of elemental concentrations in drinking water over 20 hours. The analytical errors based on counting statistics are less than ± 16 % for all elements except As, Br and Pb, for which much larger errors (from ± 38 % to ± 97 %) appear due to overlapping of small peak of As-K_α with that of Pb-L_α X-rays and of As-K_β with the peak of Br-K_α X-rays. Many kinds of elements were detected in the samples of pH 6.8, but the concentrations were within the limit of quality of water to drink; [Mn] < 50 ppb, [Fe] < 300 ppb, [Ni] < 10 ppb, [Cu] and [Zn] < 1000 ppb, [As] < 10 ppb, and [Pb] < 50 ppb[16]. High sensitivity of the PIXE analysis makes it possible to clearly distinguish the change in elemental concentrations in the samples; the concentrations of Mn, Cu and Pb appreciably increase in the second sample (4 hours elapsed) and then decrease slowly, but the other elements have slowly decreasing or rather constant concentrations over the time span. The widespread elemental concentrations in the samples can be detected by PIXE; the concentrations of Zn and Fe are ten to hundred times higher than those of other elements in all samples. Since As and Br exist as anionic species in neutral solutions, these elements can be coprecipitated with metal-DBDTC complexes in the preconcentration step due to low solubility of arsenate or bromate of major transition metals in water.

Conclusion

In this study, the metal-preconcentration procedure was established to prepare a thin uniform target containing Zr as an internal standard for the PIXE analysis. The target preparation and the PIXE measurement are not time-consuming; the target preparation requires less than 10 min, and the peak areas with good statistical precision can be obtained

within 20-min irradiation (2 nA of 3 MeV proton beams) through the present PIXE system of our laboratory. The use of Zr internal standard permits simultaneous determination of seven heavy metals in ppb-concentrations by the PIXE setup without exact knowledge of the integrated charges of impinging beams and the analytical arrangement (the distance between targets and the detector, the solid angle, etc.). The data pertinent to inner shell ionization and subsequent X-ray emission, compiled by Johansson and Campbell[14], are quite useful to translate the elemental X-ray yields in PIXE spectrum into the absolute concentrations in sample solutions. The difference between the PIXE results and the nominal concentrations is found to be less than ± 14 %. No appreciable correction for the detection efficiency and the attenuation of X-rays are needed to obtain absolute values of the concentration of elements producing X-rays of medium energy (5 to 20 keV). However, these corrections are important in analyzing the yields of X-rays having lower (<5 keV) or higher (>20 keV) energy. Moreover, overlapping of peak areas in PIXE spectra makes it uncertain to identify responsible elements. Therefore, it would be preferable to develope a new methodology for the spectrum analysis in order to promote the PIXE analysis to a truly effective means of dealing with many samples of complexity as in monitoring water pollution. Development of a new analyzing method for PIXE spectrum is currently in progress in our laboratory.

References

1) Akselsson K. R., *Nucl. Instr. and Meth.*, **B3**, 425 (1984).
2) Cahill T. A., *Nucl. Instr. and Meth.* **B49**, 345 (1990).
3) Kasahara M., Yoshida K. and Takahashi K., *Nucl. Instr. and Meth.*, **B75**, 240 (1993).
4) Kasahara M., J. H. Park and Yamamoto K., *Nucl. Instr. and Meth.*, B109/110, 471 (1996).
5) Horvath H., Kasahara M. and P. Pesava, *J. Aerosol Sci.*, **27**, 417 (1996).
6) Aprilesi G.,et al., *Nucl. Instr and Meth.*, **B3**, 172 (1984).
7) Tanaka S., Durzi M. and J. W. Winchester, *Environ.* Sci. Technol., **15**, 354 (1981).
8) Yamazaki H., et al., *I. J PIXE.*, **6(3 & 4)**, 483 (1996).
9) Iwasaki S. et al., I. J. PIXE., **6(3 & 4)**, 441 (1996).
10) Baes C. F. Jr. and Mesmer R. E., John Wiley and Sons, Inc. New York (1976), 152.
11) Onishi H., Jpn. Analyst, **12**, 1153 (1963).
12) Hulanicki A., *Talanta*, **14**, 1371 (1967).
13) Private communication from Dr. Sera K. (Cyclotron Reseach Center, Iwate Medical University, Takizawa 020-01, Jpn.)
14) Johansson S. A. E. and Campbell J. L., *"P I X E. A Novel Technique for Elemental Analysis,"* John Wiley & Sons, New York (1988), p.313-329.
15) Leroux J. and Thinh, T. P., *"Revised Tables of X-ray Mass Attenuation Coefficients,"* Corporation Scientifique Claisse Inc., Quebec (1988).
16) "Water Analysis," The Japan Society for Analytical Chemistry, Hokkaido Branch (1994), p.16-24.

Table1. Effect of DBDTC amounts on the Zr-recovery

DBDTC (μmole)	Equivalent ratio (DBDTC / Metals)	Zr-recovery (%)
5.7	4.1	91～93
6.8	4.9	93～95
8.5	6.2	94～96
10.2	7.4	95～97
13.6	9.9	94～96

Table2. Reproducibility of the PIXE analysis using Zr-internal standard

Counts in Co $K_\alpha$peak		Counts in Zr $K_\alpha$peak		Ratio in counts Co / Zr	
39760		1846		21.5	
42944	±1715[1)]	2131	± 68[1)]	20.2	±0.5[1)]
42080	(4.0%)	2039	(3.3%)	20.6	(2.4%)
47907		2138		22.4	

Sample: 25cm^3 of 0.9 ppm Co solution (0.38 μmole Co^{2+}, pH4), 25 μg of Zr-standard (0.27 μmole ZrO^{2+}). 1): standard variation.

Table 3. Physical parameters used in the quantitative analysis[14)]

X-ray	σ (10^{-24} cm^2)	K_α / K_β	γ L_β / L_α	L_γ / L_α	A
Fe-K_α	173	0.136	-	-	55.49
Co-K_α	142	0.137	-	-	58.93
Ni-K_α	117	0.138	-	-	58.69
Cu-K_α	96.2	0.139	-	-	63.55
Cd-K_α	1.99	0.216	-	-	112.4
Hg-L_α	64.8	-	0.595	0.0894	200.6
Pb-L_α	54.1	-	0.595	0.0894	207.2
Zr-K_α	9.69	0.191	-	-	91.22

Table 4. Accuracy of the PIXE analysis using Zr as an internal standard

Nominal concen. [ppb][1)]	Analytical values [ppb]						
	Fe	Co	Ni	Cu	Hg	Pb	Cd
100	100±2.6*	99.8± 2.6	104 ± 2.8	107 ± 3.0	98.3± 5.0	109 ± 6.0	103± 18
75	72.9± 1.9	72.2± 2.0	73.9± 2.1	76.8± 2.3	71.1± 4.2	75.1± 4.8	72 ± 15
40	42.6± 1.2	39.4± 1.2	45.6± 1.9	37.7± 1.6	39.7± 2.6	45.1± 3.5	45 ± 12
20	20.2± 0.6	19.7± 0.6	21.6± 0.6	21.6± 0.7	17.6± 1.1	17.9± 0.8	21.9± 4.3
5	5.0 ± 0.1	4.9 ± 0.1	5.1 ± 0.1	5.7 ± 0.1	5.3 ± 0.3	5.8 ± 0.4	6.0 ± 0.6

Targets were prepared from 25 ml of solutions containing seven metals and Zr-internal standard. Irradiation condition: 2 nA of 3 MeV proton beams and 2 μC of accumulated charges. 1): ±1.6 % error due to dilution of stocked solutions of the metals. *: the precision based on the statistical deviation of the characteristic X-ray yields.

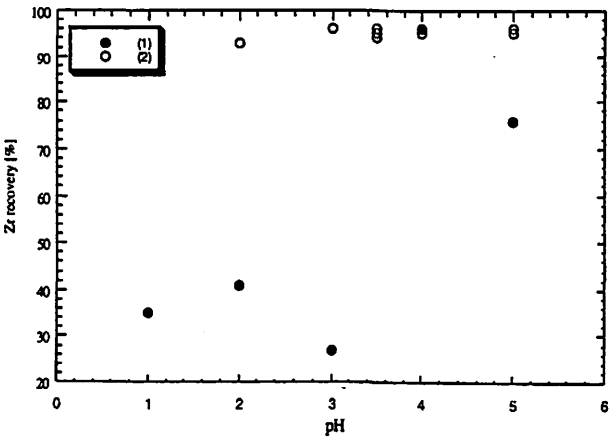

Fig. 1. Effect of pH on the Zr-recovery in the preconcentration step. (1): The pH of solutions remained at the specified value (1≤pH≤5) throughout the reaction. (2): First, DBDTC- and Zr-solutions were added to sample solutions of pH 4 and then, after 4-min stirring, the pH in the solutions was adjusted to the specified value by using HNO_3 or acetate buffer solutions.

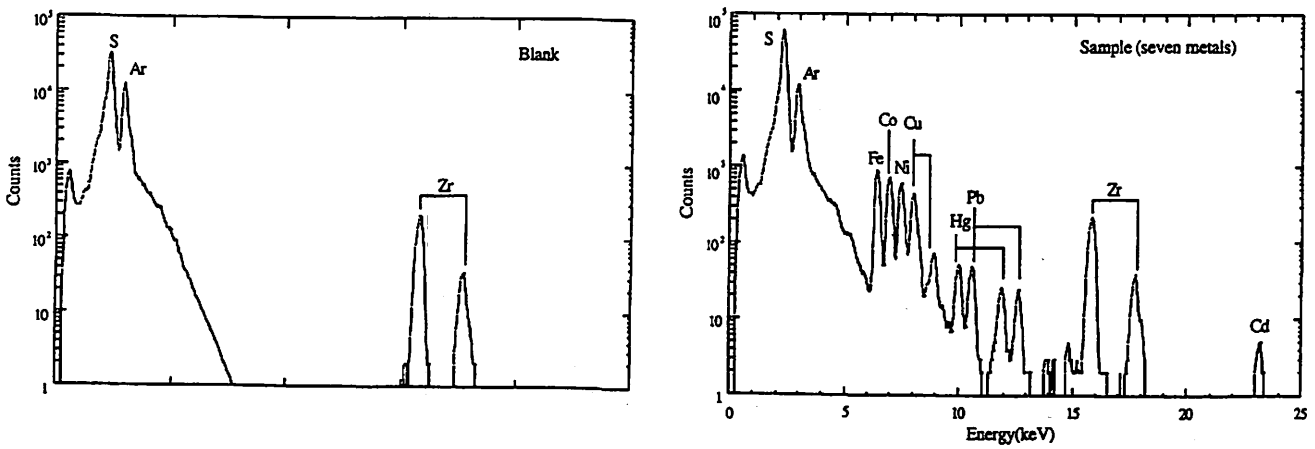

Fig. 2. Typical spectra of the in-air PIXE analyses. Targets were prepared from 25 ml of solutions containing seven metals and Zr-internal standard. Irradiation condition: 2 nA of 3 MeV proton beams and 2 μC of accumulated charges.

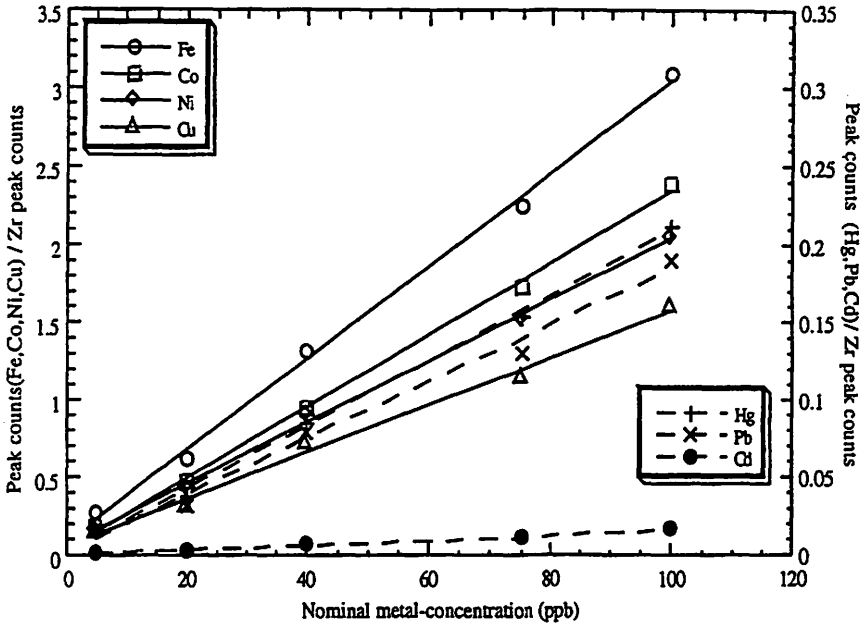

Fig. 3. Calibration curves for the PIXE analysis of heavy metals.

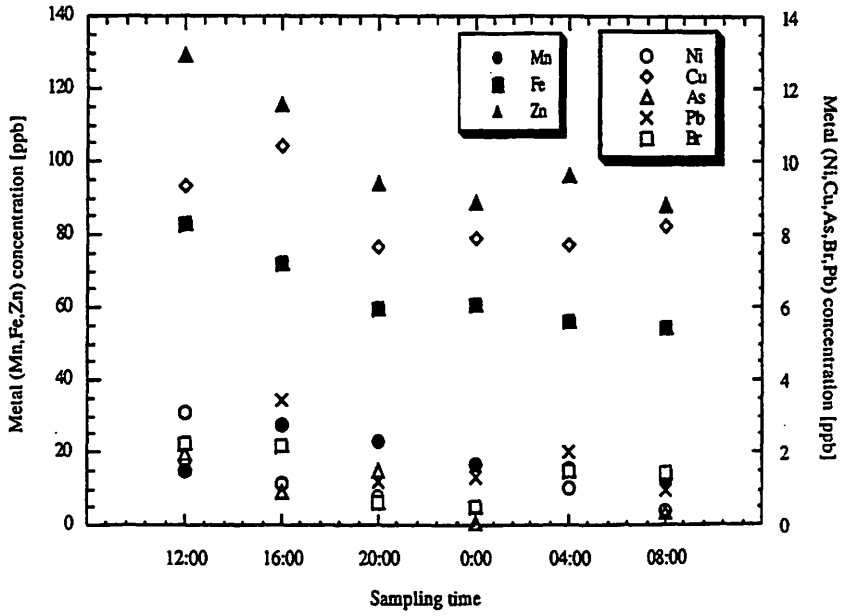

Fig. 4. Time variation of elemental concentrations in drinking water. Targets: 30ml of drinking water (pH 6.8) was chemically treated in the same manner as described in the text. Irradiation condition: 2 nA of 3 MeV proton beams and 2 μC of accumulated charges.

III. BIOLOGY AND MEDICINE (Basic)

III. 1. Regioselective Synthesis of 6-[^{18}F]-Fluoro-L-dopa via Radiofluorodestannylation

Okazaki M., Iwata R., and Ido T.

CYRIC Tohoku University

Introduction

Recently much efforts have been paid to the synthesis of 6-[^{18}F]-fluoro-L-3,4-dihydroxyphenylalanine (6-[^{18}F]-FDOPA **1**) due to its use as a probe for central dopamine metabolism *in vivo* by positron emission tomography (PET). Several methods on the electrophilic synthesis of **1** have been reported. As a pioneer work, Adam et al. described the routine synthesis of **1** by the reaction of [^{18}F]acetyl hypofluorite with L-methyl-N-acetyl-[β-(3-methoxy-4-acetoxyphenyl)]alanine to give the isomeric mixtures of **1** and 2-[^{18}F]-FDOPA in the ratio 1 : 1[1]. The EOB radiochemical yield based on AcO^{18}F was 8%. Luxen et al. improved the radiochemical yield upon the regioselective fluorodemercuration of 3,4-dimethoxy-6-trifluoroacetoxy-mercuric-L-phenyl alanine ester, followed by hydrolysis to give **1** in 11% EOB yield based on [^{18}F]F_2[2]. Due to toxicity of the mercuric precursor, the method was not widely accepted as a versatile route of **1**. This annual report describes an easily accessible synthetic method of a pure tin-precursor for **1**. The [^{18}F]-fluorodestannylation of the tin-precursor with [^{18}F]F_2 or [^{18}F]AcOF, followed by thermal hydrolysis afforded **1** in high radiochemical yields.

Experimental sections

3,4-Dihydroxy-L-phenylalanine methyl ester hydrochloride (2).

Dry hydrogen chloride was bubbled through a solution of DOPA (3,4-dihydroxy-L-phenylalanine) (8.0 g, 0.0406 mol) in absolute methanol (200 mL) at room temperature, and the solution was refluxed for 3 h. Volatiles were evaporated under reduced pressure. Crystallization of the colorless residue from methanol and 2-propanol/ethyl ether gave **2** (9.1 g, 0.0367 mol) as a white solid in 90% yield. Compound **2** can be purchased from Sigma (D1507).

N-(*t*-Butoxycarbonyl)-3,4-di(*t*-butoxycarbonyl)-L-phenylalaninmethyl ester (3).

A solution of di-t-butyl dicarbonate (9.7 g, 44.4 mol) in 12 mL of anhydrous DMF was added dropwise to a solution of **2** (2.0 g, 8.07 mmol) and anhydrous triethylamine (5.3

mL) in anhydrous DMF (10 mL) at room temperature. After stirring the mixture at room temperature for 24 h, the reaction mixture was poured into a separatory funnel together with 50 mL of ethyl acetate and 50 mL of saturated NaCl solution. The organic layer was separated from the aqueous phase and washed with saturated NaCl (50 mL×3) solution and water (50 mL×3), respectively. The organic layer was dried over magnesium sulfate. After filtration, volatiles were evaporated under reduced pressure. The colorless residue was chromatographed on silica-gel (ethyl acetate : hexane = 2 : 3) to afford a colorless oil. Crystallization from ethyl ether/hexane gave **3** (3.5 g, 6.84 mmol, 85%) as a white solid. ^{1}H NMR (400 MHz, $CDCl_3$) δ 7.18 (m, 1H, Ar), 7.01 (m, 2H, Ar), 5.01 (br. d, J = 7.8 Hz, 1H, NH), 4.57 (br. q, J = 7.8 Hz, 1H, CH), 3.70 (s, 3H, $COOCH_3$), 3.08 (m, 2H, CH_2), 1.54 (s, 9H×2, *t*-Bu×2), 1.43 (br. s, 9H, *t*-Bu). Anal. Calcd for $C_{25}H_{37}NO_{10}$: C, 58.70; H, 7.29%. Found: C, 58.71; H, 7.37%.

_N_-(*t*-Butoxycarbonyl)-3,4-di(*t*-butoxycarbonyl)-6-iodo-L-phenylalanine methyl ester (4).

To a solution of **3** (1.48 g, 2.89 mmol) and silver trifluoroacetate (0.83 g, 3.76 mmol) in 50 mL of CH_2Cl_2 was added iodine (0.88 g, 3.47 mmol) at room temperature. During the reaction, the light yellow precipitate was formed. After stirring the reaction mixture for 48 h at room temperature, the precipitate was filtered and washed with CH_2Cl_2 (10 mL×2). The combined filtrate was poured into a separatory funnel and washed with 1M sodium thiosulfate (50 mL×3) and water (50 mL×3). The organic layer was dried over magnesium sulfate and evaporated under reduced pressure. The residue was chromatographed on silica-gel (ethyl acetate : hexane = 1 : 2) to give a colorless oil. Ethyl ether (10 mL) was added, and the solution was concentrated under reduced pressure to give **4** (1.24 g, 1.95 mmol, 68%) as a white powder. ^{1}H NMR (400 MHz, $CDCl_3$) δ 7.73 (s, ^{1}H, Ar), 7.11 (s, ^{1}H, Ar), 5.06 (br. d, J = 8.3 Hz, 1H, NH), 4.60 (br. q, J = 8.3 Hz, 1H, CH), 3.72 (s, 3H, $COOCH_3$), 3.17 (m, 2H, CH_2), 1.54 (s, 9H, *t*-Bu), 1.54 (s, 9H, *t*-Bu), 1.40 (br. s, 9H, *t*-Bu). Anal. Calcd for $C_{25}H_{36}INO_{10}$: C, 47.10; H, 5.69%. Found: C, 47.38; H, 5.62%.

N-(*t*-Butoxycarbonyl)-3,4-di(*t*-butoxycarbonyl)-6-(trimethylstannyl)-L-phenylalanine methyl ester (5).

To a solution of **4** (0.50 g, 0.74 mmol) and tetrakis(triphenylphosphine)palladium(0) (40 mg) in anhydrous 1,4-dioxane (12 mL) was added hexamethylditin (0.36 g, 1.10 mmol), and the mixture was refluxed under an Ar atmosphere. During the thermal reaction, the black solid was precipitated. After 5 h, the reaction mixture was filtered to remove the black precipitates. The filtrate was concentrated under reduced pressure, and the residue was subjected to a silica-gel chromatography (ethyl acetate : hexane = 1 : 2) to give a colorless oil. Ethyl ether was added, and the solution was concentrated under reduced pressure to afford **5**

(0.40 g, 0.59 mmol, 80%) as a white powder. ^{1}H NMR (400 MHz, $CDCl_3$) δ 7.27 (s with Sn satellites ^3J(H-Sn) = 47 Hz, 1H, Ar), 7.09 (s with Sn satellites ^4J(H-Sn) = 15 Hz, 1H, Ar), 4.89 (br. d, J = 9.0 Hz, 1H, NH), 4.51 (br. q, J = 9.0 Hz, 1H, CH), 3.71 (s, 3H, $COOCH_3$), 3.06 (m, 2H, CH_2), 1.55 (s, 9H, *t*-Bu), 1.54 (s, 9H, *t*-Bu), 1.40 (br. s, 9H, *t*-Bu), 0.35 (s with Sn satellites ^2J(H-Sn) = 53 Hz, 9H, $SnMe_3$). Anal. Calcd for $C_{28}H_{45}NO_{10}Sn$: C, 49.87; H, 6.73%. Found: C, 49.89; H, 6.72%.

Fluorination of a tin-precursor 5 with [^{18}F]Acetyl hypofluorite via destannylation.

Typical procedure was as follows: Compound **5** (30 mg, 44 μmol) was dissolved in acetic acid (10 mL) and placed in a reaction vessel. [^{18}F]Acetyl hypofluorite was bubbled through the above solution at room temperature. After fluorination, the reaction mixture was transferred to a rotary evaporator and concentrated under reduced pressure. The residue was hydrolyzed with 6N HCl (3 mL) at 120 °C for 15 min, and the mixture was evaporated to dryness under reduced pressure. The crude 6-[^{18}F]-FDOPA **1** (22.3 mCi) was dissolved in 0.1%CH_3COOH and analyzed by HPLC (radiochemical purity 97%).

Results and discussions

Synthesis of the tin-precursor

The tin-precursor was prepared from commercially available L-dopa. Thermolysis of L-dopa in methanol in the presence of hydrogen chloride gave the methyl ester hydrochloride **2** as a white power in 90% yield. NH_2 and OH groups in **2** was easily protected with t-butoxycarbonyl group (Boc) by the reaction of **2** with di-t-butyl dicarbonate in the presence of triethylamine to produce **3** as a white power in 85% yield. Subsequently, regioselective iodination was achieved by the reaction of **3** with iodine in the presence of silver trifluoroacetate. Workup of the resulting mixture afforded a white power of **4** in 80% yield. The resulting iodo-compound **4** reacted with $Me_3SnSnMe_3$ at 110 °C in the presence of catalytic amount of $Pd(PPh_3)_4$ to give a tin-precursor **5** as a white powder in 80% yield. The total yield from the commercially available L-dopa to **5** is 44% *via* four steps.

[^{18}F]-Fluorination of a tin-precursor via destannylation

Fluorodestannylation of the tin-precursor **5** was carried out as illustrated in Table 1. Treatment of **5** with [^{18}F]F_2 or [^{18}F]AcOF caused radiochemically clean [^{18}F]-fluorodestannylation. The resulting [^{18}F]-labeled fluoro intermediate was easily converted to 6-[^{18}F]-FDOPA **1** quantitatively upon hydrolysis with 6N HCl at 120 °C.

Conclusions

We succeeded in the synthesis of the organotin precursor for 6-[^{18}F]-FDOPA **1** in excellent total yield. The tin-precursor can be [^{18}F]-fluorinated regioselectively with [^{18}F]F_2

or [^{18}F]AcOF. The resulting [^{18}F]-fluorinated compound was easily hydrolyzed in the relatively mild acidic conditions (6N HCl, 120 °C) to produce 6-[^{18}F]-FDOPA **1**. This work will promote the synthesis of 6-[^{18}F]-FDOPA **1** *via* fluorodestannylation.

References

1. M. J. Adam, T. J. Ruth, J. R. Grierson, B. Abeysekera, and B. D. Pate, J. Nucl. Med. **27**, 1462-1466 (1986).
2. A. Luxen, M. Perlmutter, G. T. Bida, G. V. Moffaert, J. S. Cook, N. Satyamurthy, M. E. Phelps, and J. R. Barrio, Appl. Radiat. Isot., **41**, 275-281 (1990).

Table 1. Decay corrected radiochemical yields for the production of 6-[^{18}F]-FDOPA **1**.

[^{18}F] source	solvent	radiochemical yield based on [^{18}F]F_2 (%)
F_2	$CFCl_3$	17
CH_3COOF	$CFCl_3$	19
CH_3COOF	CH_3COOH	23

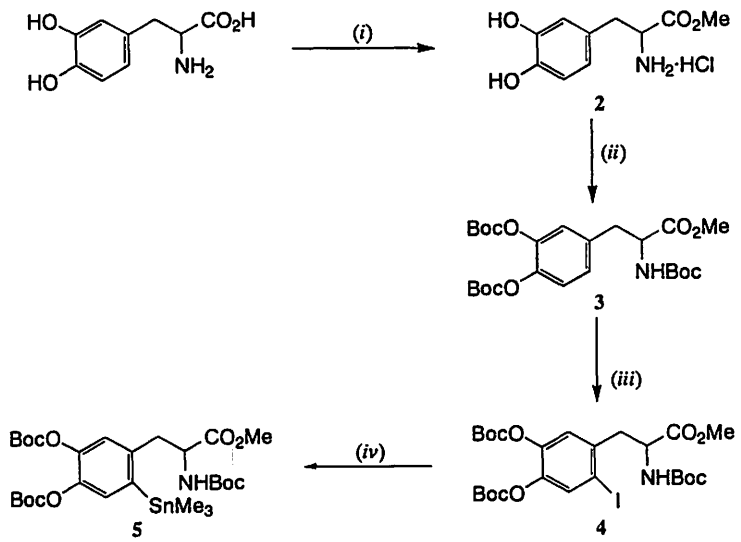

Fig 1. Synthesis of N-(t-Butoxycarbonyl)-3,4-di(t-butoxycarbonyl)-6-(trimethylstannyl)-L-phenylalanine methyl ester (**5**). (i) +HCl, MeOH, 3h, reflux; (ii) +$(Boc)_2O$, NEt_3, DMF, 24 h, r.t.; (iii) +I_2, $AgOCOCF_3$, CH_2Cl_2, 48 h, r.t.; (iv) +Me_6Sn_2, $Pd(PPh_3)_4$, 1,4-dioxane, 5 h, reflux.

III. 2. Tissue Distribution Study of Murine Monoclonal anti-GD_3 Antibody in Nude Mice Bearing Human Melanoma Xenografts

Ojima F., Ido T., Kijima-Suda I.**, and Nakagawa Y.*

Department of Pharmacy, Yamagata University Hospital
*Cyclotron and Radioisotope Center, Tohoku University**
*Tokyo Pharmaceutical Reserch Laboratories, Nissin Food Products Co., LTD.***

Tissue distribution of radiolabeled monoclonal anti-GD_3 antibody (IgM) was studied in normal mice and nude mice bearing the human melanoma xenograft. Tissue-to-blood distribution ratios of the antibody in the liver, spleen and kidney increased with time in both normal and melanoma transplanted mice, however, no significant changes were observed in other tissues. Specific accumulation of the antibody to human melanoma (HMV-II) was observed 4 and 5 days after injection. On the other hand, no specific accumulation of standard murine IgM to HMV- II was observed in mice bearing the HMV-II xenograft for 5 days after injection. Since the tissue-to-blood ratio of the distribution ratio became larger than that of other tissues 4 and 5 days after administration, 4 days after the administration of the antibody were required for immunoscintigraphy. Accumulation of the antibody to other human melanoma cells (HMV-I, HMY-1 and MEL188) inoculated into mice was also observed 4 days after the antibody administration. The monoclonal anti-GD_3 antibody would be useful in immunodetection or immunotherapy.

Introduction

The anti-tumor marker monoclonal antibody (mAb) has been developed for immunodetection in human tumors[1,2]. Monoclonal Ab is useful for in vivo immunodetection and the in vitro immunoassay system[1-4].

Disialoganglioside GD_3 was reported to be associated on the cell surface of lymphoblastic leukemia and other tumor cells[3]. The anti-GD_3 mAb reacts with human melanoma cells and some other human cells in vitro as analyzed by the fluoresein immunodetection system[3]. Therefore, GD_3 is an important tumor marker associated with human melanoma. There are many differences around the GD_3 on the cell surface situations between in vivo and in vitro. It is necessary to investigate tissue distribution of the mAb in nude mice bearing human tumor xenografts for immunoimaging and immunothrapeutics[5]. We examined the tissue accumulation of the anti-GD_3 mAb in human melanoma-bearing nude

mice in vivo and the timing necessary for detecting human melanoma using immunoscintigraphy.

Materials and methods

Anti-GD_3 mAb

Anti-GD_3 murine mAb (IgM) established in our group was purified from the ascitic fluid of male BALB/c mice (Funabashi Farm) previously inoculated with antibody-producing hybridoma. The mAb was partially purified by Sephacryl S-300 (Pharmacia) gel exclusion chromatography. This mAb reacts to ganglioside GD_3 in vitro.

Tumor models

Human melanoma cells were cultured and subcutaneously injected (10^7/100μL/mouse) in the back of male BALB/c nu/nu mice (Funabashi Farm). The mice were given 0.1 % NaI solution 3 days before mAb injection to reduce specific uptake of iodine into the thyroid. Melanoma transplanted nude mice were used in this study at 3-4 weeks after transplantation. Three or four mice were used in each study.

Radioiodination of anti-GD_3 mAb

Radioiodination of anti-CD_3 mAb was performed using an ENZYMOBEADS (Radioiodination System, Bio-Rad). One hundred μL of mAb solution and 37 MBq of ^{131}I were added to 100μL of ENZYMOBEADS suspension. The iodination was started by the addition of 1 % β-D-glucose (25μL) and then the reaction mixture was allowed to stand for 30 min at room temperature. After centrifugation, the supernatant was applied to a Sephadex G-25M column (PD-10, Pharmacia) to purify the labeled mAb with phosphate buffered saline as the elution buffer. Immunoreactivity of the labeled mAb was determined by comparison with the residual radioactivity in the wells coated with GD_3 or no GD_3 after incubation at 37°C for 120 min followed by three washings. The labeled mAb solution was filtered to sterilize it before administration to the mice through the tail vein (7.5-11.5μg/100μL/mouse).

Investigation of the tissue distribution of ant-GD_3 mAb in the mice bearing human melanoma.

HMV-II bearing nude mice were sacrificed on 3, 4 and 5 days after administration of labeled mAb through the tail vein. Blood, liver, heart, pancreas, spleen, small and large intestines, kidney, brain, muscle and bone were taken. The solid tissues were washed with 0.9 % NaCl, wiped and weighed. The samples and labeled mAb solution were counted using an auto-well gamma counter. Tissue distribution was expressed as the differential absorption ratio (DAR, counts of tissue/total injected counts) × (g body wt/g tissue) for normalizing the body weight of each mouse. The tissue-blood ratio was also obtained to determine if accumulation would occur. The tissue distribution of anti-GD_3 mAb was also measured in the HMY-1 and MEL188 human melanoma bearing mice 4 days after the mAb adminstration.

Standard murine IgM was iodinated using the same method as mentioned above and its tissue distribution ratio in HMV-II melanoma bearing mice were examined on 4 days after one hundred μL of standard murine IgM solution injection through the tail vein to certain specificity of anti-GD_3 mAb accmulation to HMV-II.

Autoradiography

In the HMV-I and HMV-II inoculated mice, the mice were sacrificed on 4 days after labeled mAb injection and frozen in hexane-dry ice to make a 3 % sodium carboxy methyl cellulose block. Slice samples were cut from the frozen whole body block with a -20°C cryotome and exposed to X-ray film.

Results

Time course of tissue distribution of labeled anti-GD_3 mAb in the normal mice

Biodistribution of labeled ant-GD_3 mAb in normal mice was investigated on 1, 2, 3 and 4 days after injection. Radioactivities in the tissues all decreased with time (Fig. 1), however, the tissue-to-blood radioactivity ratios were the same level with time except for the liver, spleen and kidney (Fig. 2). The tissue-to-blood radioactivity ratios of the liver, spleen and kidney increased with time (Fig. 2).

Time course of tissue distribution of labeled anti-GD_3 mAb in the nude mice bearing HMV-II xenografts

The results of the tissue distribution study of the labeled mAb are shown in Fig. 3. The distribution ratio of the radioactivity declined with time in all tissues except for HMV-II and liver. The tissue-to-blood ratio is shown in Fig. 4. In the HMV-II, liver, spleen and kidney, the tissue-to-blood ratio increased with time, however, no changes were observed in any of other tissues on 3, 4 and 5 days after mAb injection.

Autoradiography

The accumulation of the anti-GD_3 mAb was observed in nude mice bearing both HMV-I and HMV-II human melanoma 4 days after mAb administration. Fig. 5 shows the whole body autoradiogram. In the melanoma, a nonuniform uptake was observed, however, the accumulation was uniform in the other normal tissues. The radioactivity ratios of the other tissues to liver in HMV-I bearing mice are shown in Table 1. In the HMV-I, the mean melanoma to liver ratio was 1.1 and the maximum was 3.9. The mean melanoma to liver ratio was 7.9, and the maximum distribution ratio to liver was more than 10 in the HMV-II (Table 1).

Tissue distribution of labeled murin standard IgM antibody in the nude mice bearing HMV-II xenografts

The tissue-to-blood distribution ratios of labeled murine standard IgM and anti-GD_3 Ab in HMV-II bearing nude mice 4 days after antibody injection are represented in Fig. 6. No specific accumulation in the murine standara IgM was observed in HMV-II compared to the anti-GD_3 mAb distribution ratio.

Distribution ratio of Ab in HMY-1 and MEL188 human melanoma

The tissue-to-blood distribution ratios of anti-GD_3 mAb in HMY-1 and MEL188 bearing nude mice 4 days after mAb injection are represented in Fig. 7. The mean distribution ratio of mAb in HMY-1 was same as in the blood, however, specific accumulation of mAb was also seen in the MEL188 tissue.

Discussion

The tissue distribution of mAb is of significant importance in order to develop the mAb for delivering radionuclei or anti tumaor drugs to objective tumors. The immunoscintigraphy and/or immunotherapy of tumors would depend on the ratio of specific radioactivity delivered to tumors versus normal tissues. The murine monoclonal anti-GD_3 mAb was investigated for its biodistribution in the normal mice and nude mice bearing some human melanoma xenografts in this study.

In the HMV-II study, the accumulation of labeled mAb seemed to occur 3 days after injection. Since no specific accumulation was seen in standard murine IgM in HMV-II bearing nude mice, the accumulation of antibody in HMV-II was specific for anti-GD_3 mAb. Because the concentration of the radioactivity in the blood was higher than that of HMV-II, it was not suitable for immunoscintigraphy till 3 days after administration. Compared to all other tissues, the highest accumulation of mAb in HMV-II was observed on 4 and 5 days after injection. The tissue accumulation dose was higher on 4 days after mAb injection compared to the tissue accumulation ratio on 5 days after mAb injection. Therefore, it was suitable for the immunodetection of melanoma in this IgM subclass murine anti-GD_3 mAb on 4 days after injection. An autoradiography and tissue distribution study was performed 4 days after mAb administration. At the point of the mean distribution ratio, the HMV-I and HMY-1 human melanoma seems not to be detectable with this mAb, but as shown in the autoradiograms and Table 1, nonuniform accumulation in the melanoma tissues were seen, however, the accumulation was uniform in other normal tissues. This suggested that the highest accumulating regions in the melanoma tissue were detectable with immunoscintigraphy. These results indicated that the melanoma region was detectable despite their shape and volume were not exactly detectable. The nonuniform accumulation in the melanoma was based on the capillaries in the tumor tissue and affinity of antibody and cell

surface antigen. For example, a high affinity antibody is difficult to separate from the antigen near the capillary and diffuse into inner region of the tumor tissues.

The accumulation ratio of this mAb was approximately 1 % of the injected dose per gram wet tissue 4 days after injection. A lager accumulation ratio was reported when using the IgG subclass Ab[6,7]. A higher accumulation was necessary for immunotherapeutics. The mAb used in this study was the IgM subclass, because of its high molecular weight, it is difficult for it to pass through the capillaries in the melanoma tissues. It is necessary to study the biodistribution of Fab or F(ab') obtained from enzyme digestion in the melanoma-bearing nude mice and other radiolabeling methods[1,8-11].

References

1) Eary, J. F., Schroff, R. W., Abrams, P.G., et al., *J. Nucl. Med.*, **30**, 25-32, 1989.
2) Taylor, A. Jr., Milton, W., Eyer, H., et al., *J. Mucl. Med.*, **29**, 329-337, 1988.
3) Reman, G. H., Tayler, B. J., and Merit W. D., *Cancer Res.*, **50**, 202-205, 1990.
4) Thakur, M. L., Marcus, C. S., Henneman, P., et al., *J. Nucl. Med.* **37**, 1789-1795, (1996).
5) Sakahara, H., Endo, K., Koizumi, M., et al., *J. Nucl. Ned*, **28**, 235-246, 1988.
6) Halpern, S. E., Hagan, P. L., Garver, P. R., et al., *Cancer Res.*, **43**, 5347-5355, 1983.
7) Buchegger, F., Haskell, C. M., Schreyer, M., et al., *J. Exp. Med.*, **158**, 413-427, 1983.
8) Beaumier, P. L., Krohn, K .A., Carrasquillo, J. A., et al., *J. Nucl. Med.*, **26**, 1172-1179, 1985.
9) Wahl, R. L., Parker, C. W., and Philpott, G. W., *J. Nucl. Med.*, **24**, 316-325, 1983.
10) Koizumi, M., Endo, K., Watanabe, Y., et al., *Cncer Res.*, **48**, 1752-1757, 1989.
11) Sakahara, H., Endo, K., Nakashima, T., et al., *J. Nucl. Med.*, **26**, 750-755, 1985.

Table 1. Ratio of tissue radioactivity intensity compared to liver in HMV-I and HMV-II bearing mice in autoradiograms (Fig. 5).

Melanoma	Radioactivity intensity ratio to liver
HMV-I	Mean (whole): 1.1, Most accumulated region: 3.9
	Blood: 0.93, Lung: 0.64, Spleen: 0.59, Kidney: 0.59
HMV-II	Mean (whole): 7.9, Most accumulated region: > 10

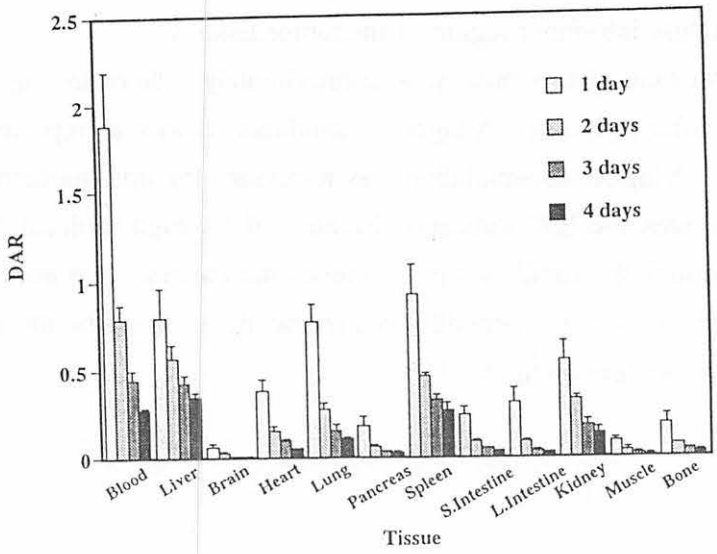

Fig. 1. Time course of tissue distribution ratio of anti-GD_3 ^{131}I mAb in normal mice.

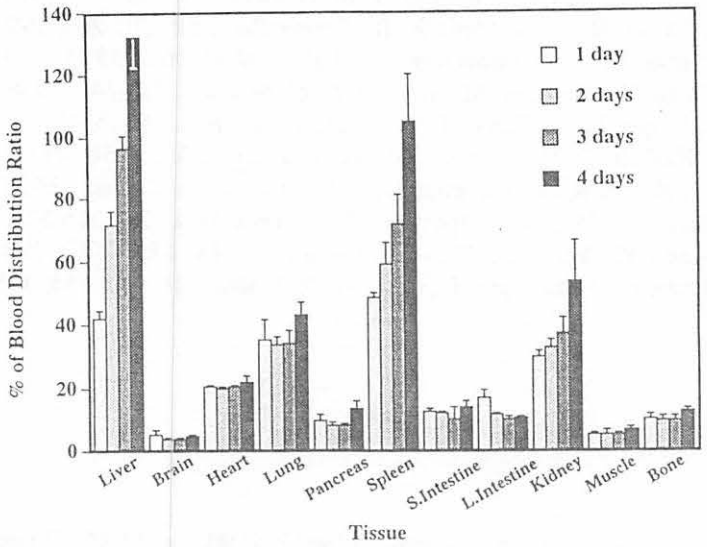

Fig. 2. Time course of tissue distribution ratio of ^{131}I anti-GD_3 mAb compared to blood radioactivity in normal mice.

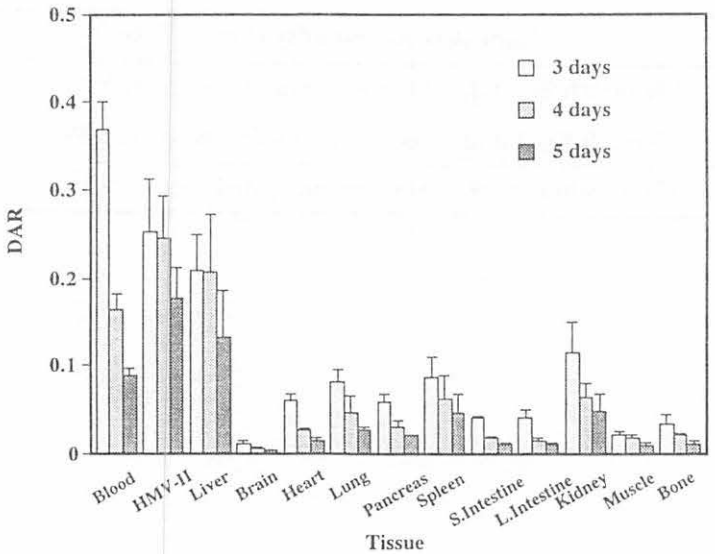

Fig. 3. Time course of tissue distribution of anti-GD_3 mAb labeled with ^{131}I in HMV-II bearing mice.

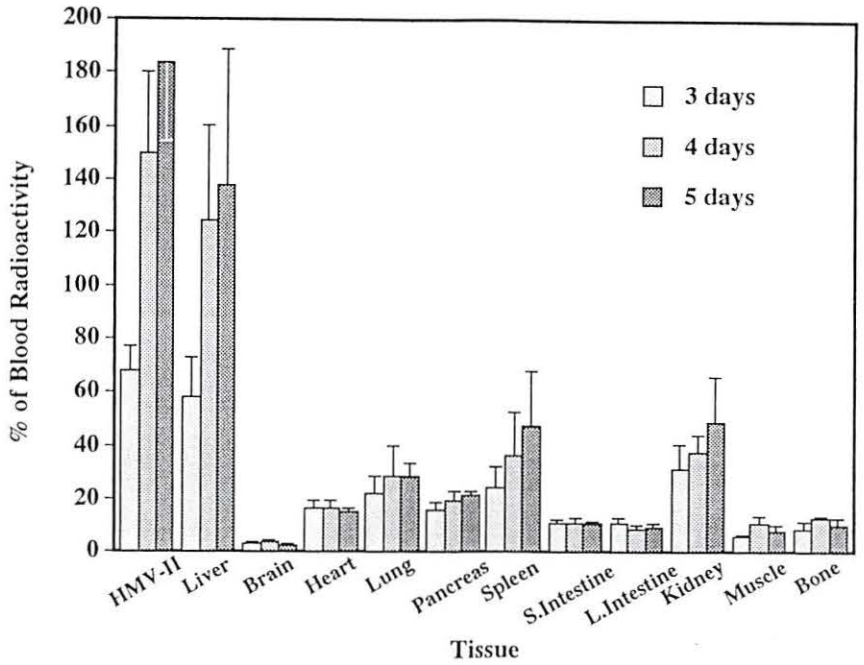

Fig. 4. Time course of tissue distribution ratio of anti-GD_3 mAb labeled with ^{131}I compared to blood in HMV-II bearing mice.

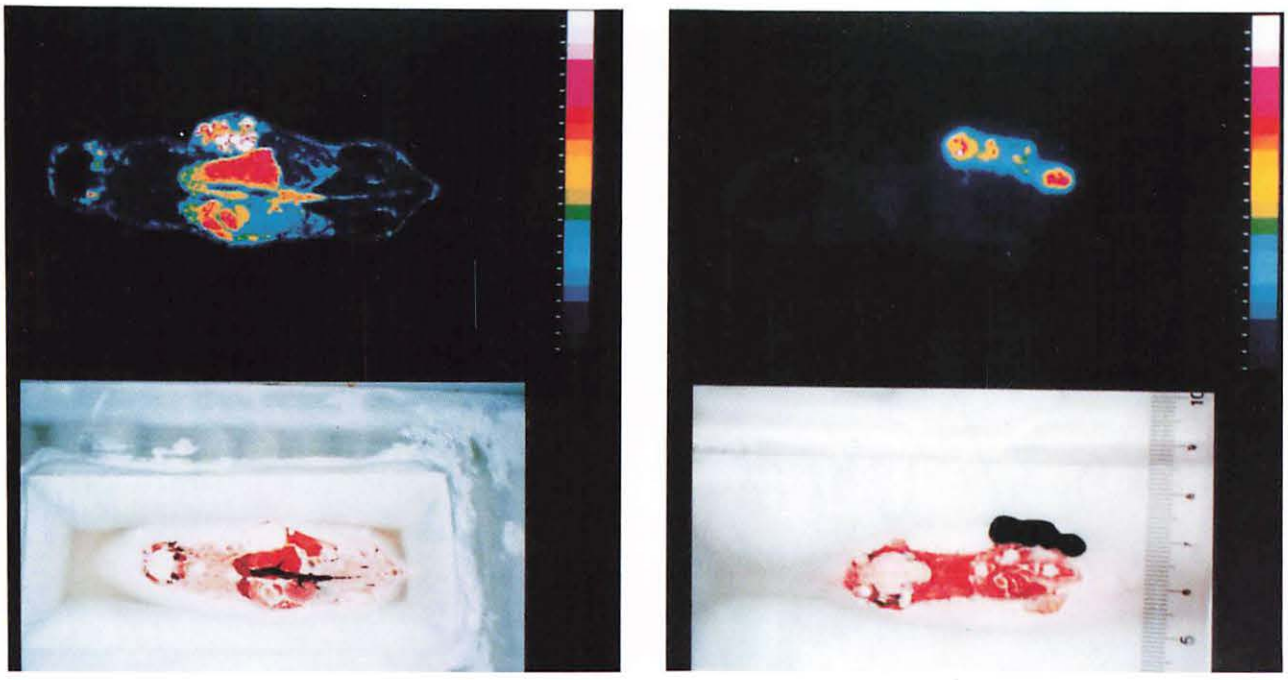

(A) (B)

Fig. 5. Autoradiograms of whole body 4 days after ^{131}I anti-GD_3 mAb injection in HMV-I (A) and HMV-II (B) bearing mouse. Arrows indicate the melanoma.

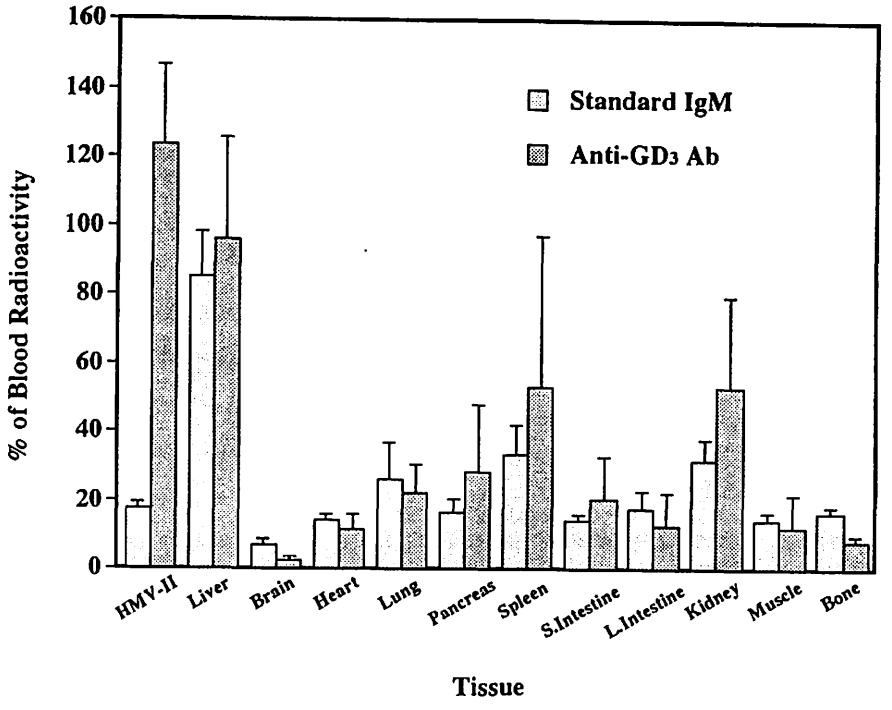

Fig. 6. Tissue distribution ratio of standard murine IgM and anti-GD_3 mAb compared to blood 4 days after injection in HMV-II bearing mice.

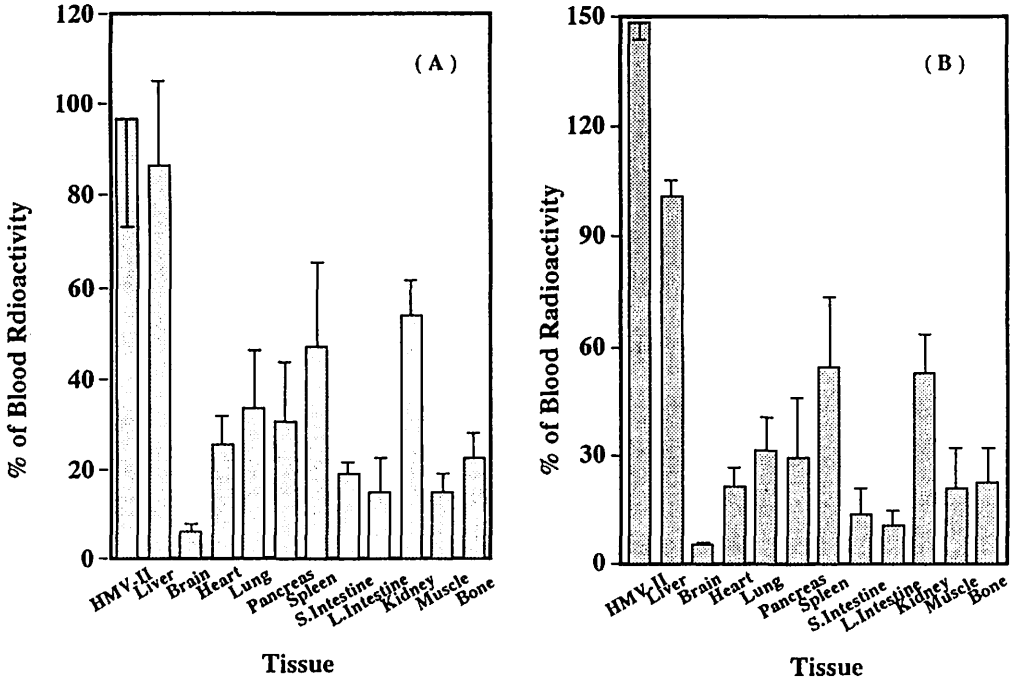

Fig. 7. Tissue distribution ratio of ^{131}I anti-GD_3 mAb compared to blood radioactivity in HMY-1 (A) and MEL188 (B) bearing mice 4 days after injection.

III. 3. Mechanism of Mastoparan-induced Histamine Release from RBL-2H3 Cells

Mizuno K., Nakahata N., and Ohizumi Y.

Department of Pharmaceutical Molecular Biology, Faculty of Pharmaceutical Sciences, Tohoku University

Introduction

Mastoparan is a tetradecapeptide purified from wasp venom[1], acting as a strong secretagogue in rat peritoneal mast cells[2,3]. The mastoparan-induced histamine release from rat peritoneal mast cells is inhibited by pertussis toxin (PT)[3], showing the involvement of PT-sensitive G proteins. Mastoparan has been shown to activate several purified G proteins including G_i, which is a substrate of PT[4-6]. On the other hand, mastoparan stimulates phosphoinositide hydrolysis and elevates cytosolic Ca^{2+} concentration in polymorphonuclear leukocytes[7], which is also inhibited by PT. Thus, it is assumed that mastoparan-induced exocytosis may be triggered by the activation of PT-sensitive G proteins.

Rat mast cells can be divided into two phenotypes, mucosal type and tissue connective type[8]. Rat peritoneal mast cells are known as a connective tissue type. Rat basophilic leukemia, RBL-2H3 cells are known as a model for mucosal mast cells, which have been used for the study of the degranulation process induced by cross-linking of the high affinity IgE receptor[9]. This process involves activation of the Src family protein tyrosine kinase[10], activation of phosphoinositide-specific phospholipase C leading to phosphoinositide hydrolysis[11], subsequent elevation of intracellular calcium concentration[12], and activation of protein kinase C[13]. Besides the above biochemical events, recent evidence suggests that phospholipase D (PLD) also plays an important role in IgE-dependent degranulation from RBL-2H3 cells[13,14].

Previously, we reported that mastoparan stimulated PLD activity in 1321N1 human astrocytoma cells and several cell lines including RBL-2H3 cells[15]. In the present study, we examined the effect of mastoparan on histamine release in RBL-2H3 cells.

Mterials and Methods

Materials. Dinitrophenylated bovine serum albumin (DNP_9-BSA) was produced in the manner described in the previous paper[16]. Phosphatidylbutanol (PBut) was produced from

soybean phosphatidylcholine using crude cabbage PLD by the method of Yang et al.[17]. Other chemicals or drugs were of reagent grade or highest quality available.

Cell culture. RBL-2H3 cells were grown in Eagle's minimal essential medium with 10% heat-inactivated fetal bovine serum at 37°C in an atmosphere of 5% CO_2 in air. For experiments, the cells were seeded at a density of 10^5 cells/well in a 12-well culture plate and were used 1-2 days after seeding. In the study of immunological stimuli, the cells were previously sensitized by incubating with 0.5 μg/ml anti-DNP IgE for 2 h.

Analytical methods of biological activities. The amount of histamine in the supernatant was determined by the fluorometric assay[18]. PLD activity was monitored by measuring PBut as previously described[15]. Phosphoinositide breakdown was monitored by measuring [^{3}H]inositol phosphates (IPs) as previously described[19]. ADP-ribosylation was performed as previously described[20]. LDH activity was measured by a commercial kit (Kyokuto, Tokyo, Japan).

Data analysis. The results obtained in separate experiments were expressed as mean ± S.E. and a significant difference was determined with using a unpaired two-tailed Student's *t*-test.

Results

Mastoparan (30 μM) caused a time-dependent histamine release within 15 min and a 4 fold increase in histamine release was observed 30 min after its stimulation (Fig. 1a). Mastoparan-induced histamine release was concentration-dependent with the maximal effective concentration of 20-30 μM (Fig. 1b). As shown in Fig. 1c, the histamine release induced by 30 μM mastoparan was not inhibited by pretreatment of the cells with PT (200 ng/ml for 18 h). RBL-2H3 cells had a small amount of ADP-ribosylation substrates for PT, and the substrates were completely ADP-ribosylated by pretreatment of the cells with PT (data not shown).

In sensitized RBL-2H3 cells, DNP_9-BSA (0.1-100 μg/ml), an antigen, accumulated IPs in a concentration-dependent manner (Fig. 2a). However, mastoparan by itself did not accumulate IPs and showed a tendency to suppress the DNP_9-BSA-induced IPs accumulation in RBL-2H3 cells (Fig. 2b).

Mastoparan-induced histamine release from RBL-2H3 cells was inhibited by neomycin in a concentration-dependent manner (Fig. 3a). Mastoparan caused [^{3}H]PBut accumulation in the cells, reflecting from its activation of PLD. The [^{3}H]PBut accumulation was inhibited by neomycin (Fig. 3b).

However, mastoparan caused LDH release from the cells in a similar concentration range to its histamine release (data not shown). This LDH release was inhibited by neomycin as same as the histamine release or PLD activation by mastoparan (Table 1).

Discussion

The present study demonstrated that mastoparan caused histamine release from RBL-2H3 cells. This release was not inhibited by PT, indicating that mastoparan induced exocytosis not mediated via PT-sensitive G proteins in RBL-2H3 cells. It has been reported that mucosal mast cell lacks responsiveness to polycationic agents, which stimulate degranulation from the peritoneal mast cell through the activation of PT-sensitive G proteins[8,21]. Moreover, RBL-2H3 cells have a small amount of ADP-ibosylation substrates for PT. These observations suggest the existence of histamine-releasing mechanism which does not involve PT-sensitive G proteins in RBL-2H3 cells. It has been shown that the secretory response stimulated by mastoparan is not inhibited by PT in other cells[22,23].

Neomycin inhibited the histamine release as well as the PLD activation induced by mastoparan. It is well known that neomycin is able to inhibit phosphoinositide-specific phospholipase C besides PLD[24]. However, mastoparan by itself did not induce phosphoinositide hydrolysis in RBL-2H3 cells, suggesting that phospholipase C does not contribute to the histamine release by mastoparan in the cells. It is reported that PLD is activated upon cross-bridging of IgE receptors on surface of RBL-2H3 cells and that this may be a pivotal step in the signal transduction cascade leading to histamine release[14]. One of interpretations may be that neomycin inhibits mastoparan-induced histamine release through the inhibition of PLD in RBL-2H3 cells. However, mastoparan caused considerable leakage of LDH, indicating that mastoparan enhanced the membrane permeability. Accordingly, the mastoaran-induced histamine release may be in part due to enhancement of membrane permeability.

Neomycin is known to bind strongly and selectively to phosphoinositides[25]. Thus, neomycin may interfere with the interaction between mastoparan and phosphoinositides, resulting in inhibition of histamine release by mastoparan from RBL-2H3 cells.

References

1) Hirai Y., Yasuhara T., Yoshida H., Nakajima T., Fujino M. and Kitada C. Chem. Pharm. Bull. **27** (1979) 1942.
2) Okano Y., Takagi H., Tohmatsu T., Nakashima S., Kuroda Y., Saito K. and Nozawa Y., FEBS Lett. **188** (1985) 363.
3) Higashijima T., Uzu S., Nakajima T. and Miyazawa T., Peptide Chemistry 1986, ed. T. Miyazawa, (1987) pp. 75, Protein Research Foundation, Osaka.
4) Higashijima T., Uzu S., Nakajima T. and Ross E. M., J. Biol. Chem. **263** (1988) 6491.
5) Higashijima T., Burnier J. and Ross E. M., J. Biol. Chem. **265** (1990) 141766.
6) Higashijima T. and Ross E. M., J. Biol. Chem. **266** (1991) 12655.
7) Perianin A. and Snyderman R., J. Immunol. **143** (1989) 1669.
8) Shanahan F., Denburg J. A., Fox J., Bienenstock J. and Befus D., J. Immunol. **135** (1985) 1331.
9) Metzger H., Alcaraz G., Hohman R., Kinet J. P., Pribluda V. and Quarto R., Annu. Rev. Immunol. **4** (1986) 419.
10) Eiseman E. and Bolen J. B., Nature **355** (1992) 78.

11) Cunha-Melo J. R., Dean N. M., Moyer J. D., Maeyama K. and Beaven A., J. Biol. Chem. **262** (1987) 11455.
12) Beaven M. A., Rogers J., Moore J. P., Hesketh T. R., Smith G. A. and Metcalfe J. C., J. Biol. Chem. **259** (1984) 7137.
13) Lin P. and Gilfilan A. M., Eur. J. Biochem. **207** (1992) 163.
14) Lin P., Wiggan A. G. and Gilfilan A. M., J. Immunol. **146** (1991) 1609.
15) Mizuno K., Nakahata N. and Ohizumi Y., Br. J. Pharmacol. **116** (1995) 2090.
16) Schmitt-Verhulist A. M., Pettinelli C. B., Henkart P. A., Lunney J. K. and Shearer G. M., J. Exp. Med. **147** (1978) 352.
17) Yang S. F., Freer S. and Benson A. A., J. Biol. Chem. **242** (1967) 477.
18) Shore P. A., Burkhalter A. and Cohn, V.A., J. Pharmacol. Exp. Ther. **127** (1959) 183.
19) Nakahata N., Abe M. T., Matsuoka I. and Nakanishi H., FEBS Lett. **260** (1990) 91.
20) Nakahata N., Abe M. T., Matsuoka I., Ono T. and Nakanishi N., J. Neurochem. **57** (1991) 963.
21) Swieter M., Midura R. J., Nishikata H., Oliver C., Berenstein E. H., Mergenhagen S. E., Hascall V. C. and Siraganian R. P., J. Immunol. **150** (1993) 617.
22) Komatsu M., McDermott A. M., J. Biol. Chem. **268** (1993) 23297.
23) Murayama T., Oda H. and Nomura Y., J. Cell Physiol. **169** (1996) 448.
24) Cockroft S., Howell T. M. and Gomperts B. D., J. Cell Biol. **105** (1987) 2745.
25) Schacht J., J. Lipid Res. **19** (1978) 1063.

Table 1. Effect of neomycin on mastoparan-induced LDH release

	LDH Release (%)	
Neomycin	(-)	(+)
control	2.1 ± 0.25	3.0 ± 0.46
Mastoparan	36.4 ± 1.79	6.4 ± 0.25 **

RBL-2H3 cells were incubated with 30 μM mastoparan at 37°C for 20 min in the presence or absence of 5 mM neomycin. Then, the medium was collected, and the content of LDH was measured by using a commercial kit. Data represent the mean ± S.E. of three independent experiments. Statistical significance from the coresponding value in neomycin (-): **P<0.01 (unpaired two-tailed Student's *t*-test)

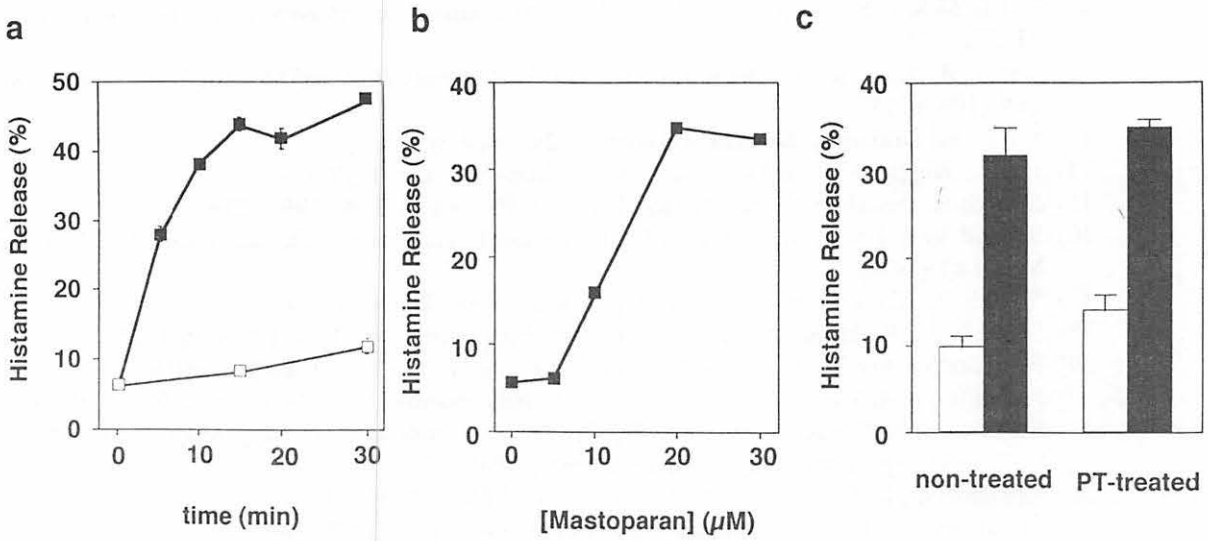

Fig. 1. Effect of mastoparan on histamine release in RBL-2H3 cells.
(a) The cells were incubated with (■) or without (□) 30 μM mastoparan at 37°C for the indicated time, (b) incubated with the indicated concentrations of mastoparan at 37°C for 20 min, or (c) cells were preincubated with 200 ng/ml PT for 18 h and then were incubated with vehicle (open column) or 30 μM mastoparan (filled column) for additional 20 min. Then, the medium was collected, and the content of histamine was measured by fluorometric assay. Data represent the mean ± S.E. of three independent experiments.

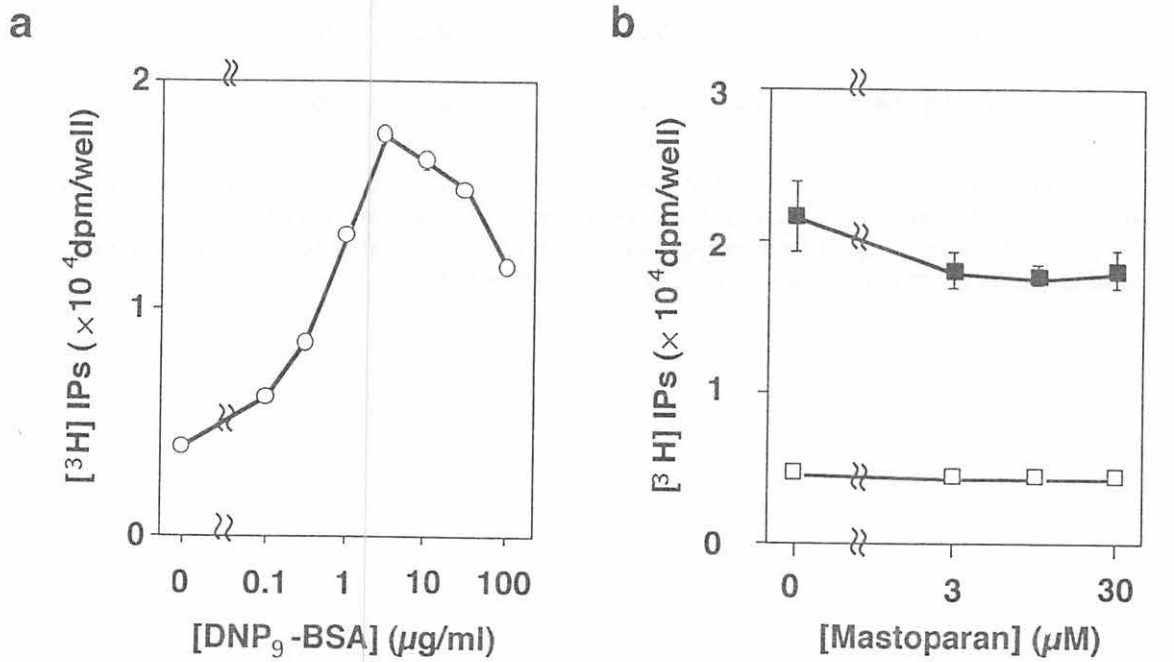

Fig. 2. Effects of antigen and mastoparan on [^{3}H]IPs accumulation in RBL-2H3 cells.
RBL-2H3 cells prelabeled with [^{3}H]myo-inositol were sensitized with anti-DNP IgE (0.5 μg/ml). Then, the cells were incubated with the indicated concentrations of DNP9-BSA at 37°C for 10 min in the presence of 10 mM LiCl (a), or incubated with the indicated concentrations of mastoparan and 10 mM LiCl, supplemented with (■) or without (□) 10 μg/ml DNP9-BSA (b). After the reaction was terminated, total IPs were separated by AG 1X-8. Data represent the mean ± S.E. of three independent experiments.

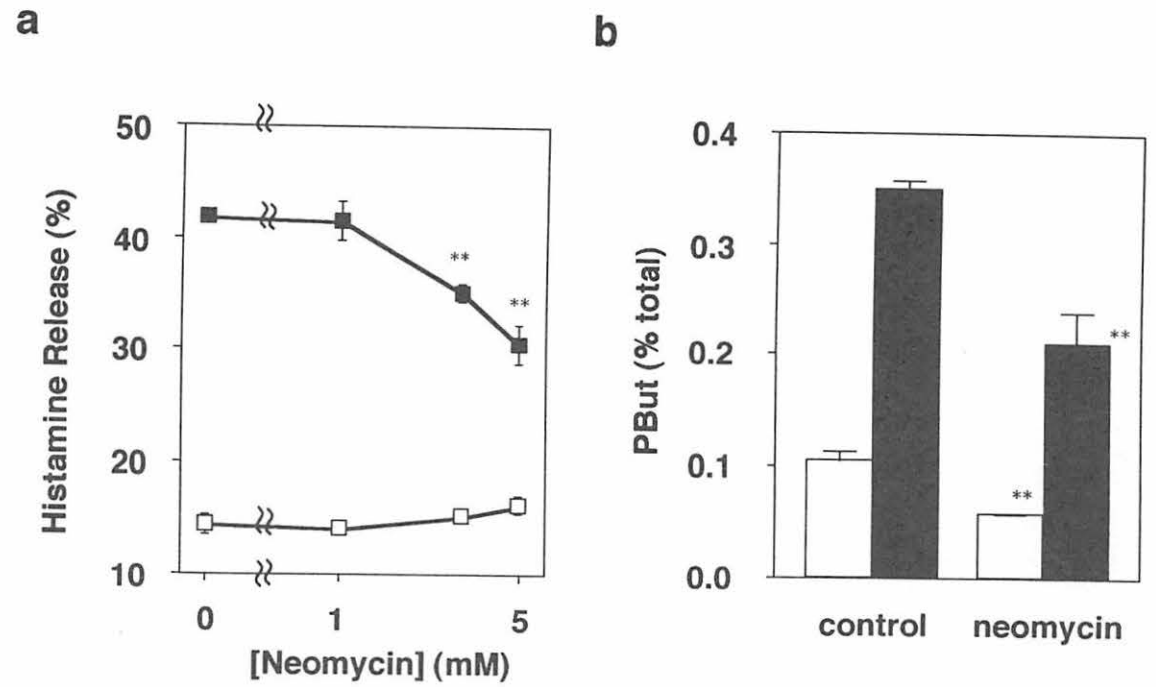

Fig. 3. Effect of neomycin on histamine release and PLD activity induced by mastoparan in RBL-2H3 cells. (a) RBL-2H3 cells were incubated with the indicated concentrations of neomycin at 37°C for 20 min, supplemented with (■) or without (□) 30 μM mastoparan. Then, the medium was collected, and the content of histamine was measured by fluorometric assay. (b) RBL-2H3 cells prelabeled with [^{3}H]palmitic acids were preincubated with 0.2% butanol in the presence or absence of 5 mM neomycin at 37°C for 10 min, and incubated for additional 10 min after addition of vehicle (open column) or 30 μM mastoparan (filled column). After the reaction was terminated, [^{3}H]PBut was determined. Data represent the mean ± S.E. of three independent experiments. Statistical significance from the corresponding value of neomycin (-): **$p<0.01$ (unpaired two-tailed Student's *t*-test)

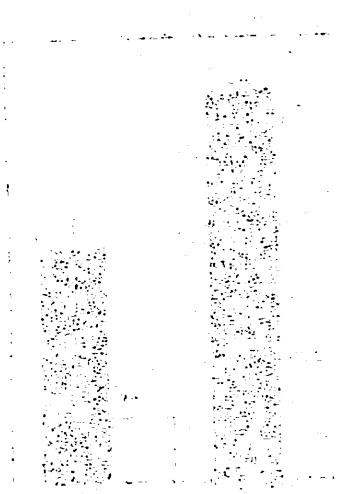

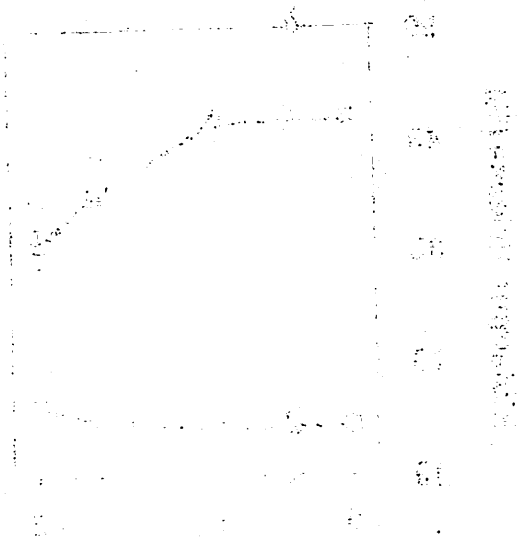

IV. BIOLOGY AND MEDICINE (Clinical)

IV. 1. Compton Scattering Correction in 3D-PET Study Based on the Unfolding Method

Shidahara M., Nakamura T., Narita Y.,*
Miyake M., Watanuki S., Fujiwara T., and Itoh M.

Cyclotron and Radioisotope Center, Tohoku University
*Chiba Cancer Center **

Introduction

Nowadays, an advanced 3D-PET (3 dimensional data acquisition PET) without Pb septa shielding has become in increasing use due to its higher efficiency, but has not been accomplished to give quantitative images in good accuracy because of poor resolution caused by global distribution of Compton scattering within a field of view (FOV).

There are several techniques to correct the contribution of Compton scatter with unique assumptions, e.g., convolution subtraction method[1] and dual energy window method[2]. Another method evaluates the scatter distribution by using the Monte Carlo simulated response function[3,4].

We are now trying to make a new Compton scattering correction method based on the unfolding technique using the SAND2 code[5]. The unfolding method requires the response function and we used the EGS4 Monte Carlo code[6] for calculation of response function of a cylindrical water phantom. We are further planning to use the EGS4 simulation code to calcurate the response function for the complicated geometry. This technique has two merits in scatter correction. First, the SAND-2 unfolding code, which we used, has a great advantage that the calculated results do not give the non-physical negative values. The second is the point that this method can be applied to various configuration of the actual PET systems. Here, we applied this unfolding method to a cylindrical water phantom filled with an uniform distribution of ^{18}F and investigated the effectiveness of the SAND-2 unfolding code using the simulated response function.

Material and Method

Unfolding calculation

The Compton scattering correction method using the unfolding technique was applied to the SET2400W PET scanner based on three-dimensinal (volume) data acquisition (Shimadzu Co. Ltd.), installed at Cyclotron and Radioisotope Center (CYRIC), Tohoku University. The SET2400W 3D-PET scanner has 32 ring BGO detectors and the data

acquisition of coincidence events is done not only within a ring but also between other rings. In this 3D-PET, relatively high contribution of scatter coincidence over 40% is observed[7]. We aimed to obtain the true coincidence event, real distribution of radioisotope in the object from the measured projection data, Y, and the response function, A, applying the SAND2 unfolding technique. The detailed algorithm of the SAND2-code modified for this purpose is described in the following.

The measured projection data have the relation

$$Y=AX, \tag{1}$$

where $Y=\{y_t, t=1,M\}$ (e.g.M = 256 bins × 63 slices for 180 angles),

$X=\{x_j, j=1,J\}$ (e.g.J = 256 bins × 63 slices for 180 angles),

$A=\{ a_{tj} \}$,

a_{tj} = probability of events stored in the t-th projected matrix from a point source virtually allocated at the j-th matrix element, which includes direct(true) and Compton scattered photons.

The unfolding to get the X values from Eq.(1) starts from the setting of the initial guess value X_0. For obtaining the faster convergence towards the appropriate results, the X_0 value is estimated from the measured Y values as

$$X_0=Y'*G, \tag{2}$$

where Y' is set to the measured Y values beyond the pre-determined threshold value of S% to Y, in order to avoid the noise data, * means the convolution integration and G means the Gaussian function for smoothing.

The iteration calculation was continued until the convergence limit was satisfied, as follows,

$$X_j^{m+1}=X_j^m \times \exp(C_j), \tag{3}$$

C_i can be given by

$$C_j = \sum_t \{0.5\times(a_{(t-1),j}\times X_j^m + a_{t,j}\times X_j^m)\}\times\log(\frac{Y_t}{U_t}) / \sum_j \sum_t \{0.5\times(a_{(t-1),j}\times X_j^m + a_{t,j}\times X_j^m)\}, \tag{4}$$

$$U_t=\sum_j^J a_{tj}\times X_j^m \quad , \tag{5}$$

where U_t is the m-th value folded from X_j^m which we estimated. As $\exp(C_i)=1$ in the ideal condition, the iteration was repeated until the convergence limit, $(1-\exp(C_i))$, becomes close to 1 within the pre-determined iteration numbers. In addition to the SAND2-code, 2

dimensional Gaussian filter to X values (FWHM=0.38cm) is introduced in between each iteration. In this process, each pixel in the projection,X, is multiplied by Gaussian filter. Although the unfolding calculation, the problem that noise level enhanced with increasing iteration number is pointed out, this filtering method in iteration process enables us to avoid this problem. The computing time was about 3h. for the matrix of [32bins×63slices for 180 angles] using the Workstation, SUN Ultra2(CPU300MHz).

Response calculation

The response functions used for the this modified SAND-2 code were calculated by Monte Carlo simulation based on EGS4 code. In order to investigate the effectiveness of this method, we selected the simple configuration, a water-filled cylindrical phantom of 20cm diam. by 20cm length in which a point isotropic gamma ray source of 511 keV energy is located. The projections for the point source configurations, in which a point source was positioned at x=0, 4 and 8cm for m the acial center and y=z=0cm (figure1), were calculated with EGS4 code with 6×10^9 histories for each source positions. Using three projection data sets, the response function,A, per one photon emitted from a source at any position in a phantom was obtained by interpolation and normalization to the history number. The accuracy of thus-interpolated response function was investigated by comparing the simulated total (true+scatter) coincidence events and the products of the response,A, and the simulated true coincidence events.

Experimental approach

This unfolding method was applied to the scatter correction of the experimental data of a simple configuration.

The projection data for water filled cylindrical phantom containing ^{18}F uniform distribution were measured by SET-2400W scanner with 3D-mode. The intensity of ^{18}F source was 144mCi (5.33×10^6Bq) at the starting time of the scan and the scan duration was 5hours. In the present performance test of this unfolding scatter correction technique, the projection data set of q=0, corresponding to a conventional 2D data acquisition, was extracted from the full 3D-projection data, then applied for scatter correction. The random coincidence events were removed in this projection by automatically subtracted by scanner to save the memory capacity. The projection data which were given in the matrix of 256 bins × 63slices × 175views were rebinned into 32 bins × 63 slices × 175 views.

Results and Discussion

Simulated response functions

Figure 1 shows three simulated point spread functions at 0, 4 and 8 cm apart from a central axis in cylindrical water phantom consisting of 32bin×63slice matrix. It is observed that the scatter components in the projections spread over outside the Field Of View (FOV).

The simulated projection data have different shapes in the Compton-scattered tail, especially near the edge of cylinder at three different source positions. These PSF data were interpolated to get the response function at arbitrary position in the phantom for unfolding calculation. The suitability of thus-obtained response function results in Fig. 2 without attenuation correction. This graph compares the simulated total coincidence events with the product of the response function and the simulated true coincidence events. As shown figure 2, the true coincidence component is much lower than the total coincidence component, which means the scatter component is dominant in this case. Within the object, the average values of these two quanties agree within 3.2%. Even under this poor circumstance which has predominant scatter events, a good agreement between these two quantities can be seen in the central part where the true coincidence events exist, which indicates that the response function has enough good accuracy. While on the other hand, the big discrepancy between these two quantities can be seen outside the object. To improve this, we must simulate much more sampling points and add z-axial dependence on the response function.

Projection analysis

The unfolding calculation was done for the measured projection of a cylindrical water phantom with ^{18}F uniform source using the response function described above. The convergence limit was set to be $(1-\exp(C_i))< 0.01$, the iteration number was five and the threshold value to get initial value was fixed to be 30% of the maximum value of Y_t. Fig. 3 shows a comparison of profiles between unfolded and measured projection data. These profiles are given without the attenuation correction in a phantom. It is clearly seen that the unfolded profile result has no scatter component outside of the object and has a similar shape as the true component inFig. 2. In Fig. 3, the projection of the true component in the unfolded data has a small dip in the center of cylinder due to the photon attenuation, but the measured projection data has no dip due to contribution of scattered events. Figure 4 shows the unfolded and measured projections having the matrices of 32bins × 63slices.

Conclusion

In this study, we investigated the possibility to apply the SAND2 unfolding method on the scatter correction in 3 dimensional PET. Since the process of attenuation correction and image reconstruction causes some errors, here in this study this scatter correction method was applied only for the projection data. The application of this method to the cylindrical water phantom with 18F uniform source revealed that the scattering correction works well. There is still however left some problem in the response function estimation. We are planning ti further investigate the effectiveness of this method to a cylindrical phantom which contains a cold spot.

References

1) Baily D. L. and Meikle S. R., Phys Med Biol. **39** (1994) 411-424.
2) Sylke Grootoonk, A thesis submitted to the University of Surrey in fulfillment for the degree of Doctor of Philosophy, Department of Physics (1995).
3) McKee B. T. A. et al., IEEE Trans. Med. Imaging MI-**11** (1992) 560.
4) Cherry S. R., Meikle S. R. and Hoffman E. J., J. Nucl. Med. **34** (1993) 671.
5) McElroy W. N. et al., AFWL-TR-67-41, Air Force Weapons Laboratory, Kirtland Air Force Base, (1967).
6) Narita Y. et al., Proceeding of First International Workshop on EGS4, (1997).
7) Fujiwara T. et al., MEDICAL NOW **26** (1996) 7.

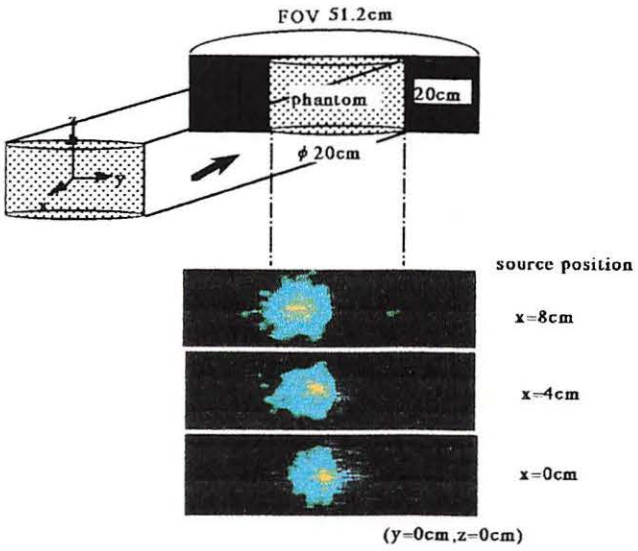

Fig. 1. Simulated PSF projection data when a point isotropic gamma-ray of 0.511 MeV energy is located at x=0,4,8cm.

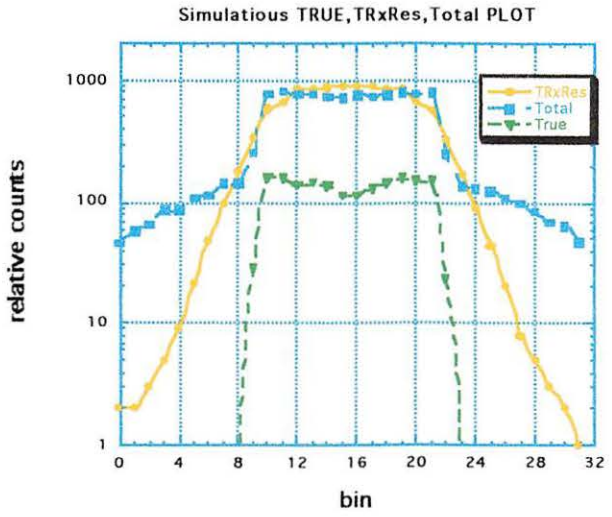

Fig. 2. Comparison of profile between (response x true coincidence) and (total coincidence).

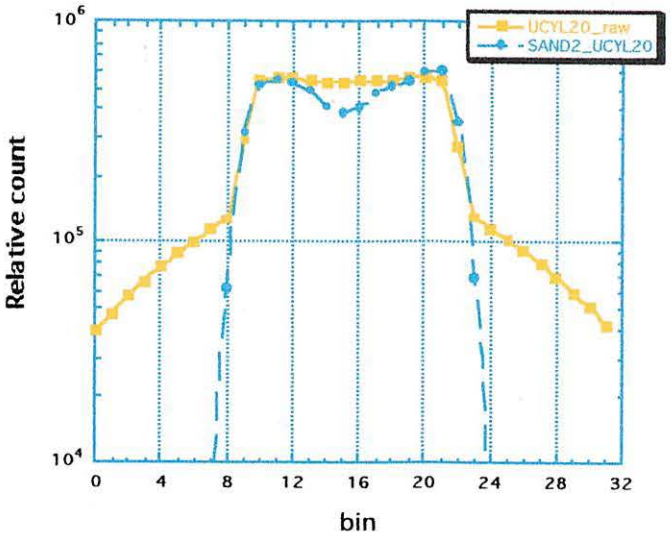

Fig. 3. Comparison of profile between unfolded projection and measured projection.

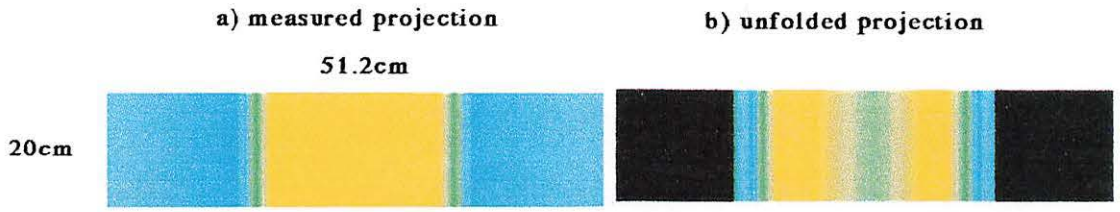

Fig. 4. Unfolded projection and measured projection.

IV. 2. Application of An Artificial Neural Network to Generation of Parametric Images in A [^{11}C]Doxepin-PET Study

Yamaki A., Higuchi M., Yanai K.**, Itoh M.***, Fujiwara T.***, Okamura N.*, Arai H.*, Sasaki H.*, and Takahashi Y.*

Laboratory of Neuroinformation Science, Tohoku Gakuin University
*Department of Geriatric Medicine, Tohoku University School of Medicine**
*Department of Pharmacology I, Tohoku University School of Medicine***
*Cyclotron and Radioisotope Center, Tohoku University****

Introduction

Estimation of the parameters describing the tracer kinetics by means of positron emission tomography (PET) and a radioligand can provide a quantitative information of the neurotransmission in human brain[1]. In an analysis on a voxel-by-voxel basis for generating images of the kinetic parameters from PET data, fitting procedure using a compartment model, which is widely utilized to obtain respective parameters[2,3], is unlikely to be practical, since it requires repeated iterations and thus much time.

An artificial neural network (ANN) yields a very fast calculation of the output parameters with only a single pass, once trained adequately. Accordingly it is expected to be of great use in construction of the parametric images. To date, the ANN has been applied to the parameter estimation for cerebral glucose metabolism in PET studies[4,5].

The primary goal of this study is to apply the ANN and a compartment model using reference tissue data to generation of parametric images for the tracer delivery and binding to the central histamine H_1 receptors in a PET measurement with [^{11}C]doxepin, a selective radioligand for histamine H_1 receptors.

Subjects and methods

The normal volunteers studied here were divided into two groups, group 1 (8 males, aged 28.9 ± 14.1 years (mean ± SD)) and group 2 (1 male and 1 female, aged 25 and 65 years, respectively).

A dynamic PET scan was performed with ECAT PT931/04-12 (CTI Inc, Knoxville, TN, USA) or SET-2400W (Shimadzu Inc, Japan) positron emission tomograph. [^{11}C]doxepin was prepared as described previously[6], and injected intravenously, followed by an acquisition of emission data for 80 min. A region of interest (ROI) was placed on the cerebellum in PET images, and a cerebellar time-activity curve (TAC) was obtained as data in the reference tissue.

A three-layer neural network constructed with a 44-node input layer, a 25-node hidden layer and a 3-node output layer was employed for estimating the kinetic parameters (Fig. 1). The network was trained by a back-propagation algorithm[7] using a set of input-output samples, which was generated with a two-tissue compartment model. This model requires a TAC in the reference tissue and a standard plasma TAC, and enables generation of a TAC in the specific region from assigned values of R_0 (a relative value of the tracer delivery between plasma and tissue), k_3 and k_4 (rate constants of the tracer for association with and dissociation from the receptors, respectively). Here the binding potential of the tracer for the receptors is calculated as k_3/k_4.

Two sets of input-output samples, i. e. group 1 and group 2 samples were generated, and the group 1 samples were used in the training of the network. To assess results of the training, values of R_0, k_3, k_4 and BP estimated by the ANN were compared with the assigned values, using the group 1 samples. In addition, estimated and assigned values of the kinetic parameters were compared in a use of the group 2 samples, in order to evaluate the ability of the ANN for generalization.

Parametric images of R_0, k_3, k_4 and BP were constructed by applying the ANN to a voxel-by-voxel analysis of the dynamic PET images in each subject.

Results

Plots of the R_0, k_3, k_4 and BP values estimated by the ANN (trained with 3,000 cycle and 2,500 samples) versus the assigned values for the group 1 (= training) samples are shown in Figs. 2A through 2D, respectively. A good agreement between the estimated and assigned values was observed for any of the kinetic parameters, indicating that errors in

Comparisons between the estimated and assigned values of the kinetic parameters for the group 2 (= non-training) samples are exhibited in Figs. 3A through 3D. Here the plots are for the data of 1 male subject, and the discrepancy between the estimated and assigned values was found to be small. Similar results were also obtained for the data of 1 female subject (data not shown). These findings suggest that the ANN can be generalized for an analysis of the data that are not used in the training.

Parametric images of the R_0, k_3, k_4 and BP for 1 subject in group 1 (aged 25 years) generated by the ANN are shown in Fig. 4. The time for generating 63 slices of parametric images by the ANN and a workstation (TITAN2, Kubota Computer Inc, Japan) was approximately 2 minutes, which is comparable to the calculation time using a graphical analysis.

Discussion

The present study demonstrates that the ANN with only one hidden layer is capable of learning the model function for the radioligand kinetics. This analytical system enables a fast construction of the parametric images from noisy TAC data in voxels. However, the accuracy

of the parameter estimation for noisy data may be further improved by training the ANN with 'noisy' TACs, which are created mathematically and are added random noises.

Although several assessments will be required, the ANN is likely to be feasible for constructing parametric images in PET studies with various types of radioligands. The stability and ability for generalization indicated by the results in this study will be advantages in utilizing the ANN as an analytical tool.

References

1) Frost J. J. Trends Pharmacol. Sci. **7** (1986) 490.
2) Farde L., Hall H., Ehrin E., Sedvall G. Science **231** (1986) 258.
3) Sawle G. V., Playford E. D., Brooks D. J., et al. Brain **116** (1993) 867.
4) Graham M. M., O'Sullvan F. Quantification of brain function using PET (Myers R., et al., eds.) Academic Press (1996) 277.
5) Svarer C., Law I., Holm S., et al. Quantification of brain function using PET (Myers R., et al., eds.) Academic Press (1996) 271.
6) Yanai K., Watanabe T., Yokoyama H., et al. Neurosci. Lett. **137** (1992) 145.
7) Karayiannis N. B., Venetsanopoulos A. N. Artificail neural networks: Learning algorithms, performance evaluation, and applications, Kluwer Academic Publishers (1993) 141.

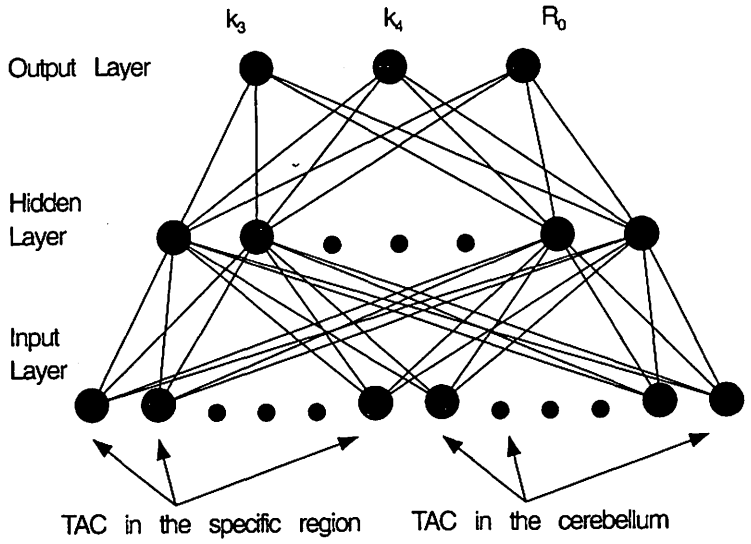

Fig. 1. A three layer back-propagation network employed in this study. All the nodes between adjacent layers are connected with a weight.

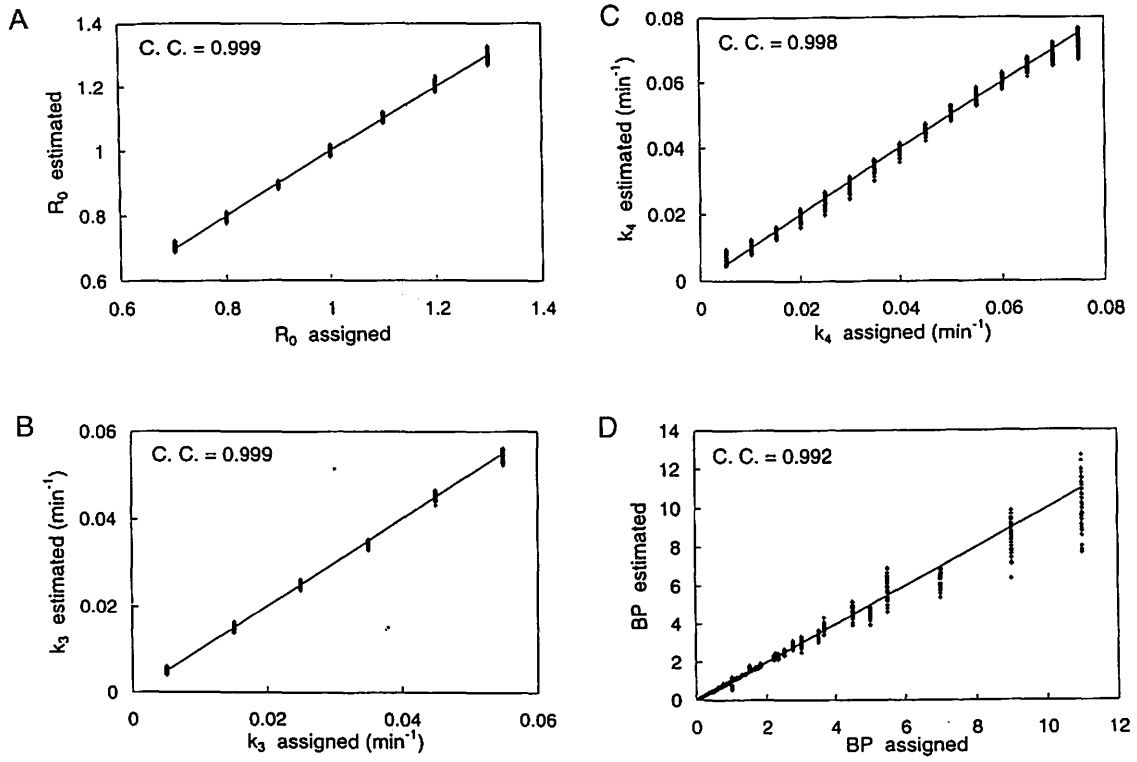

Fig. 2. Assigned and estimated values of R_0 (2A), k_3 (2B), k_4 (2C) and BP (2D) in the analysis of the group 1 samples by the ANN. The samples are identical to that used in training the ANN.

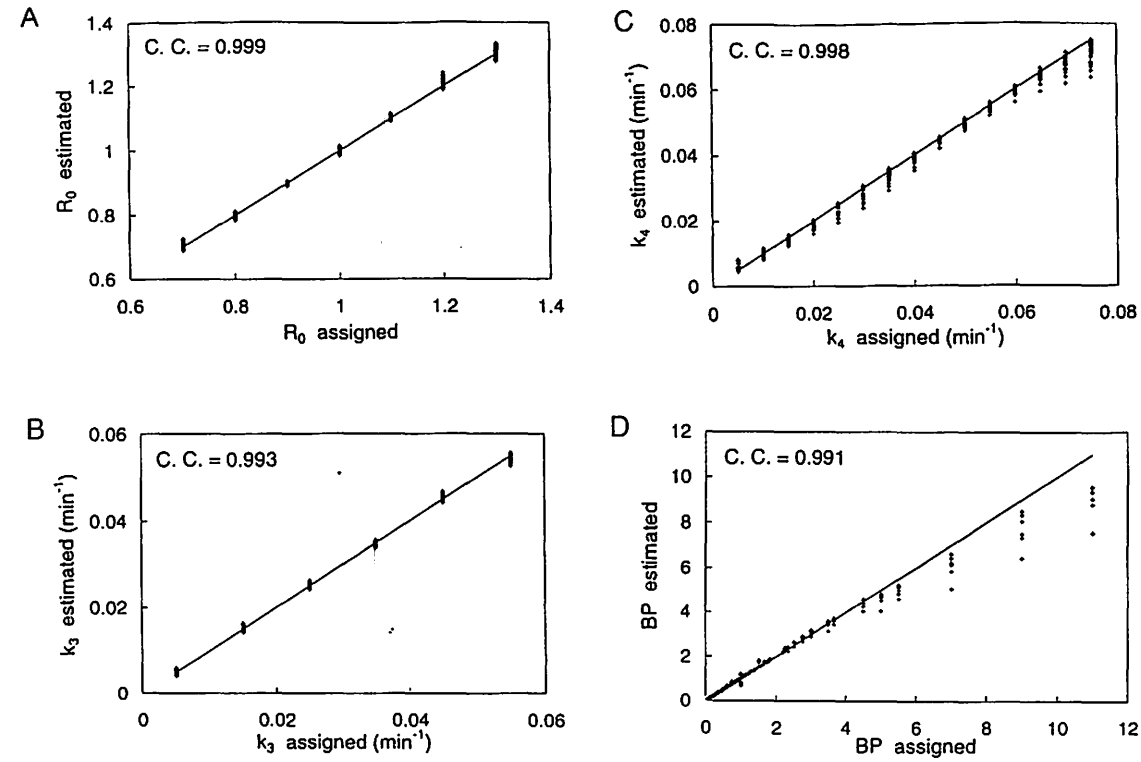

Fig. 3. Assigned and estimated values of R_0 (3A), k_3 (3B), k_4 (3C) and BP (3D) in the analysis of samples from a subject (aged 25 years) in group 2 by the ANN.

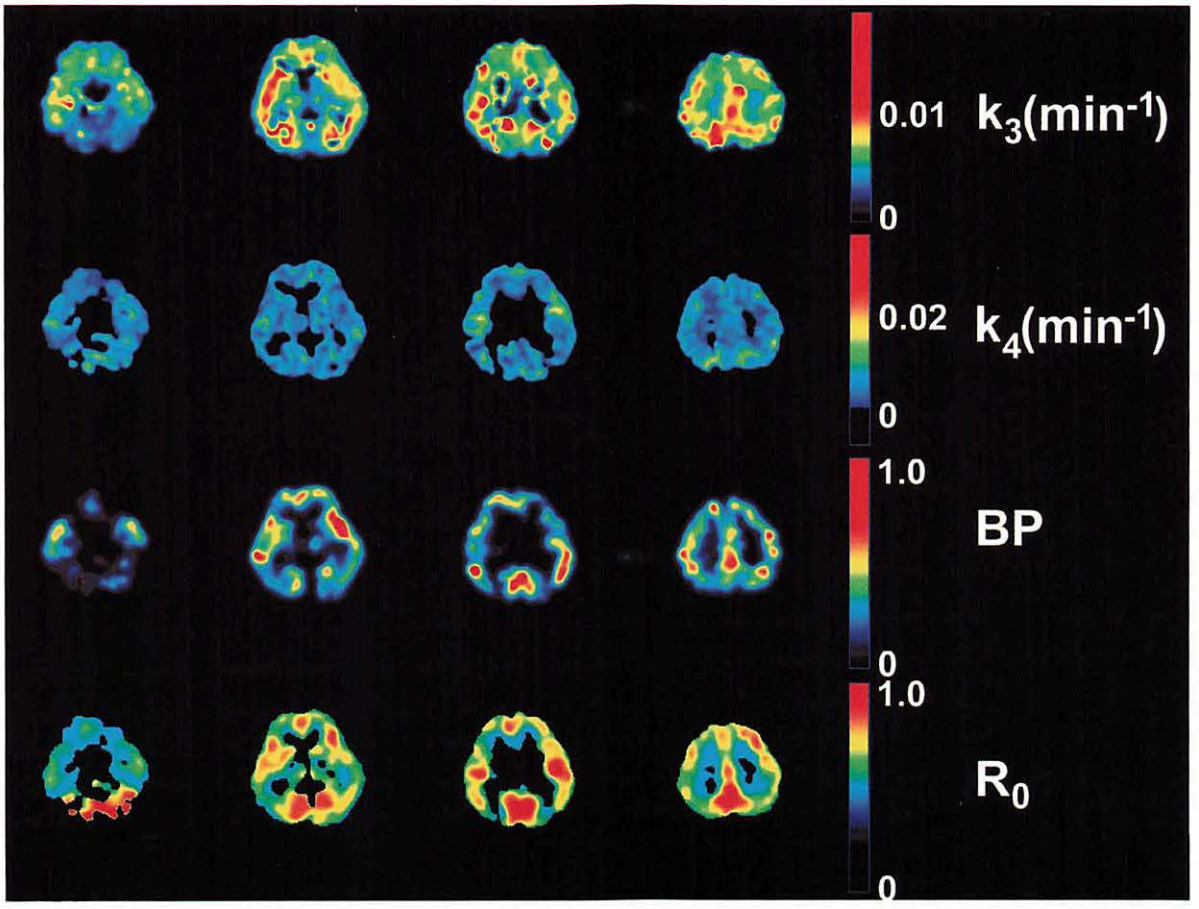

Fig. 4. Parametric images of k_3, k_4, BP and R_0 generated by the ANN for [^{11}C]doxepin-PET data of a subject (aged 25 years) in group 1.

IV. 3. FDG Uptake by Human Cancer Xenografts in Nude Mice after Chemotherapy

Yoshioka T., Fukuda H., Akaizawa T.*, Kanamaru R.*

Department of Clinical Oncology, Nuclear Medicine and Radiology, Institute of Development, Aging and Cancer, Tohoku University*

INTRODUCTION

With cancer chemotherapy, it is important to choose the most effective chemotherapeutic agents for individual patients. There have been several attempts to develop in vitro[1-6] and in vivo[7,8] systems that would predict the response of a tumor in an individual patient to a particular chemotherapeutic agent, but the results have been far from satisfactory. In clinical practice, the chemotherapist chooses chemotherapeutic agents on the basis of his experience, and by monitoring morphological changes of tumors by physical examination, X-ray studies, endoscopy, CT, US or MRI, in a continuous decision making process.

[^{18}F]Fluorodeoxyglucose (FDG) PET should also be suitable for follow up after cancer treatment, since its uptake relates to the number of viable tumor cells[9]. The response of tumors to chemotherapy might therefore be recordable earlier and more exactly in terms of FDG uptake than from morphological changes. Several clinical studies using FDG have been performed to evaluate therapeutic response in malignant tumors[10-17] and there have also been reports of experimental studies concerned with the relationship between treatment efficacy and FDG uptake[18,19]. However, detailed experimental in vivo studies on the correlation between morphologic alterations and FDG uptake in tumors caused by chemotherapy have been lacking.

In this study, we therefore compared the relationship between tumor volume and FDG uptake after chemotherapy using human cancer xenografts.

MATERIALS AND METHODS

The SC-6-JCK used in this study is a poorly differentiated human gastric adenocarcinoma cell line. Tumor tissue fragments, approximately 2 mm^2 in size, were inoculated into the subcutaneous tissue of the back of inbred 5-week-old male BALB/c nu/nu mice maintained under pathogen-free conditions. Tumors inoculated into the subcutaneous tissue of the backs of nude mice were measured (length and width) with sliding calipers every day by the same person. Utilizing the method of Geran et al[20]., the tumor volume (V) in mm^3 was calculated from the linear measurements using the formula: tumor volume (mm^3) = length

(mm) (width × (mm) ^{2}/2. On the 16th day after inoculation, tumor-bearing mice were randomized into four test groups (MMC, CDDP, ADR and control), and MMC (6 mg/Kg) and CDDP (8 mg/Kg) were administered once intraperitoneally and ADR (8 mg/Kg) once intravenously for its poor absorption the peritoneum. The relative mean tumor volume (RV) was calculated as Vi/Vo, where Vi is the mean tumor volume of a group at any given time and Vo is the mean tumor volume at the initial treatment. Growth curves after treatment were generated from the calculated RV.

Six FDG tissue distribution studies were carried out at 1, 3, 5, 7, 10 and 14 days after treatment. Each study encompassed four test groups, each consisting of five to seven nude mice (MMC, CDDP, ADR and control). FDG was dissolved in isotonic saline and approximately 20μ Ci/ 0.2ml was injected intravenously via the lateral tail vein. The mice were killed by decapitation 60 min after the injection and the tumors removed and blotted. The tumors were weighed and counted in an automated NaI well counter along with a standard sample of the injected FDG (United Technologies Packard Auto-Gamma 500/800). Radioactivity was corrected for decay and data were expressed as the differential uptake ratio (DUR):

$$\text{DUR} = \text{tissue counts} / \text{tissue weight} / \text{injected dose counts} / \text{body weight}$$

RESULTS

The growth curves after treatment are shown in Figure 1. Reduction of tumor size was largest in the MMC administered group, followed by the CDDP case, and the ADR-treated group demonstrated no reduction. In the MMC group, reduction was evident on Day 4, which became significant on Day 8 (RV=0.78±0.13) as compared with the initial volume ($p<0.01$). Likewise for the CDDP group, tumor reduction was noted on Day 5 and with significance from Day 11 (RV=0.83±0.17) ($p<0.01$).

Drug response curves of tumor uptake of FDG are shown in Figure 2. FDG tumor uptake in the MMC-administered group showed a steady decrease that became significant in comparison with the control level on Day 3 (DUR=0.96±0.27; $p<0.05$). In the CDDP case, a significant decrease was noted on Day 7 (0.93±0.21; $p<0.05$). With both drugs the uptake values remained decreased at later time points. FDG tumor uptake in the ADR-administered group demonstrated no difference from the control group, but the values were higher for the two other drugs from Day 7 to Day 14. FDG tumor uptake in the MMC group was consistently lower than that of the CDDP-administered group, but there was no statistically significant difference between the two.

DISCUSSION

Abe et al. (18) reported, using experimental murine cancer models, that FDG uptake is reduced in radiosensitive but not radioresistant tumors and that metabolic changes lead to morphologic alterations in radiosensitive tumors after radiation. Minn et al[11]. reported that successful treatment causes decrease in FDG uptake in patients with head and neck tumors, and similar tendencies were also noted in patients with other tumors[10,12-17]. In this study, a comparison of FDG uptake and tumor size allowed a good correlation to be established after administration of anticancer drugs with differing efficacy against xenograft growth. Our present findings suggest that FDG PET might be suitable for monitoring cancer chemotherapy.

The time-response of FDG uptake indicated the possibility of more rapid detection of chemotherapeutic potential than with tumor size. This was the case with both MMC and CDDP administration. The reason for this is presumably because cytotoxic effects of anticancer agents cause metabolic arrest of cancer cells, as reflected by FDG uptake, before necrosis and reduction in tumor size can occur. The latter is also complicated by inflammatory changes and fibrosis. The observations in our study suggest that FDG PET tumor imaging might allow the effectiveness of chemotherapy for an individual patient to be decided earlier than with conventional morphological methods.

This is the first study on the correlation between morphologic alterations and FDG uptake in tumors caused by chemotherapy. Heterogeneity of tumor tissue in terms of FDG kinetics is a potential source of problems in interpreting FDG PET images for assessment of response to chemotherapy. However, our observations provide evidence that FDG PET imaging is indeed useful for follow-up after cancer chemotherapy.

ACKNOWLEDGMENT

We would like to thank the staff of the Cyclotron Radioisotope Center. This work was supported in part by Grants-in-Aid (No.10670820 and No.09470196) from the Ministry of Education, Science and Culture, Japan.

References

1) Mosmann T., J. Immunol. Methods **65** (1983) 55-63.
2) Kuzmits R., Aigiger P., Frass M. et al., Adr. Exp. Med. Biol. **165** (1984) 383-388.
3) Salmon S. E., Alberts D. S., Durie B. G. M. et al., Cancer Res. **74** (1980) 300-305.
4) Tanigawa N., Kern D. H., Hikasa Y., et al., Cancer Res. **42** (1982) 2159-2164.
5) Weisenthal L. M., Marden J. A., Dill P. L., et al., Cancer Res. **43** (1983) 749-757.
6) Hoffman R. M., Connors K. M., Meerson-Monosov A. Z., et al., Proc. Natl. Acad. Sci. USA. **86** (1989) 2013-2017.
7) Povlsen C. O., Jacobsen G. K. Cancer Res. **35** (1975) 2790-2796.
8) Bogden A. E., Haskell P. M., Lepage D. J., et al., Exp. Cell Biol. **47** (1979) 281-293.
9) Higashi K., Clavo A. C., Wahl R. L., J. Nucl. Med. **34** (1993) 414-419.
10) Takahashi H., Yamagichi K., Wakui A., et al., Sci. Res. Inst. Tohoku Univ. **69** (1986) 830-838.

11) Minn H., Paul R., Ahonen A., J. Nucl. Med. **29** (1988) 1521-1525.
12) Minn H., Soini I., Eur. J. Nucl. Med. **15** (1989) 61-66.
13) Abe Y., Matsuzawa T., Fujiwara T., et al., Int. J. Radiat. Oncol. Biol. Phys. **19** (1990) 1005-1010.
14) Nagata Y., Yamamoto K., Hiraoka M., et al., J. Comput. Assist. Tomogr. **14** (1990) 370-374.
15) Wahl R. L., Zasadny K., Helvie M., et al., J. Clin. Oncol. **11** (1993) 2101-2111.
16) Haberkorn U., Strauss L. G., Dimitrakopoulou A., et al., J. Nucl. Med. **34** (1993) 12-17.
17) Bares R., Klever P., Hauptmann S., et al., Radiology **192** (1994) 79-86.
18) Abe Y., Matsuzawa T., Fujiwara T., et al., Eur. J. Nucl. Med. **12** (1986) 325-328.
19) Higashi K., Clavo A. C., Wahl R. L., J. Nucl. Med. **34** (1993) 773-779.
20) Geran R. I., Greenberg N. H., Macdonald M. M., et al., Cancer Chemother. Res. **3** (1972) 51-61.

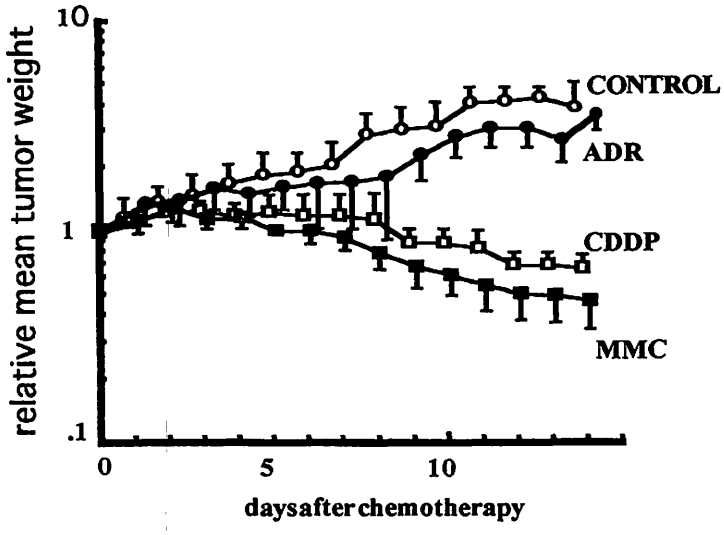

Fig. 1. Tumor growth curves after chemotherapy. Symbols are mean values and bars are s.d. The tumor proved sensitive to MMC and CDDP in that order, and not to ADR.

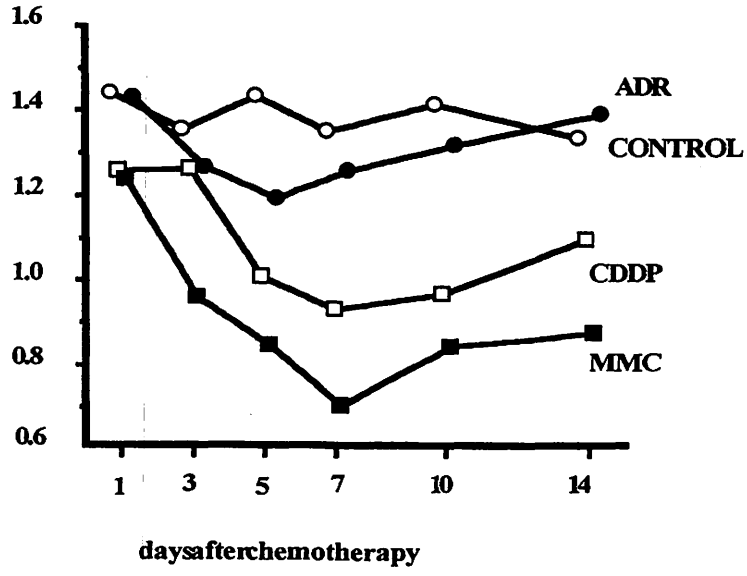

Fig. 2. Time-response curves of FDG tumor uptake after chemotherapy. Consistent decreases from Day 1 to Day 7 were observed in the sensitive drug groups, but not with ADR.

IV. 4. Functions of Parahippocampal Regions and Frontal Lobes in Alternative Judgment of Novelty and Familiarity for Auditorily Presented Words

Motooka N., Okuda J., Fujii T., Yamadori A., Tsukiura T., Kawashima R., Fukatsu R.**, Suzuki K., Ito M.***, and Fukuda H.**

Section of Neuropsychology, Division of Disability Science, Tohoku University Graduate School of Medicine
*Institute of Development, Aging & Cancer (IDAC), Tohoku University**
*Department of Neurology, Miyagi National Hospital, Miyagi, Japan***
*Cyclotron and Radioisotope Center, Tohoku University****

Introduction

Functional neuroimaging techniques have greatly contributed to our understanding of memory processes of the human brain in vivo. One of the fascinating problems recently evolved is the relationship between encoding/retrieval processes and novelty of presented stimuli. Previous studies raised a possibility that principal participants of encoding and retrieval processes are the frontal lobes and hippocampal formations[1-4], and novelty and familiarity of presented information may influence memory processing of received information[5,6]. In order to further elucidate this issue, we examined brain regions associated with processing of novelty and familiarity for auditorily presented verbal materials, by using positron emission tomography (PET).

Methods

Subjects

Seven healthy young male volunteers participated in the study. All subjects were right handed. A written informed consent was obtained from each subject.

Task procedures

Subjects participated in two experimental sessions. In the first session, the subjects heard 30 words once every three seconds and were requested to memorize the words until they could recall 80 percent of them. No PET scan was performed in this session. In the second session performed on the following day, the subjects underwent six PET scan measurements (one for control task and five for experimental tasks). In experimental tasks, the subjects listened to 30 words at a rate of one per three seconds and were requested to judge whether the words were identical to those learned in the first session (OLD words) or not (NEW words). They were asked to respond to repeat a word for OLD one and to say

"no" for NEW one as soon as each word was presented. Through the five scans of the experimental tasks, numbers of OLD and NEW words in each task were systematically altered. That is, NEW/OLD ratio for the task 1, 2, 3, 4, 5 was set to be 30/0, 22/8, 15/15, 8/22, 0/30, respectively. In the control task, the subjects heard a list of 30 NEW words one per three seconds and were requested to only say "no" for all the words without any judging. The order of the six tasks in the session was counterbalanced across the subjects.

Scanning Methods and Regional Analysis

Regional cerebral blood flow (rCBF) was measured using PET (SET2400W, Shimadzu) and ^{15}O labeled water (approximately 35 mCi for each injection). Subjects had a catheter placed in the right brachial vein for tracer administration, closed their eyes, and wore an individual stereotaxic fixation helmet. Each PET data acquisition started at the time of bolus injection and the start of each task, and lasted 120 sec. All PET data were reconstructed to rCBF images and were transformed into the standard anatomical format using the Human Brain Atlas System[7] and each subject's MRI. After spatial smoothing and normalization of global cerebral blood flow[8,9], all images were analyzed using the Statistical Parametric Mapping (SPM96)[10]. First, to find out areas involved in novelty and familiarity processes, two subtractions were performed, i.e., experimental task 1 minus control, and experimental task 5 minus control. Second, to further elucidate novelty and familiarity difference, two other subtractions were performed, i.e., experimental task 1 minus 5, and experimental task 5 minus 1. Finally, novelty and familiarity activations were again estimated using covariation analysis which reveals regions associated with correlations between appearing rate of NEW (OLD) words in each task and normalized rCBF images at each voxel. All statistical parameters were transformed to standardized Z-score and thresholded at 3.09 ($p=0.001$, uncorrected). Each activation was superimposed onto an average reformatted MRI of the seven subjects. Finally, anatomical localization of areas of activation was estimated in relation to this MRI.

Results

Activations associated with processing of novel and familiar words are summarized in Table 1 and 2, respectively. The activations associated with novelty processing included the left parahippocampal gyrus (subtraction of the control task and the experimental task 5 from the task 1; see Fig. 1a) and the right inferior/middle frontal gyrus (subtraction of the task 5 from the task1; Fig. 1b, correlation analysis related to novelty; Fig. 1c). The activations associated with familiarity processing included the right parahippocampal gyrus (subtraction of the control task from the task 5; see Fig. 2a) and the left inferior/middle frontal gyrus (subtraction of the task 1 from the task 5; Fig. 2b, correlation analysis related to familiarity; Fig. 2c).

Discussion

Previous studies reported that the hippocampo-parahippocampal areas were associated with novelty assessment process[5,11]. Studies dealing with encoding of novel verbal information also demonstrated the left hippocampo-parahippocampal gyral activation[12,13]. In the present study, the left parahippocampal area was activated during novelty assessment (task 1 minus control, task 1 minus 5) but was not activated during familiarity assessment (task 5 minus control, task 5 minus 1). According to these data and the previous studies, it is very likely that the left parahippocampal area is much involved in novelty assessment and episodic encoding of auditorily presented words than the right parahippocampal area.

Our data showed an involvement of the right parahippocampal area (task 5 minus control, task 5 minus 1), but not the left parahippocampal area (task 1 minus control, task 1 minus 5), in familiarity assessment process. These data confirmed our previous results in which the right and the left parahippocampal areas were differentially involved with matching to sample and non-matching to sample strategies of verbal recognition process[6]. We assume that the right parahippocampal area is more involved in episodic retrieval and familiarity assessment process of verbal materials than the left parahippocampal area, while the left parahippocampal area is more associated with episodic encoding and novelty assessment process as discussed above.

We observed the left inferior frontal activation in subtraction of task 1 from 5 and in correlation analysis related to familiarity assessment, and the right inferior frontal activation in subtraction of task 5 from 1 and in correlation analysis related to novelty assessment. The laterality of activation was reversed with that of the parahippocampal activation. Some of the previous studies suggested that the left, but not the right frontal lobe was associated with episodic encoding and semantic retrieval[1,4]. Our data is clearly inconsistent with these results and interpretation. Since the old words in our experiments were frequently repeated as stimuli, it is quite conceivable that they were incorporated into the semantic word store in the left hemisphere. When a familiar word appeared, the decision that it was familiar may have been easier for the ipsilateral left frontal lobe to make than the right. The interpretation that the left frontal lobe plays an important role in episodic retrieval process may be supported by one previous study in which, using similar tasks, the left inferior frontal lobe close to our result was activated by familiarity assessment task[5]. Also, activation of the left lateral frontal pole was reported when subjects were engaged in episodic retrieval and familiarity assessment[14].

In the present study activation of the right inferior frontal lobe was demonstrated in relation to novelty assessment of auditorily presented words. There were few studies which were compatible with this result in terms of memory processing or novelty/familiarity processing. However, activation of the right Brodmann area 46 was reported by Bottini and others[15] with metaphor interpretation. In this task subjects were presented with a sentence and was asked to decide whether a sentence was a plausible metaphor or not. In this study,

along with other areas, the right BA 47 was activated. This data suggests that decision making about a certain nature of a verbal stimulus might have been a crucial element in activating the right inferior frontal region. In the present study the novelty assessment of a word was judged by having subjects respond by saying 'no', rather than by simply neglecting the word. This may have required an active process of decision making like Bottini's study.

In summary, this study demonstrated participation of the left parahippocampal region in novelty assessment to which activity concerning episodic encoding of a verbal stimulus is inherently related, and the right parahippocampal region in familiarity assessment, in which episodic retrieval processes are greatly involved. Unexpectedly, the right inferior frontal region was activated in association with the left parahippocampal activity, while the left inferior frontal lobe was activated in association with the right parahippocampal activity. According to the nature of our tasks, we hypothesized that the activations of the left inferior frontal lobe was much related to episodic retrieval, while those of the right inferior frontal lobe was related to decision making process.

Acknowledgment

This work was partly supported by a Grant-in Aid(08279103) for scientific research from the Ministry of Education, Science and Culture, Japan, and by "Research for the Future" Program (JSPS-RFTF97L00202) from the Japan Society for the Promotion of Science.

References

1) Kapur, S., Craik, F.I.M., Tulving, E., et al., Proc. Natl. Acad. Sci. USA **91** (1994) 2008.
2) Shallice, T., Fletcher, P., Frith, C.D., et al., Nature **368** (1994) 633.
3) Tulving, E., Kapur, S., Markowitsch, H.J., et al., Proc. Natl. Acad. Sci. USA **91** (1994) 2012.
4) Fletcher, P.C., Frith, C.D., Grasby, P.M., et al., Brain **118** (1995) 401.
5) Tulving, E., Markowitsch, H.J., Craik, F.E., et al., Cerebral Cortex **6** (1996) 71.
6) Fujii, T., Okuda, J., Kawashima, R., et al. NeuroReport **8** (1997) 1113.
7) Roland, P., Graufelds, C.J., Wahlin, J., et al., Hum. Brain Map. **1** (1994) 173.
8) Herscovitch, P., Markham, J. & Raichle, M.E., J. Nucl. Med. **24** (1983) 782.
9) Raichle, M.E., Martin, W.R.W., Herscovitch, P., et al., J. Nucl. Med. **24** (1983) 790.
10) Friston, K.J., et al., Hum. Brain Map. **2** (1995) 189.
11) Schacter, D.L., Reiman, E., Uecker, A., et al., Nature **376** (1995) 587.
12) Dolan, R.J. & Fletcher, P.C., Nature **388** (1997) 582.
13) Nyberg, L., Mcintosh, A. R., Cabeza, R., et al., Proc Natl Acad Sci USA **93** (1996) 11280.
14) Rugg, M.D., Fletcher, P.C., Frith, C.D., et al., Brain **119** (1996) 2073.
15) Bottini, G., Corcoran, R., Sterzi, R., et al., Brain **117** (1994) 1241.
16) Talairach, J. & Tournoux, P. Co-Planar Stereotactic Atlas of the Human Brain. Stuttgart: Thieme (1988).

Table 1. Activated regions related to processing of novel words.

	Regions (Brodmann areas)	Talairach coordinates x	y	z	Z-score
Task 1 minus controll					
Left	Middle occipital gyrus (19)	-50	-58	-14	3.88
	Fusiform gyrus (37/20)	-34	-40	-20	3.74
	Middle temporal gyrus (37)	-42	-62	10	3.61
	Internal capsule	-14	-2	8	3.55
	Cingulate gyrus (23)	-6	-26	30	3.55
	Parahippocampal gyrus (28)	-16	-8	-18	3.52
Right	Precuneus (7)	4	-52	58	3.51
	Precentral gyrus (6)	42	8	8	3.49
Task 1 minus 5					
Left	Parahippocampal gyrus (30)	-16	-38	-4	4.36
	Middle occipital gyrus (37)	-50	-68	2	3.54
Right	Inferior frontal gyrus (45)	32	24	18	4.11
Correlation analysis associated with novelty assessment					
Right	Inferior frontal gyrus (45/46)	30	26	18	4.26
	Middle frontal gyrus (46)	28	28	28	3.46

Stereotaxic coordinates refer to the maximal activation indicated by the highest Z-values in a particular cerebral structure. Distances refer to the stereotactic space defined by Talairach and Tournoux[20] and are expressed in mm. Numbers in parenthesis refer to Brodmann areas.

Table 2. Activated regions related to processing of familiar words.

	Regions (Brodmann areas)	Talairach coordinates x	y	z	Z-score
Task 5 minus controll					
Left	Middle occipital gyrus (19)	-44	-60	-16	3.78
Right	Rectal gyrus (11/25)	6	24	-16	3.74
	Parahippocampal gyrus (28)	10	-6	-10	3.68
	Fusiform gyrus (36)	28	-36	-14	3.67
Task 5 minus 1					
Left	Inferior frontal gyrus (44)	-50	10	20	3.74
Correlation analysis associated with familiarity assessment					
Left	Inferior frontal gyrus (44)	-48	10	18	3.87
	Inferior frontal gyrus (45)	-54	16	20	3.5
	Middle occipital gyrus (19)	-38	-58	-8	3.76
	Cingulate gyrus (30)	-24	-52	4	3.36
Right	Precuneus (31)	12	-60	16	3.65

Stereotaxic coordinates refer to the maximal activation indicated by the highest Z-values in a particular cerebral structure. Other detailes are the same as the Table 1.

Table 1. Additional machine learning [illegible] and [illegible] models.

[illegible]	[illegible]	[illegible]	[illegible]	[illegible]	[illegible]
[illegible]					
[illegible]	[illegible]	[illegible]	[illegible]	[illegible]	[illegible]

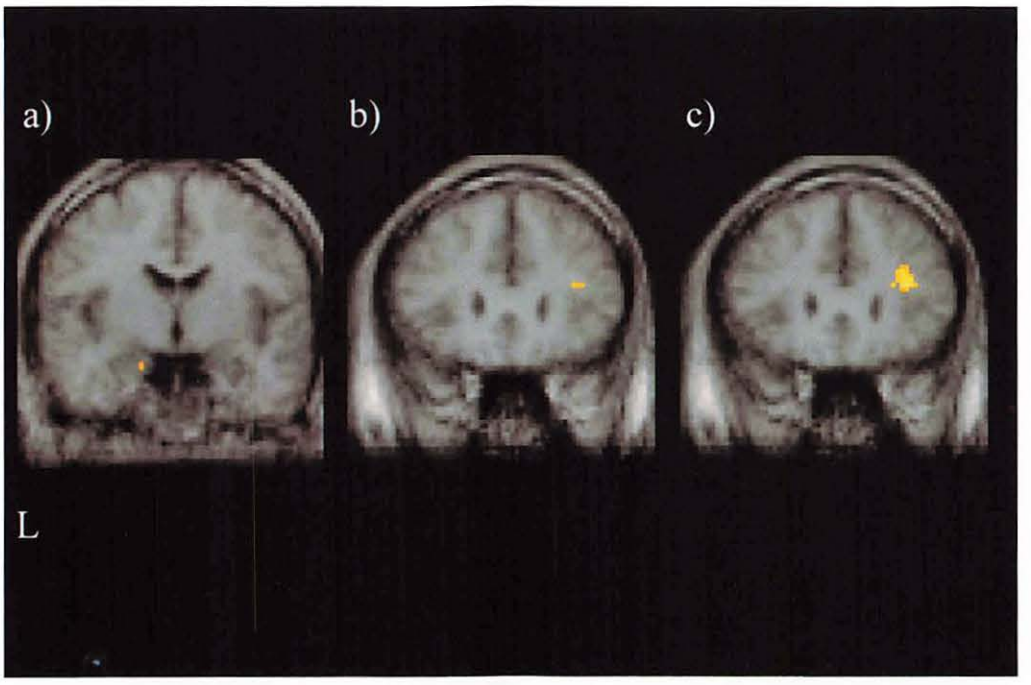

Figure 1. The left parahippocampal and the right frontal activations associated with novelty processing. SPMs are superimposed onto coronal sections of averaged MRI of the subjects. a) The left parahippocampal gyrus (subtraction of the control task from the task 1), b) the right inferior frontal gyrus (subtraction of the task 5 from the task 1), c) the right inferior frontal gyrus (correlation analysis related to novelty of words).

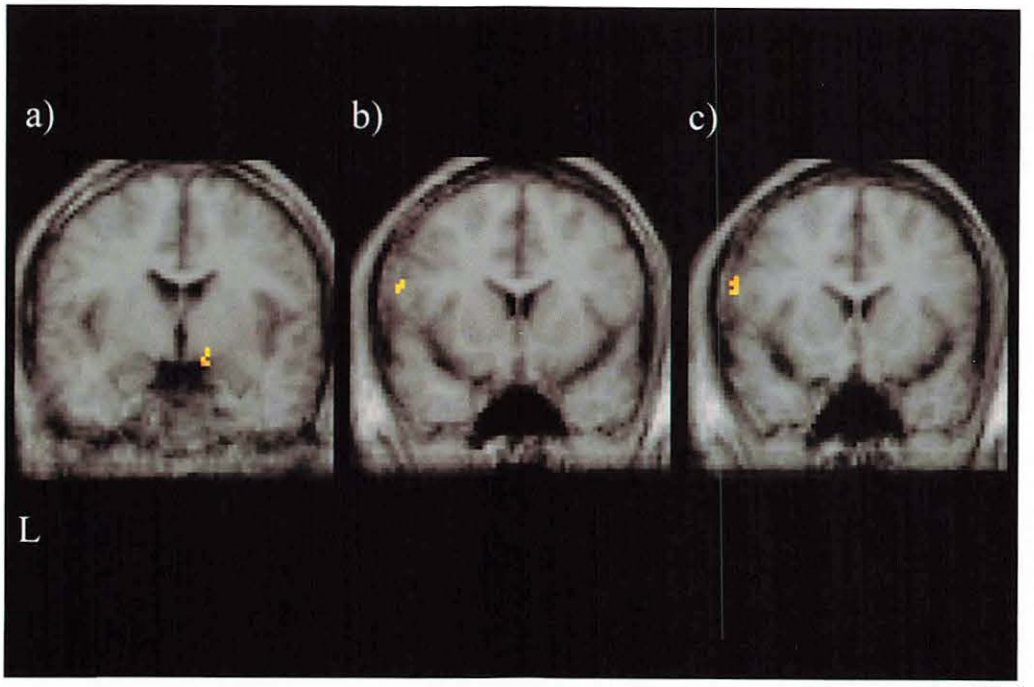

Figure 2. The right parahippocampal and the left frontal activations associated with familiarity processing. SPMs are superimposed onto coronal sections of averaged MRI of the subjects. a) The right parahippocampal gyrus (subtraction of the control task from the task 5), b) the left inferior frontal gyrus (subtraction of the task 1 from the task 5), c) the left inferior frontal gyrus (correlation analysis related to familiarity of words).

V. RADIATION PROTECTION AND TRAINING OF SAFE HANDLING

V. 1. Fast Neutron Profiling with Imaging Plate (2)

-Response of IP with a Converter for Energy and the Converter Thickness-

Sanami T., Saito K., Yamazaki T., Baba M., Ibara Y., Sato J., Hirakawa N. Yamadera A., Taniguchi S.*, and Nakamura T.*,*

Quantum Science and Energy Engineering, Tohoku University
*Cyclotron Radioisotope Center, Tohoku University**

A systematic method of fast neutron profiling using an imaging plate with a polyethylene neutron converter is reported. The relation of the neutron energy and the converter thickness was investigated for the above combination. A fading curve was also obtained and proved to be similar to that by a proton beam. From these results, appropriate conditions were found for the neutron energy, a converter thickness and cooling time after exposure.

Introduction

A method of fast neutron profile measurement will be useful in various applications of fast neutron beam, such as neutron radiography for non-destructive inspection and medical application. To obtain the spatial profile, a two-dimensional fast neutron detector is indispensable. An imaging plate (IP) is an integral type two-dimensional detector which has very high sensitivity and position resolution for X, γ, β-ray and charged particles[1]. In addition, successful application of IP containing Li or Gd was reported for thermal neutrons [2]. For fast neutrons, however, there are few reports of application of IP since it has low sensitivity to fast neutrons despite of its high sensitivity to γ-rays associated with fast neutron.

We have developed a method to measure a fast neutron profile using IP with a polyethylene converter in front of IP (IP-CH_2). In this method, the image of fast neutrons is obtained by detecting recoil protons from the converter and γ-ray contamination can be eliminated by taking difference between the measurement with and without the converter[3]. By this method, we obtained a profile of the 14.1 MeV neutrons collimated by 20cm Cu collimator and the spatial profile of 1, 2, 5 and 15 MeV mono-energetic neutrons after passing acrylic steps of 1 to 5 cm thick or Fe slabs 3.5 and 5 cm thick. To compare the results among the measurements and to improve image quality (S/N), we studied fading property and an appropriate converter thickness.

In this paper, we report the response of IP-CH_2 for 1, 2, 5 and 15 MeV neutrons, the fading curve of IP-CH_2 for 15MeV neutrons, the relationship between the converter thickness and the output (PSL) of IP.

Response for neutron energy

The IP was irradiated by neutrons obtained with a 4.5 MV Dynamitron accelerator at Fast Neutron Laboratory in Tohoku University. In this facility, we tested the responses of IP-CH_2 for various neutron energies. Figure 1 shows the experimental setup. Incident neutrons of 1, 2, 5 and 15 MeV were produced via T(p,n), D(d,n) and T(d,n) reaction, respectively. The distance between the target and IP was fixed to 100 cm to obtain parallel neutron beam. The polyethylene converter was 0.5 cm thick for all the measurements. The converter was set on the surface of IP, X-ray type obtained from Fuji Film Co. Ltd. (BAS-UR), 12.5cm×12.5cm. An NE213 scintillation counter was used to monitor the target condition. The exposure time was about 2 hours with a 4 μA direct beam current for all the neutron energy. We scanned IP and analyzed PSL distribution about 1 hour after the exposure. Scanning was performed by the Bas 3000 system (Fuji Film Co. Ltd.) at CYRIC. Scanning parameters were same for all the scanning, i.e. latitude 4, sensitivity 10000 and gradation 4095. Scanned images were analyzed by Scion Image on Windows PC. From the image, we took values of Photo Simultaneous Luminescence (PSL) for both regions of IP with and without the converter, and deduced the ratio of these two PSL values (S/N) as the quality indicator of the image.

Table 1 summarizes the irradiation conditions and S/N values. Estimated neutron flux is calculated based on the reference data[4]. Figure 2 shows the 300×300-pixel image around the converter edge in 5 MeV measurement. From these results, it is found that S/N becomes higher with neutron energy except for 15 MeV. It can be explained in terms of an effective thickness that is governed by the maximum recoil proton range. The effective thickness indicates the effective number of atoms contributing to the n-p conversion. The reason of lower S/N value for 15MeV is that the maximum proton range exceeds the converter thickness and the H(n,p) cross section is smaller than for 5 MeV. We would get better S/N for 15 MeV neutron, if we use a thicker converter. As a conclusion, 5 and 15 MeV neutron energies are suitable for the IP-CH_2.

Fading property of IP with a polyethylene converter

The experimental setup is same as the above experiment. Imaging Plate (BAS-UR) covered with a 2mm thick polyethylene converter was exposed to 15 MeV neutrons at 840 mm from the neutron producing target. The exposure time was about 1 hour with 4 μA direct beam current. Estimated neutron flux on the IP was 1.5×10^7 #/cm^2. After the exposure, we cut the IP into nine pieces and scanned each piece in every fifteen minutes. The Bas 1000 scanning system was used since it can scan IP with the various sizes.

Figure 3 shows the experimental result and its fitting result using following equation;

$$PSL = A_1 \exp(-\ln 2 \cdot t / B_1) + A_2 \exp(-\ln 2 \cdot t / B_2)$$

In this equation, A_1 and A_2 are amplitude factors for each exponential, B_1 and B_2 are time constants of exponential decay and t is time. The result is B_1 = 24.50 and B_2=2428 min. From this result, it is shown the fading curve has two components. After 1 hour, the fading curve becomes almost flat level, since the first term exponential has rather short decay time constant and the second one has very long. Therefore, to compare the PSL values among the different exposure times, we had better to scan the IPs after cooling time of at least 1 hour. Recently, a fading curve for tens MeV proton was reported by Nohtomi et al.[5] and shown in figure 3. The parameters of the curve is B_1 = 15.5 and B_2=3400 min. Their results are slightly different from ours, but also supports the adoption of 1 hour cooling time.

Response of converter thickness

We measured the PSL value as a function of converter thickness to check the response of IP-CH_2, and compared with the Monte-Carlo calculation.

Experiments were carried out for 5 and 15 MeV neutrons. The step converter was set in front of IP (BAS-UR) that located at 840mm from target. The converters are 60μm to 300 μm thick in 60 μm steps for 5MeV, and, 60μm to 300 μm thick in 60 μm steps and 100μm to 500μm thick in 100 μm steps for 15 MeV. The thickest converter of each step is almost equivalent to the maximum range of recoil protons. Estimated neutron flux on the IP is 3.3×10^7 and 1.4×10^7 for 5 and 15 MeV, respectively. Scanning was carried out by Bas 3000 system after 1 hour exposure. Figure 4 shows two-dimensional image obtained by the 15 MeV experiment.

To estimate PSL values for converters with different thickness and the neutron energy, we developed a program that calculates the energy deposit in IP by Monte-Carlo method. The program calculates the energy deposit under the following assumptions: (1) The protect layer of IP (BAS-UR) is a 10 μm thick polyethylene-terephthalate, (2) the effective area of IP is made of $BaFBr_{0.85}I_{0.15}$ (Ba:33%, F:33%, Br:28%, I:6%), (3) γ-ray contamination is eliminated completely by subtraction, (4) all deposited energy is measured as PSL (ignoring the depth effect), (5) amount of PSL is proportional to LET (ignoring the LET effect). The energy loss data were calculated by the TRIM code based on the equation of Ziegler.

Figures 5 and 6 show comparison between experiment and calculation for 5 and 15 MeV neutrons, respectively. The calculation is normalized to the experimental data at maximum PSL value. The calculations are in fair agreement with the experimental ones in both neutron energies. It indicates that the above assumptions are appropriate and the dominant components on the PSL value are the incident number of protons and total energy deposit in the effective layer of IP. In addition, we can conclude that almost all the PSL is originated by recoil protons. It is preferable to use the converter which is as thick as the

maximum proton range, to get better S/N result. However, we have to check the effects of converter thickness to spatial resolution.

Conclusion

To obtain fast neutron spatial distribution, we have investigated a method to measure the fast neutron profile with IP using a polyethylene converter. From the effect of a neutron energy and a converter thickness, it was found that good S/N is achieved using 5 or 15 MeV neutron and the converter whose thickness is equivalent to the maximum proton range. The response to the different thickness converter was in fair agreement with the Monte-Carlo calculation.

Acknowledgment

The authors would like to express their appreciation to Prof. Julius Csikai from Kossuth University, Debrecen, Hungary for his useful advice and discussion.

References

(1) Takahashi K., Tazaki S., Miyahara J., Karasawa Y. and Niimura N., Nucl. Instrm. and Meth., **A377** (1996) 119.

(2) Niimura N., Karasawa Y., Tanaka I., Miyahara J., Takahashi K., Saito H., Koizumi S. and Hidaka M., Nucl. Instrm. and Meth., **A349** (1994) 521.

(3) Sanami T., Baba M., Saito K., Ibara Y., Hirakawa N., Yamadera A., Taniguchi S. and Nakamura T., Proc. of 11th Workshop on Radiation Detector and Their Uses (1997 KEK, Japan) p74.

(4) Baba M., Takada M., Iwasaki T., Matsuyama S., Nakamura T., Ohguchi H., Nakao T., Sanami T. and Hirakawa N., Nucl. Instrm. and Meth., **A376** (1996) 115.

(5) Nohtomi A., private communication.

Table 1 Irradiation neutron flux and output values of IP in various energies. Distance from target to IP is 100cm and converter thickness is 0.5 mm

En [MeV]	Neutron Flux [#/cm^2]	With converter [PSL/pixel]	Without converter [PSL/pixel]	S/N [without/with]
1	2.58E+06	0.67	0.64	1.05
2	4.99E+06	1.73	1.49	1.16
5	2.94E+07	2.50	0.75	3.57
15	1.83E+07	3.03	1.73	1.75

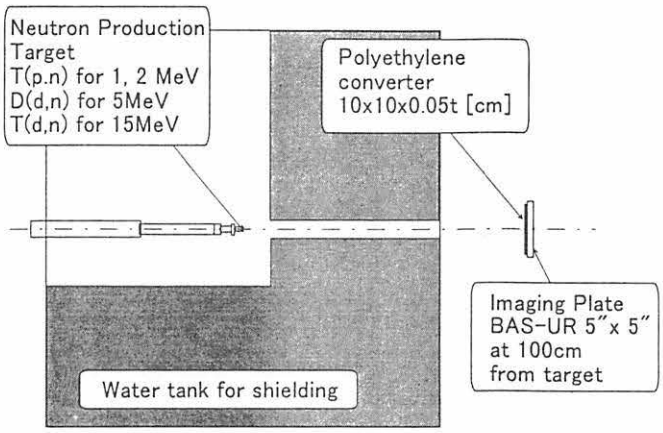

Fig. 1. Experimental setup for exposure IP.

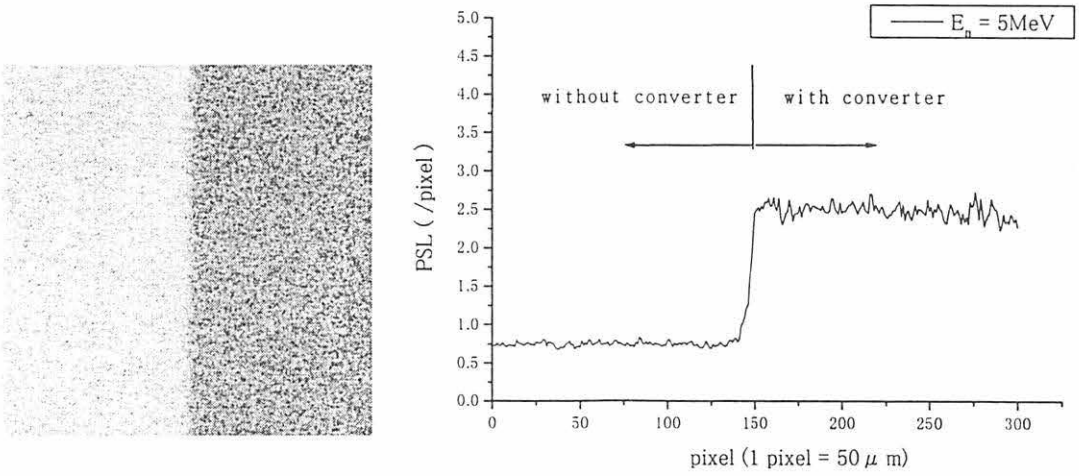

Fig. 2. 300×300pixcel image around converter edge in 5MeV measurement.

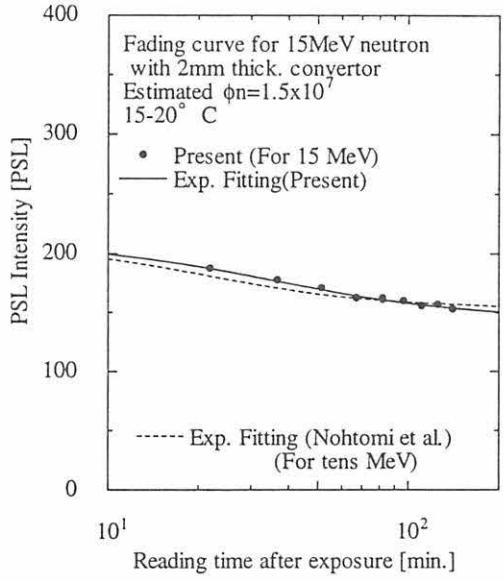

Fig. 3. The experimental result of fading curve for IP with polyethylene converter.

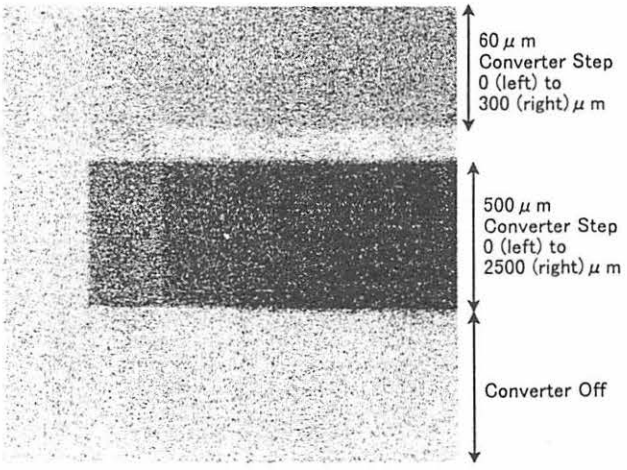

Fig. 4. Two-dimensional image of 15 MeV measurement for converter steps.

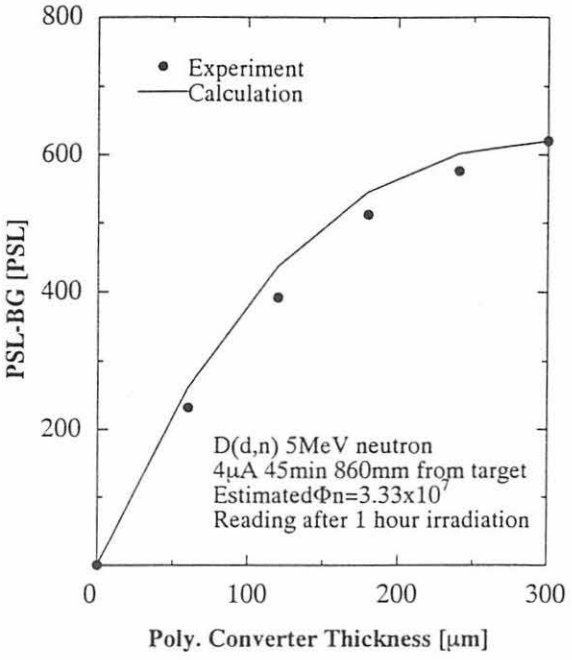

Fig. 5. The relationship of converter thickness and PSL 5MeV neutrons.

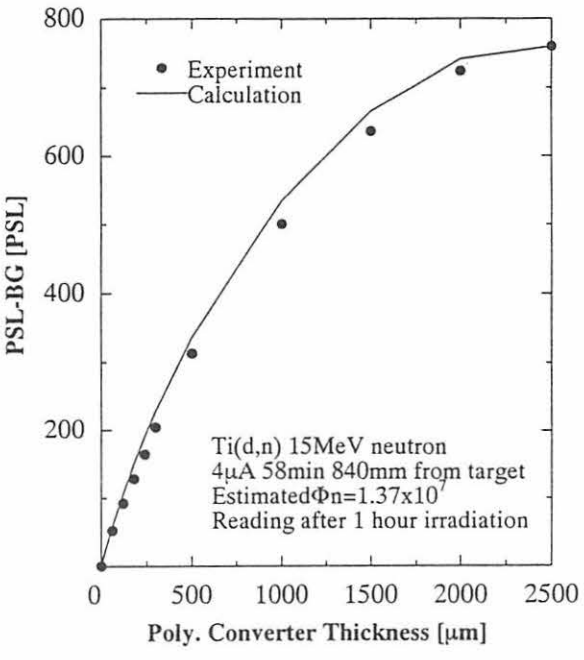

Fig. 6. The relationship of converter thickness for and PSL for 15MeV neutrons.

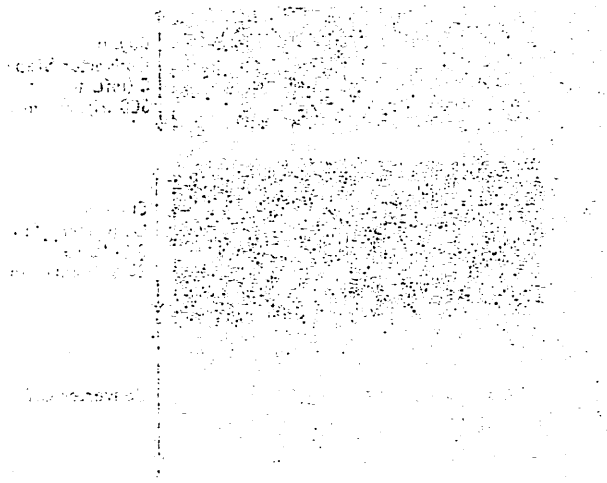

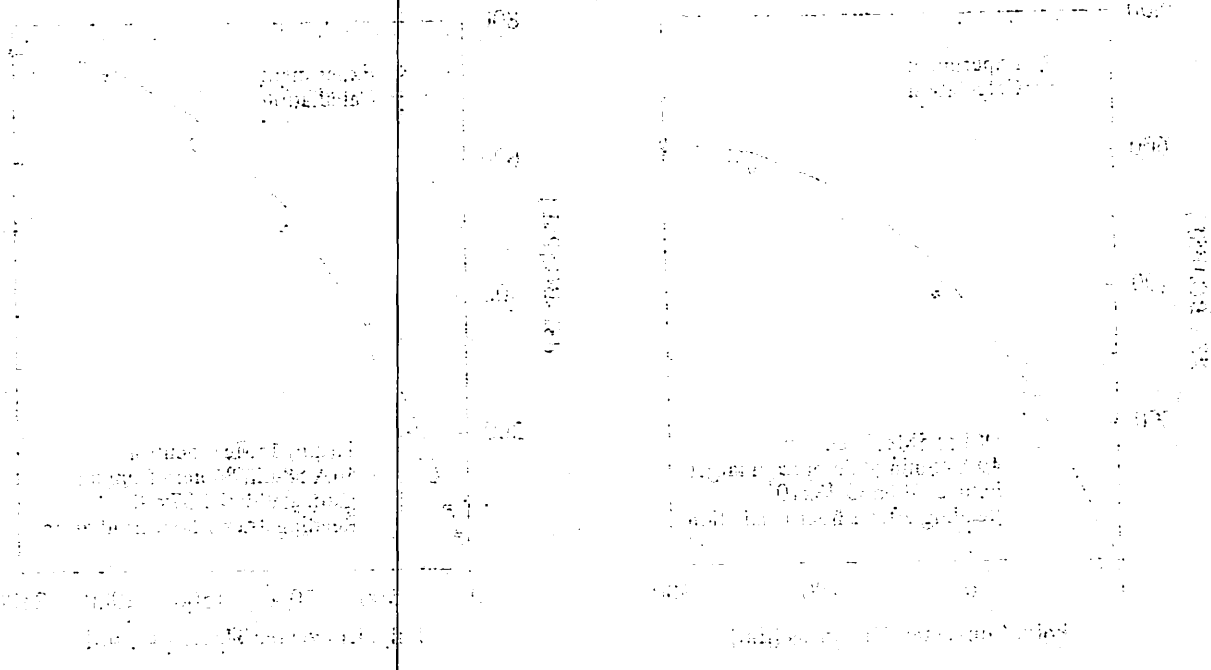

V. 2. Application of Self-TOF high Energy Neutron Detector for Neutron Scattering Cross Section Measurements

Sasaki M., Nakao M., Nakamura T., Nakao N., and Shibata T.**

Cyclotron and Radioisotope Center, Tohoku University
High Energy Accelerator Research Organization Tokyo 188, Japan*

Introduction

A self-TOF which measures the neutron-induced proton time of flight (TOF) has been developed[1,2] for high energy neutron spectrometry This detector is composed of a VETO counter for elimination of charged particles, START and STOP detectors for measurement of recoiled proton energy by the TOF method. The VETO counter is a 150 mm × 150 mm × 5 mm-thick, the START detector is a 80 mm diam. × 0.5 mm-thick and the STOP detector is a 200 mm × 200 mm × 20 mm-thick NE102A plastic scintillator. The performance of this detector was tested under a quasi-monoenergetic p-Li neutron field at CYRIC[3] (Cyclotron and Radioisotope Center, Tohoku University). This detector is planned to be applied for measurements of neutron scattering cross section.

Experiment

The experimental setup at CYRIC is shown in Fig. 1. The proton beams accelerated up to 35 MeV by a cyclotron were transported to the scattering chamber through a beam swinger in the No. 5 target room. A proton beam was focused onto a 2 mm thick natural Li target which has about 2 MeV loss of incident proton energy. The proton beam was inclined at 10° to the horizontal line with a beam swinger in order to shield neutrons produced from a Faraday cup. The neutrons emerging from the Li target at 10° were transported down to the TOF extension room.

The VETO counter was used to discriminate the neutrons and charged particles incident to the radiator, since neutrons do not scintillate the VETO counter. The radiator was put between the VETO counter and the START detector and the recoiled protons from the radiator due to the H(n,p) elastic scattering reaction were measured between the START and the STOP detectors by the TOF method. The proton energy E_p is obtained from the proton flight time and the neutron energy E_n is then determined by $E_n = E_p / cos^2\theta$ where θ is the scattering angle.

In the experiment, three types of radiators, polyethylene (POLY), graphite (GRA) and nothing (BLANK), were used to subtract the contribution of protons produced from carbon in the polyethylene radiator and from other detectors.

Data analysis

The pulse height distributions of scintillation light outputs from the VETO, START and STOP detectors were stored with integrating-type ADC(LeCroy 2249W) which was gated by coincidence signals of the START and STOP detectors . The proton TOF spectra were stored with TDC together with the neutron TOF spectra using the RF (Radio Frequency) signal from a cyclotron as a start signal for comparison.

As the events to be analyzed for estimation of neutron energy spectra are the proton events produced from radiator, the VETO pulse height was fixed to be noise level to avoid the primary charged particles and START pulse height to be high enough to discriminate the protons induced in the START detector. Fig. 2 shows the two dimensional distribution of light outputs of the STOP detector and the recoiled proton TOF spectrum. The left graph gives two gamma-ray peaks and proton events. The right graph shows the same two dimensional plot after selection of proton events.

The proton energy spectra given for three radiators, polyethylene (f_{POLY}), graphite (f_{GRA}) and nothing (f_{BLANK}), which are shown in Fig. 3, were determined from relativistic kinematics using the recoiled proton TOF spectra after correction of energy loss in the START scintillator. The proton events induced by only H(n,p) elastic scattering from polyethylene radiator($f_{H(n,p)}$) can be obtained by using the above three neutron energy spectra from the following formula which subtracts unnecessary components,

$$f_{H(n,p)} = (f_{POLY} - f_{BLANK}) - (f_{GRA} - f_{BLANK}) \times \eta$$

,where η is the ratio of carbon density of the polyethylene radiator to that of the graphite radiator.

Detection efficiency

The neutron fluence $f(E_n)$ for incident neutron energy is given by

$$\phi(E_n) = \frac{1}{4\pi S^2 \varepsilon(E_n)} \frac{dE_p}{dE_n} \phi_{H(n,p)},$$

where $\varepsilon(E_n)$ is the detection efficiency of a self TOF detector, $Y(E_p)$ is the yield of recoil protons measured with a self TOF detector as a function of recoil proton energy E_p, and S is the distance between Li target and radiator. The detection efficiency $\varepsilon(E_n)$ was calculated analytically[3] with the angular differential n-p scattering cross section $\sigma(\theta_{np})$ when radiator and detector are circular, as follows

$$\varepsilon(E_n) = \frac{N\tau D}{4\pi}\int_0^{R_s}\tau_s d\tau_s \int_0^{2\pi} d\omega \int_0^{R_d}\tau_d d\tau_d \int_0^{2\pi} d\psi \frac{\sigma(\theta_{np})}{s^2 d^3}$$

where N is the number density of hydrogen in a radiator, τ is the radiator thickness, D is the distance between radiator and STOP detector, R_s is the radiator radius and R_d is the detector radius. As the STOP detector has a shape of square, R_d was approximated to be a radius of the detector which has the same area as this STOP detector. s is the distance between Li target and the n-p reaction point in the radiator, d is the distance from the n-p reaction point in the radiator to the recoil proton injection point onto the STOP detector, as seen in Fig. 4.

Results and discussions

Fig. 5 shows the experimental data together with the neutron spectrum obtained by the PRT (Proton Recoil Telescope). The peak energy is about 1 MeV lower and the fluence of peak component is about 15 % smaller compared with the PRT spectrum. The difference of peak energy is reduced to the neglection of energy loss correction caused by proton flight of 1 m in air. The underestimation of peak fluence comes from various factors which are necessary to correct. We are now considering these correction.

Conclusions

The performance test of the self TOF detector for measurements of neutrons was done at CYRIC. By using three type of radiators, the contribution of carbon reaction in polyethylene radiator and background was able to be subtracted. This detector is now applying for the neutron scattering cross section measurements.

References

1) M. Nakao et al., KEK Proc. of 11th Workshop on Radiat. Detec. and Their Uses, p102, (1997).
2) N. Nakao et al., RIKEN Accel. Prog. Rep. **29** (1996).
3) M. Takada et al., Nucl. Instrum. Methods, A 372, p253 (1996).

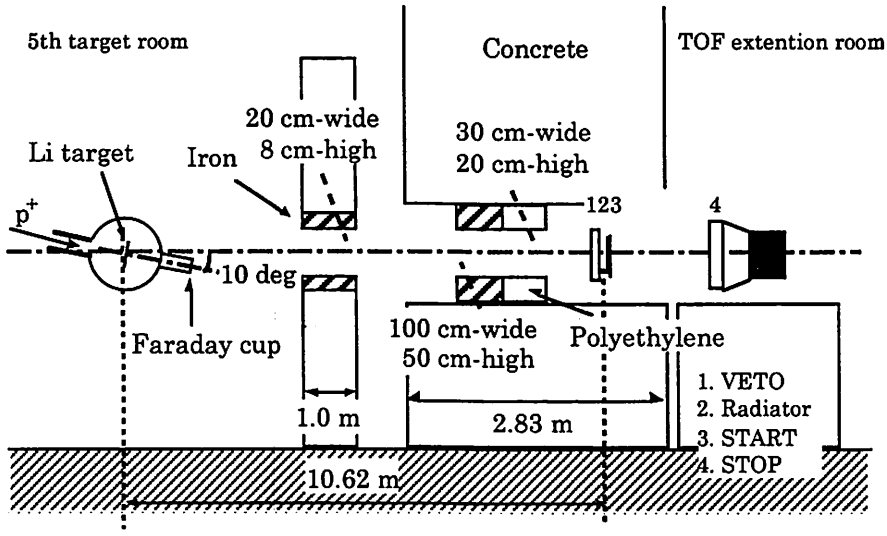

Figure 1. Experimental setup at CYRIC. The distance from START to STOP was 1 m.

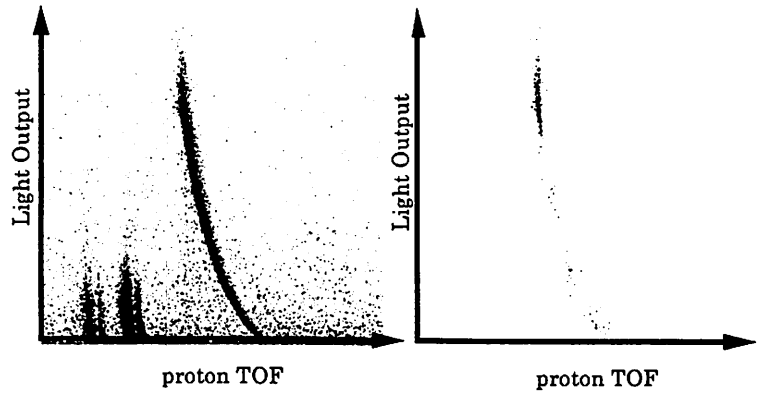

Figure 2. Two dimensional plots of proton TOF outputs and STOP's light outputs of raw data(left) and after selection of proton events(right).

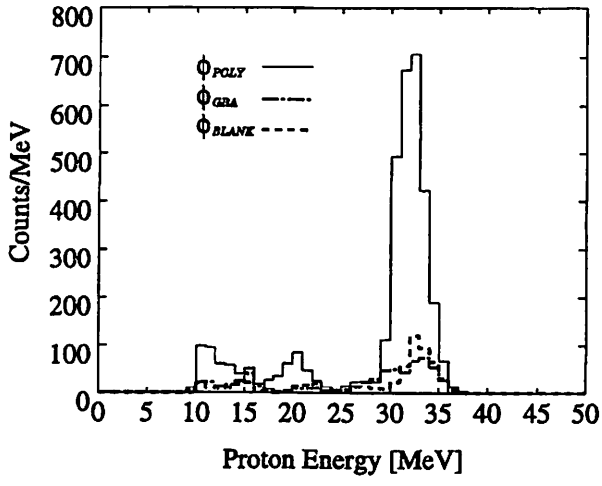

Figure 3. The proton energy spectra for three radiators.

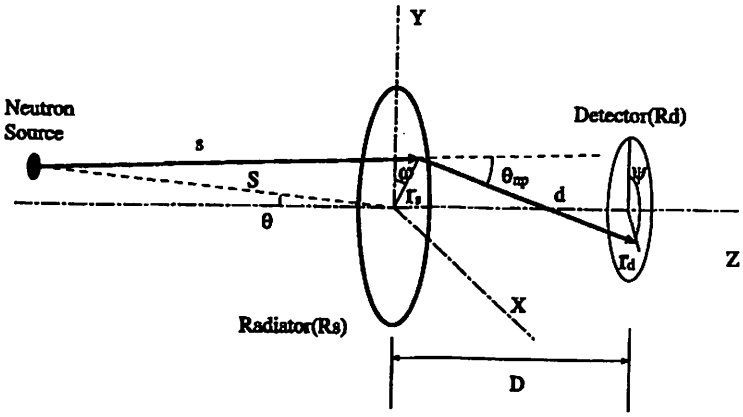

Figure 4. Schematic diagram for detection efficiency calculation.

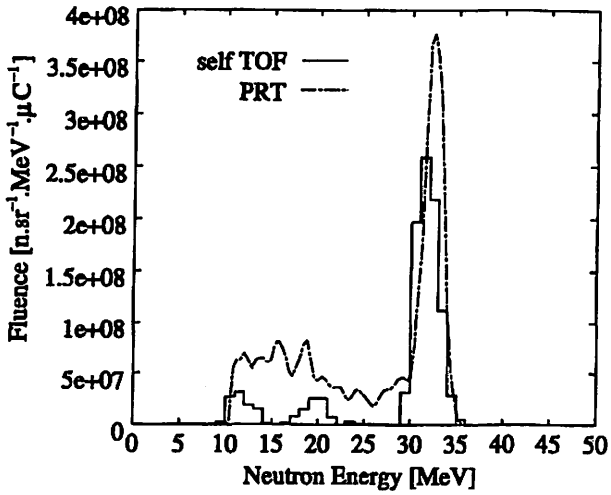

Figure 5. Comparison of neutron energy spectra given by the self-TOF detector(line) and of the PRT (proton recoil telescope).

V. 3. Radiation Protection and Management

*Miyata T., Yamadera A., Nakamura T., and Watanabe N.**

Cyclotron and Radioisotope Center, Tohoku University
*Japan Radiation Protection Co., Ltd.**

Cyclotron and Radioisotope Center, Tohoku University
*Japan Radiation Protection Co., Ltd.**

(1) Unsealed radionuclides used in the center

The kinds and activities of unsealed radionuclides handled in the center in 1997 are shown in Table 1. The table includes the isotopes produced by the cyclotron, purchased from the Japan Isotope Association and took over from another RI institutes.

(2) Individual monitoring

The exposure doses of the workers in the center in 1997 is given in Table 2. They were less than the permissible doses.

(3) Monitoring of the workplace

Radiation dose rates inside and outside of the controlled areas were monitored periodically and as needed. They were below the legal permissible levels. Surface contamination levels of the floors inside the controlled areas were measured by smear method and with survey meters periodically and as needed. They also cleared under the legal regulation levels.

(4) Wastes management

The radioactive wastes delivered to the Japan Radioisotope Association in 1997 are shown in Table 3. The concentration of radioisotopes in the air released after filtration from the stack was monitored with stack gas monitors. The levels were less than the legal regulation levels. The radioactive water was storaged at the tanks at least for 3 days and then released to the sewerage after confirming that the concentration was less than permissible levels.

The treated volume of radioactive waste of organic scintillator was 1586 l by the incinerator made by Fujikogyo Co., Ltd.

Table 1. Unsealed radionuclides used in the center in 1997.

(a)Cyclotron Building	(kBq)
group 3	
^{11}C	235,595,320.000
^{13}N	4,000.000
^{15}O	15,569,600.000
^{28}Mg	2,595.000
^{111}In	1,603,530.000
^{45}Ti	888,000.000
total	253,663,045.000
group 4	
^{18}F	464,298,200.000
total	464,298,200.000

(b) RI Building	(kBq)
group 1	
^{90}Sr	120.000
total	120.000
group 2	
^{45}Ca	169,837.875
^{60}Co	3,468.540
^{65}Zn	34,438.600
^{68}Ge	67,962.000
^{85}Sr	26,725.000
^{109}Cd	5,268.660
^{125}I	110,462.999
^{137}Cs	17,776.800
total	435,940.474

^{131}I	150,305.100
^{34m}Cl	2,000.000
^{45}Ti	1,295,000.000
total	4,574,413.964
group 4	
^{3}H	519,957.424
^{14}C	264,198.304
^{18}F	302,178,750.000
total	302,962,905.728

(c)Research Building	(kBq)
group3	
^{11}C	921,300.000
^{15}O	69,819,000.000
total	70,740,300.000
group 4	
^{18}F	5,516,700.000
total	5,516,700.000

group 3	
^{11}C	186,000.000
^{13}N	2,000.000
^{28}Mg	1,964.000
^{32}P	1,478,208.134
^{35}S	18,446.650
^{99}Mo	718,910.000
^{99m}Tc	718,910.000
^{100}Rh	2,670.000

Table 2. Occupational radiation exposures at the center in 1997.

Dose range (mSv)	Number of individuals
No measurable exposure	39
Measurable exposure less than 1.0	6
1.0 to 2.5	5
Total persons monitored	50

Table 3. Radioactive wastes delivered to the Japan Radioisotope Association in 1997.

Wastes	Container	Number
solids		
Combustible Type I	50 ℓ drum	24
Combustible Type II	50 ℓ drum	18
Incombustibles	50 ℓ drum	5
Annimal carcasses	50 ℓ drum	17
Filters	1 ℓ /unity	454
liquids		
inorganic liquids	25 ℓ PE bottle	13

Type I:Cloth and Paper made of natural cellulose.
Type II:Combustible Plastics such as Polyethylene and Polypropylene.

V. 4. Training for Safehandling of Radiation and Radioisotopes and X-Ray Machines for Beginners in Tohoku University

Nakamura T., Yamadera A., and Miyata T.

Cyclotron and Radioisotope Center, Tohoku University

Training for safehandling of radiation and radioisotopes for beginners has been conducted twice a year from 1977 in Tohoku University. The contents of lectures and practices are shown in Table 1. In 1997 the training was performed for 553 persons. The departments to which they belong are given in Table 2.

Training for safehandling of X-ray machines and electron microscopes began from the end of 1983. The training is scheduled to be held twice a year at the same time as the safehandling of radiation and radioisotopes. Only lectures are given and not practices. The contents of the lectures and the distributions of trainees are shown in Tables 3 and 4, respectively.

Training for safehandling of synchrotron radiation began from the end of 1995. The contents of the lectures are the same as safehandling of radiation and radioisotopes for beginners and not practices. In 1997 the training was performed for 87 persons.

Table 1. Contents of lectures and practices for safehandling of radiation and radioisotopes in 1997.

Lectures (one day)	
Radiation physics and measurements	1.5 (hours)
Chemistry of radioisotopes	1.0
Radiological protection ordinance	1.5
Effects of radiation on man	1.0
Safehandling of radioisotopes	1.5

Practices (one day)	
Treatment of unsealed radioactive solution	4.0 (hours)
Measurements of surface contamination and decontaminatio	1.0
Measurements of gamma rays and beta rays	2.0

Table 2. Distribution of trainees for safehandling of radiation and radioisotopes in 1997.

Department	Staff	Student	Total
Medicine	36	108	144
Dentistry	1	9	10
Pharmacy	1	43	44
Science	4	91	95
Engineering	3	71	74
Agriculture	1	93	94
Research Institutes	7	74	81
The others	3	8	11
Total	56	497	553

Table 3. Contents of lectures for safehandling of X-ray machines and electron microscopes in 1997.

Safehandling of X-ray machines	1.5 (hours)
Radiological protection ordinance	1.0
VTR for safehandling of radiation and radioisotopes	1.0

Table 4. Distribution of trainees for safehandling of X-ray machines and electron microscopes in 1997.

Department	Staff	Student	Total
Science	2	29	31
Engineering	6	69	75
Research Institutes	13	94	107
Total	21	192	213

Table 5. Distribution of trainees for synchrotron radiation in 1996.

Department	Staff	Student	Total
Science	0	19	19
Engineering	0	50	50
Research Institutes	1	17	18
Total	1	86	87

VI. PUBLICATIONS

VI. PUBLICATIONS

(January 1997 ~ December 1997)

A

1. A Convenient Cryogenic Trap with Liquid Nitrogen for the Concentration of [^{11}C]CO_2
   R. IWATA, T. IDO, Z. KOVACS and I. MAHUNKA
   Applied Radiation and Isotopes, Vol. 48, No. 4, pp. 483-485, (1997)

2. Performance study of a miniature gamma ray scintillation vivo probe for tumor localization
   Hossain M. DELOAR, Hiroshi WATABE, Yoshiharu HAYASHI, Masayasu MIYAKE, Takashi NAKAMURA, Hiromu TAKAHASHI, Takashi YOSHIOKA, Ryunosuke KANAMARU, Takehiko Fujiwara and Masatoshi ITOH
   Annals of Nuclear Medicine, Vol. 11, No. 2, pp. 173-181, (1997)

3. Analog transitions in sd- and f-shell nuclei and the isovector part of optical potentials studied by the (p, n) reaction at 35 MeV
   G. C. Jon, H. Orihara, T. Niizeki, M. Oura, K. Ishii, A. Terakawa, M. Hosaka, K. Itoh, C. C. Yun, Y. Fujii, T. Nakagawa, K. Miura, and H. Ohnuma
   PHYSICAL REVIEW C, Vol. 56, No. 2, pp. 900-907, (1997)

4. Internal Dose Estimation Including the Nasal Cavity and Major Airway for Continuous Inhalation of $C^{15}O_2$, $^{15}O_2$ and $C^{15}O$ Using the Thermoluminescent Dosimeter Method
   H. M. Deloar, H. Watabe, T. Nakamura, Y. Narita, A. Yanadera, T. Fujiwara and M. Itoh
   The Journal of Nuclear Medicine, Vol. 38, No. 10, pp. 1603-1613, (1997)

5. Performance evaluation of a large axial field-of-view PET scanner: SET-2400W
   Takehiko FUJIWARA, Shoichi WATANUKI, Seiichi YAMAMOTO, Masayasu MIYAKE, Shinya SEO, Masatoshi ITOH, Keizou ISHII, Hikonojo ORIHARA, Hiroshi FUKUDA, Tomohiko SATOH, Keishi KITAMURA, Kazumi TANAKA and Shigeru TAKAHASHI
   Annals of Nuclear Medicine Vol. 11 No. 4, 307-313, (1997)

6. Effects of Haloperidol and Cocaine Pretreatments on Brain Distribution and Kinetics of [^{11}C]Methamphetamine in Methamphetamine Sensitized Dog: Application of PET t o Drug Pharmacokinetic Study
   Hitoshi Nakamura, Takanori Hishinuma, Yoshihisa Tomioka, Shunji Ishiwata Tatsuo Ido, Ren Iwata, Yoshihito Funaki, Masatoshi Itoh, Takehiko Fujiwara, Kazuhiko Yanai, Mitsumoto Sato, Yohtaro Numachi, Sumiko Yoshida and Michinao Mizugaki
   Nuclear Medicine & Biology, Vol. 24, pp. 165-169, (1997)

7. Monte Carlo Evaluation of Accuracy and Noise Properties of Two Scatter Correction Methods for ^{201}Tl Cardiac SPECT
   Yuichiro Narita, Hidehiro Iida, Stefan Eberl, Takashi Nakamura
   IEEE TRANSACTION ON NUCLEAR SCIENCE 44(1997)2465-2472

B

8. Assessment of Cancer Recurrence in Residual Tumors after Fractionated Radiotherapy: A Comparison of Fluorodexyglucose, L-Methionine and Thymidine
Michael J. Reinhardt, Kazuo Kubota, Susumu Yamada, Ren Iwata and Hiroshi Yaegashi
The Journal of Nuclear Medicine, Vol. 38, No. 2, pp. 280-287, (1997)

9. Age-related Changes in [^{3}H]Nimodipine and [^{3}H]Rolipram Binding in the Rat Brain
T. ARAKI, H. KATO, K. SHUTO, AND Y. ITOYAMA
J. Pharm. Pharmacol., Vol. 49, pp. 310-314, (1997)

10. Effect of aging on dopaminergic receptors and uptake sites in the rat brain studied by receptor autoradiography
Tutomu Araki, Hiroyuki Kato, Katsuro Shuto, Takehiko Fujiwara, Yasuto Itoyama
Journal of Neurological Sciences, Vol. 148, pp. 131-137, (1997)

11. Effect of Nitric Oxide Synthase Inhibitor on Age-related Changes in Second Messenger Systems and Calcium Channels in Rats
T. Araki, H. Kato, K. Shuto, T. Fujiwara and Y. Itoyama
Metabolic Brain Disease, Vol. 12, No. 1, pp. 83-92, (1997)

12. Effects of vinconate on age-related alterations in [^{3}H]MK-801, [^{3}H]glycine, sodium-dependent D-[^{3}H]aspartate, [^{3}H]FK-506 and [^{3}H]PN200-110 binding in rats
Tutomu Araki, Hiroyuki Kato, Sumiko Nagaki, Katsuro Sutou, Takehiko Fujiwara, Yasuto Itoyama
Mechanisms of Aging and Development, Vol. 95, pp. 13-29, (1997)

13. Effects of chronic treatment with a cyclic AMP-selective phosphodiesterase inhibitor, rolipram, on excitatory amino acid neurotransmission systems in young and aged rat brains
H. Kato, T. Araki, T. Chen, X.-H. Liu, T. Hiranuma, K. Murase, Y. Itoyama, and K. Kogure
Journal of Neural Transmission, Vol. 104, pp. 269-280, (1997)

14. Age-related changes of sodium-dependent D-[^{3}H]aspartate and [^{3}H]FK506 binding in rat brain
T. Araki, H. Kato, K. Shuto, T. Fujiwara, and Y. Itoyama
Journal of Neural Transmission, Vol. 104, pp. 259-267, (1997)

15. Transport efficiency of fission products in IGISOL
H. Kudo, M. Maruyama, M. Tanikawa, M. Fujita, T. Shinozuka, M. Fujioka
Nuclear Instruments and Methods in Physics Research B, Vol. 126, pp. 209-212, (1997)

16. Different roles of the left and right parahippocampal regions in verbal recognition: a PET study
T. Fujii, J. Okuda, R. Kawashima, A. Yamadori, R. Fukatsu, K. Suzuki, M. Ito, R. Goto and H. Fukuda
NeuroReport, Vol. 8, No. 5, pp. 1113-1117, (1997)

17. Myocardial Glucose Metabolism is Different between Hypertrophic Cardiomyopathy and Hypertensive Heart Disease Associated with Asymmetrical Septal Hypertrophy
NOBUYUKI SHIBA, YUTAKA KAGAYA, NOBUMASA ISHIDE, DAIYA TAKEYAMA, YURIKO YAMANE, MASANOBU CHIDA, HIROKI OTANI, TATSUO IDO, AND KUNIO SHIRATO
Tohoku J. Exp. Med., Vol. 182, pp. 125-138, (1997)

18. Effect of NG-Nitro-L-Arginine on Age-Related Changes of Glutamate Receptor Systems and Immunophilin in Rats
Tsutomu Araki, Yoshiteru Oshima, Hiroyuki Kato, Katsuro Shuto and Yasuto Itoyama
Meth Find Exp Clin Pharmacol, Vol. 19, No. 6, pp. 373-381, (1997)

19. Stimulated Glucose Uptake in the Ischemic Border Zone: Its Dependence on Glucose Uptake in the Normally Perfused Area
Yuriko Yamane, Nobumasa Ishide, Yutaka Kagaya, Daiya Takeyama, Nobuyuki Shiba, Masanobu Chida, Tetsuji Nozali, Toshihiro Takahashi, Tatsuo Ido and Kunio Shirato
The Journal of Nuclear Medicine, Vol. 38, No. 10, pp. 1515-1521, (1997)

20. Decreased corticalglucose metabolism correlates with hippocampal atrophy in Alzheimer's disease as shown by MRI and PET.
Yamaguchi S. Meguro K. Itoh M. Hayasaka C. Shimada M. Yamazaki H. Yamadori A.
Journal of Neurology, Neurosurgery & Psychiatry. 62(6):596-600, (1997)

21. Influence of chemotherapy on FDG uptake by human cancer xenografts in nude mice.
Yoshioka T. Takahashi H. Oikawa H. Maeda S. Ido T. Akaizawa T. Fukuda H. Kanamaru R.
Journal of Nuclear Medicine. 38(5):714-7, (1997)

22. Regional cerebral glucose utilization is modulated by the dosage of apolipoprotein E type 4 allele and alpha1-antichymotrypsin type A allele in Alzheimer's disease.
Higuchi M. Arai H. Nakagawa T. Higuchi S. Muramatsu T. Matsushita S. Kosaka Y. Itoh M. Sasaki H.
Neuroreport. 8(12):2639-43, (1997)

23. Striatal dopamine metabolism correlated with frontotemporal glucose utilization in Alzheimers-disease - A double-tracer PET study.
Meguro K. Yamaguchi S. Itoh M. Fujiwara T. Yamadori A.
Neurology. 49(4):941-945, (1997)

24. Psychiatric wandering behaviour in dementia patients correlated with increased striatal dopamine D-2 receptor as shown by [C-11]YM-09151-2 and positron emission tomography.
Meguro K. Itoh M. Yanai K. Takase K. Yamaguchi S. Ido T. Yamadori A.
European Journal of Neurology. 4(3):221-226, (1997)

25. Activity in the parietal area during visuomotor learning with optical rotation
Ketaro Inoue, Ryuta Kawashima, Kazunori Satoh, Shigeo Kinomura, Ryoi Goto, Motoaki Sugiura, Masatoshi Itoh and Hiroshi Ukuda
NeuroReport 8, 3979-3983(1997)

VII. MEMBERS OF COMMITTEES

VII. Members of Committees (as of Jan. 1, 1998)

General

(Chairman)	Hikonojo	Orihara	(CYRIC)
	Osamu	Hashimoto	(Faculty of Science)
	Hiroshi	Kudo	(Faculty of Science)
	Kohshi	Yoshimoto	(School of Medicine)
	Tadashi	Yamada	(School of Dentistry)
	Tetsuya	Terasaki	(Faculty of Pharmaceutical Sciences)
	Katsunori	Abe	(Faculty of Engineering)
	Yoshiyuki	Kamio	(Faculty of Agriculture)
	Reimon	Hanada	(Institute for Materials Research)
	Minoru	Issiki	(Research Institute for Mineral Dressing and Metallurgy)
	Hiroshi	Fukuda	(Institute for Development, Aging and Cancer)
	Jirohta	Kasagi	(Laboratory of Nucler Science)
	Syogo	Yamada	(School of Medicine)
	Manabu	Fujioka	(CYRIC)
	Tatsuo	Ido	(CYRIC)
	Takashi	Nakamura	(CYRIC)
	Masatoshi	Itoh	(CYRIC)
	Ren	Iwata	(CYRIC)
	Akira	Yamadera	(CYRIC)
	Keizo	Ishii	(Faculty of Engineering)
	Tadao	Saitou	(Faculty of Agriculture)
	Sadaei	Yamaguchi	(Institute for Materials Research)
	Michiharu	Katoh	(Institute for Chemical Reaction Science)

Research Program

(Chairman)	Takashi	Nakamura	(CYRIC)
	Takemi	Nakagawa	(Faculty of Science)
	Tsutomu	Sekine	(School of Medicine)
	Takehiko	Watanabe	(Faculty of Science)

	Kohshi	Yoshimoto	(School of Medicine)
	Hidetada	Sasaki	(School of Medicine)
	Katsunori	Abe	(Faculty of Engineering)
	Mieko	Kawamura	(Faculty of Agriculture)
	Reimon	Hanada	(Institute for Materials Research)
	Hiroshi	Fukuda	(Institute for Development, Aging and Cancer)
	Manabu	Fujioka	(CYRIC)
	Tatsuo	Ido	(CYRIC)
	Keizo	Ishii	(Faculty of Engineering)
	Masatoshi	Itoh	(CYRIC)

Cyclotron

(Chairman)	Manabu	Fujioka	(CYRIC)
	Osamu	Hashimoto	(Faculty of Science)
	Takemi	Nakagawa	(Faculty of Science)
	Satoru	Kunii	(Faculty of Science)
	Tsutomu	Sekine	(Faculty of Science)
	Kazushige	Maeda	(Faculty of Science)
	Ken	Abe	(Faculty of Engineering)
	Kyuya	Kodajima	(Faculty of Engineering)
	Keizo	Ishii	(Faculty of Engineering)
	Akira	Hasegawa	(Faculty of Engineering)
	Reimon	Hanada	(Institute for Materials Research)
	Minoru	Issiki	(Research Institute for Mineral) Dressing and Metallurgy)
	Tatsuo	Ido	(CYRIC)
	Takashi	Nakamura	(CYRIC)
	Masatoshi	Itoh	(CYRIC)
	Ren	Iwata	(CYRIC)
	Tsutomu	Shinozuka	(CYRIC)
	Astuki	Terakawa	(CYRIC)

Radiation Protection and Training of Safe Handling

(Chairman)	Tadashi	Yamada	(School of Dentistry)
	Yoshiaki	Fujii	(Faculty of Science)
	Hiroshi	Kudo	(Faculty of Science)

	Yoshio	Hosoi	(School of Medicine)
	Yoshihiro	Takai	(University Hospital)
	Kazuo	Ouchi	(Faculty of Pharmaceutical Sciences)
	Naohiro	Hirakawa	(Faculty of Engineering)
	Toshiyasu	Yamaguchi	(Faculty of Agriculture)
	Masayuki	Hasegawa	(Institute for Materials Research)
	Hiroshi	Fukuda	(Inute for Dstitevelopment, Aging and Cancer)
	Manabu	Fujioka	(CYRIC)
	Takashi	Nakamura	(CYRIC)
	Akira	Yamadera	(CYRIC)
	Akira	Nagamuma	(Faculty of Pharmaceutical Sciences)

Life Science

(Chairman)	Tatsuo	Ido	(CYRIC)
	Kazuo	Yamamoto	(Faculty of Science)
	Yasuhito	Itoyama	(School of Medicine)
	Kazuie	Iinuma	(School of Medicine)
	Syogo	Yamada	(School of Medicine)
	Masahiko	Yamamoto	(School of Medicine)
	Michinao	Mizugaki	(University Hospital)
	Shin	Maruoka	(University Hospital)
	Reizo	Shirane	(School of Medicine)
	Kazuo	Ouchi	(Faculty of Pharmaceutical Sciences)
	Keizo	Ishii	(Faculty of Engineering)
	Mieko	Kawamura	(Faculty of Agriculture)
	Hiroshi	Fukuda	(Institute for Development, Aging and Cancer)
	Kazuo	Kubota	(Institute for Development, Aging and Cancer)
	Manabu	Fujioka	(CYRIC)
	Takashi	Nakamura	(CYRIC)
	Masatoshi	Itoh	(CYRIC)
	Takehiko	Fujiwara	(CYRIC)
	Yoshihito	Funaki	(CYRIC)

Prevention of Radiation Hazards

(Chairman)	Takashi	Nakamura	(CYRIC)
	Takemi	Nakagawa	(Faculty of Science)
	Tsutomu	Sekine	(Faculty of Science)
	Ken	Abe	(Faculty of Engineering)
	Manabu	Fujioka	(CYRIC)
	Tatsuo	Ido	(CYRIC)
	Akira	Yamadera	(CYRIC)
	Takehiko	Fujiwara	(CYRIC)
	Muneo	Aoyama	(CYRIC)
	Takamoto	Miyata	(CYRIC)

VIII. PERSONNEL

VIII. Personnel (as of Jan. 1, 1998)

Director Hikonojo Orihara

Division of Accelerator

Manabu	Fujioka
Osamu	Hashimoto[1)]
Tsutomu	Shinozuka
Minoru	Tanigaki
Masahiro	Fujita
Shizuo	Kan[6)]
Shizuo	Chiba[6)]
Naoto	Takahashi[6)]
Yasuaki	Ohmiya[6)]

Division of Instrumentations

Hikonojo	Orihara
Keizo	Ishii[2)]
Astuki	Terakawa
Yasuhisa	Tajima
Sho-ichi	Watanuki
Tsutomu	Ichikawa

Division of Radiopharmaceutical Chemistry

Tatsuo	Ido
Ren	Iwata
Yoshihito	Funaki
Hiroaki	Wada
Hideo	Takahashi
Yo-ichi	Ishikawa[7)]

Division of Cyclotron Nuclear Medicine

Masatoshi	Itoh
Takehiko	Fujiwara
Kazuhiko	Yanai[4)]
Masayasu	Miyake

Division of Radiation Protection and Safety Control

Takashi	Nakamura
Akira	Yamadera
Takamoto	Miyata
Noboru	Watanabe[7)]

Graduate Student and Researcher

Yasumori	Kanai	(Graduate School, Division of Science)
Kenichi	Sekiguchi	(Graduate School, Division of Science)
Tsuyoshi	Hoshino	(Graduate School, Division of Science)
Takero	Baba	(Graduate School, Division of Science)
Kazuya	Itoh	(Graduate School, Division of Science)
Chong-Cheoul	Yun	(Graduate School, Division of Science)
Asaki	Yamamoto	(Graduate School, Division of Science)
Kenji	Kawami	(Graduate School, Division of Science)
Hiroshi	Suzuki	(Graduate School, Division of Science)
Gen	Kamurai	(Graduate School, Division of Science)
Hideyuki	Mizuno	(Graduate School, Division of Science)
Yasuo	Saito	(Graduate School, Division of Science)
Shinji	Nagata	(Graduate School, Division of Pharmaceutical Sciences)
Hiroyuki	Nagao	(Graduate School, Division of Pharmaceutical Sciences)
Minoru	Hatushika	(Graduate School, Division of Pharmaceutical Sciences)
Yoshikazu	Morita	(Graduate School, Division of Pharmaceutical Sciences)
Takehisa	Kawata	(Graduate School, Division of Pharmaceutical Sciences)
Yoshitaka	shimizu	(Graduate School, Division of Pharmaceutical

		Sciences)
Syozou	Furumoto	(Graduate School, Division of Pharmaceutical Sciences)
Nobuyuki	Okamura	(Graduate School, Division of Medicine)
Manabu	Tashiro	(Graduate School, Division of Medicine)
Yu-ichiro	Narita	(Graduate School, Division of Engineering)
Hossain	Deloar	(Graduate School, Division of Engineering)
Eun Ju Kim		(Graduate School, Division of Engineering)
Tadahiro	Kurosawa	(Graduate School, Division of Engineering)
Osamu	Satoh	(Graduate School, Division of Engineering)
Hiroyuki	Handa	(Graduate School, Division of Engineering)
Shingo	Taniguchi	(Graduate School, Division of Engineering)
Makoto	Nakao	(Graduate School, Division of Engineering)
Michiya	Sasaki	(Graduate School, Division of Engineering)
Miho	Shidahara	(Graduate School, Division of Engineering)
Takashi	Kuboyama	(Researcher)

Office Staff

Muneo	Aoyama
Hiroshi	Syoji
Hashime	Wako
Kyoko	Fujisawa
Seiji	Kikkukawa
Keietsu	Aizawa
Fumiko	Mayama
Mitsuko	Endo
Yu-ko	Yamashita
Yuri	Okumura
Noriko	Suzuki
Noriko	Fukuda
Hitomi	Inoue
Akari	Kagaya
Toshiyuki	Watanabe[7)]

1) Faculty of Science

2) Faculty of Engineering

3) Institute for Materials Research

4) School of Medecine

5) Institute for Development, Aging and Cancer

6) SUMI-JU Accelerator Service Ltd.

7) Japan Radiation Protection Co., Ltd.